DESIGN AND IMPLEMENTATION OF COUPLED INDUCTOR CUK CONVERTER OPERATING IN CONTINUOUS CONDUCTION MODE

A THESIS SUBMITTED TO
THE GRADUATE SCHOOL OF NATURAL AND APPLIED SCIENCES
OF
MIDDLE EAST TECHNICAL UNIVERSITY

BY

MUSTAFA TUFAN AYHAN

IN PARTIAL FULLFILLMENT OF THE REQUIREMENTS
FOR
THE DEGREE OF MASTER OF SCIENCE
IN
ELECTRICAL AND ELECTRONICS ENGINEERING

DECEMBER 2011

Approval of the thesis:

DESIGN AND IMPLEMENTATION OF COUPLED INDUCTOR CUK CONVERTER OPERATING IN CONTINUOUS CONDUCTION MODE

submitted by **MUSTAFA TUFAN AYHAN** in partial fulfillment of the requirements for the degree of **Master of Science in Electrical and Electronics Engineering Department, Middle East Technical University** by,

Prof. Dr. Canan ÖZGEN
Dean, Graduate School of **Natural and Applied Sciences** ____________

Prof. Dr. İsmet ERKMEN
Head of Department, **Electrical and Electronics Engineering** ____________

Prof. Dr. Aydın ERSAK
Supervisor, **Electrical and Electronics Engineering Dept., METU** ____________

Examining Committee Members:

Prof. Dr. Muammer ERMİŞ
Electrical and Electronics Engineering Dept., METU ____________________

Prof. Dr. Aydın ERSAK
Electrical and Electronics Engineering Dept., METU ____________________

Prof. Dr. Işık ÇADIRCI
Electrical and Electronics Engineering Dept., HU ____________________

Dr. Faruk BİLGİN
Space Technologies Research Institute, TÜBİTAK ____________________

Özgür YAMAN, M.Sc.
REHİS, ASELSAN ____________________

Date: 09.12.2011

I hereby declare that all information in this document has been obtained and presented in accordance with academic rules and ethical conduct. I also declare that, as required by these rules and conduct, I have fully cited and referenced all material and results that are not original to this work.

Name, Last name : Mustafa Tufan AYHAN

Signature :

ABSTRACT

DESIGN AND IMPLEMENTATION OF COUPLED INDUCTOR CUK CONVERTER OPERATING IN CONTINUOUS CONDUCTION MODE

AYHAN, Mustafa Tufan

M. Sc., Department of Electrical and Electronics Engineering
Supervisor: Prof. Dr. Aydın ERSAK

December 2011, 253 pages

The study involves the following stages: First, coupled-inductor and integrated magnetic structure used in Ćuk converter circuit topologies are analyzed and the necessary information about these elements in circuit design is gathered. Also, benefits of using these magnetic elements are presented. Secondly; steady-state model, dynamic model and transfer functions of coupled-inductor Ćuk converter topology are obtained via state-space averaging method. Third stage deals with determining the design criteria to be fulfilled by the implemented circuit. The selection of the circuit components and the design of the coupled-inductor providing ripple-free input current waveform are performed at this stage. Fourth stage introduces the experimental results of the implemented circuit operating in open loop mode. Besides, the controller design is carried out and the closed loop performance of the implemented circuit is presented in this stage.

Keywords: Ćuk converter, coupled-inductor, integrated magnetic structure, state-space averaging method

ÖZ

SÜREKLİ İLETİM KİPİNDE ÇALIŞAN BAĞLAŞIK İNDÜKTÖRLÜ CUK ÇEVİRİCİ TASARIMI VE GERÇEKLENMESİ

AYHAN, Mustafa Tufan

Yüksek Lisans, Elektrik Elektronik Mühendisliği Bölümü
Tez Yöneticisi: Prof. Dr. Aydın ERSAK

Aralık 2011, 253 sayfa

Bu çalışma şu aşamaları içermektedir: İlk olarak, Ćuk çevirici topolojilerinde kullanılan bağlaşık indüktör ve bütünleşmiş manyetik yapı analiz edilmektedir ve bu elemanlarla ilgili devre tasarımında gerekli olan bilgiler derlenmektedir. Ayrıca, bu manyetik elemanları kullanmanın sağladığı yararlar sunulmaktadır. İkinci olarak, durum uzayı ortalama metodu kullanılarak bağlaşık indüktörlü Ćuk çevirici topolojisine ait kararlı durum modeli, dinamik model ve transfer fonksiyonlar elde edilmektedir. Üçüncü aşama, gerçeklenecek devrenin yerine getirmesi gereken tasarım kıstaslarının tespitinden bahsetmektedir. Devre elemanlarının seçimi ve kıpırtısız giriş akım dalga formu sağlayan bağlaşık indüktörün tasarımı bu aşamada gerçekleştirilmektedir. Dördüncü aşama, gerçeklenen devrenin açık döngü kipinde çalışırkenki deneysel sonuçlarını ortaya koymaktadır. Ayrıca bu aşamada, denetleyici tasarımı gerçekleştirilmektedir ve gerçeklenen devrenin kapalı döngü performansı sunulmaktadır.

Anahtar Kelimeler: Ćuk çevirici, bağlaşık indüktör, bütünleşmiş manyetik yapı, durum uzayı ortalama metodu

To My Fiancée

And

Our Beloved Families

ACKNOWLEDGEMENTS

I would like to express my gratitude to my supervisor Prof. Dr. Aydın ERSAK for his guidance, advice, criticism, encouragement and insight throughout the completion of the thesis.

I am indebted to all of my friends and colleagues for their support and encouragements. I am also grateful to ASELSAN Inc. for the facilities that made my work easier and TÜBİTAK for the scholarship that supported my work.

Finally I am grateful to my family together with my fiancée and her family for their continuous support and encouragements.

TABLE OF CONTENTS

CHAPTERS

LIST OF TABLES

TABLES

LIST OF FIGURES

FIGURES

LIST OF ABBREVIATIONS

ADC	Analog to Digital Conversion
CCM	Continuous Conduction Mode
CIĆC	Coupled-Inductor Ćuk Converter
CICM	Constant Input Current Mode
CIPM	Constant Input Power Mode
DCM	Discontinuous Conduction Mode
ESR	Equivalent Series Resistance
IMĆC	Integrated Magnetic Ćuk Converter
LVR	Linear Voltage Regulator
MMF	Magneto Motive Force
PI	Proportional Integral
PWM	Pulse Width Modulation
SMPS	Switched-Mode Power Supply
SSAM	State-Space Averaging Method

NOMENCLATURE

L_1 / L_2	Input / output inductance of a basic or coupled-inductor Ćuk converter
Q	Switch (MOSFET) of a basic or coupled-inductor Ćuk converter
D	Complementary switch (diode) of a basic or coupled-inductor Ćuk converter
C_1	Energy transferring (middle) capacitance of a basic or coupled-inductor Ćuk converter or Primary side energy transferring capacitance of an integrated magnetic Ćuk converter
C_2	Secondary side energy transferring capacitance of an integrated magnetic Ćuk converter
C_o	Output capacitance of a basic or coupled-inductor Ćuk converter
K / k	Mean / instantaneous value of duty factor
f_s / T_s	Switching frequency / period
R_{L_1} / R_{L_2}	Parasitic resistance of input / output inductor
R_{C_1} / R_{C_o}	Parasitic resistance of energy transferring / output capacitor
R_{DS}	Drain-to-source on-state resistance of the switch (MOSFET)
R_D	On-state resistance of the diode
V_D	On-state voltage drop of the diode
N_1 / N_2	Number of turns of first (L_1) / second (L_2) winding (Turns)
Φ_1 / Φ_2	Instantaneous flux linkage of N_1 / N_2 winding (Weber)
Φ_m	Instantaneous mutual flux linking N_1 and N_2 windings

$\mathbb{R}_m$	Reluctance of the path of Φ_m (H^{-1})
Φ_{l1} / Φ_{l2}	Instantaneous leakage flux of the first / second winding
$\mathbb{R}_{l1}$ / $\mathbb{R}_{l2}$	Reluctance of the path of Φ_{l1} / Φ_{l2} generally through air
N_a / N_b	Number of turns of the transformer's primary / secondary winding (Turns)
Φ_a / Φ_b	Instantaneous flux linkage of the transformer's primary (N_a) / secondary (N_b) winding
	The summation of the core reluctance and the air gap if it exists
Φ_{la} / Φ_{lb}	Instantaneous leakage flux of the transformer's primary / secondary winding It links only the primary/secondary winding.
$\mathbb{R}_{la}$ / $\mathbb{R}_{lb}$	Reluctance of the path of Φ_{la} / Φ_{lb} generally through air
Φ_{lab}	Instantaneous flux linking transformer's both primary and secondary windings while linking neither of the inductors' windings In other words, it is that part of the mutual flux of the transformer's windings which does not link any of the inductor windings.
$\mathbb{R}_{lab}$	Reluctance of the path of Φ_{lab} generally through air
$\mathbb{R}_c$	Reluctance of the middle branch of the core (generally negligible among the reluctance of the intentional air gaps, namely $\mathbb{R}_1$ and $\mathbb{R}_2$)
$\mathbb{R}_1$ / $\mathbb{R}_2$	Reluctance of the left / right branch in Figure 2-27 It is the summation of the reluctance of the air gap on the left/right branch and the reluctance of the left/right branch of the core.
L_{11} / L_{22}	Self inductance of N_1 / N_2 winding
L_{12}	Mutual inductance between N_1 and N_2 windings
L_{l1} / L_{l2}	Leakage inductance of N_1 / N_2 winding
L_m / $L_m{}'$	Magnetizing inductance referred to L_1 / L_2 side
L_{aa} / L_{bb}	Self inductance of N_a / N_b winding
L_{1a}	Mutual inductance between N_1 and N_a windings (H)
L_{2b}	Mutual inductance between N_2 and N_b windings
L_{la} / L_{lb}	Leakage inductance of N_a / N_b winding
L_{l2}^{adj}	Additional leakage inductance (or adjustment inductor)

$L_1^{\mathrm{L_2\_open}}$	Measured inductance of L_1 winding while L_2 winding is open-circuited
$L_1^{\mathrm{L_2\_short}}$	Measured inductance of L_1 winding while L_2 winding is short-circuited
$L_2^{\mathrm{L_1\_open}}$	Measured inductance of L_2 winding while L_1 winding is open-circuited
$L_2^{\mathrm{L_1\_short}}$	Measured inductance of L_2 winding while L_1 winding is short-circuited
i_1 or i_{L_1}	Instantaneous value of input inductor current (A)
I_1 or I_{L_1}	Mean value of input inductor current
i_2 or i_{L_2}	Instantaneous value of output inductor current
I_2 or I_{L_2}	Mean value of output inductor current
I_{C_1} / i_{C_1}	Mean / instantaneous value of energy transferring capacitor current
I_{C_1} / i_{C_1}	Mean / instantaneous value of energy transferring capacitor current
$I_{C_1}^{rms}$ / $I_{C_o}^{rms}$	RMS value of energy transferring / output capacitor current
$I_{L_1}^{rms}$ / $I_{L_2}^{rms}$	RMS value of input / output inductor current
I_{C_o} / i_{C_o}	Mean / instantaneous value of output capacitor current
i_a / i_b	Instantaneous current value of the transformer's primary / secondary winding (A)
I_Q^{rms}	RMS value of the switch current
I_D^{rms} / I_D	RMS / mean value of the diode current
I_{tot}	Sum of the mean values of input and output inductor currents
I_{batt}	Current sourced by the li-ion battery pack
V_i / v_i	Mean / instantaneous value of the input voltage (V)
V_{C_o} / v_{C_o}	Mean / instantaneous value of output capacitor voltage
V_o / v_o	Mean / instantaneous value of output (load) voltage
V_{C_1} / v_{C_1}	Mean / instantaneous value of energy transferring capacitor voltage
V_o / v_o	Mean / instantaneous value of the output (load) voltage

V_{L_1} / v_{L_1}	Mean / instantaneous value of input inductor voltage
V_{L_2} / v_{L_2}	Mean / instantaneous value of output inductor voltage
V_{tot}	Sum of the mean values of input and output voltages
V_{batt}	Voltage of the li-ion battery pack
P_i / P_o	Mean value of input / output power of the converter (W)
P_Q^{on} / P_Q^{sw}	Power dissipation of the switch due to conduction / switching
P_Q^{tot}	Total power dissipation of the switch
P_D^{on}	Power dissipation of the diode due to conduction
$P_{C_1}^{each}$ / $P_{C_o}^{each}$	Power dissipation of each energy transferring / output capacitor
$P_{C_1}^{tot}$ / $P_{C_o}^{tot}$	Total power dissipation of all energy transferring / output capacitors
P_{L_1} / P_{L_2}	Resistive power dissipation of input / output inductor
$P_{L_2}^{adj}$	Resistive power dissipation of adjustment inductor
P_L^{tot}	Sum of resistive power dissipations of input, output and adjustment inductors
P_{sys}	Power demand of the system (load) or the military equipment
P_{batt}	Power delivered to the load by the li-ion battery pack
η	Efficiency of the converter (P_o/P_i)
F_{tot}	Resultant magneto-motive force of the coupled input and output inductors
B_{max}	Maximum magnetic flux density present in the core
δ	Skin-depth of a conductor (m)
ω	Angular frequency (radian/sec)
ρ	Electrical resistivity (for copper $\approx 1.68 \times 10^{-8}$Ωm @20C°)
μ_o	Magnetic permeability of free space (4π × 10^{-7} H/m)
μ_r	Relative magnetic permeability (for copper ≈ 1)
$x(t)$	$(n \times 1)$ vector consisting of state-variables. Symbol n is an integer.
X / $\tilde{x}(t)$	Mean / perturbed value of $x(t)$
$\dot{x}(t)$	$(n \times 1)$ vector consisting of derivatives of state-variables
$a(t)$	$(n \times n)$ matrix relating state-variables to their derivatives
A / $\tilde{a}(t)$	Mean / perturbed value of $a(t)$

$u(t)$	$(m \times 1)$ vector consisting of input variables. Symbol m is an integer.
U / $\tilde{u}(t)$	Mean / perturbed value of $u(t)$
$b(t)$	$(n \times m)$ matrix relating input variables to derivatives of state variables
B / $\tilde{b}(t)$	Mean / perturbed value of $b(t)$
$y(t)$	$(p \times 1)$ vector consisting of output variables. Symbol p is an integer.
Y / $\tilde{y}(t)$	Mean / perturbed value of $y(t)$
c(t)	(p × n) matrix relating state-variables to output variables
C / $\tilde{c}(t)$	Mean / perturbed value of $c(t)$
d(t)	(p × m) matrix relating input variables to output variables
D / $\tilde{d}(t)$	Mean / perturbed value of $d(t)$
$G_{v_o/k}$	Duty factor-to-output voltage transfer function of the converter with ideal elements
G_{v_o/v_i}	Input voltage-to-output voltage transfer function of the converter with ideal elements
G_{v_o/i_o}	Output current-to-output voltage transfer function of the converter with ideal elements
$G_{i_i/k}$	Duty factor-to-input current transfer function of the converter with ideal elements
G_{i_i/v_i}	Input voltage-to-input current transfer function of the converter with ideal elements
G_{i_i/i_o}	Output current-to-input current transfer function of the converter with ideal elements
$G^p_{v_o/k}$	Duty factor-to-output voltage transfer function of the converter with parasitic elements included
$G^p_{v_o/v_i}$	Input voltage-to-output voltage transfer function of the converter with parasitic elements included
$G^p_{v_o/i_o}$	Output current-to-output voltage transfer function of the converter with parasitic elements included

$G^{p}_{i_i/k}$	Duty factor-to-input current transfer function of the converter with parasitic elements included
$G^{p}_{i_i/v_i}$	Input voltage-to-input current transfer function of the converter with parasitic elements included
$G^{p}_{i_i/i_o}$	Output current-to-input current transfer function of the converter with parasitic elements included
V_o^{ref} / V_o^{err}	Output voltage reference / error
I_i^{ref} / I_i^{err}	Input current reference / error
G_C^{v} / G_C^{i}	Transfer function of output voltage / input current controller
Q_i / Q_v	Characteristic equation of the input current / output voltage control loop
G_{OL}^{i} / G_{CL}^{i}	Open-loop / closed-loop transfer function of the input current control loop
G_{OL}^{v} / G_{CL}^{v}	Open-loop / closed-loop transfer function of the output voltage control loop
K_p^{i} / K_i^{i}	Proportional / integral gain of the input current PI controller
K_p^{v} / K_i^{v}	Proportional / integral gain of the output voltage PI controller
T_{samp}	Sampling period of the control loops
$I_o^{no-load}$	No-load output current. Minimum required output current that should be drawn for proper output voltage regulation.

CHAPTER 1

INTRODUCTION

1.1 HISTORY

Dc-to-dc power conversion is performed either with linear voltage regulators, LVRs or with switched-mode power supplies, SMPS. LVRs can only decrease the input voltage i.e. boosting operation is impossible. Also, their efficiencies decrease linearly as the difference between the input and output voltages increases. Besides, isolation cannot be provided in LVR usage. However, since LVRs contain no switching action, their voltage and current waveforms are very clean. In SMPSs, however, switching instants can be observed at any voltage and current waveforms. Their efficiencies are under control up to a degree and can be very high. Isolation can also be provided in SMPS usage. Buck and/or boost operations are possible according to the circuit topology.

There exist some generic SMPS topologies and the derivatives of them. They can be categorized as isolated and non-isolated. Examples of the non-isolated converters are buck, boost, buck-boost, Ćuk and Sepic converters. Flyback, forward, push-pull and isolated half/full bridge converters are the examples of isolated dc-to-dc converters. Since an isolated SMPS contains an isolation transformer; its volume, weight and cost turn out to be higher than a non-isolated converter. Hence, isolated SMPSs are preferred only when isolation is needed. Besides, using an isolation transformer enables buck and boost operation if it is properly adjusted previously.

The topic of thesis has been determined according to a real need. As it will be explained in detail later, a dc-to-dc converter which is capable of both increasing and decreasing the input voltage is desired. Isolation is not needed. Especially the input current waveform is desired to be as ripple-free as possible. Based on these requirements, a converter type must be determined. While buck converter only decreases the input voltage, boost converter only increases it. Hence, they cannot be a solution. Buck-boost converter has a pulsating input current waveform, which is not desired. Sepic and Ćuk converters are the alternatives. Both of them have input inductors and provide a desirable input current waveform. However, an extension of Ćuk converter, namely coupled-inductor Ćuk converter, provides a better input current waveform. Therefore, the thesis concentrates on this topology. The detailed explanation on this choice will be given later.

1.2 THESIS ORGANIZATION

The thesis is organized as follows. In CHAPTER 2, theoretical analysis of the magnetic elements used in dc-to-dc Ćuk converter topologies, namely coupled-inductor and integrated magnetic structure, are given in details. Benefits of using these magnetic elements are presented there. As an addition, parasitic resistances are also included in the model and the necessary data in order to obtain a state-space model are prepared for coupled-inductor. In CHAPTER 3, state-space averaging method is used in order to introduce the steady-state and dynamic models of the coupled-inductor Ćuk converter both with ideal and parasitic elements. Also, the transfer functions of the circuits are obtained and verified by the simulations. CHAPTER 4 defines the operating conditions of the converter, determines the technical requirements and then presents the detailed design of a coupled-inductor Ćuk converter. The design and the selection of the circuit elements are verified by the simulations. Design of the circuit is followed by the design of the controller, in CHAPTER 5. By considering the control requirements of the circuit and using the derived transfer functions, a cascaded control loop of current mode control is formed and the transfer functions of suitable current and voltage controllers are obtained.

Then, how the controller functions will be implemented by a microcontroller, more specifically by a digital signal controller, is also discussed in this chapter. In CHAPTER 6, experimental results of the implemented circuit running in open-loop mode are given as a verification of the design. Especially, the operation of the implemented coupled-inductor is investigated. Then, the experimental results belonging to the closed-loop implementation of the circuit are presented. Dynamic response measurements of the circuit are presented as an evaluation of the controller performance. In CHAPTER 7, the overall work is evaluated and the important points are highlighted. Some concluding marks are noted, and the topics and discussions suitable for future works are presented.

1.3 CONTRIBUTIONS OF THESIS

In the thesis, repetition of the previous works is strictly tried to be avoided. It can be claimed that there is no essential contribution; however, there are many small contributions throughout the thesis. They are listed below.

The first contribution may be regarded in the coupled-inductor analysis. As mentioned in the references, using a coupled-inductor in Ćuk converter provides ripple-free input or output current waveforms if some conditions are satisfied. Derivations of these conditions have been performed by its inventor, Ćuk, in a clever way because he is aware of the physics behind it. In this thesis, however, reluctance model of the coupled-inductor and the claims, namely ripple-free input current or output current waveforms, are considered as the inputs to the analysis and the conditions are obtained as the outputs. By evaluating the feasibility of the conditions, the claims are verified. This derivation is evaluated as basic and systematic. Since it establishes a connection between the basic electrical and magnetic quantities, any magnetic element can be analyzed by utilizing or inspired by this derivation.

The second contribution is in the investigation of the effect of the parasitic elements on the ripple-free current waveforms in coupled-inductor Ćuk converter. It is shown by the simulations.

The third contribution is on the magnetic structure analysis. The same derivation method is followed in this method. This may be regarded as a contribution. More importantly, however, a contribution to the reluctance model of the magnetic structure is made. Using this model, the conditions for the ripple-free input and output current waveforms at the same time are obtained clearly, some of which are not mentioned explicitly in the references.

The fourth contribution can be regarded in composing a magnetic circuit in simulation programs. In most of the simulation programs, ordinary magnetic elements such as transformer and inductor can be used in an electrical circuit. However, any magnetic circuit/element different than the ordinary ones may be desired to implement and use in conjunction with an electrical circuit. At the beginning of the thesis, an immoderate difficulty has been faced with in the simulation of the Ćuk converter topologies including extraordinary magnetic elements. This difficulty is overcome by the magnetic circuit elements presented in Ansoft Simplorer. Explicitly showing the utilization of the magnetic circuit elements together with the electrical circuit elements in a simulation program is considered as an important contribution.

In design process, in order to provide coupling condition in the coupled-inductor, adjustment inductor method is suggested and implemented. Ćuk has preferred to adjust the air gap in order to provide coupling. Since it necessitates very sensitive positioning and seems to be not practical, adjustment inductor method is suggested. It is verified by the simulations and the implementation. Utilization of this method eases the implementation very much. Hence, it may be considered as a contribution.

Obtaining the possible transfer functions of the coupled-inductor Ćuk converter both with ideal elements and parasitic elements using state-space averaging method can be evaluated as another contribution.

Step by step design of a coupled-inductor Ćuk converter providing ripple-free input current waveform at the power rating of 250W can be regarded as a contribution. Important points in component selection are pointed out. More importantly, coupled-inductor design is realized in a detailed manner.

Open-loop experimental results of the designed and implemented coupled-inductor Ćuk converter seem to be a complementary contribution. By the help of the experimental results, all the claims throughout the thesis are proven to be practical or not.

Design and implementation of the control of a coupled-inductor Ćuk converter, CIĆC is evaluated as an important contribution. Owing to its four energy storing elements, basic Ćuk converter has fourth-order transfer functions. Furthermore, coupling of the inductors in CIĆC causes a non-minimum phase system, with some zeros on the right half-plane in s-domain. Control of such systems is known to be problematic. By utilizing the derived transfer functions of CIĆC with parasitic elements included, the controller transfer functions of the cascaded current and voltage loops are determined in a reasonable manner and a stable closed loop is obtained. The output variables does not deviate much even at the most dramatic load changes.

Digital PI control of CIĆC with a digital signal controller with the control loop frequency equal to the switching frequency is considered as an important contribution. Closing the control loop within a switching period (10usec) means that the duty-factor is refreshed at each switching cycle. This is actually what is done in analog control. Hence, the speed advantage of analog control is combined with the modifiability of digital control in this work.

CHAPTER 2

MATHEMATICAL ANALYSIS OF MAGNETIC ELEMENTS IN CUK CONVERTER TOPOLOGIES

2.1 INTRODUCTION

Analysis of basic Ćuk dc-to-dc converter topology has been investigated before in detail both with ideal elements and with parasitic elements.[2] That study forms the basis of this work. As an addition to [2], some derivations on basic Ćuk converter are given in this work. Those derivations are definitely needed for the design process. Since they may not appear to be closely related for the analysis purposes, they are given in the design section instead of this section.

At first, coupled-inductor Ćuk converter, CIĆC topology with both ideal and parasitic elements accounted in the circuit is handled in this section. Since the difficulty in analysis is on the coupled-inductor element and the rest is almost the same with basic Ćuk converter, only the analysis of coupled-inductor is presented here. The output of this analysis is used in the next chapter, and steady-state and dynamic models are developed there. Also, the benefits obtained by using coupled-inductor in this topology are given theoretically and verified by the simulation results in this chapter. Secondly, integrated-magnetic Ćuk converter, IMĆC topology with both ideal and parasitic elements is handled. Similarly, integrated-magnetic structure is emphasized. The benefits obtained by using integrated-magnetic structure in this topology are given theoretically and verified by the simulation results. Since this work mainly focuses on CIĆC, IMĆC is not dealt with in the rest of the work except this chapter. However, its advantages are desired to be presented and verified by simulation results as a complementary analysis in this chapter.

2.2 ANALYSIS OF COUPLED-INDUCTOR

Coupled-inductor analysis of Ćuk converter is divided into two: ideal model and parasitic model. The analyses of both of the models are accomplished because:

- Ideal model gives results which are easy-to-understand whereas parasitic model brings complexity to resultant equations. Complex equations may lead to loss of possible deductions from the equations. Hence, the analysis with ideal model seems to be necessary.
- Parasitic effects play an important role in the analysis. Since the theoretical results will be compared with the experimental results at the end, adding parasitic effects to the model makes the model outputs get closer to the experimental results.

2.2.1 Analysis of Ideal Model

Circuit schematic of CIĆC composed of ideal components only is seen in Figure 2-1. Dashed line between L_1 and L_2 represents the coupling of the inductors.

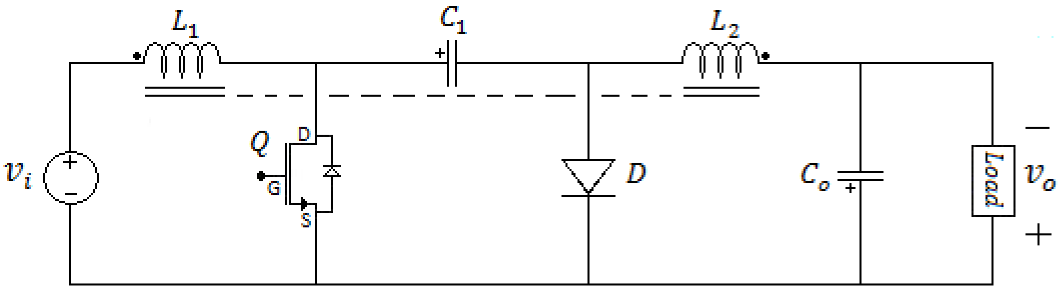

Figure 2-1 Circuit schematic of CIĆC with ideal elements

Coupled-inductor is obtained by winding both inductors' on the same magnetic core, just like in a transformer. Therefore, concepts such as mutual inductance, leakage inductance and turns ratio as in the case of a transformer also apply to the coupled-inductor. The only but important difference is that while the MMFs of the two windings –namely primary and secondary- are subtractive in transformers case, that of the coupled-inductor windings – namely L_1 and L_2- are additive in coupled-inductor case. Therefore, coupling leads to a situation that rather than the electrical model, its reluctance model is more proper to use in the analysis. The reluctance model of the coupled-inductor formed by input inductor, L_1 and output inductor, L_2 is shown in Figure 2-2.[16, 27]

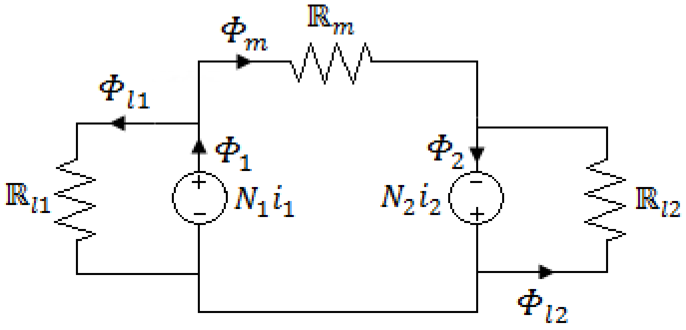

Figure 2-2 Reluctance model of a coupled-inductor [16, 27]

Transformers have almost the same reluctance model with the only difference in the respective polarities of MMFs $N_1 i_1$ and $N_2 i_2$.

As mentioned earlier, both electrical and magnetic circuits will be analyzed here. Voltage mesh equations will be utilized on both circuits. In magnetic circuit, node equations will also be needed.

The analysis of the converter will be made in continuous conduction mode, CCM in which there exist two modes: Mode 1 and Mode 2. The first applies to analysis within a time interval in which the switch, Q is in conduction, briefly referring as state 'on' and the diode, D not conducting, namely state 'off'. Mode 2 applies to analysis into the complementary time interval of Mode 1, i.e. the time interval in which Q is off and D is on. As expected, equations governing the behaviour of the converter electrical circuit in both modes differ from each other. Hence, electrical equations are grouped into two: Mode 1 and Mode 2. Unlike electrical equations, however, magnetic equations are same for both modes.

2.2.1.1 Electrical Mesh Equations

The following meshes are active in the equivalent circuit for CIĆC operating steadily in Mode 1. The superscripts ‘elc’ or ‘mag’ used in loop names are for the purpose of differentiation of the same names used in electrical and magnetic loops, respectively.

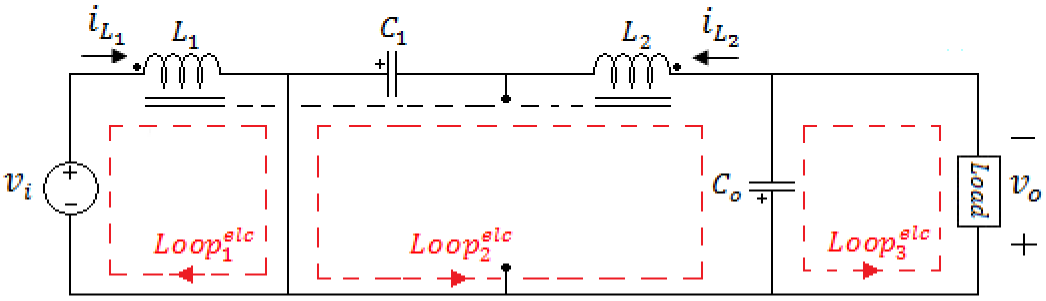

Figure 2-3 Active meshes in Mode 1 in the equivalent electrical circuit for CIĆC

Recalling that the instantaneous current, i_L through a simple inductor, L (i.e. not a coupled one) and the voltage, v_L developed on it are related over

$$v_L = L\frac{d}{dt}i_L \tag{2-1}$$

Since a coupled-inductor is a kind of transformer rather than an inductor, it is better to use the simplest relationship between flux and voltage given by Faraday’s law of induction as;

$$v = N\frac{d}{dt}\Phi \tag{2-2}$$

Throughout the analyses, voltages of the windings are replaced by the help of this law.

In Mode 1, (2-3)-(2-5) are the electrical mesh equations for the equivalent circuit:

$Loop_1^{elc}$: $-v_i + N_1 \frac{d}{dt}\Phi_1 = 0$ (2-3)

$Loop_2^{elc}$: $+v_{C_o} + N_2 \frac{d}{dt}\Phi_2 - v_{C_1} = 0$ (2-4)

$Loop_3^{elc}$: $-v_{C_o} + v_o = 0$ (2-5)

In Mode 2, active meshes in the equivalent circuit for CIĆC are shown in Figure 2-4.

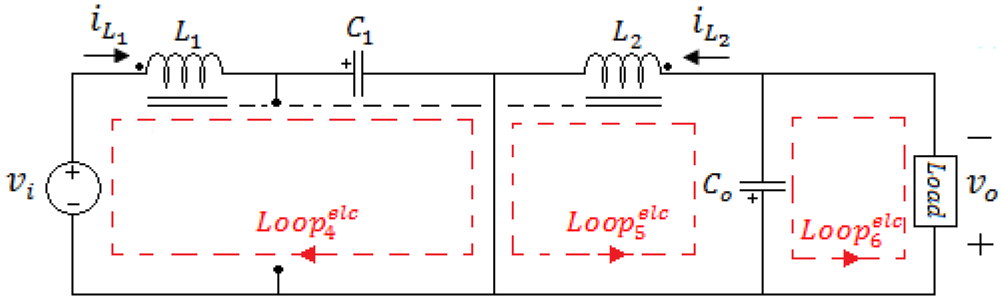

Figure 2-4 Active meshes in Mode 2 in the equivalent electrical circuit for CIĆC

Electrical mesh equations for this mode of operation are given as (2-6)-(2-8):

$Loop_4^{elc}$: $-v_i + N_1 \frac{d}{dt}\Phi_1 + v_{C_1} = 0$ (2-6)

$Loop_5^{elc}$: $+v_{C_o} + N_2 \frac{d}{dt}\Phi_2 = 0$ (2-7)

$Loop_6^{elc}$: $-v_{C_o} + v_o = 0$ (2-8)

2.2.1.2 Magnetic Mesh and Node Equations

The magnetic circuit for a coupled-inductor is shown in Figure 2-5. Mesh and node equations are given in (2-9)-(2-13) for such a circuit.

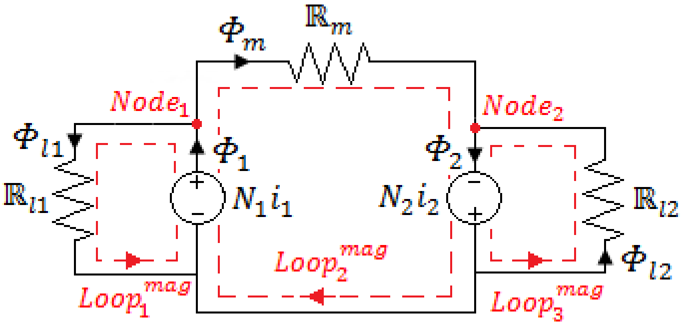

Figure 2-5 Meshes and nodes in the magnetic equivalent circuit for a coupled-inductor

$$Loop_1^{mag}: \qquad -N_1 i_1 + \mathbb{R}_{l1}\Phi_{l1} = 0 \tag{2-9}$$

$$Loop_2^{mag}: \qquad -N_1 i_1 + \mathbb{R}_m\Phi_m - N_2 i_2 = 0 \tag{2-10}$$

$$Loop_3^{mag}: \qquad -N_2 i_2 + \mathbb{R}_{l2}\Phi_{l2} = 0 \tag{2-11}$$

$$Node_1: \qquad -\Phi_1 + \Phi_{l1} + \Phi_m = 0 \tag{2-12}$$

$$Node_2: \qquad -\Phi_m - \Phi_{l2} + \Phi_2 = 0 \tag{2-13}$$

$\frac{d}{dt}\Phi_1$ and $\frac{d}{dt}\Phi_2$ terms should be obtained in order to proceed in electrical mesh equations. These terms can be obtained from magnetic mesh and node equations.

Using (2-12), (2-13), (2-9), (2-10) and (2-11) respectively:

$$\frac{d}{dt}\Phi_1 = \frac{d}{dt}\Phi_{l1} + \frac{d}{dt}\Phi_m \tag{2-14}$$

$$\frac{d}{dt}\Phi_2 = \frac{d}{dt}\Phi_{l2} + \frac{d}{dt}\Phi_m \tag{2-15}$$

$$\frac{d}{dt}\Phi_{l1} = \frac{N_1}{\mathbb{R}_{l1}}\frac{d}{dt}i_1 \tag{2-16}$$

$$\frac{d}{dt}\Phi_m = \frac{N_1}{\mathbb{R}_m}\frac{d}{dt}i_1 + \frac{N_2}{\mathbb{R}_m}\frac{d}{dt}i_2 \tag{2-17}$$

$$\frac{d}{dt}\Phi_{l2} = \frac{N_2}{\mathbb{R}_{l2}}\frac{d}{dt}i_2 \tag{2-18}$$

Using (2-14), (2-16) and (2-17):

$$\frac{d}{dt}\Phi_1 = \frac{N_1}{\mathbb{R}_{l1}//\mathbb{R}_m}\frac{d}{dt}i_1 + \frac{N_2}{\mathbb{R}_m}\frac{d}{dt}i_2 \tag{2-19}$$

Using (2-15), (2-18) and (2-17):

$$\frac{d}{dt}\Phi_2 = \frac{N_1}{\mathbb{R}_m}\frac{d}{dt}i_1 + \frac{N_2}{\mathbb{R}_{l2}//\mathbb{R}_m}\frac{d}{dt}i_2 \tag{2-20}$$

2.2.1.3 Combination of Electrical and Magnetic Equations

Derivatives of the fluxes are obtained in terms of the derivatives of the currents. Now, these results can be reflected to electrical mesh equations. As mentioned earlier, magnetic equations are independent of the switch state. Hence (2-19) and (2-20) are used for both electrical mesh equation sets.

In Mode 1, (2-21)-(2-23) are the magnetic mesh equations for the equivalent circuit:

Using (2-3) and (2-19):

$$v_i = \frac{N_1^2}{\mathbb{R}_{l1}//\mathbb{R}_m}\frac{d}{dt}i_1 + \frac{N_1N_2}{\mathbb{R}_m}\frac{d}{dt}i_2 \tag{2-21}$$

Using (2-4) and (2-20):

$$v_{C_1} - v_{C_0} = \frac{N_1N_2}{\mathbb{R}_m}\frac{d}{dt}i_1 + \frac{N_2^2}{\mathbb{R}_{l2}//\mathbb{R}_m}\frac{d}{dt}i_2 \tag{2-22}$$

Using (2-5):

$$v_{C_o} = v_o \tag{2-23}$$

In Mode 2, (2-24)-(2-26) are the magnetic mesh equations for the equivalent circuit:

Using (2-6) and (2-19):

$$v_i - v_{C_1} = \frac{N_1^2}{\mathbb{R}_{l1}//\mathbb{R}_m}\frac{d}{dt}i_1 + \frac{N_1N_2}{\mathbb{R}_m}\frac{d}{dt}i_2 \tag{2-24}$$

Using (2-7) and (2-20):

$$-v_{C_o} = \frac{N_1N_2}{\mathbb{R}_m}\frac{d}{dt}i_1 + \frac{N_2^2}{\mathbb{R}_{l2}//\mathbb{R}_m}\frac{d}{dt}i_2 \tag{2-25}$$

Using (2-8):

$$v_{C_o} = v_o \tag{2-26}$$

Note that all the parameters are in terms of electrical quantities while taking into account the magnetic connections and parameters.

In this work, state-space averaging method will be used in order to get steady-state and dynamic model of the circuit. State variables are inductor currents and capacitor voltages. Derivatives of capacitor voltages will be obtained in the next chapter. For the derivatives of inductor currents, however, basic inductor equation (2-1) cannot be used. Since a coupled-inductor is utilized, derivatives of inductor currents should be obtained in terms of electrical quantities. Further simplification of (2-21) and (2-22) in Mode 1 and (2-24) and (2-25) in Mode 2 gives the necessary and ready-to-use information for the derivatives of the inductor currents. (2-23) and (2-26) are written up to now just for mesh completeness and will not be used anymore. Further simplification of (2-21) and (2-22) in Mode 1 gives:

$$\frac{d}{dt}i_1 = \frac{-\alpha_1}{\Delta_1}v_{C_1} + \frac{\alpha_1}{\Delta_1}v_{C_0} + \frac{\alpha_2}{\Delta_1}v_i \tag{2-27}$$

$$\frac{d}{dt}i_2 = \frac{\alpha_3}{\Delta_1}v_{C_1} - \frac{\alpha_3}{\Delta_1}v_{C_0} - \frac{\alpha_4}{\Delta_1}v_i \tag{2-28}$$

where

$$\alpha_1 \overset{\text{def}}{=} \frac{N_1N_2}{\mathbb{R}_m} \qquad \alpha_2 \overset{\text{def}}{=} \frac{N_2^2}{\mathbb{R}_{l2}//\mathbb{R}_m} \tag{2-29}$$

$$\alpha_3 \overset{\text{def}}{=} \frac{N_1^2}{\mathbb{R}_{l1}//\mathbb{R}_m} \qquad \alpha_4 \overset{\text{def}}{=} \frac{N_1N_2}{\mathbb{R}_m} \tag{2-30}$$

$$\mathit{\Delta}_1 \overset{\text{def}}{=} \frac{N_1^2 N_2^2 (\mathbb{R}_{l1}+\mathbb{R}_{l2}+\mathbb{R}_m)}{\mathbb{R}_{l1}\mathbb{R}_{l2}\mathbb{R}_m} \tag{2-31}$$

(2-27) and (2-28) shows the representations of the derivatives of the inductor currents in terms of the state-variables, namely $v_{C_1}$and v_{C_0}, and the input variable, namely v_i, in Mode 1. Note that they do not include any flux-variable. When similar simplification is applied to (2-24) and (2-25) in Mode 2, the following equations are obtained:

$$\frac{d}{dt} i_1 = \frac{-\alpha_2}{\mathit{\Delta}_1} v_{C_1} + \frac{\alpha_1}{\mathit{\Delta}_1} v_{C_0} + \frac{\alpha_2}{\mathit{\Delta}_1} v_i \tag{2-32}$$

$$\frac{d}{dt} i_2 = \frac{\alpha_4}{\mathit{\Delta}_1} v_{C_1} - \frac{\alpha_3}{\mathit{\Delta}_1} v_{C_0} - \frac{\alpha_4}{\mathit{\Delta}_1} v_i \tag{2-33}$$

At this point (2-27)-(2-28) and (2-32)-(2-33) are left as inputs to the next chapter. This chapter continues with the merits of using coupled-inductor in basic Ćuk converter.

2.2.2 Merits of Coupling

In this section, by the help of some reasonable assumptions, merits of coupling will be proven theoretically. Those merits are either ripple-free input current waveform or ripple-free output current waveform. (2-21)-(2-22) and (2-24)-(2-25) are the input equations to this section. Then, some simplifications and assumptions are needed in order to proceed. These assumptions are either mentioned explicitly or implied in [8, 16, 26].

Assumption 2-1: Input voltage is constant.

$$v_i \cong V_i \tag{2-34}$$

Assumption 2-2: Voltage on the output capacitor, v_{C_o} is almost constant i.e. its voltage ripple is negligible.

$$v_{C_o} = v_o \cong V_{C_o} = V_o \tag{2-35}$$

Simplification 2-1: Mean value of the voltage on C_1, V_{C_1} is the sum of the mean value of the input voltage, V_i and the mean value of the output voltage, V_{C_o}.[2] This fact, which is obtained in CHAPTER 3, is also explained below in another way. When the outermost loop voltage equation –starting with v_i in the clockwise direction- is written, the following equation is obtained.

$$-v_i + v_{L_1} + v_{C_1} - v_{L_2} - v_o = 0 \tag{2-36}$$

As known, the mean values of the inductors' voltages are zero at steady-state.

$$V_{L_1} = 0 \tag{2-37}$$

$$V_{L_2} = 0 \tag{2-38}$$

Therefore, taking the mean values of both sides of the equation gives that:

$$V_{C_1} = V_i + V_o \tag{2-39}$$

Negligible ripple assumption permits this simplification be utilized in the electrical mesh equations.

Assumption 2-3: Voltage on C_1 capacitor, v_{C_1} is almost constant i.e. its voltage ripple is negligible.

$$v_{C_1} \cong V_{C_1} \tag{2-40}$$

As a result of these assumptions and the simplification, the following equation sets are obtained.

In Mode 1:

Using (2-21) and (2-34):

$$V_i = \frac{N_1^2}{\mathbb{R}_{l1}//\mathbb{R}_m}\frac{d}{dt}i_1 + \frac{N_1 N_2}{\mathbb{R}_m}\frac{d}{dt}i_2 \tag{2-41}$$

Using (2-22), (2-39), (2-34) and (2-35):

$$V_i = \frac{N_1 N_2}{\mathbb{R}} \frac{d}{dt} i_1 + \frac{N_2^2}{\mathbb{R}_{l2}//\mathbb{R}_m} \frac{d}{dt} i_2 \tag{2-42}$$

In Mode 2:

Using (2-24), (2-39), (2-34) and (2-35):

$$-V_o = \frac{N_1^2}{\mathbb{R}_{l1}//\mathbb{R}_m} \frac{d}{dt} i_1 + \frac{N_1 N_2}{\mathbb{R}_m} \frac{d}{dt} i_2 \tag{2-43}$$

Using (2-25) and (2-35):

$$-V_o = \frac{N_1 N_2}{\mathbb{R}_m} \frac{d}{dt} i_1 + \frac{N_2^2}{\mathbb{R}_{l2}//\mathbb{R}_m} \frac{d}{dt} i_2 \tag{2-44}$$

Following two sections present the conditions for ripple-free current either at input or output and also the simulation results that verify the theoretical analyses.

2.2.2.1 Ripple-Free Input Current

The requirement is to obtain ripple-free input current. Input current is the same as the current of L_1, i_{L_1} or simply i_1.

$$i_i = i_{L_1} = i_1 \overset{\text{def}}{=} I_1 \tag{2-45}$$

Since it is constant, its derivative is zero.

$$\frac{d}{dt} i_1 = \frac{d}{dt} I_1 = 0 \tag{2-46}$$

When this condition is applied to (2-41)-(2-44), some restrictions arises. If those restrictions turn out to be applicable, it means that zero-ripple input current waveform is possible to obtain. Moreover, the restrictions should be applicable for both modes.

In Mode 1:

Using (2-41) and (2-46):

$$V_i = \frac{N_1 N_2}{\mathbb{R}_m} \frac{d}{dt} i_2 \tag{2-47}$$

Using (2-42) and (2-46):

$$V_i = \frac{N_2^2}{\mathbb{R}_{l2} // \mathbb{R}_m} \frac{d}{dt} i_2 \tag{2-48}$$

In Mode 2:

Using (2-43) and (2-46):

$$-V_o = \frac{N_1 N_2}{\mathbb{R}_m} \frac{d}{dt} i_2 \tag{2-49}$$

Using (2-44) and (2-46):

$$-V_o = \frac{N_2^2}{\mathbb{R}_{l2} // \mathbb{R}_m} \frac{d}{dt} i_2 \tag{2-50}$$

For the input current to be ripple-free in Mode 1, the following condition has to be satisfied.

Using (2-47) and (2-48):

$$\frac{N_1 N_2}{\mathbb{R}_m} = \frac{N_2^2}{\mathbb{R}_{l2} // \mathbb{R}_m} \tag{2-51}$$

The same condition is also required for the input current to be ripple-free in Mode 2.

Using (2-49) and (2-50):

$$\frac{N_1 N_2}{\mathbb{R}_m} = \frac{N_2^2}{\mathbb{R}_{l2} // \mathbb{R}_m} \tag{2-52}$$

Since the same condition makes the input current ripple-free in both modes, namely the entire period, it can be proven that applying this condition satisfies to obtain a ripple-free input current. (2-52) can be simplified into the following form.

$$\frac{N_1}{N_2} = \frac{\mathbb{R}_m}{\mathbb{R}_{l2}//\mathbb{R}_m} \tag{2-53}$$

Since $\mathbb{R}_{l2}$ is much larger than $\mathbb{R}_m$, equivalent reluctance of $\mathbb{R}_{l2}//\mathbb{R}_m$ turns out to be a little bit smaller than $\mathbb{R}_m$. Hence, (2-53) dictates that N_1 has to be a little bit larger than N_2, which seems to be reasonable and applicable.

Simply equating (2-47) to (2-48) and (2-49) to (2-50) gives the requirement for ripple-free input current mathematically. How can it be possible? What is its physical interpretation? There is a condition here. Actually, the left hand sides of these four equations represent the voltage applied to the windings. V_i is applied to inductors in Mode 1 and $-V_o$ in Mode 2. That is, inductors have the same voltage waveforms. It is this result which leads to an applicable condition on turns ratio and reluctances. Otherwise, the resultant condition would turn out to be meaningless and not applicable, which would imply that ripple-free input current is not possible.

When it is worked on, it is seen that the exact condition on coupling the inductors is a little bit different: Inductors have to have proportional waveforms rather than equal.[8, 10, 13] Although it was first suggested by Ćuk, coupled-inductor is not specific to Ćuk converter only. It can be used in output filter inductors of multiple output converters, as well. There, voltage waveforms of output inductors are not generally equal but proportional. Since only Ćuk converter is considered in this work and it has equal voltage waveforms on its coupled-inductors, proportional voltage waveform condition will not be proven here.

Now, ripple-free input current analysis will be proven by simulation. Ansoft Simplorer simulation program will be used for this purpose. It presents the facility of designing any magnetic element and establishing any magnetic circuitry. In that program, coupled-inductor can be implemented in two ways. It only differs according to the implementation of the leakage inductances.

In Figure 2-6, first possible CIĆC implementation in Simplorer is shown. It is a snapshot of the circuit implementation in the simulation program. Only the labels are modified in order to provide label consistency. Orange lines represent magnetic connections. N_1 and N_2 generate $N_1 i_{L_1}$ and $N_2 i_{L_2}$ MMFs respectively. In this configuration, leakage inductances are implemented in electrical circuit side.

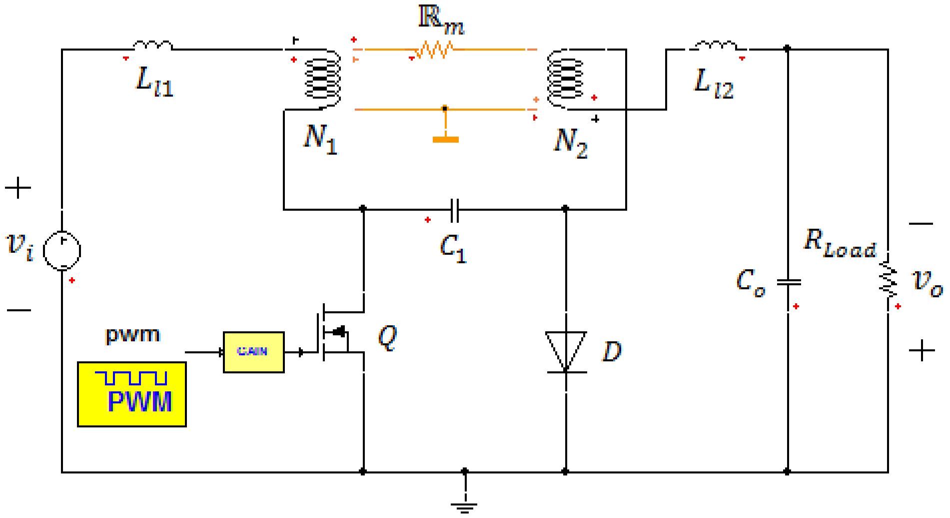

Figure 2-6 First possible CIĆC implementation in Simplorer

In second possible configuration, leakage inductances are also embedded in magnetic circuit side as shown in Figure 2-7. Leakage parameters in these

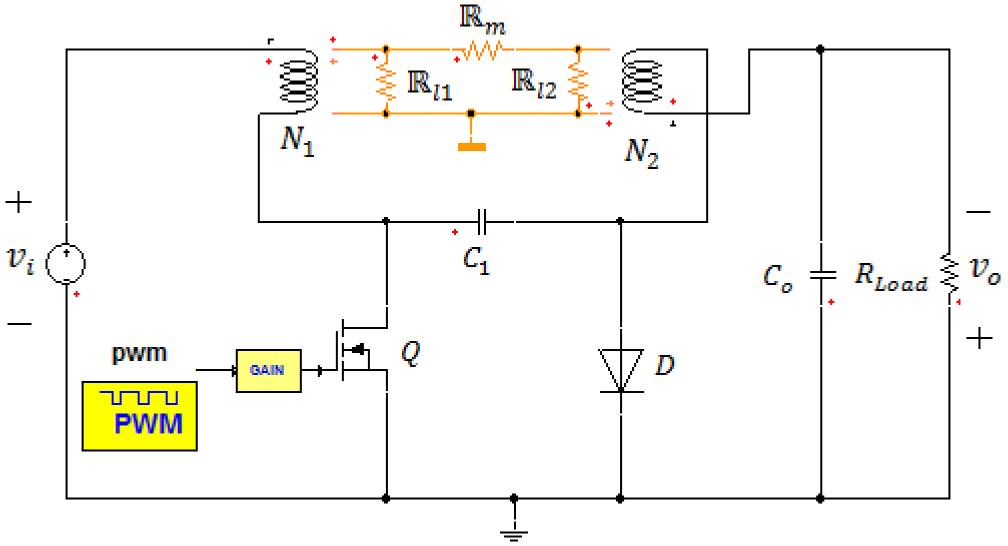

Figure 2-7 Second possible CIĆC implementation in Simplorer

configurations are related to each other as dictated by (2-63) and (2-64). Both configurations give the same waveform results.

Simulation is conducted at the following operating point.

$f_s = 100kHz$

$V_i = 10\,V$

$V_o \approx 24\,V$

$P_i = 262\,W$

$P_o = 262\,W$

Simulation is performed with the ideal electrical components. In other words; the switch, the diode and the capacitors are assumed to be ideal. C_1 and C_o are the ones that have been selected in the design chapter in terms of capacitance values.

Q: Ideal switch

D: Ideal diode

C_1: Ideal capacitor, 3000uF

C_o: Ideal capacitor, 23.5uF

As a magnetic element, the following values are used. These values belong to the designed coupled-inductor in the design chapter. Detailed information is presented there.

$N_1 = 19.5\,Turns$

$N_2 = 18.25\,Turns$

$\mathbb{R}_m = 3.037 \times 10^6\,H^{-1}$

$\mathbb{R}_{l1} = 345.682 \times 10^6\,H^{-1}$

$\mathbb{R}_{l2} = 44.408 \times 10^6\,H^{-1}$

Above values give the following parameters.

$L_m = 125.2\,uH$

$L_m{}' = 109.7\,uH$

$L_{l1} = 1.1\,uH$

$L_{l2} = 7.5\,uH$

$L_{12} = 117.2\,uH$

$L_{11} = 126.3\,uH$

$L_{22} = 117.2\,uH$

As adjusted beforehand, L_{12} and L_{22} turn out to be equal. With these parameters, the input current is expected to be constant. In Figure 2-8, almost ripple-free input current, i_{L_1} waveform is seen as trace 1 (blue). Trace 2 (red) is L_2 current, i_{L_2}. Current-axis is in ampere and time-axis is in second, like all the other current-time graphs of the simulation results throughout this work. Note that the envelope of i_{L_1} waveform is very thin and negligible with respect to its mean value.

Figure 2-8 i_{L_1} and i_{L_2} waveforms in ripple-free input current case at full load

Figure 2-9, shows the input current in much detailed form. The maximum of i_{L_1} is seen as 26.292A and with the minimum is at 26.217A. Its ripple percent is not zero but 0.29%. Actually, this result is expected because of the assumptions made in the analysis. Still, the result is considered as satisfactory. Besides, an oscillation to which the switching ripple is superimposed is observed in i_{L_1} waveform. Its period is seen to be approximately eight times the switching period. This oscillation may be the resonance between the inductors and capacitors. Since the ideal electrical elements are used and no damping element such as parasitic resistances exists in the circuit, resonance may be observed seriously.

i_{L_2} waveform is shown in Figure 2-10. Its average is 10.68A and peak-to-peak ripple current amplitude is 0.7A. Hence, 6.5% ripple content is seen in this operating point in i_{L_2}. Generally, 20% peak-to-peak ripple current at the worst case at full load is regarded as reasonable in inductor design.[5] This limitation is adopted in this work. However, this operating point is not the worst case. Instead, it is probably the best case, because the currents are at their maximum. This is why there is a big

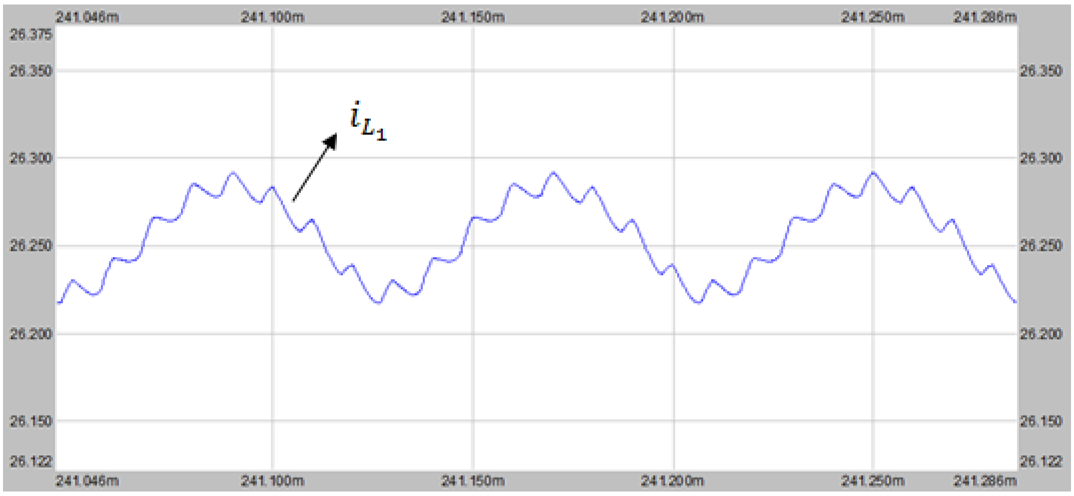

Figure 2-9 Detailed i_{L_1} waveform in ripple-free input current case at full load

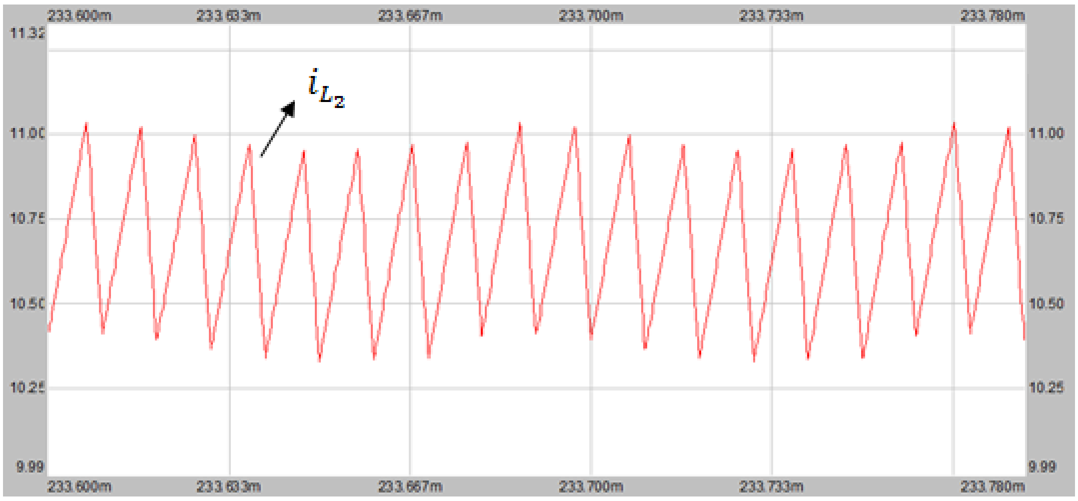

Figure 2-10 Detailed i_{L_2} waveform in ripple-free input current case at full load

gap between 6.5% and 20%, and small gap between 6.5% and 0.29%. Besides, note that the same oscillation is observed in i_{L_2} waveform.

As mentioned earlier, ripple-free property is independent of current and voltage levels. To show this fact, the load resistance is increased to its 500%. Envelopes of the resultant current waveforms are presented in Figure 2-11. As seen in Figure 2-12, i_{L_1} is again almost ripple-free. Its maximum is 5.362A and minimum is 5.348A. As a result, peak-to-peak ripple percent is 0.26%.

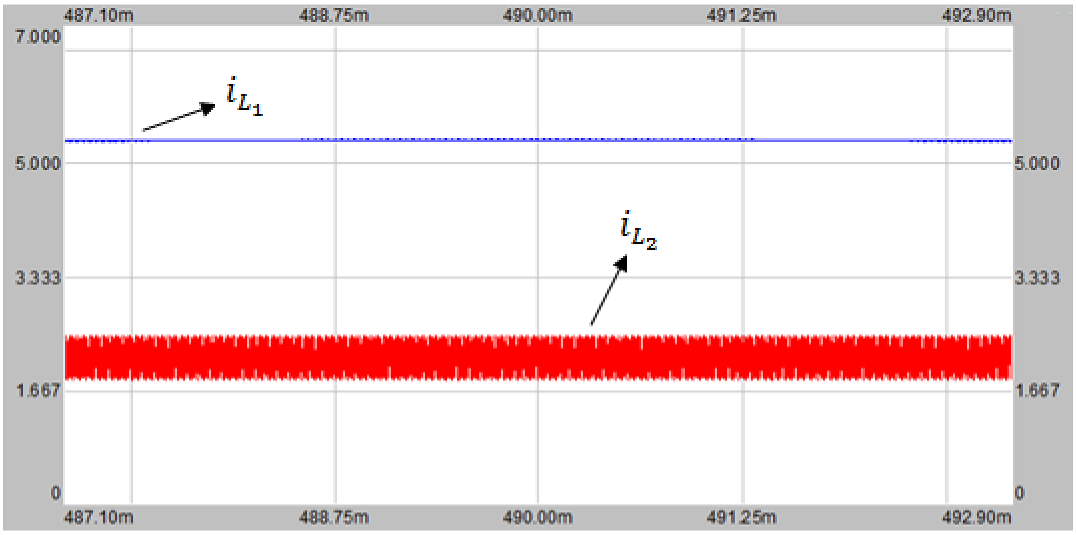

Figure 2-11 i_{L_1} and i_{L_2} waveforms in ripple-free input current case at light load

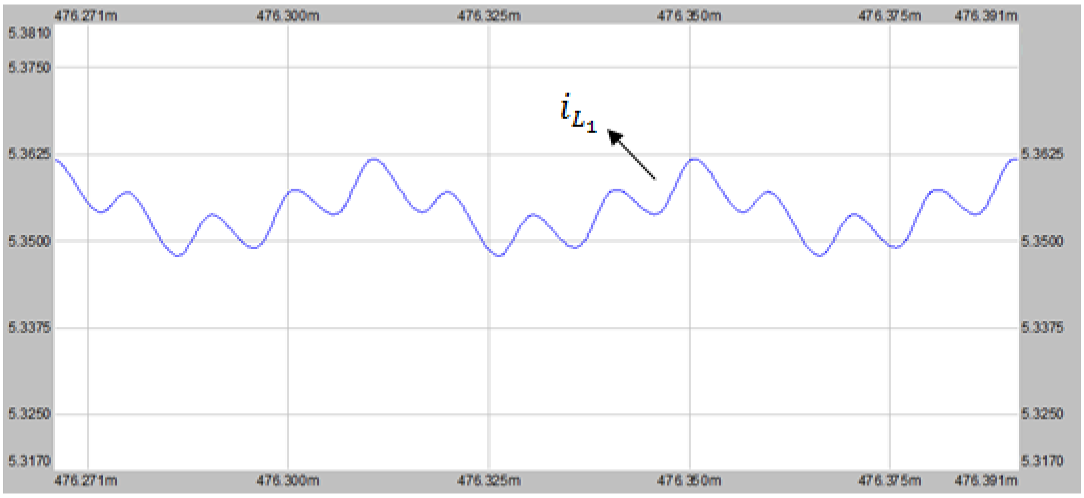

Figure 2-12 Detailed i_{L_1} waveform in ripple-free input current case at light load

i_{L_2} waveform is shown in Figure 2-13. Its maximum is 2.47A and minimum is 1.82A. Peak-to-peak ripple amplitude of i_{L_2} remains almost the same, but its average decreases as expected. Hence, its ripple percent increases to 30.3% at this light load. These waveforms and multiples of them, which are not given in order to prevent graph redundancy, prove the independency of ripple-free waveform from current levels. Since its voltage independency is obvious, the simulation result of it is not needed to be given here.

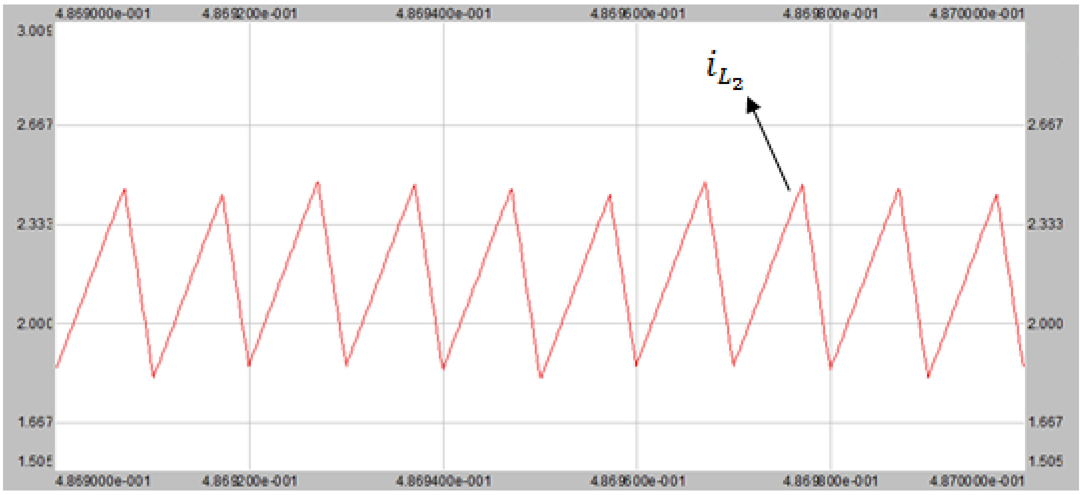

Figure 2-13 Detailed i_{L_2} waveform in ripple-free input current case at light load

The ripple-free input current condition in (2-53) dictates about the proportion between the input and the output inductances only, and says nothing about the inductance values. From this condition, it is understood that the ripple-free input current can be obtained as long as the condition is satisfied and it is independent of the inductance values. Since the input current is ripple-free, the allowable output current ripple percent is determined first and then the required output inductance is obtained. Once the output inductance is determined, what the input inductance should be is found automatically by the help of (2-53). An example may clarify the explanations above: If the inductances were halved while conserving the ripple-free input current condition, ripple percent of i_{L_2} would double but i_{L_1} would still remain as ripple-free. This fact is also observed in simulation but the result is not given here. This argument is also valid for the ripple-free output current case.

Another argument is about decoupling of the inductors. If inductors were decoupled without changing their inductances, i_{L_2} would show the same waveform and i_{L_1} would have a waveform and ripple content similar to i_{L_2}. Further information on this issue can be found in [8, 10].

2.2.2.2 Ripple-Free Output Current

This time the requirement is to obtain a ripple-free output current. The output current is not the same as i_{L_2} because of the intervention of output capacitor current. However, constant output current requirement brings the fact that output capacitor current is always zero. Hence, i_{L_2} is equal to the output current for this requirement.

$$i_o = i_{L_2} = i_2 \overset{\text{def}}{=} I_2 \tag{2-54}$$

In this case, i_2 current is defined as a constant.

$$\frac{d}{dt} i_2 = \frac{d}{dt} I_2 = 0 \tag{2-55}$$

The same procedure is applied for ripple-free output current case. At the end, the following condition is obtained for a ripple-free output current waveform.

Using (2-41)-(2-44) and (2-55):

$$\frac{N_1 N_2}{\mathbb{R}_m} = \frac{N_1^2}{\mathbb{R}_{l1} // \mathbb{R}_m} \tag{2-56}$$

Further simplification gives that:

$$\frac{N_1}{N_2} = \frac{\mathbb{R}_{l1} // \mathbb{R}_m}{\mathbb{R}_m} \tag{2-57}$$

Similarly, since $\mathbb{R}_{l1}$ is much larger than $\mathbb{R}_m$, equivalent reluctance of $\mathbb{R}_{l1}//\mathbb{R}_m$ turns out to be a little bit smaller than $\mathbb{R}_m$. Hence, (2-57) dictates that N_2 has to be a little bit larger than N_1. As a result, remembering the ripple-free input current case, the side which is desired to have ripple-free current waveform should have a little bit larger number of turns.

The requirement for coupling the inductors –namely proportional voltage waveforms on inductors- also applies here.

Now, ripple-free output current waveform will be verified by simulation. For this purpose, there is no need to design a new coupled-inductor. Just toggling L_1 and L_2 in ripple-free input current case is enough. That is, the same parameters will be used, but N_1-N_2 and $\mathbb{R}_{l1}$-$\mathbb{R}_{l2}$ values will be interchanged.

$N_1 = 18.25\ Turns$ $\qquad$ $N_2 = 19.5\ Turns$

$\mathbb{R}_m = 3.037 \times 10^6\ H^{-1}$ $\qquad$ $\mathbb{R}_{l1} = 44.408 \times 10^6\ H^{-1}$

$\mathbb{R}_{l2} = 345.682 \times 10^6\ H^{-1}$

These parameters give that:

$L_m = 109.7\ uH$ $\qquad$ $L_m{}' = 125.2\ uH$

$L_{l1} = 7.5\ uH$ $\qquad$ $L_{l2} = 1.1\ uH$

$L_{12} = 117.2\ uH$ $\qquad$ $L_{11} = 117.2\ uH$

$L_{22} = 126.3\ uH$

In this situation, $L_{12} = L_{11}$ is satisfied and output current is expected to be ripple-free. As seen in Figure 2-14, Figure 2-15 and Figure 2-16; i_{L_2} is almost ripple-free and i_{L_1} has considerable ripple content as expected. In these figures, again trace 1 (blue) represents i_{L_1} and trace 2 (red) i_{L_2}. Envelopes of the current waveforms are shown in Figure 2-14. Envelope of i_{L_2} is very thin, which means that its ripple content is very low.

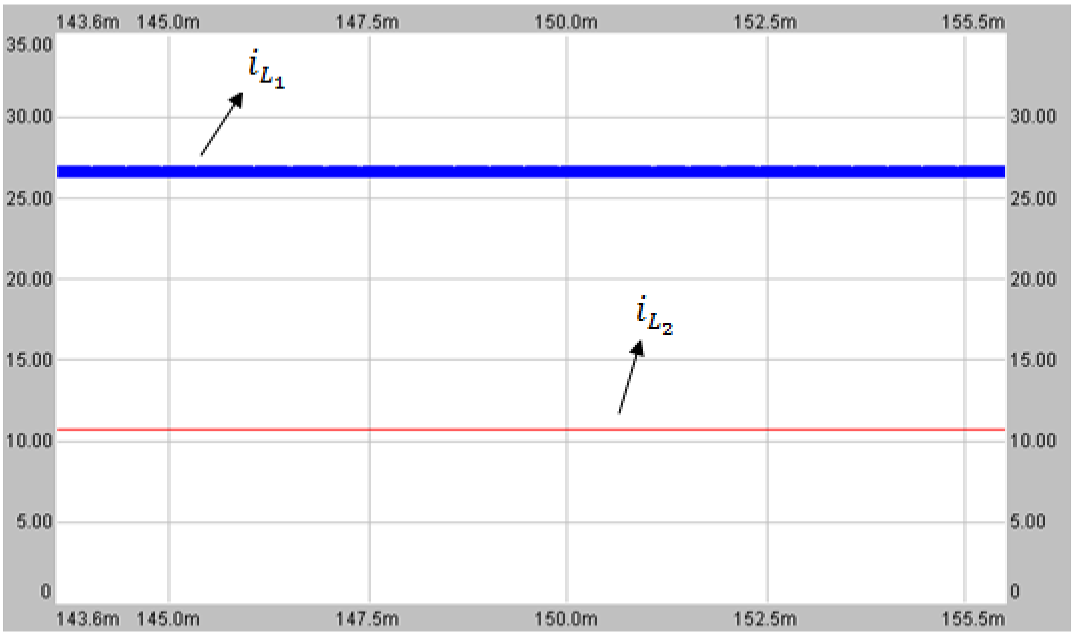

Figure 2-14 i_{L_1} and i_{L_2} waveforms in ripple-free output current case at full load

Detailed i_{L_1} waveform is seen in Figure 2-15. Its maximum is 26.97A and minimum is 26.33A. Its ripple percent is calculated as 2.4%. Note that whereas i_{L_2} ripple percent in ripple-free input current case is 6.5%, i_{L_1} ripple percent in

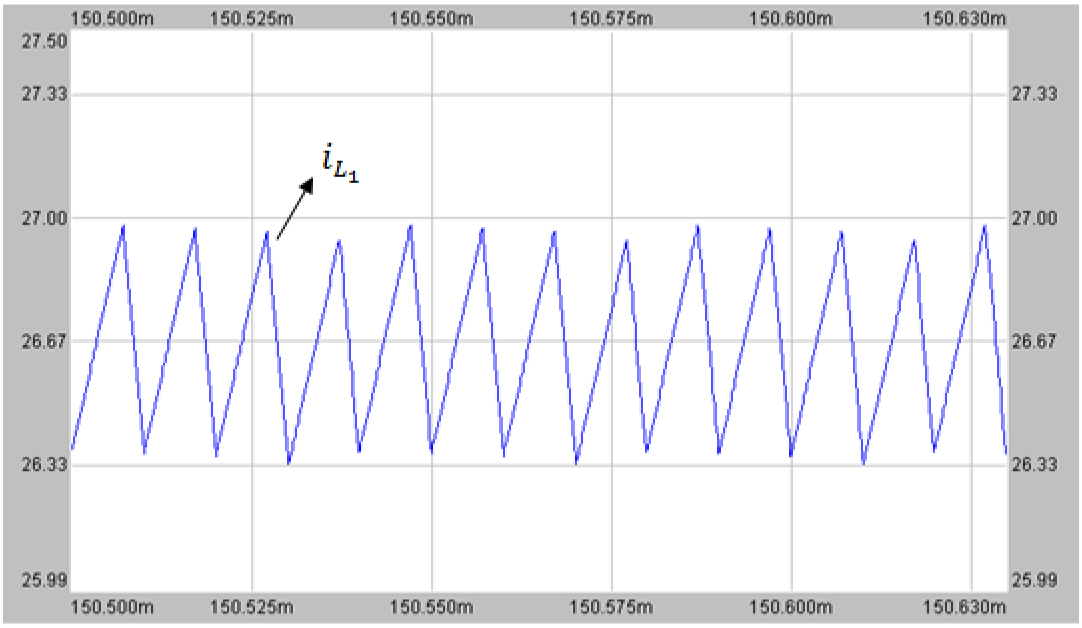

Figure 2-15 Detailed i_{L_1} waveform in ripple-free output current case at full load

ripple-free output current case is 2.4% with the same inductance values. Actually, this is an expected result. Since the inductances and the operating points are the same, current ripple amplitudes are also the same. However, since the mean value of i_{L_1} is about 2.7 times that of i_{L_2}, current ripple percents show the inverse of the same ratio.

As expected, the ripple percent of i_{L_2} is about 0.04%. It is almost ripple-free. This result is shown in Figure 2-16.

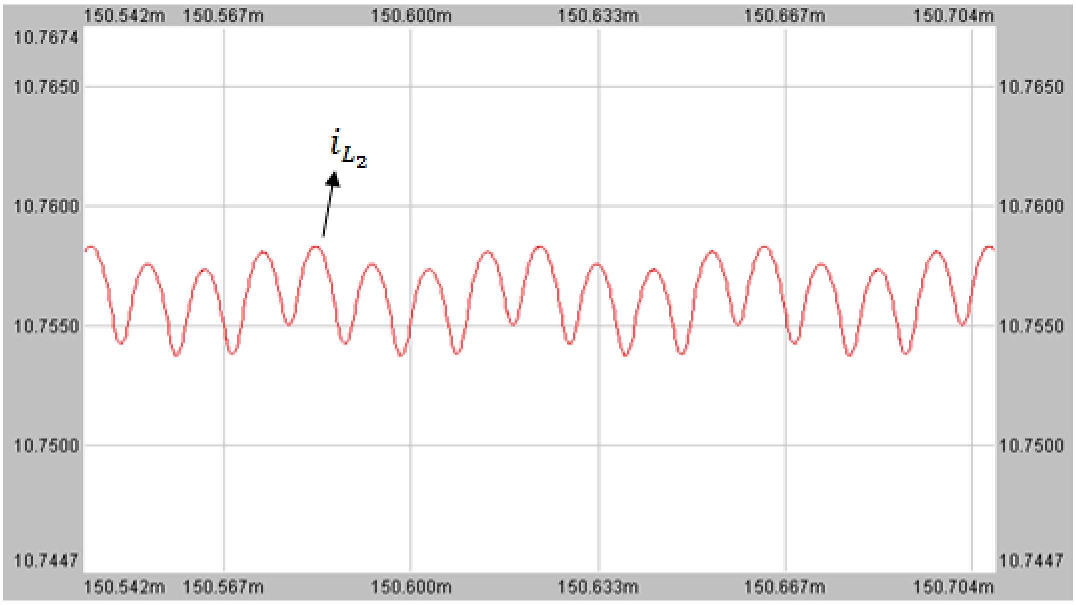

Figure 2-16 Detailed i_{L_2} waveform in ripple-free output current case at full load

Independency of ripple-free output current property from current and voltage levels can be similarly proven as performed in ripple-free input current case.

2.2.2.3 Physical Interpretation

The analysis of 'ripple-free Ćuk converter on one side only (either on input or output)' is completed. What the conditions (2-53) and (2-57) say can be physically explained and verified by derivations of leakage inductance, mutual inductance, magnetizing inductance, self inductance, coupling coefficient and effective turns ratio terms. Ćuk generally prefers to express the conditions in terms of coupling coefficient (k) and effective turns ratio (n) definitions. Since physical parameters give the simplest understandable conditions, they are preferred in this work. Ćuk has also used these physical parameters in expressing the conditions.[16] Those derivations which form a bridge between the conditions expressed in terms of k and n definitions and physical parameters can be found in [24]. Actually, all says the same thing but with different terms. For example, one-to-one corresponding condition of (2-53) is:

$$L_{12} = L_{22} \tag{2-58}$$

In other words, if input current is desired to be ripple-free, mutual inductance between L_1 and L_2 must be equal to the self inductance of L_2. Similarly, one-to-one corresponding condition of (2-57) is:

$$L_{12} = L_{11} \tag{2-59}$$

That is to say, if output current is desired to be ripple-free, mutual inductance between L_1 and L_2 must be equal to the self inductance of L_1.

As a physical interpretation, another explanation is given below. Consider a coupled-inductor model in Figure 2-17. As mentioned in [10], it is T model of a transformer at the same time. The only difference is the direction of i_{L_2}. While four

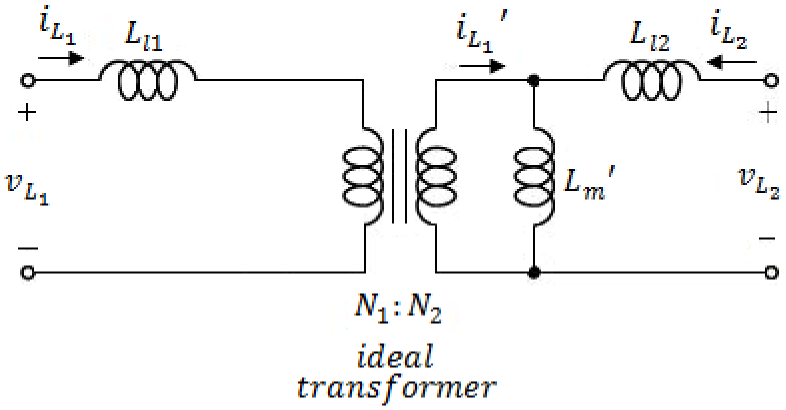

Figure 2-17 Equivalent coupled-inductor model

electrical variables ($v_{L_1}, v_{L_2}, i_{L_1}, i_{L_2}$) are all positive or negative with respect to the model in coupled-inductor operation, the polarity of i_{L_2} is the inverse of the other three variables in transformer operation with respect to the model in Figure 2-17.

The derivations of the following basic relationships can be found in [24].

$$L_m = \frac{{N_1}^2}{\mathbb{R}_m} \tag{2-60}$$

$$L_m' = \frac{{N_2}^2}{\mathbb{R}_m} = \frac{{N_2}^2}{{N_1}^2}\frac{{N_1}^2}{\mathbb{R}_m} = \frac{{N_2}^2}{{N_1}^2}L_m \tag{2-61}$$

$$L_{12} = L_{21} = \frac{N_1 N_2}{\mathbb{R}_m} = L_m\frac{N_2}{N_1} = L_m'\frac{N_1}{N_2} \tag{2-62}$$

$$L_{l1} = \frac{{N_1}^2}{\mathbb{R}_{l1}} \tag{2-63}$$

$$L_{l2} = \frac{{N_2}^2}{\mathbb{R}_{l2}} \tag{2-64}$$

$$L_{11} = L_m + L_{l1} \tag{2-65}$$

$$L_{22} = L_m' + L_{l2} \tag{2-66}$$

By using these basic relationships, ripple-free current conditions can be obtained. Let’s consider the ripple-free input current case. For i_{L_1} to be ripple-free, voltage on L_{l1} should always be zero, otherwise L_{l1} current –hence i_{L_1}- would change. How can it be possible? If voltage applied to the negative terminal of L_{l1} is always equal to the voltage applied to the positive terminal of L_{l1}, its current remains at the same level. It is known that v_{L_1} is equal to v_{L_2}. Let it be v. Although they have two different values in a period, they are always equal in time.

$$v_{L_1} = v_{L_2} = v \tag{2-67}$$

Then, by voltage division rule, voltage on L_m' is calculated as in (2-68). At first look it seems that i_{L_1}' current interferes with i_{L_2}, hence voltage division cannot be applied. However, this voltage division is due to the derivative of the current term rather than the current itself. Since ${i_{L_1}}'$ is constant, voltage division can be applicable. That is, there is no voltage induced on ${L_m}'$ due to ${i_{L_1}}'$.

$$v_{L_m'} = v\frac{{L_m}'}{{L_m}'+L_{l2}} \tag{2-68}$$

Since the same flux links the both windings, voltages induced on L_m and ${L_m}'$ are proportional to their number of turns.

$$v_{L_m} = v\frac{{L_m}'}{{L_m}'+L_{l2}}\frac{N_1}{N_2} \tag{2-69}$$

Using (2-69), (2-62) and (2-66):

$$v_{L_m} = v\frac{L_{12}}{L_{22}} \tag{2-70}$$

As stated in (2-58), L_{12} is adjusted to be equal to L_{22} for ripple-free input current case. That condition leads to the following simplification.

$$v_{L_m} = v \tag{2-71}$$

Voltage applied to the negative terminal of L_{l1} is found to be v. Since the voltage applied to the positive terminal of L_{l1} is also v, L_1 current remains constant. Note that it is valid as long as the voltages applied to both windings are the same and independent of the voltage or current levels. Similarly, the same procedure can be applied to the ripple-free output current case and the same results can be obtained.

2.2.3 Analysis of Parasitic Model

Circuit schematic of coupled-inductor Ćuk converter composed of ideal components together with their well-known parasitic elements is shown in Figure 2-18. Derivation of this model can be found in [2]. R_{C_1} and R_{C_o} represent the ESRs of the corresponding capacitances. R_{L_1} and $R_{L_2}$are the resistances of the corresponding inductors. R_{DS} is the on-state resistance of the switch, which is a

MOSFET. V_D is the forward voltage drop and R_D is the forward resistance of the diode. As understood from the capital letters, parasitic elements are assumed to be constant.

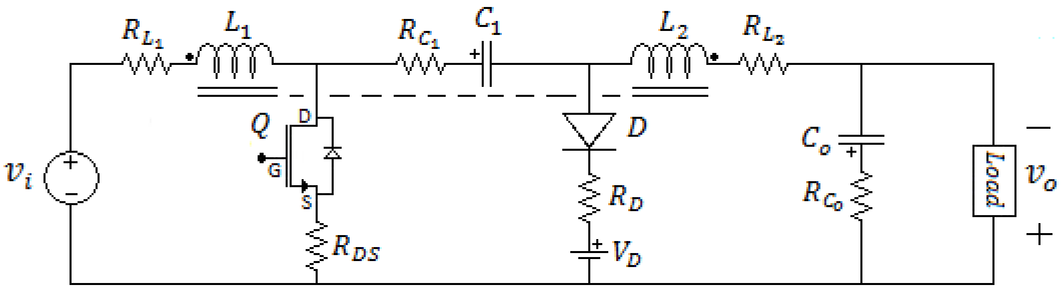

Figure 2-18 Circuit schematic of CIĆC with ideal components together with their well-known parasitic elements

The procedure that was applied to CIĆC with ideal components will be applied to this model. In order not to cause repetition, some steps are omitted.

2.2.3.1 Electrical Mesh Equations

This time, $Loop_1^{elc}$ and $Loop_2^{elc}$ in Figure 2-3 are written for the parasitic model.

In Mode 1:

$Loop_1^{elc}$: $$-v_i + R_{L_1} i_{L_1} + N_1 \frac{d}{dt}\Phi_1 + R_{DS}(i_{L_1} + i_{L_2}) = 0 \qquad (2\text{-}72)$$

$Loop_2^{elc}$: $$+R_{C_o}\left(i_{L_2} - i_o\right) + v_{C_o} + R_{L_2} i_{L_2} + N_2 \frac{d}{dt}\Phi_2 - v_{C_1} + R_{C_1} i_{L_2} + R_{DS}\left(i_{L_1} + i_{L_2}\right) = 0 \qquad (2\text{-}73)$$

In Mode 2:

$Loop_1^{elc}$: $$-v_i + R_{L_1} i_{L_1} + N_1 \frac{d}{dt}\Phi_1 + R_{C_1} i_{L_1} + v_{C_1} + R_D\left(i_{L_1} + i_{L_2}\right) + V_D = 0 \qquad (2\text{-}74)$$

$$Loop_2^{elc}: \qquad +R_{C_o}\left(i_{L_2}-i_o\right)+v_{C_o}+R_{L_2}i_{L_2}+N_2\frac{d}{dt}\Phi_2+R_D\left(i_{L_1}+i_{L_2}\right)+\ V_D=0 \tag{2-75}$$

2.2.3.2 Magnetic Mesh and Node Equations

Magnetic circuit already includes the parasitic elements, namely the reluctances. Hence, (2-19) and (2-20) will directly be utilized for this analysis.

2.2.3.3 Combination of Electrical and Magnetic Equations

In Mode 1, the following equation set is obtained.

In Mode 1:

Using (2-72) and (2-19):

$$\frac{N_1^2}{\mathbb{R}_{l1}//\mathbb{R}_m}\frac{d}{dt}i_1+\frac{N_1N_2}{\mathbb{R}_m}\frac{d}{dt}i_2=-\left(R_{L_1}+R_{DS}\right)i_{L_1}-R_{DS}i_{L_2}+v_i \tag{2-76}$$

Using (2-73) and (2-20):

$$\frac{N_1N_2}{\mathbb{R}_m}\frac{d}{dt}i_1+\frac{N_2^2}{\mathbb{R}_{l2}//\mathbb{R}_m}\frac{d}{dt}i_2=-R_{DS}i_{L_1}+v_{C_1}-\left(R_{DS}+R_{C_1}+R_{L_2}+R_{C_o}\right)i_{L_2}-v_{C_o}+R_{C_o}i_o \tag{2-77}$$

Similarly, in Mode 2, the following equation set is obtained.

In Mode 2:

Using (2-74) and (2-19):

$$\frac{N_1^2}{\mathbb{R}_{l1}//\mathbb{R}_m}\frac{d}{dt}i_1+\frac{N_1N_2}{\mathbb{R}_m}\frac{d}{dt}i_2=-\left(R_{L_1}+R_{C_1}+R_D\right)i_{L_1}-v_{C_1}-R_Di_{L_2}+v_i-V_D \tag{2-78}$$

Using (2-75) and (2-20):

$$\frac{N_1N_2}{\mathbb{R}_m}\frac{d}{dt}i_1+\frac{N_2^2}{\mathbb{R}_{l2}//\mathbb{R}_m}\frac{d}{dt}i_2=-R_Di_{L_1}-\left(R_D+R_{L_2}+R_{C_o}\right)i_{L_2}-v_{C_o}+R_{C_o}i_o-V_D \tag{2-79}$$

Using (2-76)-(2-79), derivatives of the two state-variables –namely i_{L_1} and i_{L_2}- can be written in terms of state-variables and input variables. Before that, some simplification should be done as an addition to (2-29)-(2-31).

$\alpha_5=-\left(R_{L_1}+R_{DS}\right)$ $\qquad$ $\alpha_6=-R_{DS}$

$\alpha_7=-R_{DS}$ $\qquad$ $\alpha_8=-\left(R_{DS}+R_{C_1}+R_{L_2}+R_{C_o}\right)$

$\alpha_9=R_{C_o}$ $\qquad$ $\alpha_{10}=-\left(R_{L_1}+R_{C_1}+R_D\right)$

$\alpha_{11}=-R_D$ $\qquad$ $\alpha_{12}=-R_D$

$\alpha_{13}=-\left(R_D+R_{L_2}+R_{C_o}\right)$ $\qquad$ $\alpha_{14}=R_{C_o}$

In Mode 1:

Using (2-76) and (2-77):

$$\frac{d}{dt}i_1=\frac{\alpha_2\alpha_5-\alpha_1\alpha_7}{\Delta_1}i_{L_1}-\frac{\alpha_1}{\Delta_1}v_{C_1}+\frac{\alpha_2\alpha_6-\alpha_1\alpha_8}{\Delta_1}i_{L_2}+\frac{\alpha_1}{\Delta_1}v_{C_o}+\frac{\alpha_2}{\Delta_1}v_i-\frac{\alpha_1\alpha_9}{\Delta_1}i_o \tag{2-80}$$

$$\frac{d}{dt}i_2=\frac{\alpha_3\alpha_7-\alpha_4\alpha_5}{\Delta_1}i_{L_1}+\frac{\alpha_3}{\Delta_1}v_{C_1}+\frac{\alpha_3\alpha_8-\alpha_4\alpha_6}{\Delta_1}i_{L_2}-\frac{\alpha_3}{\Delta_1}v_{C_o}-\frac{\alpha_4}{\Delta_1}v_i+\frac{\alpha_3\alpha_9}{\Delta_1}i_o \tag{2-81}$$

In Mode 2:

Using (2-78) and (2-79):

$$\frac{d}{dt}i_1=\frac{\alpha_2\alpha_{10}-\alpha_1\alpha_{12}}{\Delta_1}i_{L_1}-\frac{\alpha_2}{\Delta_1}v_{C_1}+\frac{\alpha_2\alpha_{11}-\alpha_1\alpha_{13}}{\Delta_1}i_{L_2}+\frac{\alpha_1}{\Delta_1}v_{C_o}+\frac{\alpha_2}{\Delta_1}v_i-\frac{\alpha_1\alpha_{14}}{\Delta_1}i_o+\frac{\alpha_1-\alpha_2}{\Delta_1}V_D \tag{2-82}$$

$$\frac{d}{dt}i_2 = \frac{\alpha_3\alpha_{12}-\alpha_4\alpha_{10}}{\Delta_1}i_{L_1} + \frac{\alpha_4}{\Delta_1}v_{C_1} + \frac{\alpha_3\alpha_{13}-\alpha_4\alpha_{11}}{\Delta_1}i_{L_2} - \frac{\alpha_3}{\Delta_1}v_{C_o} - \frac{\alpha_4}{\Delta_1}v_i + \frac{\alpha_3\alpha_{14}}{\Delta_1}i_o + \frac{\alpha_4-\alpha_3}{\Delta_1}V_D \tag{2-83}$$

Δ_1 and all α terms are composed of parasitic resistances, reluctances or number of turns. In other words, they are all constants. These constants are multiplied by state-variables and inputs of the circuit. Hence, (2-82) and (2-83) are ready to use in state-space averaging method in the next chapter.

2.2.3.4 Simulation Results

In order to see the effects of these parasitic elements, simulations will be implemented. By the help of these simulations, effect of parasitic elements on ripple-free input current and ripple-free output current cases will be investigated. Again, input and output current waveforms will be observed. The following simulation model is used in Ansoft Simplorer.

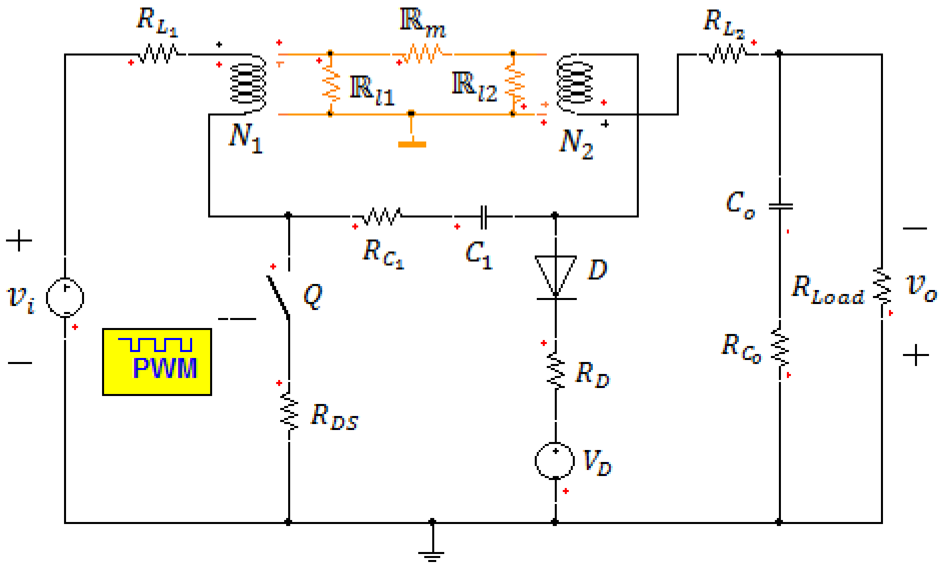

Figure 2-19 CIĆC simulation model with parasitic elements

List of the parasitic elements and their values are seen below. They belong to designed or selected elements in the design chapter. Detailed information can be found in CHAPTER 4.

$R_{L_1} = 6.28\ m\Omega$

$R_{C_1} = 17m\ \Omega$

$V_D = 0.62\ V$

$R_{C_o} = 6\ m\Omega$

$R_{DS} = 14\ m\Omega$

$R_D = 3\ m\Omega$

$R_{L_2} = 14.7\ m\Omega$

These values are given with respect to ripple-free input current case simulation. As mentioned earlier, L_1 and L_2 interchanges for ripple-free output current case. At that case, in addition to N_1-N_2 and $\mathbb{R}_{L_1}$-$\mathbb{R}_{L_2}$, R_{L_1}-$R_{L_2}$are also interchanged and simulation is done with those parameters. Besides, simulations are performed at the same operating point given in ideal electrical circuit element cases.

Figure 2-20, Figure 2-21 and Figure 2-22 belong to ripple-free input current case. As seen in Figure 2-20, both i_{L_1} and i_{L_2} waveforms have a band-like envelope

Figure 2-20 i_{L_1} and i_{L_2} waveforms in ripple-free input current case with parasitic elements at full load

rather than a line. Detailed i_{L_1} waveform is seen in Figure 2-21. Its maximum is 28.116A and minimum is 27.980A. Its ripple percent is calculated as 0.49%. Although its waveform resembles to current waveforms of unbalanced inductors, its ripple percent is very low, as in the case of ideal electrical elements. Remind that this value is 0.29% in ideal case.

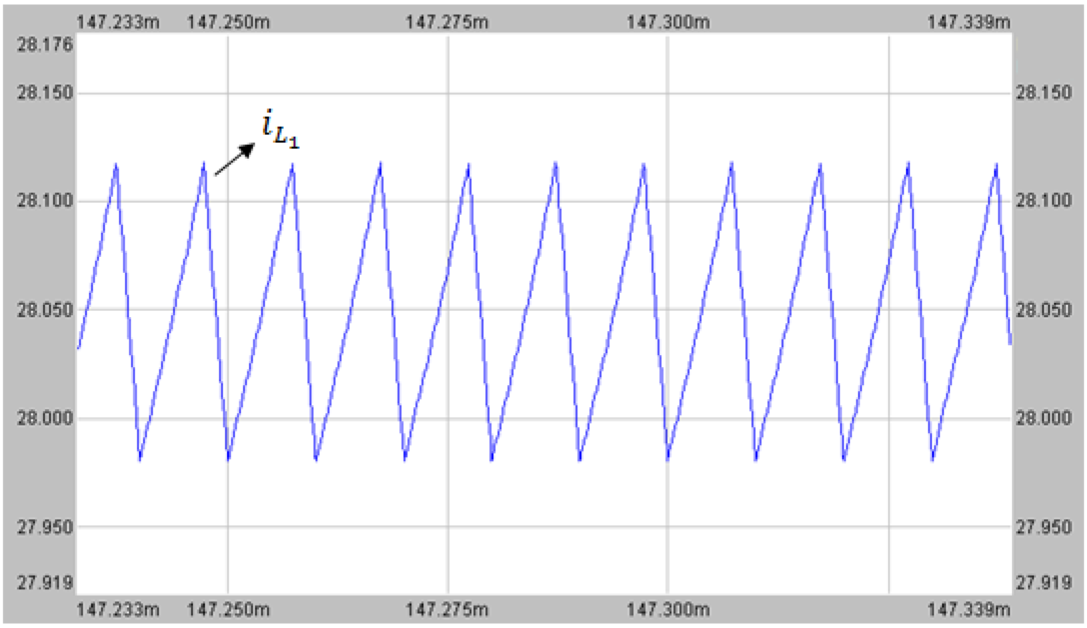

Figure 2-21 Detailed i_{L_1} waveform in ripple-free input current case with parasitic elements at full load

Detailed i_{L_2} waveform is seen in Figure 2-22. Its maximum is 10.55A and minimum is 10.13A. Its ripple percent is calculated as 4.1%. Remind that this value is 6.5% in ideal case. It is a surprising fact that L_2 current ripple percent in parasitic element case turns out to be less than that in ideal element case. Since the applied voltages to the inductors are disturbed because of the parasitic elements, the balance between the inductors fails a little. Hence, ripple is shared between the inductors rather than carried only by L_2 inductor. While the current ripple of L_1 inductor increases, that of L_2 inductor decreases because of this reason.

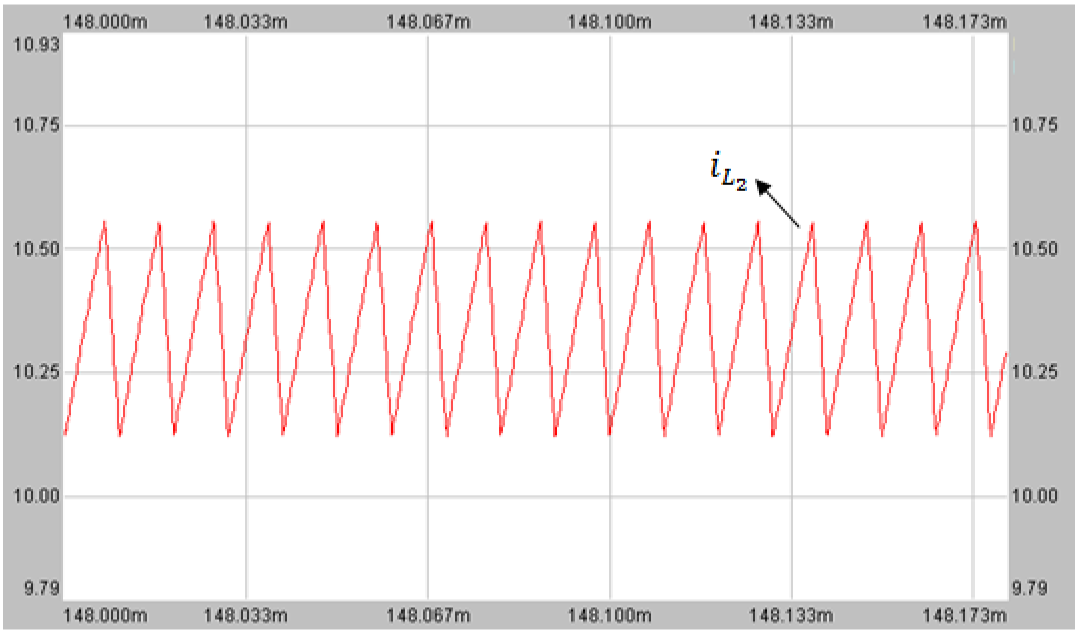

Figure 2-22 Detailed i_{L_2} waveform in ripple-free input current case with parasitic elements at full load

Now, the results of the ripple-free output current case with parasitic elements

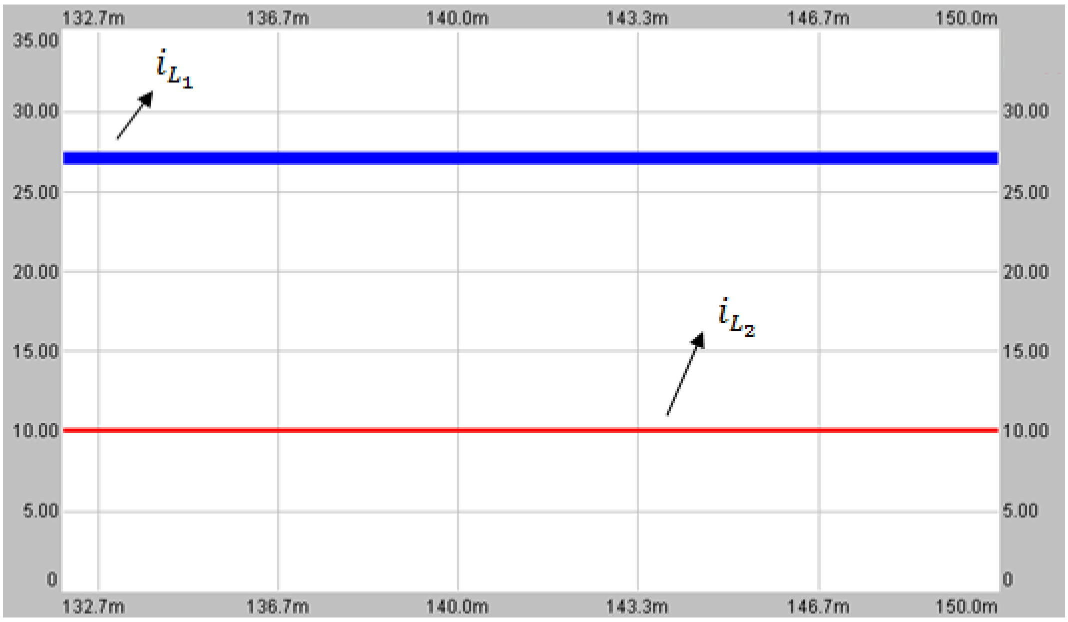

Figure 2-23 i_{L_1} and i_{L_2} waveforms in ripple-free output current case with parasitic elements at full load

will be presented. As shown in Figure 2-23, i_{L_2} waveform envelope is thicker than that in ideal case. Detailed i_{L_1} waveform is shown in Figure 2-24. Its maximum is 27.82A and minimum is 27.14A. Its ripple percent is calculated as 2.5%. Remind that this value is 2.4% in ideal case. There is almost no change in this situation.

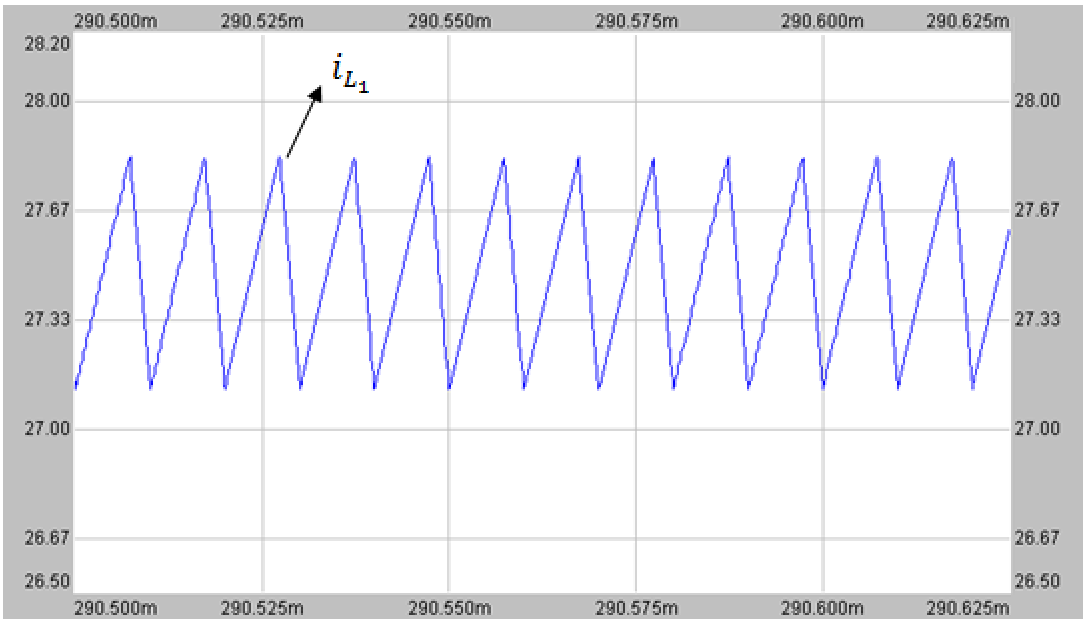

Figure 2-24 Detailed i_{L_1} waveform in ripple-free output current case with parasitic elements at full load

When it comes to i_{L_2}, a difference is observed in the waveform. It is shown in Figure 2-25. It is similar to the waveform of an independent inductor, like the other but unbalanced coupled-inductor. Its maximum is 10.20A and minimum is 10.06A. Its ripple percent is calculated as 1.4%. Remind that this value is 0.04% in ideal case. As expected, parasitic elements degrades the ripple percent in this situation.

From the simulation results, it can be said that 1-2% deviation from the simulation results in current ripples may stem from the parasitic elements. This is an expected result, because the assumptions are violated more in parasitic element case. Due to the voltage drops on parasitic elements, voltages applied to the inductors may differ much from each other. Hence, ripple cancellation on one side is not performed perfectly. Instead, small portion of the current ripple is reflected to the balanced inductor.

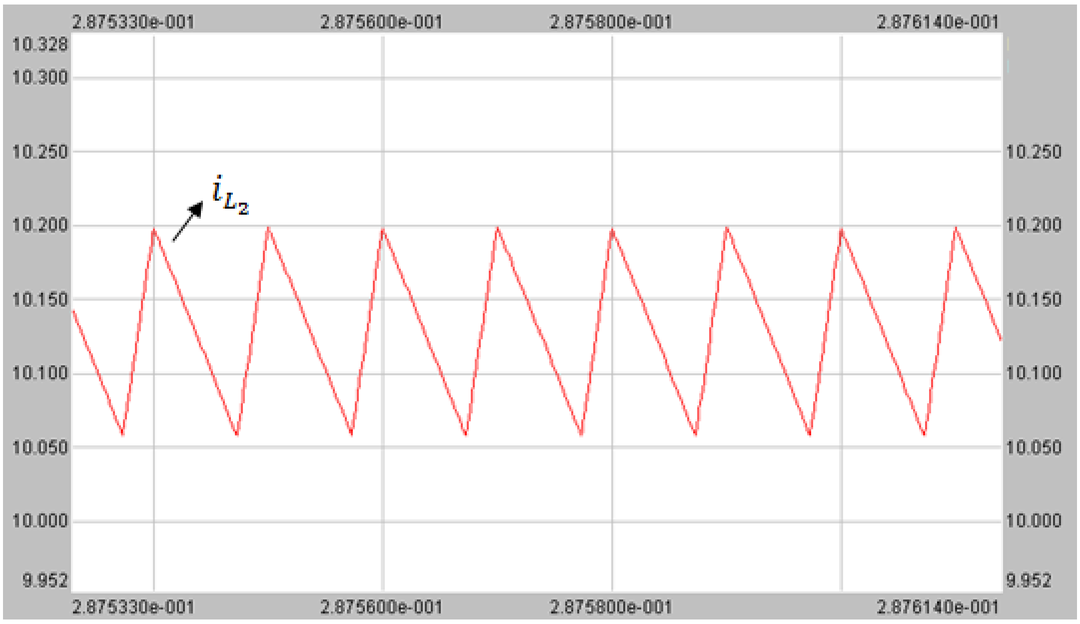

Figure 2-25 Detailed i_{L_2} waveform in ripple-free output current case with parasitic elements at full load

While evaluating the experimental results, some facts should be kept in mind. For example, the current ripple percents in the simulation results strictly depend on the operating point, especially the current levels. Besides, the simulations are done at full load and at the operating point at which both L_1 and L_2 current amplitudes are at their maximum. As a result, the smallest possible ripple percents are observed in the simulations.

2.3 ANALYSIS OF INTEGRATED MAGNETIC STRUCTURE

One of the sub topologies of Ćuk converter is integrated magnetic Ćuk converter, IMĆC. All the information about this topology can be found in [10, 13, 16]. In this topology, basic Ćuk converter may be assumed to be divided into two parts from C_1 and an isolation transformer is added to the separation point.

Therefore, output is galvanically isolated from input. ‘Integrated magnetic’ name is fitted to this topology because not only the input and output inductors but also the transformer share the same magnetic core. Transformer’s primary and secondary windings together with the input and output inductors are wound on the same core. Hence, this component is called integrated magnetic structure.

IMĆC brings another advantage together with isolation. By the presence of integrated magnetic structure, it is possible to obtain ripple-free input and output waveforms at the same time. As expected, this is possible as long as some conditions are satisfied in design of the integrated magnetic structure. Also, as in case of CIĆC, this property is independent of the operating condition. When all the properties of IMĆC are considered, it is possible to say that this topology simulates a dc-to-dc transformer with variable turns ratio.[10, 12] Because

- it is isolated,
- it has totally dc input/output voltage/current waveforms,
- and its turns ratio can be adjusted with duty-factor.

Inspired by the integrated magnetic structure models proposed in [16], complete reluctance model of integrated magnetic structure is proposed in this section. Its analysis will be done and then verified by the simulations. Analysis will be done with ideal electrical circuit components. Its parasitical model is left for further studies. At the end of the analysis, it is intended to obtain the conditions for ripple-free input and output waveforms at the same time. Contrary to the case of coupled-inductor, obtaining the derivatives of the two state-variables –namely i_{L_1} and i_{L_2}- in terms of other state-variables and input variables is not aimed here. It is again left for further studies. Therefore, i_{L_1} and i_{L_2} are replaced by the requirement –that is, they are constants- whenever they are faced with throughout the analysis for simplicity.

2.3.1 Analysis of Ideal Model and Merits of Coupling

The circuit schematic of IMĆC is seen in Figure 2-26.

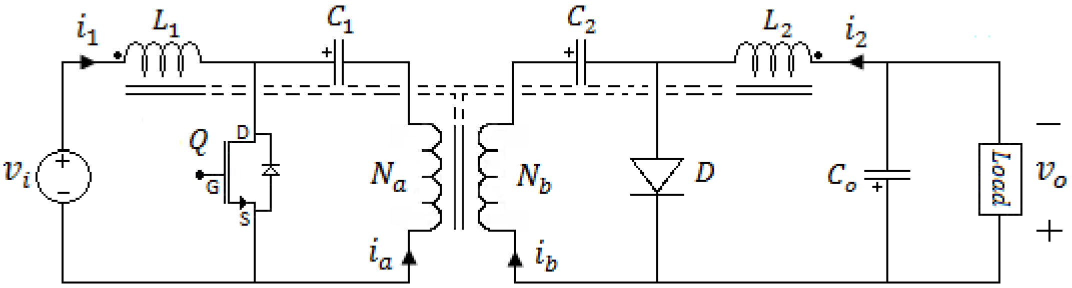

Figure 2-26 Circuit schematic of IMĆC

Integrated magnetic structure includes L_1 and L_2 inductors together with N_a and N_b isolation transformer windings on the same magnetic core. One of the recommended structures that can be seen in [27] is given in Figure 2-27. This structure is used in the analysis.

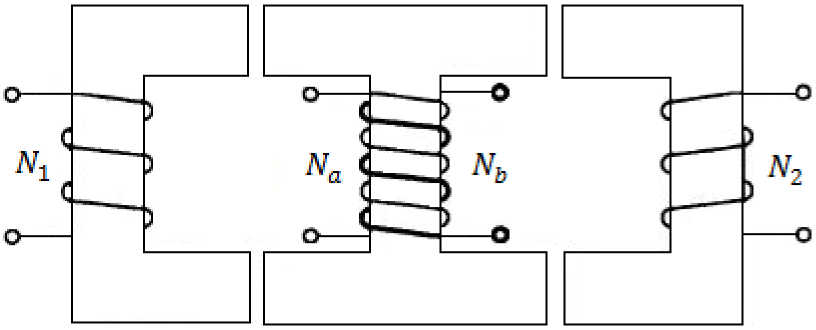

Figure 2-27 Proposed integrated magnetic structure [27]

Complete reluctance model of the integrated magnetic structure is given in Figure 2-28. As mentioned earlier, it is slightly different than the proposed reluctance model of integrated magnetic structure in [16].

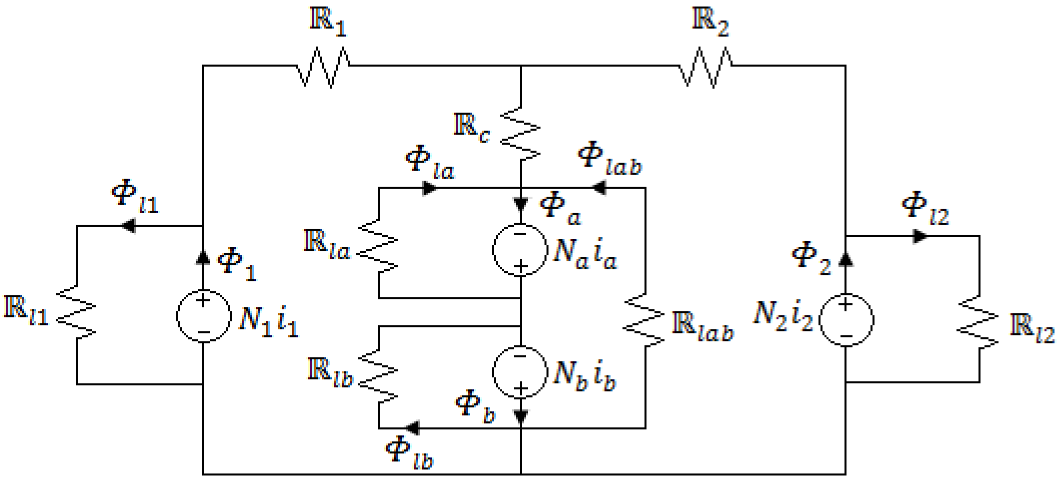

Figure 2-28 Complete reluctance model of the proposed integrated magnetic structure

2.3.1.1 Electrical Mesh Equations

In Mode 1, active meshes in the equivalent circuit for IMĆC are shown in Figure 2-29.

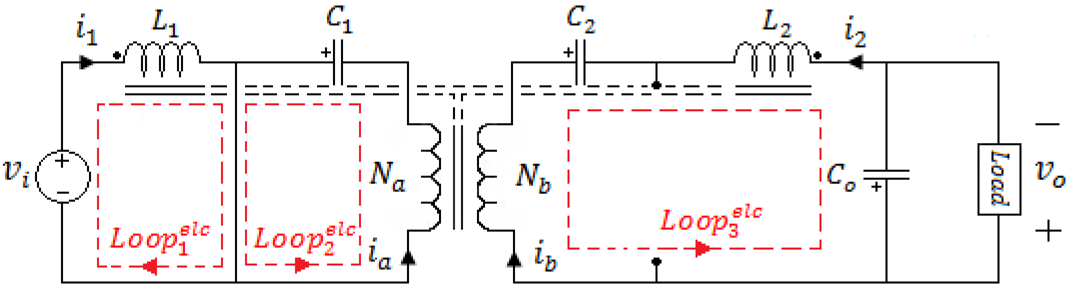

Figure 2-29 Active meshes in Mode 1 in the equivalent electrical circuit for IMĆC

In Mode 1:

$Loop_1^{elc}$: $$-v_i + N_1 \frac{d}{dt}\Phi_1 = 0 \quad (2\text{-}84)$$

$Loop_2^{elc}$: $$+N_a \frac{d}{dt}\Phi_a - v_{C_1} = 0 \quad (2\text{-}85)$$

$Loop_3^{elc}$: $$+v_o + N_2\frac{d}{dt}\Phi_2 - v_{C_2} - N_b\frac{d}{dt}\Phi_b = 0 \tag{2-86}$$

Magnetic node equations are utilized at this step. They give the following equations.

Using Figure 2-28:

$$\Phi_a = \Phi_1 - \Phi_{l1} + \Phi_2 - \Phi_{l2} + \Phi_{la} + \Phi_{lab} \tag{2-87}$$

$$\Phi_b = \Phi_1 - \Phi_{l1} + \Phi_2 - \Phi_{l2} + \Phi_{lb} + \Phi_{lab} \tag{2-88}$$

Hence, the following equation set is obtained.

In Mode 1:

Using (2-84):

$$-v_i + N_1\frac{d}{dt}\Phi_1 = 0 \tag{2-89}$$

Using (2-85) and (2-87):

$$+N_a\frac{d}{dt}(\Phi_1 - \Phi_{l1} + \Phi_2 - \Phi_{l2} + \Phi_{la} + \Phi_{lab}) - v_{C_1} = 0 \tag{2-90}$$

Using (2-86) and (2-88):

$$+v_o + N_2\frac{d}{dt}\Phi_2 - v_{C_2} - N_b\frac{d}{dt}(\Phi_1 - \Phi_{l1} + \Phi_2 - \Phi_{l2} + \Phi_{lb} + \Phi_{lab}) = 0 \tag{2-91}$$

Active meshes in Mode 2 are given in Figure 2-30.

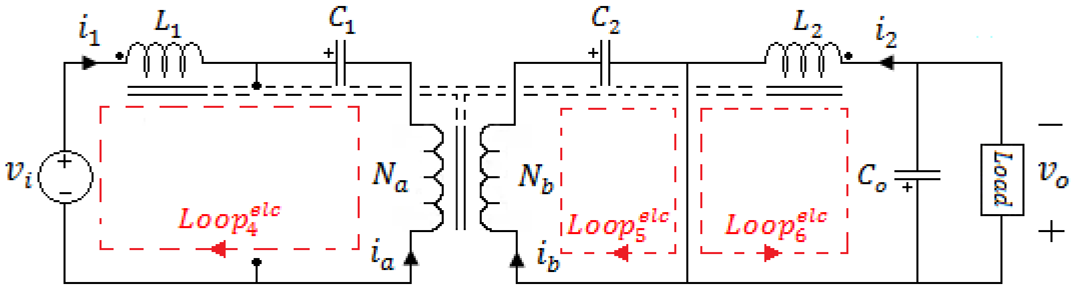

Figure 2-30 Active meshes in Mode 2 in the equivalent electrical circuit for IMĆC

In Mode 2:

$Loop_4^{elc}$: $$-v_i + N_1 \frac{d}{dt}\Phi_1 + v_{C_1} - N_a \frac{d}{dt}\Phi_a = 0 \qquad (2\text{-}92)$$

$Loop_5^{elc}$: $$+N_b \frac{d}{dt}\Phi_b + v_{C_2} = 0 \qquad (2\text{-}93)$$

$Loop_6^{elc}$: $$+v_o + N_2 \frac{d}{dt}\Phi_2 = 0 \qquad (2\text{-}94)$$

By the replacement of Φ_a and Φ_b, the following equation set is obtained.

In Mode 2:

Using (2-92) and (2-87):

$$-v_i + N_1 \frac{d}{dt}\Phi_1 + v_{C_1} - N_a \frac{d}{dt}(\Phi_1 - \Phi_{l1} + \Phi_2 - \Phi_{l2} + \Phi_{la} + \Phi_{lab}) = 0 \qquad (2\text{-}95)$$

Using (2-93) and (2-88):

$$+N_b \frac{d}{dt}(\Phi_1 - \Phi_{l1} + \Phi_2 - \Phi_{l2} + \Phi_{lb} + \Phi_{lab}) + v_{C_2} = 0 \qquad (2\text{-}96)$$

Using (2-94):

$$+v_o + N_2 \frac{d}{dt}\Phi_2 = 0 \qquad (2\text{-}97)$$

Assumptions utilized in the coupled-inductor analysis are also used here. However, there are some differences stemming from the isolation transformer. (2-39) were valid in the previous analysis. In this analysis, however, the followings are valid.

$$V_{C_1} = V_i \qquad (2\text{-}98)$$

$$V_{C_2} = V_o \qquad (2\text{-}99)$$

When these simplifications together with the previous assumptions made in coupled-inductor analysis are applied, the following equation set is obtained.

In Mode 1:

Using (2-89) and (2-34):

$$V_i = N_1 \frac{d}{dt} \Phi_1 \tag{2-100}$$

Using (2-90), (2-40) and (2-98):

$$V_i = N_a \frac{d}{dt} (\Phi_1 - \Phi_{l1} + \Phi_2 - \Phi_{l2} + \Phi_{la} + \Phi_{lab}) \tag{2-101}$$

Using (2-91), (2-35), (2-40) and (2-99):

$$N_2 \frac{d}{dt} \Phi_2 = N_b \frac{d}{dt} (\Phi_1 - \Phi_{l1} + \Phi_2 - \Phi_{l2} + \Phi_{lb} + \Phi_{lab}) \tag{2-102}$$

In Mode 2:

Using (2-95), (2-34), (2-40) and (2-98):

$$N_1 \frac{d}{dt} \Phi_1 = N_a \frac{d}{dt} (\Phi_1 - \Phi_{l1} + \Phi_2 - \Phi_{l2} + \Phi_{la} + \Phi_{lab}) \tag{2-103}$$

Using (2-96), (2-40) and (2-99):

$$-V_o = N_b \frac{d}{dt} (\Phi_1 - \Phi_{l1} + \Phi_2 - \Phi_{l2} + \Phi_{lb} + \Phi_{lab}) \tag{2-104}$$

Using (2-97) and (2-35):

$$-V_o = N_2 \frac{d}{dt} \Phi_2 \tag{2-105}$$

2.3.1.2 Magnetic Mesh Equations

Using the following magnetic circuit, mesh equations can be obtained.

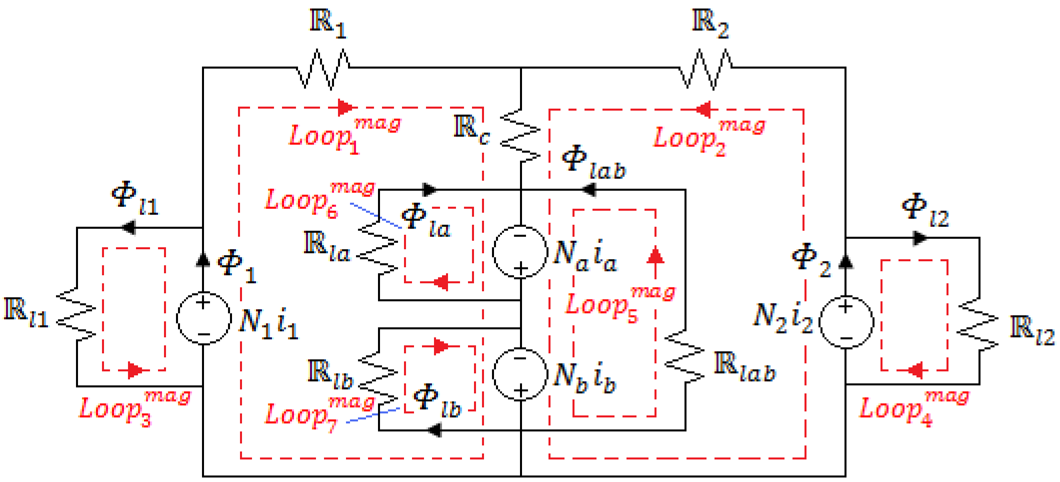

Figure 2-31 Active meshes in magnetic circuit schematic of integrated magnetic structure

Two Major Loops:

$Loop_1^{mag}$:
$$-N_1 i_1 + \mathbb{R}_1(\Phi_1 - \Phi_{l1}) + \mathbb{R}_c(\Phi_1 - \Phi_{l1} + \Phi_2 - \Phi_{l2}) - N_a i_a - N_b i_b = 0 \tag{2-106}$$

$Loop_2^{mag}$:
$$-N_2 i_2 + \mathbb{R}_2(\Phi_2 - \Phi_{l2}) + \mathbb{R}_c(\Phi_1 - \Phi_{l1} + \Phi_2 - \Phi_{l2}) - N_a i_a - N_b i_b = 0 \tag{2-107}$$

Five Minor Loops:

$Loop_3^{mag}$:
$$-N_1 i_1 + \mathbb{R}_{l1}\Phi_{l1} = 0 \tag{2-108}$$

$Loop_4^{mag}$:
$$-N_2 i_2 + \mathbb{R}_{l2}\Phi_{l2} = 0 \tag{2-109}$$

$Loop_5^{mag}$:
$$-N_a i_a + \mathbb{R}_{la}\Phi_{la} = 0 \tag{2-110}$$

$Loop_6^{mag}$:
$$-N_b i_b + \mathbb{R}_{lb}\Phi_{lb} = 0 \tag{2-111}$$

$Loop_7^{mag}$:
$$-N_a i_a - N_b i_b + \mathbb{R}_{lab}\Phi_{lab} = 0 \tag{2-112}$$

$\frac{d}{dt}\Phi_1$, $\frac{d}{dt}\Phi_2$, $\frac{d}{dt}\Phi_{l1}$, $\frac{d}{dt}\Phi_{l2}$, $\frac{d}{dt}\Phi_{la}$, $\frac{d}{dt}\Phi_{lb}$ and $\frac{d}{dt}\Phi_{lab}$ terms should be obtained in order to proceed in electrical mesh equations. These terms can be obtained from magnetic mesh equations.

In this configuration, it is claimed that both input and output current can be made ripple-free. Hence, derivatives of input and output current can be equated to zero.

$$\frac{d}{dt}i_1 = \frac{d}{dt}i_2 = 0 \tag{2-113}$$

Note: By using (2-113) or the assumptions such as constant capacitor voltages that will be used later, the chance of obtaining $\frac{d}{dt}i_1$ and $\frac{d}{dt}i_2$ in terms of state-variables and input variables is lost intentionally. If state-space averaging method were to be applied to IMĆC in this work, $\frac{d}{dt}i_1$ and $\frac{d}{dt}i_2$ terms would be easily prepared as inputs to that method. However, only the conditions for ripple-free input and output current are intended to give in this section.

By taking the derivative of the magnetic loop equations and using (2-113), the following equation set is obtained.

Five Minor Loops:

Using (2-108)-(2-112) and (2-113):

$$\frac{d}{dt}\Phi_{l1} = 0 \tag{2-114}$$

$$\frac{d}{dt}\Phi_{l2} = 0 \tag{2-115}$$

$$\frac{d}{dt}\Phi_{la} = \frac{N_a}{\mathbb{R}_{la}}\frac{d}{dt}i_a \tag{2-116}$$

$$\frac{d}{dt}\Phi_{lb} = \frac{N_b}{\mathbb{R}_{lb}}\frac{d}{dt}i_b \tag{2-117}$$

$$\frac{d}{dt}\Phi_{lab} = \frac{N_a}{\mathbb{R}_{lab}}\frac{d}{dt}i_a + \frac{N_b}{\mathbb{R}_{lab}}\frac{d}{dt}i_b \tag{2-118}$$

Two Major Loops:

Using (2-106), (2-113)-(2-115):

$$(\mathbb{R}_1 + \mathbb{R}_c)\frac{d}{dt}\Phi_1 + \mathbb{R}_c\frac{d}{dt}\Phi_2 = N_a\frac{d}{dt}i_a + N_b\frac{d}{dt}i_b \tag{2-119}$$

Using (2-107), (2-113)-(2-115):

$$\mathbb{R}_c\frac{d}{dt}\Phi_1 + (\mathbb{R}_2 + \mathbb{R}_c)\frac{d}{dt}\Phi_2 = N_a\frac{d}{dt}i_a + N_b\frac{d}{dt}i_b \tag{2-120}$$

$\frac{d}{dt}\Phi_{l1}$, $\frac{d}{dt}\Phi_{l2}\frac{d}{dt}\Phi_{la}$, $\frac{d}{dt}\Phi_{lb}$ and $\frac{d}{dt}\Phi_{lab}$ terms are expressed in terms of $\frac{d}{dt}i_a$ and $\frac{d}{dt}i_b$, which are electrical parameters. Now, $\frac{d}{dt}\Phi_1$ and $\frac{d}{dt}\Phi_2$ terms should be expressed in the same manner. Using (2-119) and (2-120), they can be obtained easily.

$$Loop_1^{mag}: \quad \frac{d}{dt}\Phi_1 = \frac{\mathbb{R}_2 N_a}{(\mathbb{R}_1\mathbb{R}_2 + \mathbb{R}_1\mathbb{R}_c + \mathbb{R}_2\mathbb{R}_c)}\frac{d}{dt}i_a + \frac{\mathbb{R}_2 N_b}{(\mathbb{R}_1\mathbb{R}_2 + \mathbb{R}_1\mathbb{R}_c + \mathbb{R}_2\mathbb{R}_c)}\frac{d}{dt}i_b \tag{2-121}$$

$$Loop_2^{mag}: \quad \frac{d}{dt}\Phi_2 = \frac{\mathbb{R}_1 N_a}{(\mathbb{R}_1\mathbb{R}_2 + \mathbb{R}_1\mathbb{R}_c + \mathbb{R}_2\mathbb{R}_c)}\frac{d}{dt}i_a + \frac{\mathbb{R}_1 N_b}{(\mathbb{R}_1\mathbb{R}_2 + \mathbb{R}_1\mathbb{R}_c + \mathbb{R}_2\mathbb{R}_c)}\frac{d}{dt}i_b \tag{2-122}$$

For further simplification, Mode 1 and Mode 2 can be considered separately for magnetic loop equations. From Figure 2-29 it is clearly seen that $i_b = -I_2$ during in Mode 1.

In Mode 1:

$$\frac{d}{dt}i_b = 0 \tag{2-123}$$

Similarly, i_a is equal to $-I_1$ in Mode 2. This fact can be seen in Figure 2-30.

In Mode 2:

$$\frac{d}{dt}i_a = 0 \tag{2-124}$$

Magnetic equations can now be separately written for Mode 1 and Mode 2.

In Mode 1:

Using (2-121) and (2-123):

$$\frac{d}{dt}\Phi_1 = \frac{\mathbb{R}_2 N_a}{(\mathbb{R}_1\mathbb{R}_2+\mathbb{R}_1\mathbb{R}_c+\mathbb{R}_2\mathbb{R}_c)}\frac{d}{dt}i_a \tag{2-125}$$

Using (2-122) and (2-123):

$$\frac{d}{dt}\Phi_2 = \frac{\mathbb{R}_1 N_a}{(\mathbb{R}_1\mathbb{R}_2+\mathbb{R}_1\mathbb{R}_c+\mathbb{R}_2\mathbb{R}_c)}\frac{d}{dt}i_a \tag{2-126}$$

Using (2-114)-(2-116):

$$\frac{d}{dt}\Phi_{l1} = 0 \tag{2-127}$$

$$\frac{d}{dt}\Phi_{l2} = 0 \tag{2-128}$$

$$\frac{d}{dt}\Phi_{la} = \frac{N_a}{\mathbb{R}_{la}}\frac{d}{dt}i_a \tag{2-129}$$

Using (2-117) and (2-123):

$$\frac{d}{dt}\Phi_{lb} = 0 \tag{2-130}$$

Using (2-118) and (2-123):

$$\frac{d}{dt}\Phi_{lab} = \frac{N_a}{\mathbb{R}_{lab}}\frac{d}{dt}i_a \tag{2-131}$$

In Mode 2:

Using (2-121) and (2-124):

$$\frac{d}{dt}\Phi_1 = \frac{\mathbb{R}_2 N_b}{(\mathbb{R}_1\mathbb{R}_2+\mathbb{R}_1\mathbb{R}_c+\mathbb{R}_2\mathbb{R}_c)}\frac{d}{dt}i_b \tag{2-132}$$

Using (2-122) and (2-124):

$$\frac{d}{dt}\Phi_2 = \frac{\mathbb{R}_1 N_b}{(\mathbb{R}_1\mathbb{R}_2+\mathbb{R}_1\mathbb{R}_c+\mathbb{R}_2\mathbb{R}_c)}\frac{d}{dt}i_b \tag{2-133}$$

Using (2-114) and (2-115):

$$\frac{d}{dt}\Phi_{l1} = 0 \tag{2-134}$$

$$\frac{d}{dt}\Phi_{l2} = 0 \tag{2-135}$$

Using (2-116) and (2-124):

$$\frac{d}{dt}\Phi_{la} = 0 \tag{2-136}$$

Using (2-117):

$$\frac{d}{dt}\Phi_{lb} = \frac{N_b}{\mathbb{R}_{lb}}\frac{d}{dt}i_b \tag{2-137}$$

Using (2-118) and (2-124):

$$\frac{d}{dt}\Phi_{lab} = \frac{N_b}{\mathbb{R}_{lab}}\frac{d}{dt}i_b \tag{2-138}$$

Derivatives of the fluxes are obtained in terms of the derivates of the currents. Now, these results can be reflected to electrical mesh equations. Before that, the following notation simplification can be useful.

$$\mathbb{R}_* \overset{\text{def}}{=} \mathbb{R}_1\mathbb{R}_2 + \mathbb{R}_1\mathbb{R}_c + \mathbb{R}_2\mathbb{R}_c \tag{2-139}$$

In Mode 1:

Using (2-84), (2-125) and (2-139):

$$V_i = \frac{\mathbb{R}_2 N_a N_1}{\mathbb{R}_*}\frac{d}{dt}i_a \tag{2-140}$$

Using (2-101), (2-125)-(2-129), (2-131) and (2-139):

$$V_i = N_a^2\left(\frac{\mathbb{R}_1+\mathbb{R}_2}{\mathbb{R}_*} + \frac{1}{\mathbb{R}_{la}} + \frac{1}{\mathbb{R}_{lab}}\right)\frac{d}{dt}i_a \tag{2-141}$$

Using (2-102), (2-125)-(2-128), (2-130)-(2-131) and (2-139):

$$\frac{N_2}{N_b} = 1 + \frac{\mathbb{R}_2}{\mathbb{R}_1} + \frac{\mathbb{R}_*}{\mathbb{R}_1\mathbb{R}_{lab}} \tag{2-142}$$

(2-142) implies that N_2 will be greater than N_b, which is possible.

In Mode 2:

Using (2-103), (2-132)-(2-136) and (2-138)-(2-139):

$$\frac{N_1}{N_a} = 1 + \frac{\mathbb{R}_1}{\mathbb{R}_2} + \frac{\mathbb{R}_*}{\mathbb{R}_2 \mathbb{R}_{lab}} \tag{2-143}$$

(2-143) implies that N_1 will be greater than N_a, which is also possible.

Using (2-104), (2-132)-(2-135) and (2-137)-(2-139):

$$-V_o = N_b^2 \left(\frac{\mathbb{R}_2}{\mathbb{R}_*} + \frac{\mathbb{R}_1}{\mathbb{R}_*} + \frac{1}{\mathbb{R}_{lb}} + \frac{1}{\mathbb{R}_{lab}} \right) \frac{d}{dt} i_b \tag{2-144}$$

Using (2-105), (2-133) and (2-139):

$$-V_o = \frac{\mathbb{R}_1 N_b N_2}{\mathbb{R}_*} \frac{d}{dt} i_b \tag{2-145}$$

When analyzed, it can be seen that all four windings have the same voltage waveform: V_i in Mode 1 and $-V_o$ during in Mode 2. This fact also appears in the equation set above. As mentioned earlier, in coupled-inductor analysis, windings have to have proportional voltage waveforms. That condition is also valid here. The same arguments in coupled-inductor case can be applied to this equation set.

Further simplification may give simple conditions for ripple-free current waveforms on both sides.

Using (2-140) and (2-141):

$$\frac{N_1}{N_a} = 1 + \frac{\mathbb{R}_1}{\mathbb{R}_2} + \frac{\mathbb{R}_*}{\mathbb{R}_2 \mathbb{R}_{la}} + \frac{\mathbb{R}_*}{\mathbb{R}_2 \mathbb{R}_{lab}} \tag{2-146}$$

Using (2-143) and (2-146):

$$\frac{\mathbb{R}_*}{\mathbb{R}_2 \mathbb{R}_{la}} = 0 \tag{2-147}$$

Since $\mathbb{R}_*$ and $\mathbb{R}_2$ are intentionally put and $\mathbb{R}_{la}$ just represents the leakage, (2-147) means that $\mathbb{R}_{la}$ has to tend to infinity in order to satisfy this equality. Of course, this is not a practical result. However, $\mathbb{R}_{la}$ is expected to be very high because it represents only the leakage of the primary winding. Even its part of the mutual flux with secondary winding which does not couple any of the inductor is not included in this term. For example, twisting the primary and secondary windings of the transformer can make $\mathbb{R}_{la}$ very high. Hence, this condition can be accepted as reasonable.

Using (2-144) and (2-145):

$$\frac{N_2}{N_b} = 1 + \frac{\mathbb{R}_2}{\mathbb{R}_1} + \frac{\mathbb{R}_*}{\mathbb{R}_1\mathbb{R}_{lb}} + \frac{\mathbb{R}_*}{\mathbb{R}_1\mathbb{R}_{lab}} \tag{2-148}$$

Using (2-142) and (2-148):

$$\frac{\mathbb{R}_*}{\mathbb{R}_1\mathbb{R}_{lb}} = 0 \tag{2-149}$$

The same argument is also valid for $\mathbb{R}_{lb}$. As a result, the following four conditions have to be satisfied for ripple-free input and output current waveforms simultaneously.

2.3.1.3 Conditions for Zero-Ripple at Both Ends Simultaneously

In this section, conditions for ripple-free input and output current waveforms simultaneously are gathered together as (2-150)-(2-153).

Using (2-143), (2-147), (2-142), (2-149) respectively:

$$\frac{N_1}{N_a} = 1 + \frac{\mathbb{R}_1}{\mathbb{R}_2} + \frac{\mathbb{R}_*}{\mathbb{R}_2\mathbb{R}_{lab}} \tag{2-150}$$

$$\frac{\mathbb{R}_*}{\mathbb{R}_2\mathbb{R}_{la}} = 0 \tag{2-151}$$

$$\frac{N_2}{N_b} = 1 + \frac{\mathbb{R}_2}{\mathbb{R}_1} + \frac{\mathbb{R}_*}{\mathbb{R}_1\mathbb{R}_{lab}} \tag{2-152}$$

$$\frac{\mathbb{R}_*}{\mathbb{R}_1\mathbb{R}_{lb}} = 0 \tag{2-153}$$

Although the conditions above seem to be highly different than the coupled-inductor case, they resembles to the results obtained in that analysis much. What the conditions (2-150)-(2-153) say can be physically explained and verified by the derivations of leakage inductance, mutual inductance, magnetizing inductance, self inductance, coupling coefficient and effective turns ratio terms for integrated magnetic structure. The derivations are not given in this work. However, their results will be given in order to show the similarities between coupled-inductor and integrated magnetic structure cases. Corresponding conditions are presented below. (2-154) dictates that input current can be made ripple-free by balancing it with the first winding of the transformer. Similarly, (2-156) says that output current is made ripple-free by balancing it with the second winding of the transformer. Corresponding equations of (2-150), (2-151), (2-152) and (2-153) respectively:

$$L_{1a} = L_{aa} \tag{2-154}$$

$$L_{la} = 0 \tag{2-155}$$

$$L_{2b} = L_{bb} \tag{2-156}$$

$$L_{lb} = 0 \tag{2-157}$$

2.3.1.4 Verification by Simulation

In order to verify the conditions in (2-150)-(2-153), simulation will be done. IMĆC circuit implementation will not be realized in this work. However, its parameters are selected as if it would be implemented. In other words, its ratings are similar to the CIĆC designed and implemented in this work. The following simulation model is implemented in Simplorer. As in case of coupled-inductor, orange lines represent the magnetic connections and black lines electrical connections. The interactions of magnetic and electrical connections are windings that generate $N_x i_x$ types of MMFs. The following parameters are selected and used in the simulation.

$\mathbb{R}_1 = 3 \times 10^6\ H^{-1}$ $\mathbb{R}_{l1} = 45 \times 10^6\ H^{-1}$

$\mathbb{R}_c = 0.1 \times 10^6\ H^{-1}$ $\mathbb{R}_{lab} = 40 \times 10^6\ H^{-1}$

$\mathbb{R}_{la} = 1000 \times 10^6\ H^{-1}$ $\mathbb{R}_{lb} = 1000 \times 10^6\ H^{-1}$

$\mathbb{R}_2 = 2 \times 10^6\ H^{-1}$ $\mathbb{R}_{l2} = 30 \times 10^6\ H^{-1}$

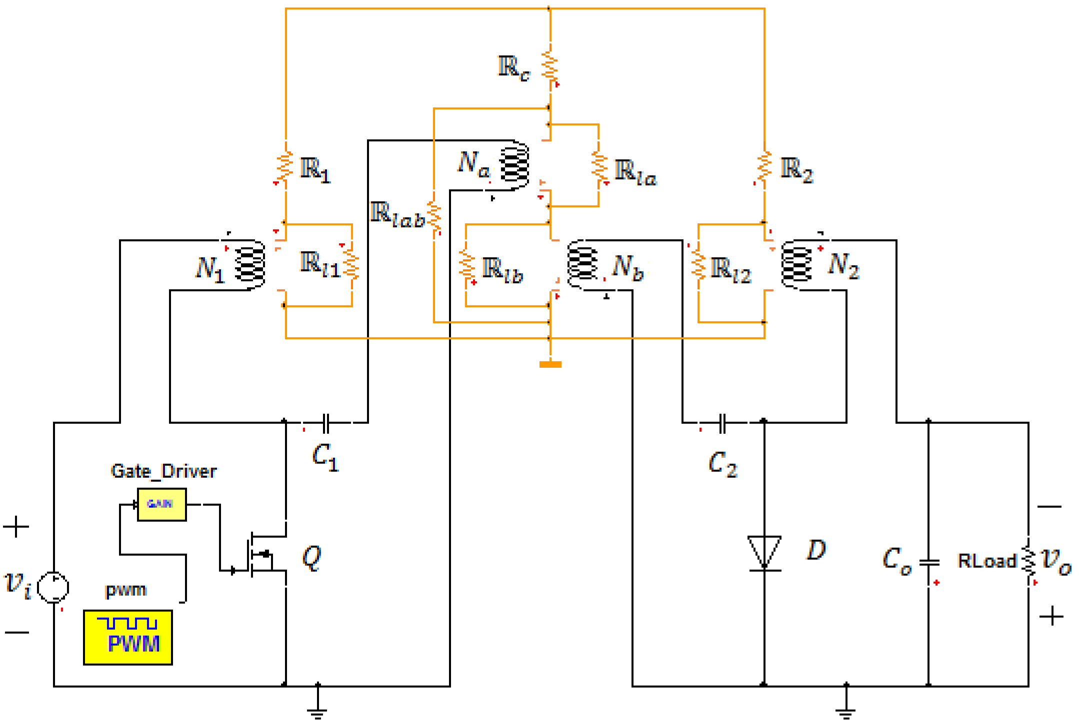

Figure 2-32 Simulation model of IMĆC in Simplorer

Note that $\mathbb{R}_{la}$ and $\mathbb{R}_{lb}$ parameters are selected very high in order to satisfy the conditions (2-151) and (2-153). Based on these parameters N_1, N_2, N_a and N_b should be determined such that other two conditions, (2-150) and (2-152), are also satisfied.

$\frac{N_1}{N_a} \cong 2.581$ and $\frac{N_2}{N_b} \cong 1.721$

After this point, as long as the above ratios are satisfied, ripple-free input and output waveforms can be observed. Note that turns ratio of the transformer is not mentioned yet. According to the conditions, it seems not to affect the result. Probably it only determines the input-to-output voltage transfer ratio. Input-to-output voltage transfer ratio is given in [12] such that:

$$\frac{V_o}{V_i} = \frac{N_b}{N_a}\frac{K}{(1-K)} \tag{2-158}$$

In order to prove this foresight, at first, N_a is selected as equal to N_b and simulation is done with this turns ratio. Secondly, a different turns ratio is selected and the above estimation is verified by another simulation.

In coupled-inductor case, N_1 and N_2 are around 20. In order to be similar, N_a and N_b are selected as around 10. Then, the following parameters are obtained.

$$N_a = N_b = 10\,Turns \qquad\qquad N_1 \cong 25.8\,Turns$$

$$N_2 \cong 17.2\,Turns$$

Although the numbers of turns seem to be selected randomly, they are chosen as practical and reasonable values. IMĆC design is not given in this work. Just an abstract of it can be given here. In that design, N_a and N_b are determined according to the allowable current ripples on the transformer windings. Then, with respect to N_a and N_b, N_1 and N_2 are determined. Selecting lower N_a and N_b results in lower N_1 and N_2 turn numbers, thereby, smaller core. This seems to be an advantage. However, although ripple-free input and output current waveforms are still obtained in this situation, higher ripple current on transformer windings leads to ,for example, higher core loss, higher copper loss and higher minimum load requirement. Higher power loss not only diminishes the efficiency but also increases the cooling requirement, cost and volume. Higher minimum load requirement means that the circuit satisfies its specifications such as ripple-free current waveforms at higher loads, which is a disadvantage of selecting lower turn numbers. That is to say, there is a limitation on N_a and N_b.

Using the above numbers of turns and reluctance values, the following simulation results are obtained. The operating conditions are the same as coupled-inductor case. i_{L_1} and i_{L_2} waveforms are seen in Figure 2-33. As in coupled-inductor case, trace 1 (blue) represents the input current or i_{L_1} and trace 2 (red) i_{L_2}. As understood form the thin envelopes, they are almost ripple-free.

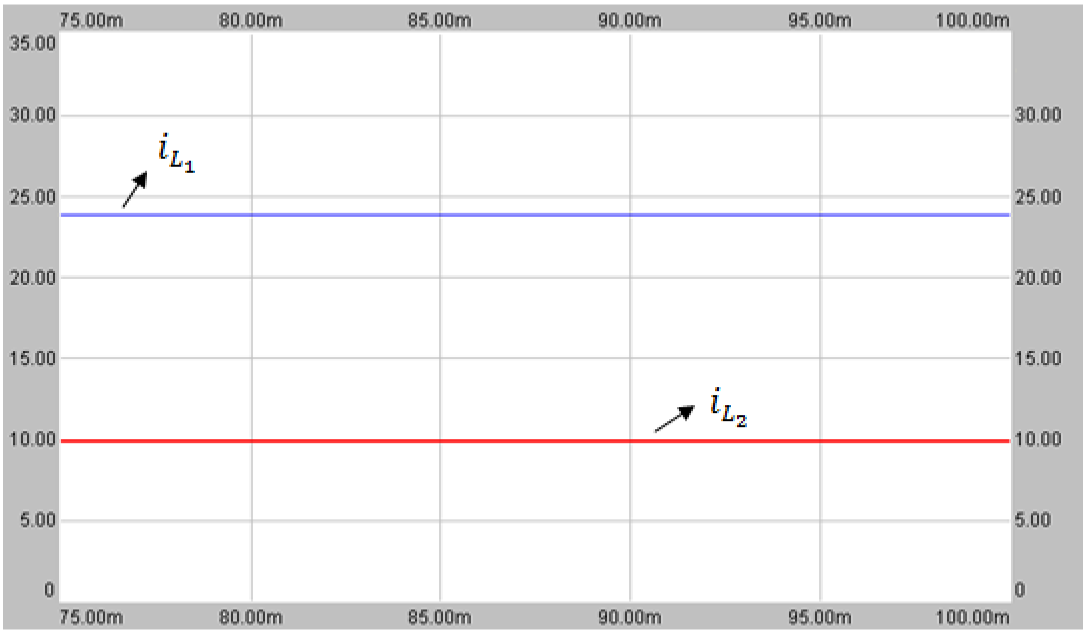

Figure 2-33 i_{L_1} and i_{L_2} waveforms in IMĆC, $N_a = N_b$, full load

Detailed waveforms of i_{L_1} and i_{L_2} can be investigated in the following two figures.

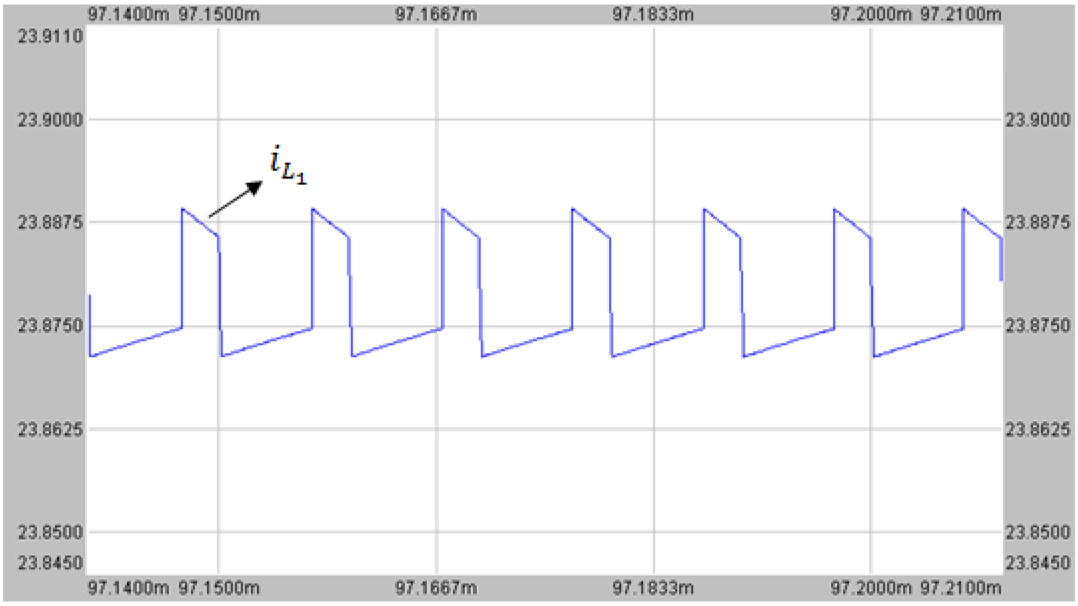

Figure 2-34 Detailed i_{L_1} waveform in IMĆC, $N_a = N_b$, full load

As seen in Figure 2-34, the maximum of input current is 23.89A and minimum is 23.87A. Hence, its peak-to-peak ripple percent is 0.08%. Its waveform can be considered as little bit strange because, as a known fact, inductor current cannot change instantly. Since its magnitude is extremely low, detailed observation seems not to be necessary.

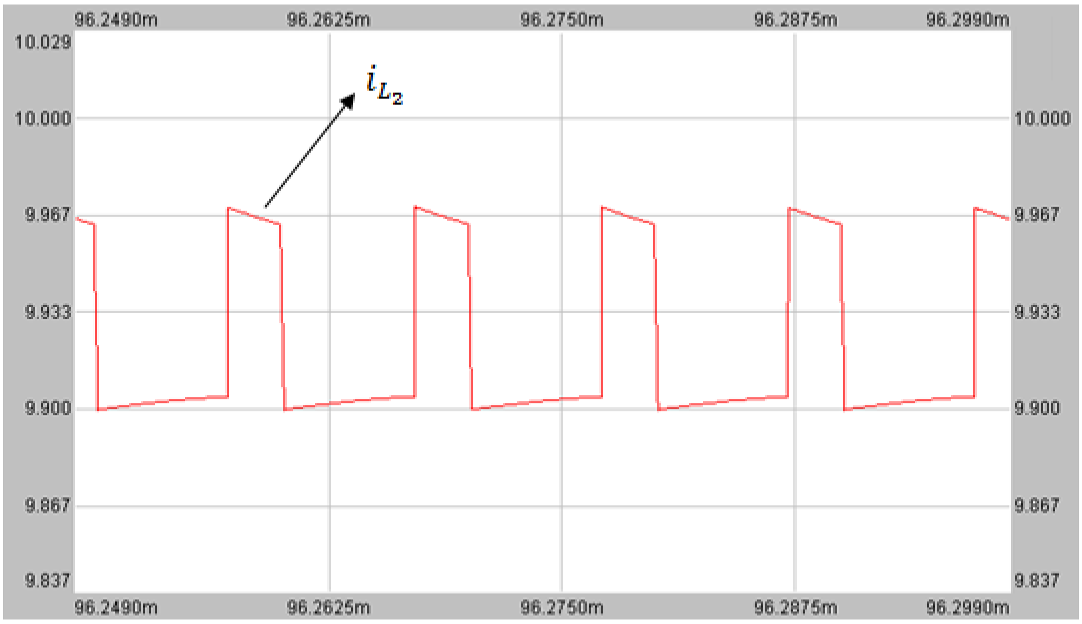

Figure 2-35 Detailed i_{L_2} waveform in IMĆC, $N_a = N_b$, full load

Detailed i_{L_2} waveform is seen in Figure 2-35. Its maximum is 9.97A and minimum is 9.90A. Hence, its peak-to-peak ripple percent is 0.7%. As expected, it is almost ripple-free too. Nevertheless, its ripple percent is greater than that of input current. This is due to the fact that the output capacitance has been selected as small at the beginning. Small capacitance results in high voltage ripple on the output capacitor, which violates one of the assumptions much. In that assumption, capacitor voltages are assumed to be constant. While the ripple on i_{L_1} is affected by input voltage source and C_1, that of i_{L_2} is determined by C_2 and C_o. Input voltage source is absolute constant. C_1 and C_2 capacitances are large enough. Since C_o is not large enough, i_{L_2} ripple percent turns out to be higher, which is an expected result.

Where are the current ripples reflected to? Actually, the ripples are on the transformer windings. Transformer's primary winding current, i_a and secondary winding, i_b can be seen in the following figures.

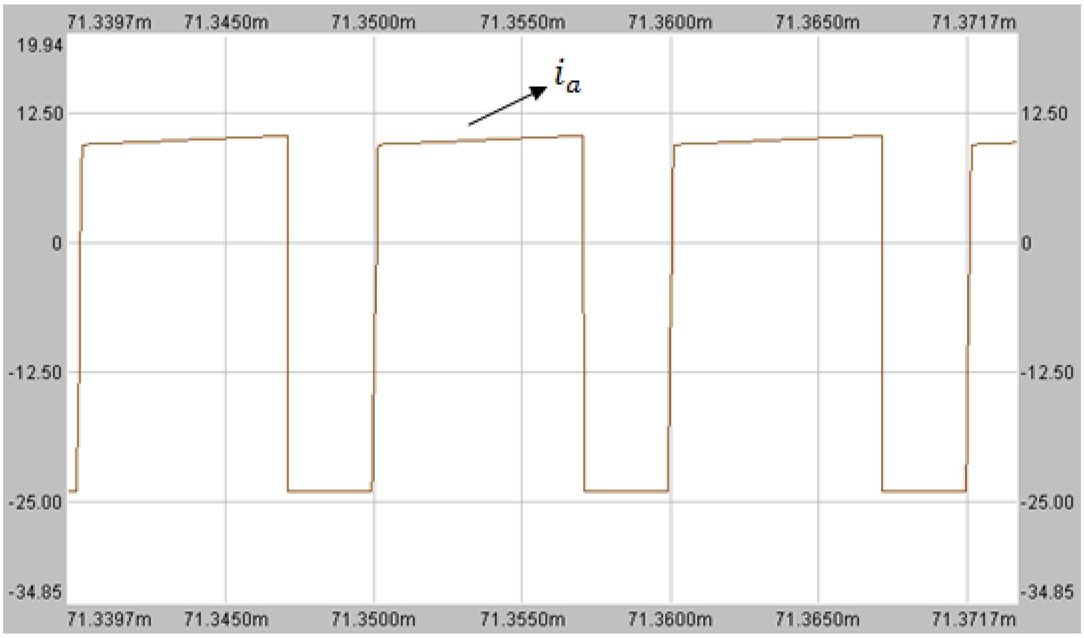

Figure 2-36 Detailed i_a waveform in IMĆC, $N_a = N_b$, full load

Primary winding current waveform is seen above. In Mode 2, its current is the same with i_{L_1} and hence constant. It can be verified by looking at the bottom of the waveform. However, in Mode 1, it has a rising waveform from 9.50A to 10.36A. Hence, its ripple percent is 8.66%. Since N_a is selected as large enough, ripple amplitude turns out to be small here. However, if N_a were selected smaller, the slope at the top of the waveform would be higher. Still, at that situation, bottom of the waveform would be constant. Similar behavior can be observed in secondary winding current waveform, in Figure 2-37. It is constant in Mode 1, but it has a falling waveform from 24.20A to 23.40A in Mode 2. Similarly, lower N_b value would result in larger ripple.

Now, the independency of turns ratio of the transformer from the ripple-free current waveforms property will be verified by simulation. All parameters and operating conditions except N_a, N_1 and duty-factor K remains the same. N_a is selected as $N_b/2$. Then, according to N_a, N_1 is determined by the help of (2-150). Similarly, duty-factor is revised using (2-158).

$$N_a = 5\,Turns \qquad\qquad N_1 \cong 12.9\,Turns$$

$$K \cong 0{,}545$$

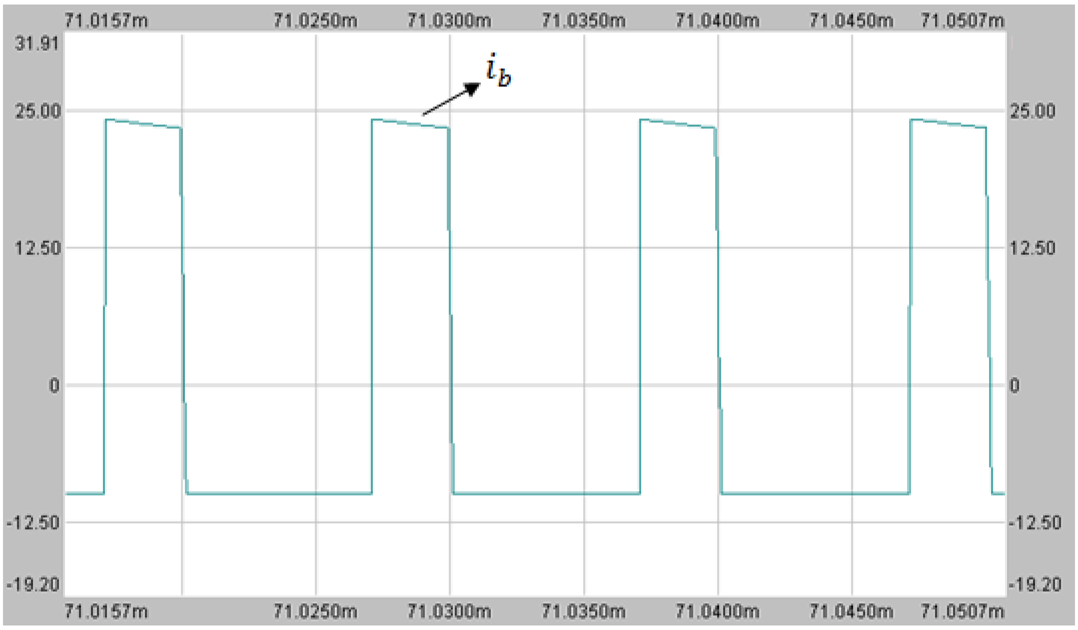

Figure 2-37 Detailed i_b waveform in IMĆC, $N_a = N_b$, full load

Simulation results are given in the following figures. As seen in Figure 2-38, input and output current waveforms are still almost ripple-free. Since it is very obvious, their zoomed in waveforms are not given here. By the help of this figure, the independency of ripple-free current waveforms from turns ratio and also (2-158) is proven. In this situation, ripple content of the transformer’s primary winding is expected to be higher. This fact can even be understood by visual comparison of Figure 2-39 with Figure 2-36. This time, current rises from 19.38A to 22.09A at the top of the waveform. Then, its ripple percent is calculated as 13.07%. This value is 8.66% in $N_a = 10$ case. Consequently, the argument that using lower number of turns in transformers winding results in larger current ripple in that winding is proven by the help of the simulation.

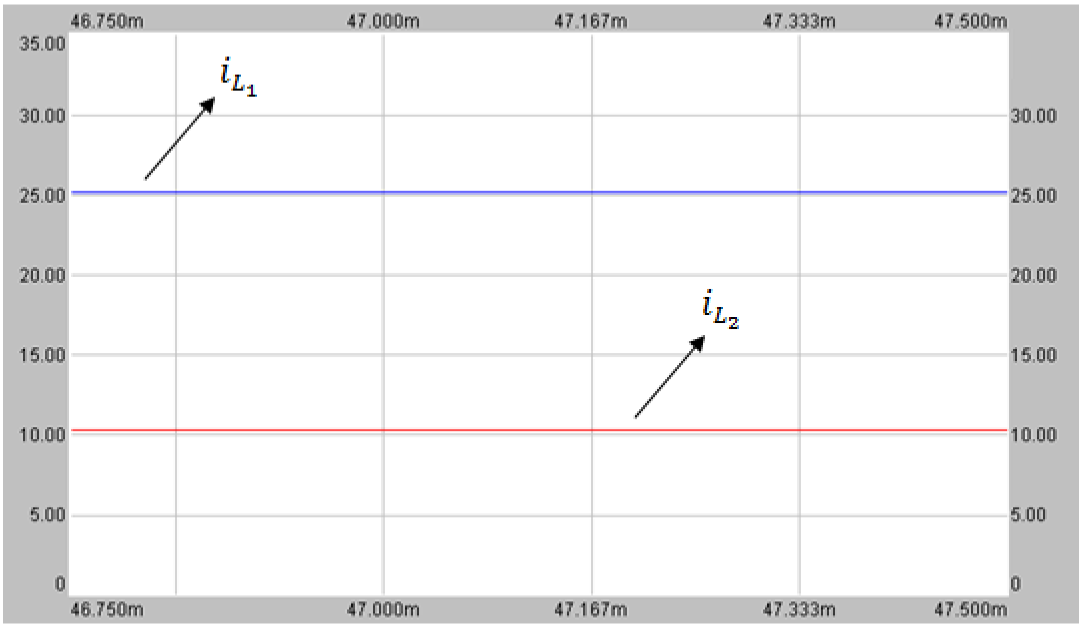

Figure 2-38 i_{L_1} and i_{L_2} waveforms in IMĆC, $2N_a = N_b$, full load

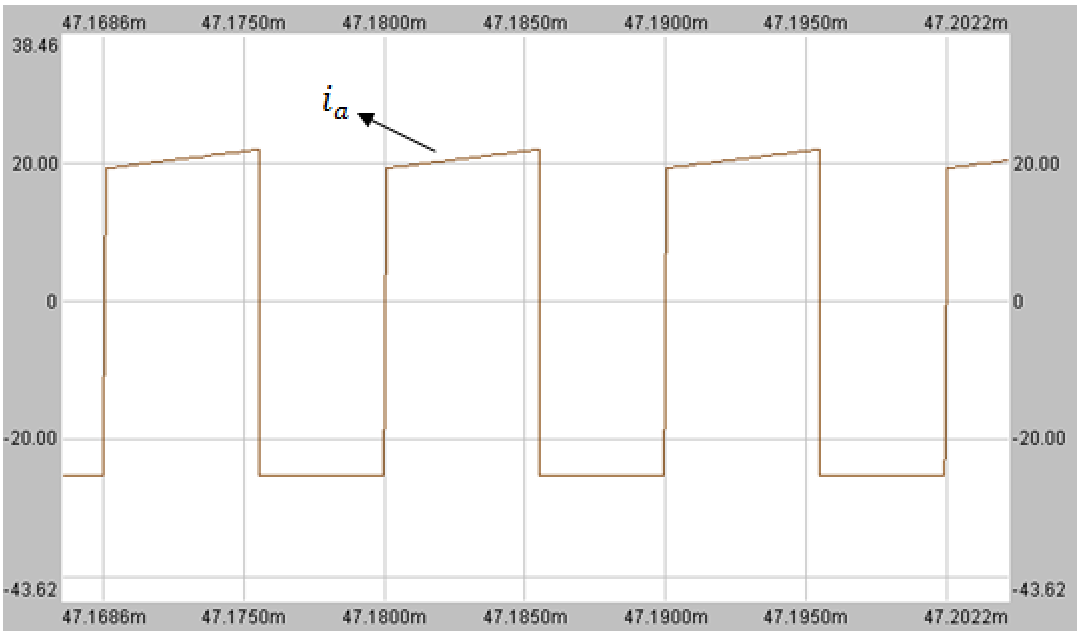

Figure 2-39 Detailed i_a waveform in IMĆC, $2N_a = N_b$, full load

CHAPTER 3

STEADY-STATE AND DYNAMIC MODEL ANALYSIS

3.1 INTRODUCTION

In this chapter; steady-state model, dynamic model and transfer functions of coupled-inductor Ćuk converter, CIĆC in continuous conduction code, CCM are obtained utilizing state-space averaging method, SSAM. SSAM is another contribution of Ćuk to power electronics. Detailed explanation about it can be found in [1]. For the sake of completeness, a summary of SSAM is given in this chapter. There, the steady-state model, dynamic model and transfer functions are derived in matrix forms. Therefore, once the state-space model of a circuit is obtained, by placing the matrices into the final equations give the steady-state model, dynamic model and transfer functions of the circuit. This process is implemented for the circuit with ideal and parasitic elements. In the previous chapter, derivatives of two state-variables –namely i_{L_1} and i_{L_2}- are brought to a suitable form for both circuits in order to use in this chapter.

3.2 STATE-SPACE AVERAGING METHOD

It is widely known that state-space equations of any system can be represented in the following manner.

$$\dot{x}(t) = a(t)x(t) + b(t)u(t) \tag{3-1}$$

$$y(t) = c(t)x(t) + d(t)u(t) \tag{3-2}$$

In continuous time domain $a(t), b(t), c(t)$ and $d(t)$ matrices are expected to be constant for time invariant circuits having only one mode. Any combination of L-C-R circuit can be given as an example of this kind of circuits. However, switching circuits are not of that type. Circuits involving diode and/or switch have more than one mode. A state-space equation set is written while the switch is conducting; but it is not same with the equation set that is valid while the switch is not conducting. In that situation, it is not possible to obtain an ordinary state-space equation set. State-space averaging method, SSAM is a solution of this problem. Equation sets of different modes are utilized in this method. It briefly argues that:

- State-space equation sets pertaining to different modes contribute to the averaged state-space equation set as much as ‘their durations/switching period’ proportions.
- Averaging process causes to lose information about state or output variables at high frequencies. Averaging is done with respect to switching period. Hence, switching ripple and the frequencies above the switching frequency is somehow filtered in this method. At low frequencies, for example below the one tenth of the switching frequency, it represents the system very approximately. At the intermediate frequencies, coming closer up to the switching frequency diverts the system model from the real system.
- Normally $a(t), b(t), c(t)$ and $d(t)$ matrices consist of L-C-R parameters, which are generally time-independent. Hence, these matrices are usually constant. However, averaging process brings duration terms such as $duty\, factor$ and $(1 - duty\, factor)$ to the averaged state-space equation set. Since *duty-factor* is generally the sole manipulated variable of the switching circuits and it is time-dependent, averaging process sometimes make $a(t), b(t), c(t)$ and $d(t)$ matrices time-dependent.
- This method gives not only steady-state model but also dynamic model. It presents the steady-state mean values of the variables such as mean value of

the capacitor voltage or inductor current. Also, it gives more valuable information about the dynamic behavior of the system i.e. small signal model. Utilizing this property, transfer functions of the system can be obtained easily.

At this point, averaged state-space equation set is assumed to be obtained. All the following derivations are based on the averaged state-space equation set.

In order to differentiate the steady-state and dynamic models, all matrices are divided into two parts as ‘mean values’ and ‘perturbed values’.

$$a(t) = A + \tilde{a}(t) \qquad x(t) = X + \tilde{x}(t) \tag{3-3}$$

$$b(t) = B + \tilde{b}(t) \qquad u(t) = U + \tilde{u}(t)$$

$$y(t) = Y + \tilde{y}(t) \qquad c(t) = C + \tilde{c}(t)$$

$$d(t) = D + \tilde{d}(t) \tag{3-4}$$

Capitals such as A and D are constant terms and represent the dc levels at that operating point. Terms with ‘~’ such as $\tilde{x}(t)$ and $\tilde{c}(t)$ are time-dependent and represent the small signal part at that operating point. As a first step, (3-3)-(3-4) are put into (3-1)-(3-2).

$$\dot{[X + \tilde{x}(t)]} = [A + \tilde{a}(t)][X + \tilde{x}(t)] + [B + \tilde{b}(t)][U + \tilde{u}(t)] \tag{3-5}$$

$$[Y + \tilde{y}(t)] = [C + \tilde{c}(t)][X + \tilde{x}(t)] + [D + \tilde{d}(t)][U + \tilde{u}(t)] \tag{3-6}$$

and rearranging them gives:

$$\dot{\tilde{x}}(t) = AX + A\tilde{x}(t) + \tilde{a}(t)X + \tilde{a}(t)\tilde{x}(t) + BU + B\tilde{u}(t) + \tilde{b}(t)U + \tilde{b}(t)\tilde{u}(t) \tag{3-7}$$

$$Y + \tilde{y}(t) = CX + C\tilde{x}(t) + \tilde{c}(t)X + \tilde{c}(t)\tilde{x}(t) + DU + D\tilde{u}(t) + \tilde{d}(t)U + \tilde{d}(t)\tilde{u}(t) \tag{3-8}$$

At this point, the following assumption highly simplifies the analysis. Actually, it can be considered as a reasonable assumption for small signal analysis.

Assumption 3-1: Magnitudes of the capitals are much larger than that of the terms with '~'.

$A \gg \tilde{a}(t)$ $\qquad$ $X \gg \tilde{x}(t)$

$B \gg \tilde{b}(t)$ $\qquad$ $U \gg \tilde{u}(t)$

$Y \gg \tilde{y}(t)$ $\qquad$ $C \gg \tilde{c}(t)$

$D \gg \tilde{d}(t)$

Hence, neglecting second-order small-signal terms in (3-7)-(3-8) gives;

$$\dot{\tilde{x}}(t) = AX + A\tilde{x}(t) + \tilde{a}(t)X + BU + B\tilde{u}(t) + \tilde{b}(t)U \tag{3-9}$$

$$Y + \tilde{y}(t) = CX + C\tilde{x}(t) + \tilde{c}(t)X + DU + D\tilde{u}(t) + \tilde{d}(t)U \tag{3-10}$$

in which steady-state and dynamic models can be separated as;

Steady-State Model:

$$0 = AX + BU \tag{3-11}$$

$$Y = CX + DU \tag{3-12}$$

Dynamic Model:

$$\dot{\tilde{x}}(t) = A\tilde{x}(t) + \tilde{a}(t)X + B\tilde{u}(t) + \tilde{b}(t)U \tag{3-13}$$

$$\tilde{y}(t) = C\tilde{x}(t) + \tilde{c}(t)X + D\tilde{u}(t) + \tilde{d}(t)U \tag{3-14}$$

As mentioned earlier, transfer functions of the system can be obtained by applying Laplace transformation to dynamic model. Since the terms with '~' represent the small signal ac part, initial conditions can be taken as zero. Actually, they are included in dc parts.

$$s\tilde{x}(s) = A\tilde{x}(s) + \tilde{a}(s)X + B\tilde{u}(s) + \tilde{b}(s)U \tag{3-15}$$

$$\tilde{y}(s) = C\tilde{x}(s) + \tilde{c}(s)X + D\tilde{u}(s) + \tilde{d}(s)U \tag{3-16}$$

At this step, $\tilde{x}(s)$ can be obtained by using (3-15).

$$\tilde{x}(s) = [sI - A]^{-1}[\tilde{a}(s)X + B\tilde{u}(s) + \tilde{b}(s)U] \tag{3-17}$$

Then, $\tilde{y}(s)$ is obtained in terms of the known quantities and inputs by using (3-16) and (3-17) as;

$$\tilde{y}(s) = C\{[sI - A]^{-1}\left[\tilde{a}(s)X + B\tilde{u}(s) + \tilde{b}(s)U\right]\} + \tilde{c}(s)X + D\tilde{u}(s) + \tilde{d}(s)U \tag{3-18}$$

3.3 ANALYSIS OF COUPLED-INDUCTOR ĆUK CONVERTER, CIĆC WITH IDEAL ELEMENTS

In this section, steady-state and dynamic model of CIĆC in continuous conduction mode, CCM are obtained. Using dynamic model, transfer functions are also derived. In [2], all these derivations are present for basic Ćuk converter. As expected, they are highly different than those of CIĆC. Therefore, it is necessary to derive them for coupled-inductor case. Besides, in [2], load –namely the output current- is not considered as a time varying input to the converter. Hence, it is not possible to obtain a transfer function reference to the output current there. Here, the output current is considered as a time varying input to the converter.

The circuit schematic of coupled-inductor Ćuk converter with ideal elements is seen in Figure 3-1. Directions of the currents are also shown.

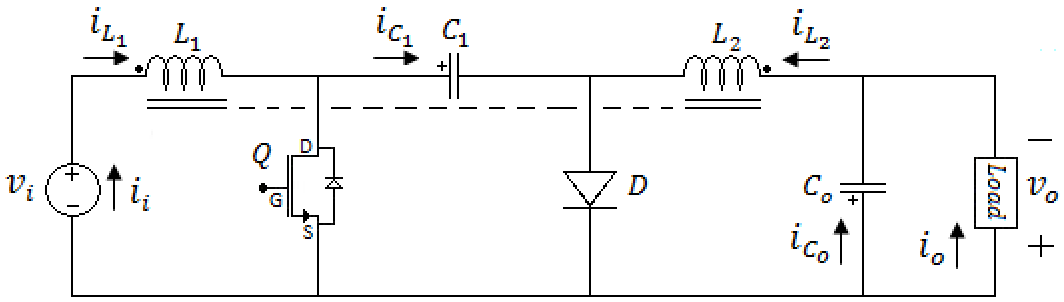

Figure 3-1 Circuit schematic of CIĆC with ideal elements and directions of currents included

Since there are four energy storage elements, four state-variables exist. They are currents in inductors and voltages in capacitors. State-space equations are written in terms of these variables, inputs and outputs. In this work, input current and output voltage are chosen as outputs.

3.3.1 State-Space Equation Set in Mode 1

The equivalent circuit in Mode 1 is as shown in Figure 3-2, where the switch is on.

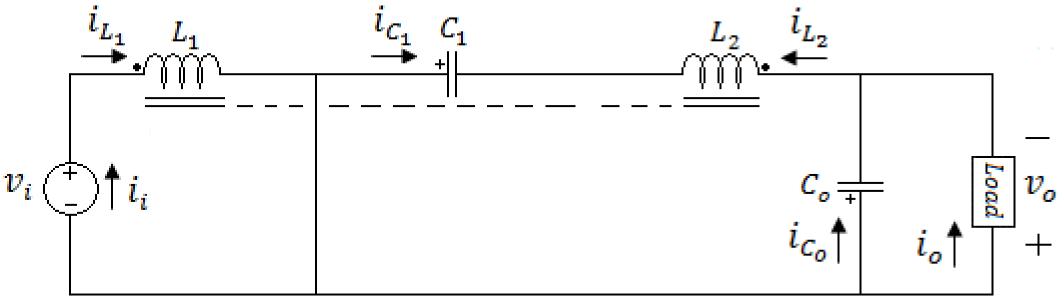

Figure 3-2: Equivalent circuit schematic of CIĆC with ideal elements in Mode 1

Burrowing the derivatives of i_{L_1} and i_{L_2} in Mode 1 derived in CHAPTER 2 as (2-27) and (2-28) and using them here directly as (3-19) and (3-20), we have;

$$\dot{i_{L_1}} = -\frac{\alpha_1}{\Delta_1} v_{C_1} + \frac{\alpha_1}{\Delta_1} v_{C_0} + \frac{\alpha_2}{\Delta_1} v_i \tag{3-19}$$

$$\dot{i_{L_2}} = \frac{\alpha_3}{\Delta_1} v_{C_1} - \frac{\alpha_3}{\Delta_1} v_{C_0} - \frac{\alpha_4}{\Delta_1} v_i \tag{3-20}$$

Now, derivatives of capacitor voltages should be obtained.

For v_{C_1}*:*

$$i_{C_1} = C_1 \frac{dv_{C_1}}{dt} \tag{3-21}$$

$$-i_{L_2} = C_1 \frac{dv_{C_1}}{dt} \tag{3-22}$$

$$\dot{v}_{C_1} = \frac{-1}{C_1} i_{L_2} \tag{3-23}$$

$\dot{v}_{C_1}$ is obtained in terms of state-variables. Similar process is applied to $\dot{v}_{C_o}$.

For v_{C_o}*:*

$$i_{C_o} = C_o \frac{dv_{C_o}}{dt} \tag{3-24}$$

$$i_{L_2} - i_o = C_o \frac{dv_{C_o}}{dt} \tag{3-25}$$

$$\dot{v}_{C_o} = \frac{1}{C_o} i_{L_2} - \frac{1}{C_o} i_o \tag{3-26}$$

Using (3-19), (3-20), (3-23) and (3-26); the following equation matrix is obtained.

$$\begin{bmatrix} \dot{i}_{L_1} \\ \dot{v}_{C_1} \\ \dot{i}_{L_2} \\ \dot{v}_{C_o} \end{bmatrix} = \begin{bmatrix} 0 & -\frac{\alpha_1}{\Delta_1} & 0 & \frac{\alpha_1}{\Delta_1} \\ 0 & 0 & -\frac{1}{C_1} & 0 \\ 0 & \frac{\alpha_3}{\Delta_1} & 0 & -\frac{\alpha_3}{\Delta_1} \\ 0 & 0 & \frac{1}{C_o} & 0 \end{bmatrix} \begin{bmatrix} i_{L_1} \\ v_{C_1} \\ i_{L_2} \\ v_{C_o} \end{bmatrix} + \begin{bmatrix} \frac{\alpha_2}{\Delta_1} & 0 \\ 0 & 0 \\ -\frac{\alpha_4}{\Delta_1} & 0 \\ 0 & -\frac{1}{C_o} \end{bmatrix} \begin{bmatrix} v_i \\ i_o \end{bmatrix} \tag{3-27}$$

As it is seen clearly, input voltage and output current are inputs to the converter. Duty-factor of the switch is defined at this stage. Symbol k represents the duty-factor.

$$k(t) = K + \tilde{k}(t) \tag{3-28}$$

As mentioned earlier, multiplying the matrices with their durations gives their contribution to the averaged matrices. Matrix $a(t)$ or simply a for Mode 1 is defined as a_1(t) or simply a_1. The same argument applies to other matrices, so that;

$$ka_1 = \begin{bmatrix} 0 & -k\frac{\alpha_1}{\Delta_1} & 0 & k\frac{\alpha_1}{\Delta_1} \\ 0 & 0 & -\frac{k}{C_1} & 0 \\ 0 & k\frac{\alpha_3}{\Delta_1} & 0 & -k\frac{\alpha_3}{\Delta_1} \\ 0 & 0 & \frac{k}{C_o} & 0 \end{bmatrix} \tag{3-29}$$

$$kb_1 = \begin{bmatrix} k\frac{\alpha_2}{\Delta_1} & 0 \\ 0 & 0 \\ -k\frac{\alpha_4}{\Delta_1} & 0 \\ 0 & -\frac{k}{C_o} \end{bmatrix} \tag{3-30}$$

$y(t)$ is written similarly. As mentioned earlier, outputs of the system are selected as the output voltage and the input current, which equals i_{L_1}.

$$y = \begin{bmatrix} v_o \\ i_i \end{bmatrix} = \begin{bmatrix} 0 & 0 & 0 & 1 \\ 1 & 0 & 0 & 0 \end{bmatrix} \begin{bmatrix} i_{L_1} \\ v_{C_1} \\ i_{L_2} \\ v_{C_o} \end{bmatrix} + \begin{bmatrix} 0 & 0 \\ 0 & 0 \end{bmatrix} \begin{bmatrix} v_i \\ i_o \end{bmatrix} \tag{3-31}$$

The following matrices are obtained.

$$kc_1 = \begin{bmatrix} 0 & 0 & 0 & k \\ k & 0 & 0 & 0 \end{bmatrix} \tag{3-32}$$

$$kd_1 = \begin{bmatrix} 0 & 0 \\ 0 & 0 \end{bmatrix} \tag{3-33}$$

3.3.2 State-Space Equation Set in Mode 2

The equivalent circuit in Mode 2 is shown in Figure 3-3, with the switch OFF and the diode ON. Similar arguments followed for $\dot{i}_{L_1}$ and $\dot{i}_{L_2}$ in Mode 1 apply also in Mode 2. (2-32) and (2-33) can be used here directly as;

$$\dot{i}_{L_1} = \frac{-\alpha_2}{\Delta_1} v_{C_1} + \frac{\alpha_1}{\Delta_1} v_{C_0} + \frac{\alpha_2}{\Delta_1} v_i \tag{3-34}$$

$$\dot{i}_{L_2} = \frac{\alpha_4}{\Delta_1} v_{C_1} - \frac{\alpha_3}{\Delta_1} v_{C_0} - \frac{\alpha_4}{\Delta_1} v_i \tag{3-35}$$

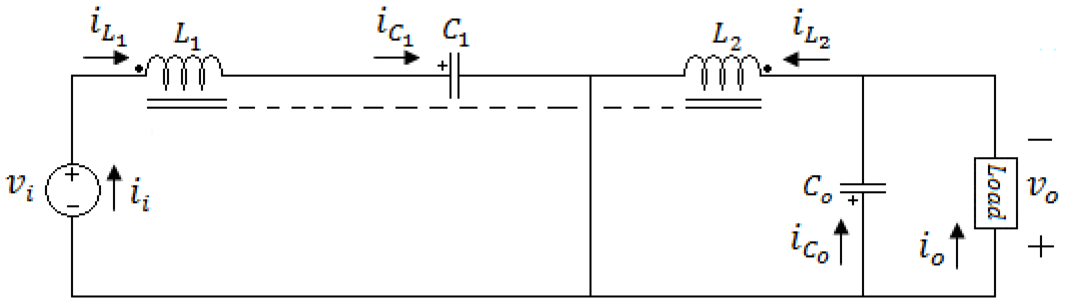

Figure 3-3: Equivalent circuit schematic of CIĆC with ideal elements in Mode 2

For v_{C_1}*:*

$$i_{L_1} = C_1 \frac{dv_{C_1}}{dt} \tag{3-36}$$

$$\dot{v}_{C_1} = \frac{1}{C_1} i_{L_1} \tag{3-37}$$

For v_{C_o}*:*

It is the same with that in Mode 1.

$$\dot{v}_{C_o} = \frac{1}{C_o} i_{L_2} - \frac{1}{C_o} i_o \tag{3-38}$$

Using (3-34), (3-35), (3-37) and (3-39); the following equation matrix is obtained.

$$\begin{bmatrix} \dot{i}_{L_1} \\ \dot{v}_{C_1} \\ \dot{i}_{L_2} \\ \dot{v}_{C_o} \end{bmatrix} = \begin{bmatrix} 0 & -\frac{\alpha_2}{\Delta_1} & 0 & \frac{\alpha_1}{\Delta_1} \\ \frac{1}{C_1} & 0 & 0 & 0 \\ 0 & \frac{\alpha_4}{\Delta_1} & 0 & -\frac{\alpha_3}{\Delta_1} \\ 0 & 0 & \frac{1}{C_o} & 0 \end{bmatrix} \begin{bmatrix} i_{L_1} \\ v_{C_1} \\ i_{L_2} \\ v_{C_o} \end{bmatrix} + \begin{bmatrix} \frac{\alpha_2}{\Delta_1} & 0 \\ 0 & 0 \\ -\frac{\alpha_4}{\Delta_1} & 0 \\ 0 & -\frac{1}{C_o} \end{bmatrix} \begin{bmatrix} v_i \\ i_o \end{bmatrix} \tag{3-39}$$

This time, the normalized duration with respect to the switching period is $(1-k)$. Hence, we have;

$$(1-k)a_2 = \begin{bmatrix} 0 & -(1-k)\frac{\alpha_2}{\Delta_1} & 0 & (1-k)\frac{\alpha_1}{\Delta_1} \\ \frac{1-k}{C_1} & 0 & 0 & 0 \\ 0 & (1-k)\frac{\alpha_4}{\Delta_1} & 0 & -(1-k)\frac{\alpha_3}{\Delta_1} \\ 0 & 0 & \frac{1-k}{C_o} & 0 \end{bmatrix} \tag{3-40}$$

$$(1-k)b_2 = \begin{bmatrix} (1-k)\frac{\alpha_2}{\Delta_1} & 0 \\ 0 & 0 \\ -(1-k)\frac{\alpha_4}{\Delta_1} & 0 \\ 0 & -\frac{1-k}{C_o} \end{bmatrix} \tag{3-41}$$

$y(t)$ is the same with that in Mode 1. Likewise, the following matrices are obtained.

$$(1-k)c_2 = \begin{bmatrix} 0 & 0 & 0 & (1-k) \\ (1-k) & 0 & 0 & 0 \end{bmatrix} \tag{3-42}$$

$$(1-k)d_2 = \begin{bmatrix} 0 & 0 \\ 0 & 0 \end{bmatrix} \tag{3-43}$$

3.3.3 Averaging of Matrices in Mode 1 and Mode 2

Averaged matrices a, b, c, d are represented by $a_1, b_1, c_1, d_1, a_2, b_2, c_2, d_2$ and k in the following manner.

$$a = ka_1 + (1-k)a_2 = \begin{bmatrix} 0 & -\frac{\alpha_2}{\Delta_1} + k\frac{\alpha_2-\alpha_1}{\Delta_1} & 0 & \frac{\alpha_1}{\Delta_1} \\ \frac{1-k}{C_1} & 0 & -\frac{k}{C_1} & 0 \\ 0 & \frac{\alpha_4}{\Delta_1} + k\frac{\alpha_3-\alpha_4}{\Delta_1} & 0 & -\frac{\alpha_3}{\Delta_1} \\ 0 & 0 & \frac{1}{C_o} & 0 \end{bmatrix} \tag{3-44}$$

$$b = kb_1 + (1-k)b_2 = \begin{bmatrix} \frac{\alpha_2}{\Delta_1} & 0 \\ 0 & 0 \\ -\frac{\alpha_4}{\Delta_1} & 0 \\ 0 & -\frac{1}{C_o} \end{bmatrix} \tag{3-45}$$

$$c = kc_1 + (1-k)c_2 = \begin{bmatrix} 0 & 0 & 0 & 1 \\ 1 & 0 & 0 & 0 \end{bmatrix} \tag{3-46}$$

$$d = kd_1 + (1-k)d_2 = \begin{bmatrix} 0 & 0 \\ 0 & 0 \end{bmatrix} \tag{3-47}$$

Thus, state-space averaged model of the circuit can be represented as;

$$\begin{bmatrix} \dot{i}_{L_1} \\ \dot{v}_{C_1} \\ \dot{i}_{L_2} \\ \dot{v}_{C_o} \end{bmatrix} = \begin{bmatrix} 0 & -\frac{\alpha_2}{\Delta_1} + k\frac{\alpha_2 - \alpha_1}{\Delta_1} & 0 & \frac{\alpha_1}{\Delta_1} \\ \frac{1-k}{C_1} & 0 & -\frac{k}{C_1} & 0 \\ 0 & \frac{\alpha_4}{\Delta_1} + k\frac{\alpha_3 - \alpha_4}{\Delta_1} & 0 & -\frac{\alpha_3}{\Delta_1} \\ 0 & 0 & \frac{1}{C_o} & 0 \end{bmatrix} \begin{bmatrix} i_{L_1} \\ v_{C_1} \\ i_{L_2} \\ v_{C_o} \end{bmatrix} + \begin{bmatrix} \frac{\alpha_2}{\Delta_1} & 0 \\ 0 & 0 \\ -\frac{\alpha_4}{\Delta_1} & 0 \\ 0 & -\frac{1}{C_o} \end{bmatrix} \begin{bmatrix} v_i \\ i_o \end{bmatrix} \tag{3-48}$$

$$y = \begin{bmatrix} v_o \\ i_i \end{bmatrix} = \begin{bmatrix} 0 & 0 & 0 & 1 \\ 1 & 0 & 0 & 0 \end{bmatrix} \begin{bmatrix} i_{L_1} \\ v_{C_1} \\ i_{L_2} \\ v_{C_o} \end{bmatrix} + \begin{bmatrix} 0 & 0 \\ 0 & 0 \end{bmatrix} \begin{bmatrix} v_i \\ i_o \end{bmatrix} \tag{3-49}$$

3.3.4 Decomposition of Averaged Model into Steady-State and Dynamic Models

When (3-3), (3-4) and (3-28) are put into (3-48) and (3-49), the following expressions are obtained as;

$$\begin{bmatrix} \dot{I}_{L_1} + \dot{\tilde{i}}_{L_1} \\ \dot{V}_{C_1} + \dot{\tilde{v}}_{C_1} \\ \dot{I}_{L_2} + \dot{\tilde{i}}_{L_2} \\ \dot{V}_{C_o} + \dot{\tilde{v}}_{C_o} \end{bmatrix} =$$

$$\begin{bmatrix} 0 & -\frac{\alpha_2}{\Delta_1} + K\frac{\alpha_2-\alpha_1}{\Delta_1} + \tilde{k}\frac{\alpha_2-\alpha_1}{\Delta_1} & 0 & \frac{\alpha_1}{\Delta_1} \\ \frac{1-K}{C_1} - \frac{\tilde{k}}{C_1} & 0 & -\frac{K}{C_1} - \frac{\tilde{k}}{C_1} & 0 \\ 0 & \frac{\alpha_4}{\Delta_1} + K\frac{\alpha_3-\alpha_4}{\Delta_1} + \tilde{k}\frac{\alpha_3-\alpha_4}{\Delta_1} & 0 & -\frac{\alpha_3}{\Delta_1} \\ 0 & 0 & \frac{1}{C_o} & 0 \end{bmatrix} \begin{bmatrix} I_{L_1} + \tilde{i}_{L_1} \\ V_{C_1} + \tilde{v}_{C_1} \\ I_{L_2} + \tilde{i}_{L_2} \\ V_{C_o} + \tilde{v}_{C_o} \end{bmatrix} +$$

$$\begin{bmatrix} \frac{\alpha_2}{\Delta_1} & 0 \\ 0 & 0 \\ -\frac{\alpha_4}{\Delta_1} & 0 \\ 0 & -\frac{1}{C_o} \end{bmatrix} \begin{bmatrix} V_i + \tilde{v}_i \\ I_o + \tilde{i}_o \end{bmatrix} \tag{3-50}$$

$$y = \begin{bmatrix} V_o + \tilde{v}_o \\ I_i + \tilde{i}_i \end{bmatrix} = \begin{bmatrix} 0 & 0 & 0 & 1 \\ 1 & 0 & 0 & 0 \end{bmatrix} \begin{bmatrix} I_{L_1} + \tilde{i}_{L_1} \\ V_{C_1} + \tilde{v}_{C_1} \\ I_{L_2} + \tilde{i}_{L_2} \\ V_{C_o} + \tilde{v}_{C_o} \end{bmatrix} + \begin{bmatrix} 0 & 0 \\ 0 & 0 \end{bmatrix} \begin{bmatrix} V_i + \tilde{v}_i \\ I_o + \tilde{i}_o \end{bmatrix} \tag{3-51}$$

Then, the matrices in (3-11)-(3-14) can be extracted from (3-50) and (3-51), respectively as;

$$\dot{X} = 0 = \begin{bmatrix} \dot{I}_{L_1} \\ \dot{V}_{C_1} \\ \dot{I}_{L_2} \\ \dot{V}_{C_o} \end{bmatrix} \qquad \dot{\tilde{x}} = \begin{bmatrix} \dot{\tilde{i}}_{L_1} \\ \dot{\tilde{v}}_{C_1} \\ \dot{\tilde{i}}_{L_2} \\ \dot{\tilde{v}}_{C_o} \end{bmatrix} \tag{3-52}$$

$$A = \begin{bmatrix} 0 & -\frac{\alpha_2}{\Delta_1} + K\frac{\alpha_2-\alpha_1}{\Delta_1} & 0 & \frac{\alpha_1}{\Delta_1} \\ \frac{1-K}{C_1} & 0 & -\frac{K}{C_1} & 0 \\ 0 & \frac{\alpha_4}{\Delta_1} + K\frac{\alpha_3-\alpha_4}{\Delta_1} & 0 & -\frac{\alpha_3}{\Delta_1} \\ 0 & 0 & \frac{1}{C_o} & 0 \end{bmatrix} \tag{3-53}$$

$$\tilde{a}=\begin{bmatrix}0 & \tilde{k}\frac{\alpha_2-\alpha_1}{\Delta_1} & 0 & 0\\ -\frac{\tilde{k}}{C_1} & 0 & -\frac{\tilde{k}}{C_1} & 0\\ 0 & \tilde{k}\frac{\alpha_3-\alpha_4}{\Delta_1} & 0 & 0\\ 0 & 0 & 0 & 0\end{bmatrix} \tag{3-54}$$

$$X=\begin{bmatrix}I_{L_1}\\ V_{C_1}\\ I_{L_2}\\ V_{C_o}\end{bmatrix} \qquad \tilde{x}=\begin{bmatrix}\tilde{i}_{L_1}\\ \tilde{v}_{C_1}\\ \tilde{i}_{L_2}\\ \tilde{v}_{C_o}\end{bmatrix} \tag{3-55}$$

$$B=\begin{bmatrix}\frac{\alpha_2}{\Delta_1} & 0\\ 0 & 0\\ -\frac{\alpha_4}{\Delta_1} & 0\\ 0 & -\frac{1}{C_o}\end{bmatrix} \qquad \tilde{b}=\begin{bmatrix}0 & 0\\ 0 & 0\\ 0 & 0\\ 0 & 0\end{bmatrix} \tag{3-56}$$

$$U=\begin{bmatrix}V_i\\ I_o\end{bmatrix} \qquad \tilde{u}=\begin{bmatrix}\tilde{v}_i\\ \tilde{i}_o\end{bmatrix} \tag{3-57}$$

$$Y=\begin{bmatrix}V_o\\ I_i\end{bmatrix} \qquad \tilde{y}=\begin{bmatrix}\tilde{v}_o\\ \tilde{i}_i\end{bmatrix} \tag{3-58}$$

$$C=\begin{bmatrix}0 & 0 & 0 & 1\\ 1 & 0 & 0 & 0\end{bmatrix} \qquad \tilde{c}=\begin{bmatrix}0 & 0 & 0 & 0\\ 0 & 0 & 0 & 0\end{bmatrix} \tag{3-59}$$

$$D=\begin{bmatrix}0 & 0\\ 0 & 0\end{bmatrix} \qquad \tilde{d}=\begin{bmatrix}0 & 0\\ 0 & 0\end{bmatrix} \tag{3-60}$$

3.3.5 Steady-State Model

The static model is given in (3-11) and (3-12). Utilizing the matrices above, the following matrix equations are obtained.

$$\begin{bmatrix}0\\0\\0\\0\end{bmatrix}=\begin{bmatrix}0 & -\frac{\alpha_2}{\Delta_1}+K\frac{\alpha_2-\alpha_1}{\Delta_1} & 0 & \frac{\alpha_1}{\Delta_1}\\ \frac{1-K}{C_1} & 0 & -\frac{K}{C_1} & 0\\ 0 & \frac{\alpha_4}{\Delta_1}+K\frac{\alpha_3-\alpha_4}{\Delta_1} & 0 & -\frac{\alpha_3}{\Delta_1}\\ 0 & 0 & \frac{1}{C_o} & 0\end{bmatrix}\begin{bmatrix}I_{L_1}\\V_{C_1}\\I_{L_2}\\V_{C_o}\end{bmatrix}+\begin{bmatrix}\frac{\alpha_2}{\Delta_1} & 0\\ 0 & 0\\ -\frac{\alpha_4}{\Delta_1} & 0\\ 0 & -\frac{1}{C_o}\end{bmatrix}\begin{bmatrix}V_i\\I_o\end{bmatrix} \tag{3-61}$$

$$\begin{bmatrix}V_o\\I_i\end{bmatrix}=\begin{bmatrix}0 & 0 & 0 & 1\\1 & 0 & 0 & 0\end{bmatrix}\begin{bmatrix}I_{L_1}\\V_{C_1}\\I_{L_2}\\V_{C_o}\end{bmatrix}+\begin{bmatrix}0 & 0\\0 & 0\end{bmatrix}\begin{bmatrix}V_i\\I_o\end{bmatrix} \tag{3-62}$$

(3-62) is just given for the sake of completeness. Required information is extracted from (3-61) as;

First row:

$$0=\left(-\frac{\alpha_2}{\Delta_1}+K\frac{\alpha_2-\alpha_1}{\Delta_1}\right)V_{C_1}+\frac{\alpha_1}{\Delta_1}V_{C_o}+\frac{\alpha_2}{\Delta_1}V_i \tag{3-63}$$

$$V_{C_1}=\frac{\alpha_1 V_{C_o}+\alpha_2 V_i}{\alpha_2-K(\alpha_2-\alpha_1)} \tag{3-64}$$

Second row:

$$0=\frac{(1-K)}{C_1}I_{L_1}-\frac{K}{C_1}I_{L_2} \tag{3-65}$$

$$\frac{I_{L_1}}{I_{L_2}}=\frac{K}{1-K} \tag{3-66}$$

Third row:

$$0=\left(\frac{\alpha_4}{\Delta_1}+K\frac{\alpha_3-\alpha_4}{\Delta_1}\right)V_{C_1}-\frac{\alpha_3}{\Delta_1}V_{C_o}-\frac{\alpha_4}{\Delta_1}V_i \tag{3-67}$$

$$V_{C_1}=\frac{\alpha_3 V_{C_o}+\alpha_4 V_i}{\alpha_4+K(\alpha_3-\alpha_4)} \tag{3-68}$$

Fourth row:

$$0=\frac{1}{C_o}I_{L_2}-\frac{1}{C_o}I_o \tag{3-69}$$

$$I_{L_2} = I_o \tag{3-70}$$

Some meaningful results can be inferred from (3-64), (3-66), (3-68) and (3-70).

- (3-70) says that mean value of L_2 current, I_{L_2} is equal to mean value of the output current, I_o. Since mean value of C_o current, I_{C_o} is zero at steady-state, this result is consistent and meaningful.
- From (3-64) and (3-68), the following equation is obtained. Note that V_{C_o} is equal to V_o.

  $$\frac{V_o}{V_i} = \frac{K}{1-K} \tag{3-71}$$

  (3-71) gives the relationship between the mean values of the input voltage, the output voltage and the duty-factor. It is the standard input/output relationship met in buck-boost structures. Moreover, the following equation is obtained from (3-64) or (3-68) by substitution of K into the equations. K can be extracted from (3-71).

  $$V_{C_1} = V_i + V_o \tag{3-72}$$

  Mean value of the voltage on C_1 is equal to the sum of the mean values of the input and the output voltages. This is another known relationship of the basic Ćuk converter.
- From (3-66) input-to-output power equality is inferred. I_{L_1} can be replaced with mean value of the input current, I_i. As inferred earlier, I_{L_2} is equal to I_o.

  $$\frac{I_o}{I_i} = \frac{1-K}{K} \tag{3-73}$$

  Multiplication of (3-71) and (3-73) gives input-to-output power equality so that,

  $$\frac{V_o I_o}{V_i I_i} = \frac{P_o}{P_i} = 1 \tag{3-74}$$

Since all electrical elements are assumed to be ideal, the efficiency turns out to be 100%. Again, this is a consistent result.

3.3.6 Dynamic Model and Transfer Functions

The dynamic model is given in (3-13) and (3-14). Since the aim is to get the transfer functions, the use of (3-18) will be more proper. Simplification can be applied before using it, because most of the matrices are constant. The simplified version of (3-18) is given in (3-75).

$$\tilde{y}(s) = C[sI - A]^{-1}[\tilde{a}(s)X + B\tilde{u}(s)] \tag{3-75}$$

$\tilde{y}(s)$ will be obtained step by step. Substituting (3-52) and (3-60) into (3-75) gives (3-76);

$$sI - A = \begin{bmatrix} s & \beta_1 & 0 & \beta_2 \\ \beta_3 & s & \beta_4 & 0 \\ 0 & \beta_5 & s & \beta_6 \\ 0 & 0 & \beta_7 & s \end{bmatrix} \tag{3-76}$$

where

$\beta_1 = \frac{\alpha_2}{\Delta_1} - K\frac{\alpha_2 - \alpha_1}{\Delta_1}$ $\beta_2 = -\frac{\alpha_1}{\Delta_1}$

$\beta_3 = -\frac{1-K}{C_1}$ $\beta_4 = \frac{K}{C_1}$

$\beta_5 = -\frac{\alpha_4}{\Delta_1} - K\frac{\alpha_3 - \alpha_4}{\Delta_1}$ $\beta_6 = \frac{\alpha_3}{\Delta_1}$

$\beta_7 = -\frac{1}{C_o}$

Then,

$$[sI-A]^{-1}=\frac{1}{\det([sI-A]^{-1})}\cdot$$

$$\begin{bmatrix} s^3-s\gamma_1 & -s^2\beta_1+\gamma_2 & s\gamma_3 & -s^2\beta_2+\gamma_4 \\ -s^2\beta_3+\gamma_5 & s^3-s\gamma_6 & -s^2\beta_4-\gamma_7 & s\gamma_8 \\ s\gamma_9 & -s^2\beta_5 & s^3-s\gamma_{10} & -s^2\beta_6+\gamma_{11} \\ -\gamma_{12} & s\gamma_{13} & -s^2\beta_7+\gamma_{14} & s^3-s\gamma_{15} \end{bmatrix} \tag{3-77}$$

where

$\gamma_1=\beta_4\beta_5+\beta_6\beta_7$ $\quad\gamma_2=\beta_1\beta_6\beta_7-\beta_2\beta_5\beta_7$

$\gamma_3=\beta_1\beta_4+\beta_2\beta_7$ $\quad\gamma_4=-\beta_1\beta_4\beta_6+\beta_2\beta_4\beta_5$

$\gamma_5=\beta_3\beta_6\beta_7$ $\quad\gamma_6=\beta_6\beta_7$

$\gamma_7=\beta_2\beta_3\beta_7$ $\quad\gamma_8=\beta_2\beta_3+\beta_4\beta_6$

$\gamma_9=\beta_3\beta_5$ $\quad\gamma_{10}=\beta_1\beta_3$

$\gamma_{11}=\beta_1\beta_3\beta_6-\beta_2\beta_3\beta_5$ $\quad\gamma_{12}=\beta_3\beta_5\beta_7$

$\gamma_{13}=\beta_5\beta_7$ $\quad\gamma_{14}=\beta_1\beta_3\beta_7$

$\gamma_{15}=\beta_1\beta_3+\beta_4\beta_5$

$$\det([sI-A]^{-1})=s^4-s^2(\beta_1\beta_3+\beta_4\beta_5+\beta_6\beta_7)+(\beta_1\beta_3\beta_6\beta_7-\beta_2\beta_3\beta_5\beta_7) \tag{3-78}$$

Next step is to obtain $C[sI-A]^{-1}$.

$$C[sI-A]^{-1}=\frac{1}{\det([sI-A]^{-1})}\cdot$$

$$\begin{bmatrix} -\gamma_{12} & s\gamma_{13} & -s^2\beta_7+\gamma_{14} & s^3-s\gamma_{15} \\ s^3-s\gamma_1 & -s^2\beta_1+\gamma_2 & s\gamma_3 & -s^2\beta_2+\gamma_4 \end{bmatrix} \tag{3-79}$$

Laplace transformations of $\tilde{a}(t)$ and $\tilde{u}(t)$ are simply $\tilde{a}(s)$ and $\tilde{u}(s)$ because initial conditions are already included in A and U.

$$\tilde{a}(s)X + B\tilde{u}(s) = \begin{bmatrix} 0 & \tilde{k}(s)\frac{\alpha_2-\alpha_1}{\Delta_1} & 0 & 0 \\ -\tilde{k}(s)\frac{1}{C_1} & 0 & -\tilde{k}(s)\frac{1}{C_1} & 0 \\ 0 & \tilde{k}(s)\frac{\alpha_3-\alpha_4}{\Delta_1} & 0 & 0 \\ 0 & 0 & 0 & 0 \end{bmatrix} \begin{bmatrix} I_{L_1} \\ V_{C_1} \\ I_{L_2} \\ V_{C_o} \end{bmatrix} + \begin{bmatrix} \frac{\alpha_2}{\Delta_1} & 0 \\ 0 & 0 \\ -\frac{\alpha_4}{\Delta_1} & 0 \\ 0 & -\frac{1}{C_o} \end{bmatrix} \begin{bmatrix} \tilde{v}_i(s) \\ \tilde{i}_o(s) \end{bmatrix} \tag{3-80}$$

$$\tilde{a}(s)X + B\tilde{u}(s) = \begin{bmatrix} \tilde{k}(s)\beta_8 \\ -\tilde{k}(s)\beta_{10} \\ \tilde{k}(s)\beta_{11} \\ 0 \end{bmatrix} + \begin{bmatrix} \tilde{v}_i(s)\beta_9 \\ 0 \\ -\tilde{v}_i(s)\beta_{12} \\ -\tilde{i}_o(s)\beta_{13} \end{bmatrix} = \begin{bmatrix} \tilde{k}(s)\beta_8 + \tilde{v}_i(s)\beta_9 \\ -\tilde{k}(s)\beta_{10} \\ \tilde{k}(s)\beta_{11} - \tilde{v}_i(s)\beta_{12} \\ -\tilde{i}_o(s)\beta_{13} \end{bmatrix} \tag{3-81}$$

where

$\beta_8 = V_{C_1}\frac{\alpha_2-\alpha_1}{\Delta_1}$

$\beta_9 = \frac{\alpha_2}{\Delta_1}$

$\beta_{10} = \frac{I_{L_1}+I_{L_2}}{C_1}$

$\beta_{11} = V_{C_1}\frac{\alpha_3-\alpha_4}{\Delta_1}$

$\beta_{12} = \frac{\alpha_4}{\Delta_1}$

$\beta_{13} = \frac{1}{C_o}$

Using (3-75), (3-79) and (3-81); the following equations are obtained.

$$\tilde{y}(s) = \begin{bmatrix} \tilde{v}_{C_o}(s) \\ \tilde{i}_{L_1}(s) \end{bmatrix} = \begin{bmatrix} \tilde{v}_o(s) \\ \tilde{i}_i(s) \end{bmatrix} = \frac{1}{det\,([sI-A]^{-1})} \cdot \begin{bmatrix} \tilde{k}(s)F_1(s) + \tilde{v}_i(s)F_2(s) + \tilde{i}_o(s)F_3(s) \\ \tilde{k}(s)F_4(s) + \tilde{v}_i(s)F_5(s) + \tilde{i}_o(s)F_6(s) \end{bmatrix} \tag{3-82}$$

where

$F_1(s) = -s^2\beta_7\beta_{11} - s\beta_{10}\gamma_{13} + (\beta_{11}\gamma_{14} - \beta_8\gamma_{12})$

$F_2(s) = s^2\beta_7\beta_{11} - (\beta_9\gamma_{12} + \beta_{12}\gamma_{14})$

$$F_3(s) = -s^3\beta_{13} + s\beta_{13}\gamma_{15}$$

$$F_4(s) = s^3\beta_8 + s^2\beta_1\beta_{10} + s(\beta_{11}\gamma_3 - \beta_8\gamma_1) - \beta_{10}\gamma_2$$

$$F_5(s) = -s(\beta_9\gamma_1 + \beta_{12}\gamma_3)$$

$$F_6(s) = s^2\beta_2\beta_{13} - \beta_{13}\gamma_4$$

There are six transfer functions to be inferred from (3-82). The outputs are $\tilde{v}_{C_o}(s) = \tilde{v}_o(s)$ and $\tilde{i}_{L_1}(s) = \tilde{i}_i(s)$; and the inputs are $\tilde{k}(s)$, $\tilde{v}_i(s)$ and $\tilde{i}_o(s)$. At this point linearity assumption is necessary. In small signal model, perturbations around operating point with small magnitudes are considered not to violate the linearity of the small signal model. By the help of this assumption, superposition theorem can be applied to (3-82). As a result, the following six transfer functions can be defined.

Duty Factor to Output Voltage Transfer Function:

$$G_{v_o/k}(s) \overset{\text{def}}{=} \frac{\tilde{v}_o(s)}{\tilde{k}(s)} = \frac{F_1(s)}{\det([sI - A]^{-1})}$$

$$G_{v_o/k}(s) = \frac{-s^2\beta_7\beta_{11} - s\beta_{10}\gamma_{13} + (\beta_{11}\gamma_{14} - \beta_8\gamma_{12})}{s^4 - s^2(\beta_1\beta_3 + \beta_4\beta_5 + \beta_6\beta_7) + (\beta_1\beta_3\beta_6\beta_7 - \beta_2\beta_3\beta_5\beta_7)} \tag{3-83}$$

Input Voltage to Output Voltage Transfer Function:

$$G_{v_o/v_i}(s) \overset{\text{def}}{=} \frac{\tilde{v}_o(s)}{\tilde{v}_i(s)} = \frac{F_2(s)}{\det([sI - A]^{-1})}$$

$$G_{v_o/v_i}(s) = \frac{s^2\beta_7\beta_{11} - (\beta_9\gamma_{12} + \beta_{12}\gamma_{14})}{s^4 - s^2(\beta_1\beta_3 + \beta_4\beta_5 + \beta_6\beta_7) + (\beta_1\beta_3\beta_6\beta_7 - \beta_2\beta_3\beta_5\beta_7)} \tag{3-84}$$

Output Current to Output Voltage Transfer Function:

$$G_{v_o/i_o}(s) \overset{\text{def}}{=} \frac{\tilde{v}_o(s)}{\tilde{i}_o(s)} = \frac{F_3(s)}{\det([sI - A]^{-1})}$$

$$G_{v_o/i_o}(s) = \frac{-s^3\beta_{13} + s\beta_{13}\gamma_{15}}{s^4 - s^2(\beta_1\beta_3 + \beta_4\beta_5 + \beta_6\beta_7) + (\beta_1\beta_3\beta_6\beta_7 - \beta_2\beta_3\beta_5\beta_7)} \tag{3-85}$$

Duty Factor to Input Current Transfer Function:

$$G_{i_i/k}(s) \overset{\text{def}}{=} \frac{\tilde{i}_i(s)}{\tilde{k}(s)} = \frac{F_4(s)}{\det([sI - A]^{-1})}$$

$$G_{i_i/k}(s) = \frac{s^3\beta_8 + s^2\beta_1\beta_{10} + s(\beta_{11}\gamma_3 - \beta_8\gamma_1) - \beta_{10}\gamma_2}{s^4 - s^2(\beta_1\beta_3 + \beta_4\beta_5 + \beta_6\beta_7) + (\beta_1\beta_3\beta_6\beta_7 - \beta_2\beta_3\beta_5\beta_7)} \tag{3-86}$$

Input Voltage to Input Current Transfer Function:

$$G_{i_i/v_i}(s) \overset{\text{def}}{=} \frac{\tilde{i}_i(s)}{\tilde{v}_i(s)} = \frac{F_5(s)}{\det([sI - A]^{-1})}$$

$$G_{i_i/v_i}(s) = \frac{-s(\beta_9\gamma_1 + \beta_{12}\gamma_3)}{s^4 - s^2(\beta_1\beta_3 + \beta_4\beta_5 + \beta_6\beta_7) + (\beta_1\beta_3\beta_6\beta_7 - \beta_2\beta_3\beta_5\beta_7)} \tag{3-87}$$

Output Current to Input Current Transfer Function:

$$G_{i_i/i_o}(s) \overset{\text{def}}{=} \frac{\tilde{i}_i(s)}{\tilde{i}_o(s)} = \frac{F_6(s)}{\det([sI - A]^{-1})}$$

$$G_{i_i/i_o}(s) = \frac{s^2\beta_2\beta_{13} - \beta_{13}\gamma_4}{s^4 - s^2(\beta_1\beta_3 + \beta_4\beta_5 + \beta_6\beta_7) + (\beta_1\beta_3\beta_6\beta_7 - \beta_2\beta_3\beta_5\beta_7)} \tag{3-88}$$

3.3.7 Verification of the Transfer Functions

In this section, the calculated transfer functions of coupled-inductor Ćuk converter with ideal elements through (3-83)-(3-88) are verified by simulations. Two different simulation tools are benefited for this purpose. One of them is Matlab. In this simulation tool, the calculated transfer functions are used as a transfer function block. Small step disturbances in the variables appearing in the denominator of the transfer functions are applied to the transfer functions and the dynamic responses are observed in time domain. Second type of simulations uses Simplorer as a simulation tool. In this simulation group, process circuit model is used instead of the transfer functions. Only the circuit model is present. The same small step disturbances are applied to the circuit model and the dynamic responses are observed, which are naturally in time domain. If the results of both simulations turn out to be the same, one may consider that the transfer function under investigation is valid.

At this point, it is useful to highlight one point. Since the transfer functions are composed of labels, it is not easy to see that they include operating point parameters such as I_{L_1}, I_{L_2}, V_{C_1}, V_{C_o} and K. That is, transfer functions are specific to the operating point. For this reason, transfer functions are calculated with respect to operating point. As the operating point, the fourth end operating point ($V_i = 10V$, $V_o = 24V$, full load) is selected.

Verification of $G_{v_o/k}(s)$:

In Figure 3-4, step response of the duty-factor-to-output voltage transfer function $G_{v_o/k}(s)$ is given. Horizontal axis is in seconds and vertical axis is in volts. As a step disturbance, 0.0025 increase in duty-factor is utilized. Mathematically, Figure 3-4 is the plot of the following function in time domain.

$$G_{v_o/k}(s) \cdot \frac{0.0025}{s}$$

It is plotted in Matlab with the following input parameters. N_1, N_2, $\mathbb{R}_m$, $\mathbb{R}_{l1}$, $\mathbb{R}_{l2}$, C_1 and C_o are the parameters of the practically implemented circuit. K, V_{C_1}, I_{L_1} and I_{L_2} are the parameters taken from the simulation which is aimed to be performed at the fourth end operating point. As it is understood, small deviation in the simulation is also reflected to the transfer function for a better comparison.

$N_1 = 19.5\ Turns$

$N_2 = 18.25\ Turns$

$\mathbb{R}_m = 3046875\ H^{-1}$

$\mathbb{R}_{l1} = 253.5 \times 10^6\ H^{-1}$

$\mathbb{R}_{l2} = 45.625 \times 10^6\ H^{-1}$

$K = 0.711$

$C_1 = 3000\ uF$

$C_o = 9.4\ uF$

$V_{C_1} = 34.6\ V$

$I_{L_1} = 25.6\ A$

$I_{L_2} = 10.4\ A$

Physically, Figure 3-4 is the plot of the output voltage of the circuit operating at steady-state and disturbed with 0.0025 increase in the duty-factor at t = 0. Now, this figure will be compared with the simulation result in Simplorer and whether the derived transfer function is valid or not will be decided. For the time being, it can only be said that the output voltage oscillates with the peak-to-peak magnitude of about 0.6V and the frequency of about 75Hz. Since all the elements are ideal and there is no damping element including the load, the oscillation continues forever.

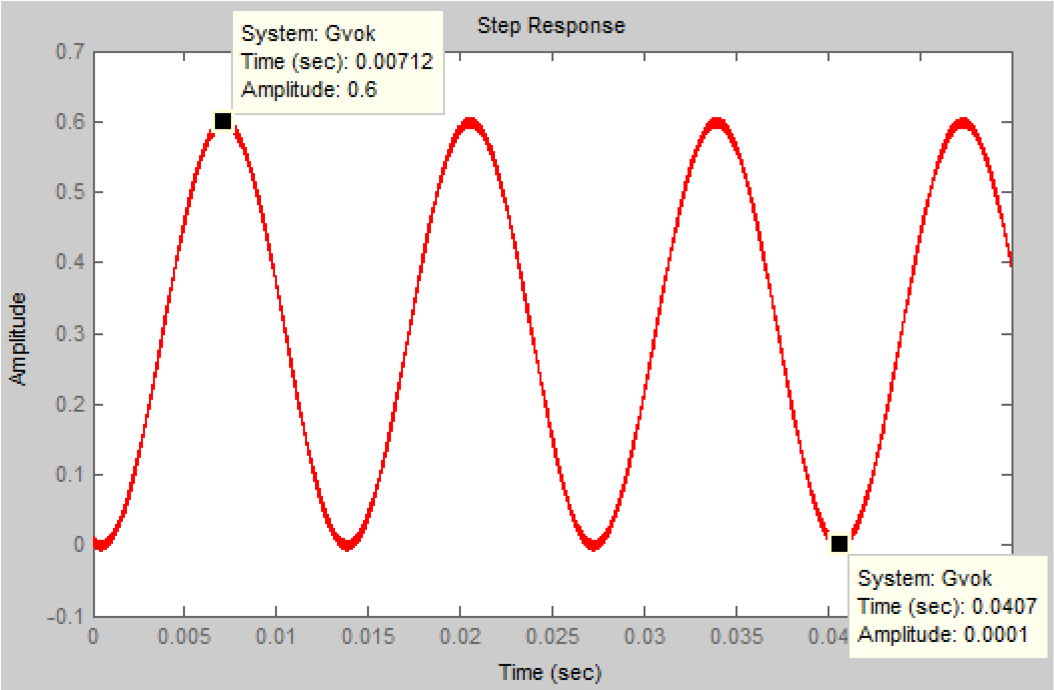

Figure 3-4: Step response of $G_{v_o/k}(s)$ in Matlab, $\Delta K = 0.0025$

In Figure 3-5, response of v_o to small step change in k at t = 200msec in Simplorer is shown. Similarly, horizontal axis is seconds and vertical axis is in volts. Since this is a small signal analysis, 24.60V-200msec point in Figure 3-16 corresponds to 0V-0sec in Figure 3-4. When this correspondence is utilized, it is seen that the figures are almost the same in terms of waveform behavior, phase, magnitude and frequency. Note that the switching action which can be observed in Simplorer is not observed in Matlab. This result is expected because of the nature of the state-space averaging method. As a result, $G_{v_o/k}(s)$ is verified.

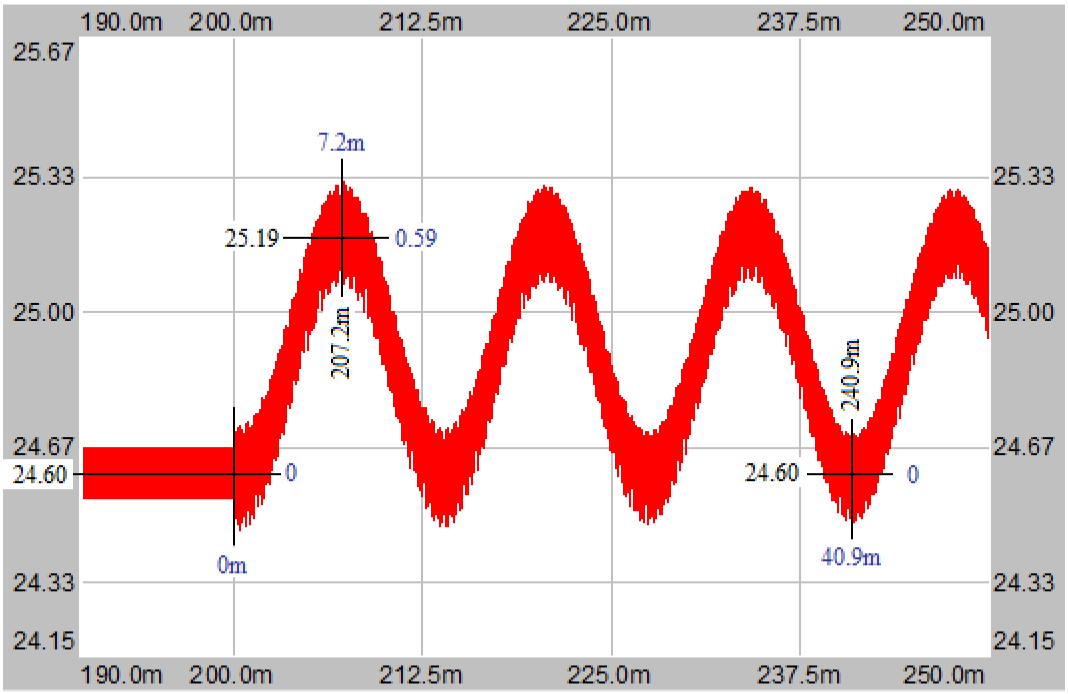

Figure 3-5: Response of v_o to small step change in k in Simplorer, ideal elements, $\Delta K = 0.0025$

Verification of $G_{i_i/k}(s)$*:*

The second output of the circuit is the input current. What the response of the input current is when the same step change in duty-factor occurs can be plotted by using the following function in time domain.

$$G_{i_i/k}(s) \cdot \frac{0.0025}{s}$$

Figure 3-6 says that when the duty-factor is increased 0.0025 much at t=0 at that operating point, the input current shows this variation in time. As expected, the horizontal axis is in seconds and the vertical axis is in Amperes. To see whether the derived transfer function is correct or not, the same situation is formed in Simplorer and the input current is observed in Figure 3-7. Note the perfect similarity between the figures.

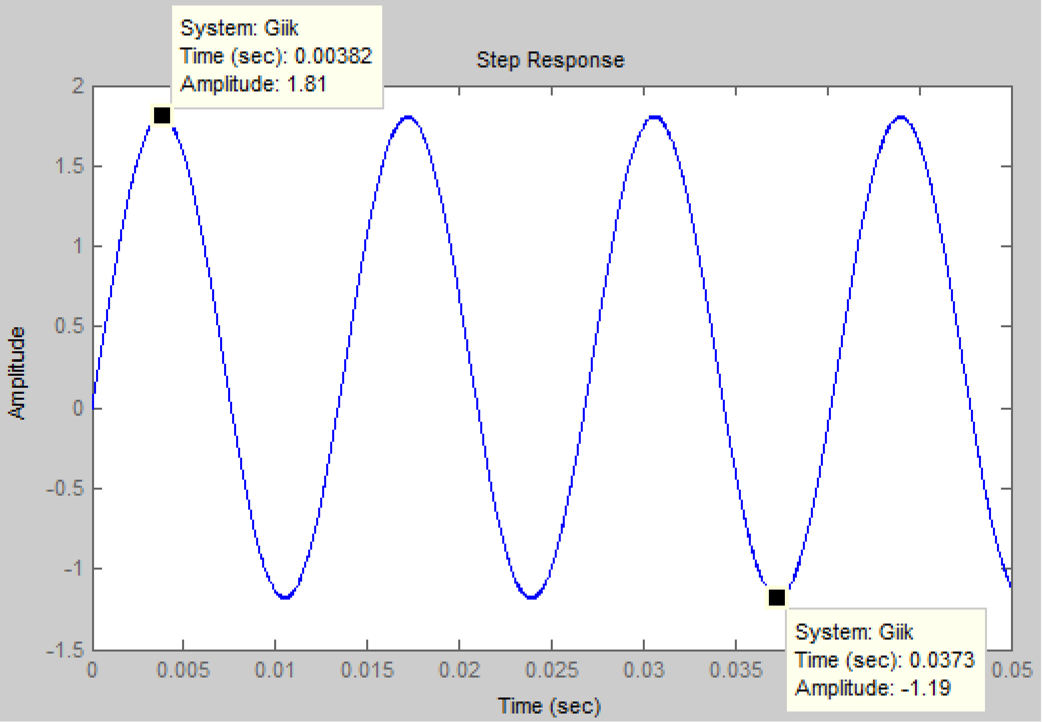

Figure 3-6: Step response of $G_{i_i/k}(s)$ in Matlab, $\Delta K = 0.0025$

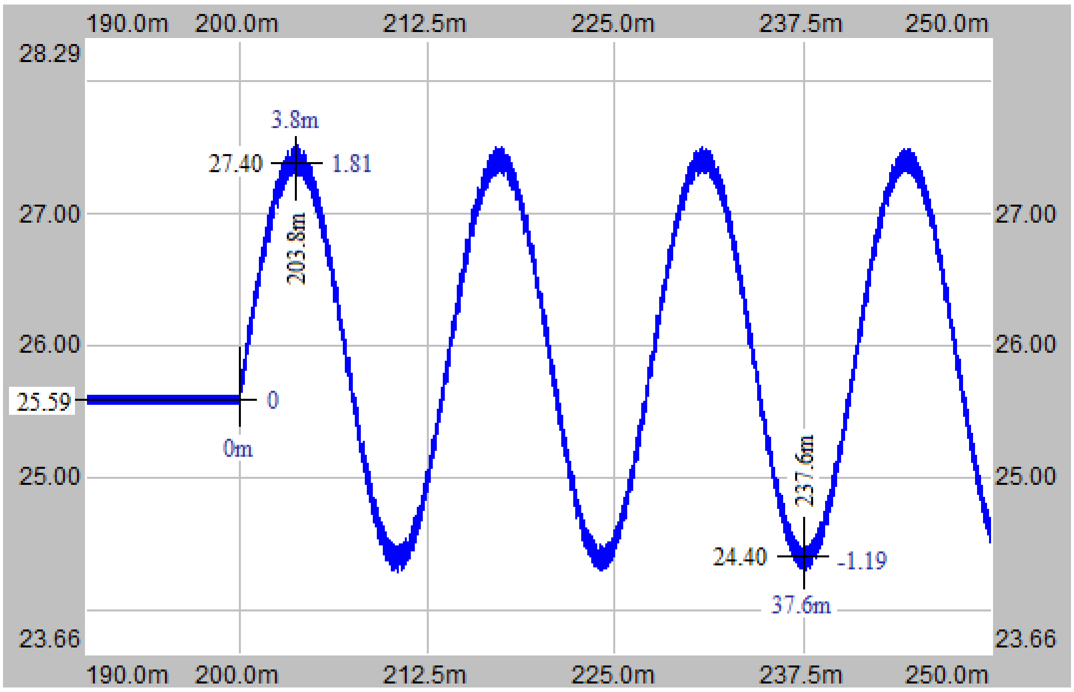

Figure 3-7: Response of i_i to small step change in k in Simplorer, ideal elements, $\Delta K = 0.0025$

Verification of $G_{v_o/v_i}(s)$*:*

The response of the output voltage when 0.1V step change in input voltage occurs is plotted in Figure 3-8 by using the following function in time domain.

$$G_{v_o/v_i}(s) \cdot \frac{0.1}{s}$$

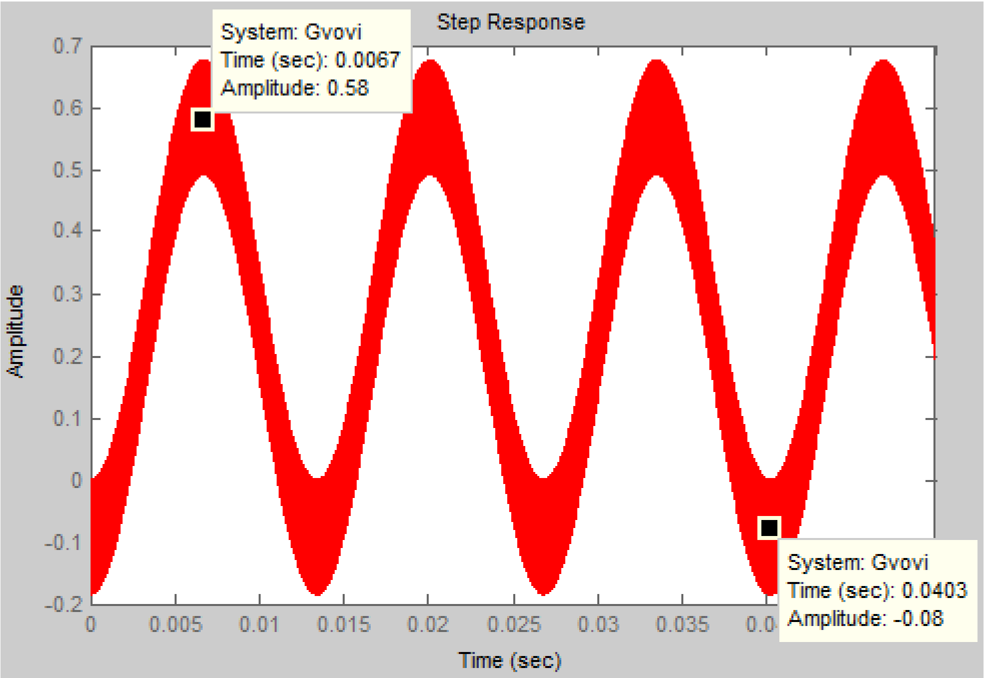

Figure 3-8: Step response of $G_{v_o/v_i}(s)$ in Matlab, $\Delta V_i = 0.1V$

The corresponding waveform in Simplorer is presented in Figure 3-9. $G_{v_o/v_i}(s)$ is validated in this way.

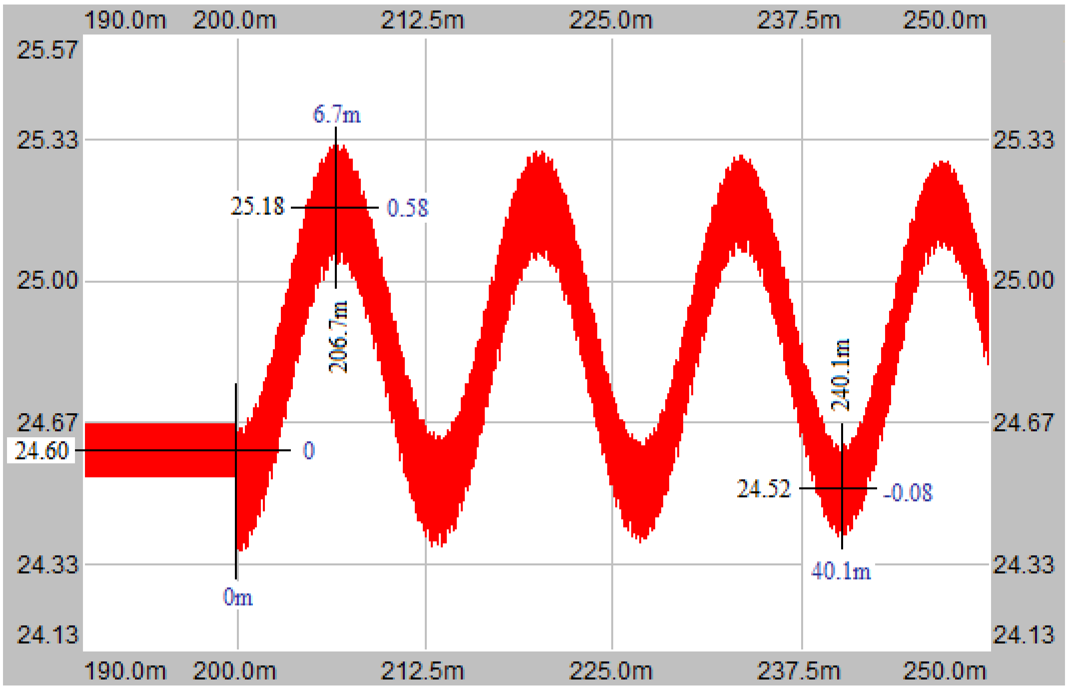

Figure 3-9: Response of v_o to small step change in v_i in Simplorer, ideal elements, $\Delta V_i = 0.1V$

Verification of $G_{i_i/v_i}(s)$*:*

The response of the input current when 0.1V step change in input voltage occurs is plotted in Figure 3-10 by using the following function in time domain.

$$G_{i_i/v_i}(s) \cdot \frac{0.1}{s}$$

The corresponding waveform in Simplorer is presented in Figure 3-11. Similarly, $G_{i_i/v_i}(s)$ is verified.

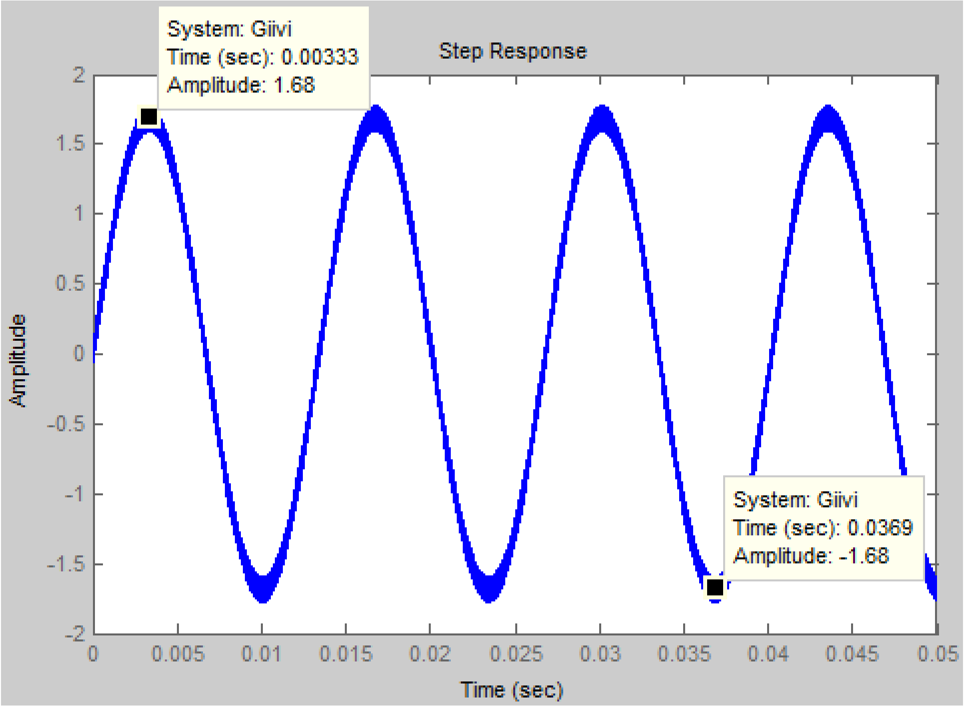

Figure 3-10: Step response of $G_{i_i/v_i}(s)$ in Matlab, $\Delta V_i = 0.1V$

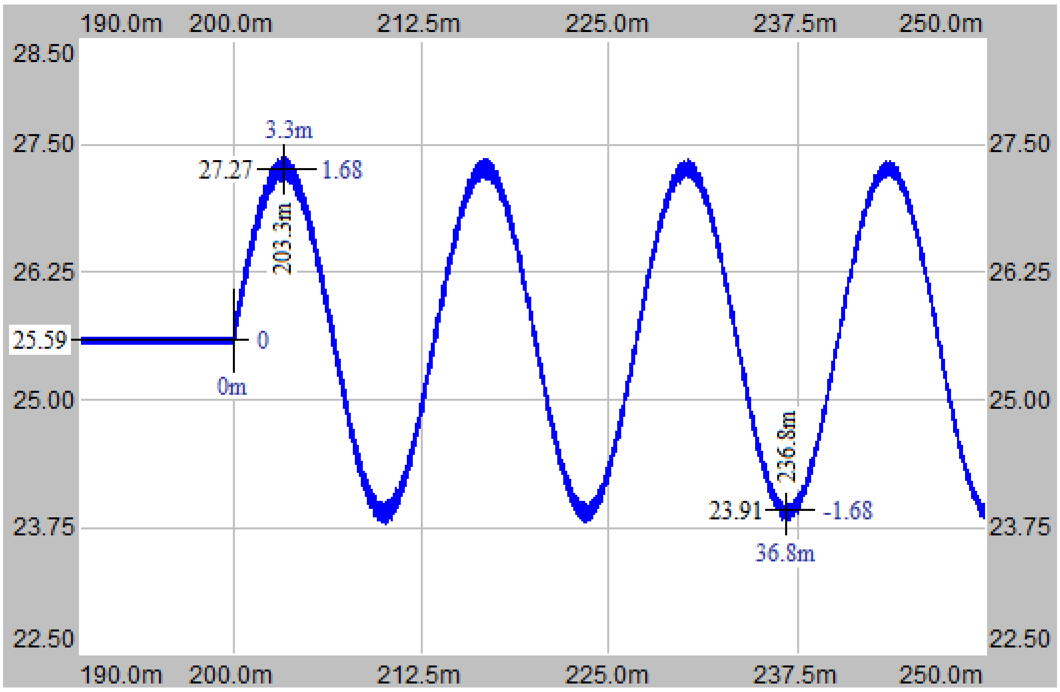

Figure 3-11: Response of i_i to small step change in v_i in Simplorer, ideal elements, $\Delta V_i = 0.1V$

Verification of $G_{v_o/i_o}(s)$*:*

The response of output voltage when 0.25A step change in output current happens is plotted in Figure 3-12 by using the following function in time domain.

$$G_{v_o/i_o}(s) \cdot \frac{0.25}{s}$$

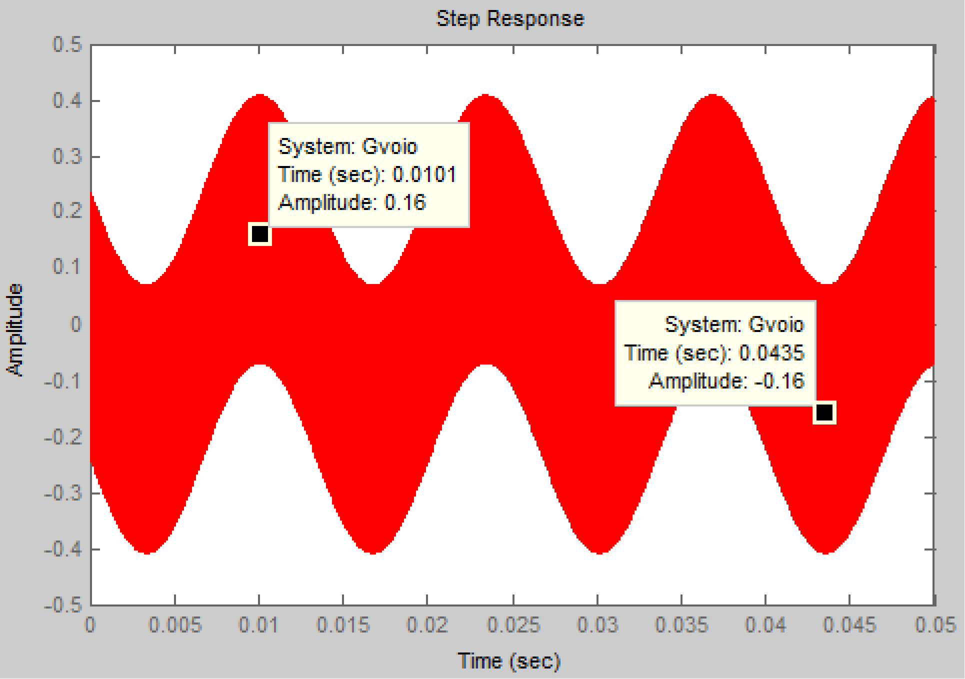

Figure 3-12: Step response of $G_{v_o/i_o}(s)$ in Matlab, $\Delta I_o = 0.25A$

The corresponding waveform in Simplorer is presented in Figure 3-13. In this figure, the output voltage seems to decrease in time at first sight. However, while its maximum is decreasing, its minimum is increasing. That is, the envelope is being thinner as time passes. However, the mid-sinusoidal passing the waveforms does not change. Most probably, the increase in the thickness of the waveform is the secondary effect of the step change. The long and the short of it, $G_{v_o/i_o}(s)$ is validated via the similarity between the figures.

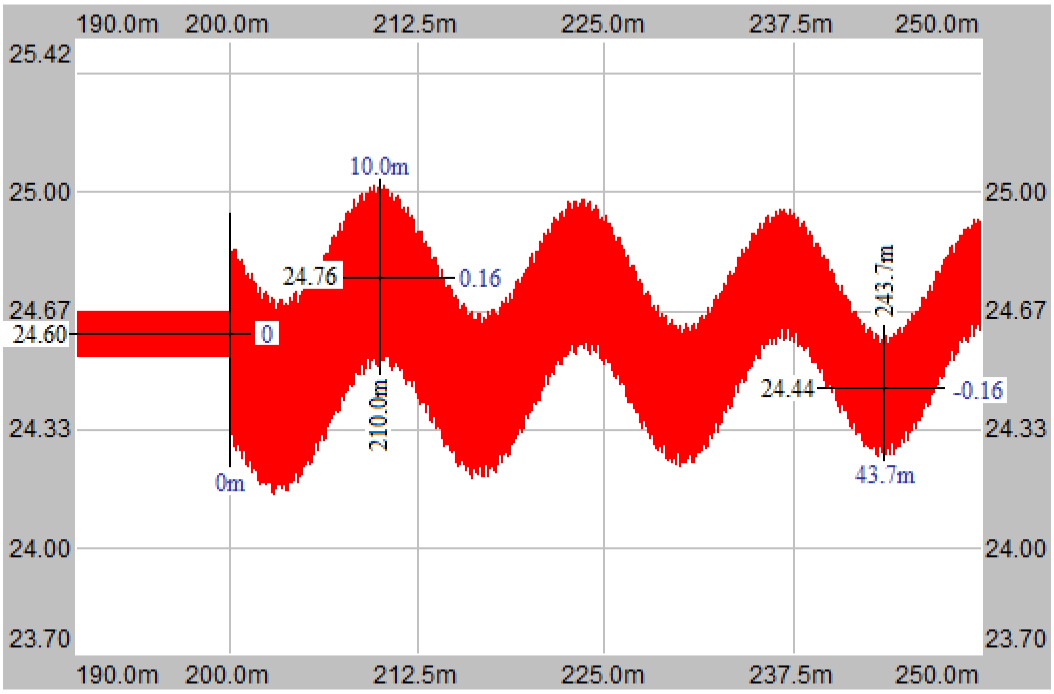

Figure 3-13: Response of v_o to small step change in i_o in Simplorer, ideal elements, $\Delta I_o = 0.25A$

Verification of $G_{i_i/i_o}(s)$*:*

The response of input current when 0.25A step change in output current happens is plotted in Figure 3-14 by using the following function in time domain.

$$G_{i_i/i_o}(s) \cdot \frac{0.25}{s}$$

The corresponding waveform in Simplorer is presented in Figure 3-15. In a similar manner, $G_{i_i/i_o}(s)$ is verified.

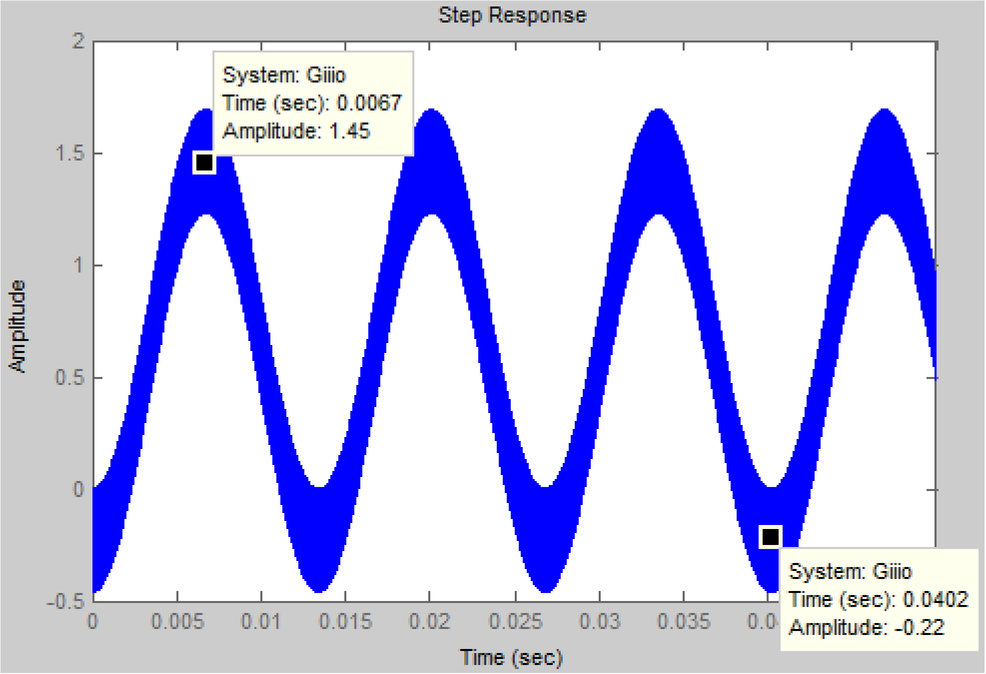

Figure 3-14: Step response of $G_{i_i/i_o}(s)$ in Matlab, $\Delta I_o = 0.25A$

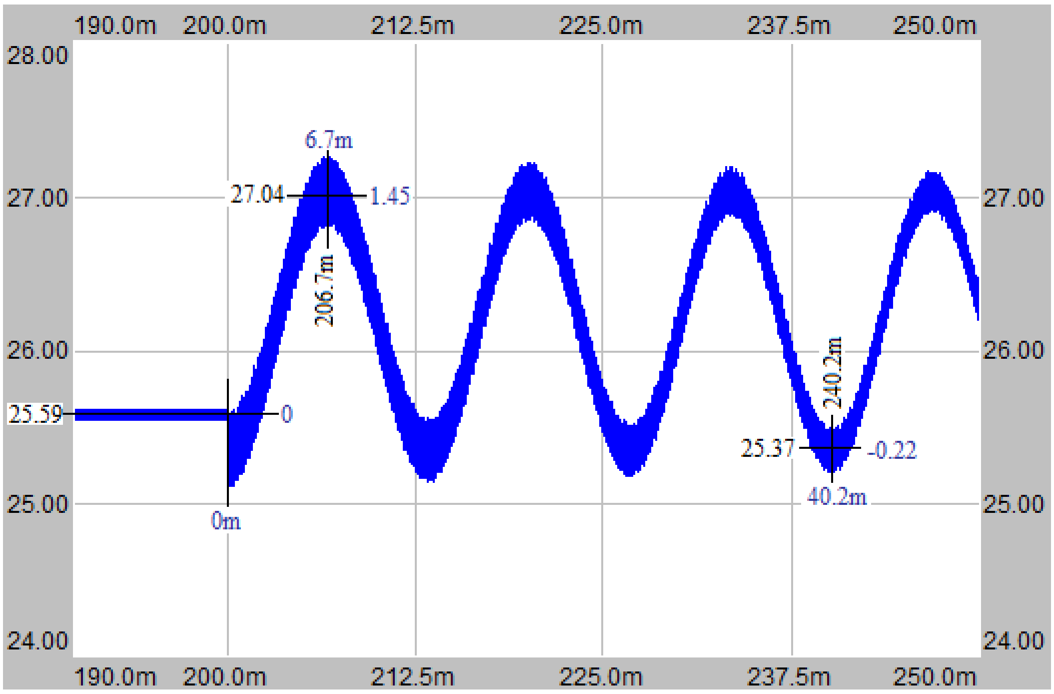

Figure 3-15: Response of i_i to small step change in i_o in Simplorer, ideal elements, $\Delta I_o = 0.25A$

To sum up, all of 6 transfer functions derived for CIĆC with ideal elements have been verified.

3.4 ANALYSIS OF COUPLED-INDUCTOR ĆUK CONVERTER WITH PARASITIC ELEMENTS

Different from the previous section, parasitic elements are included in the circuit in this section. Then, the same procedure will be repeated. Explanations given in the previous section are also valid in this section. Some steps are omitted.

The circuit schematic of CIĆC with parasitic elements is seen Figure 3-16. Directions of the currents are also shown.

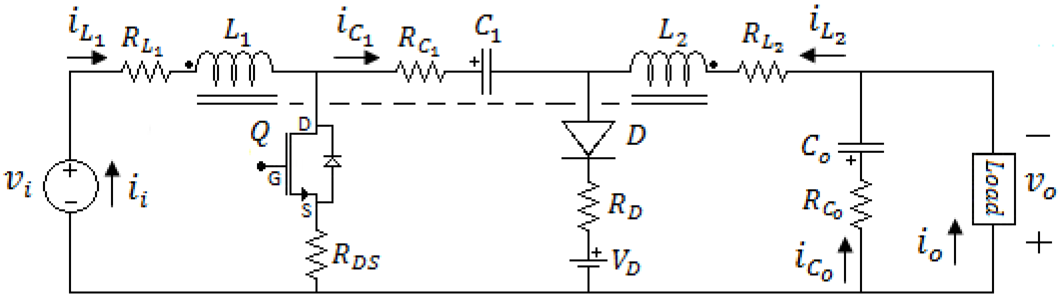

Figure 3-16 Circuit schematic of CIĆC with parasitic elements and directions of currents included

3.4.1 State-Space Equation Set in Mode 1

Equivalent circuit schematic in Mode 1 is shown in Figure 3-17.

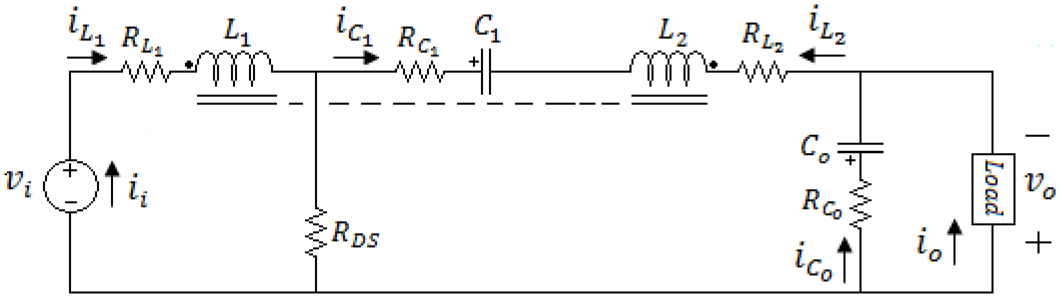

Figure 3-17 Equivalent circuit schematic of CIĆC with parasitic elements (directions of currents included) in Mode 1

Burrowing the derivatives of i_{L_1} and i_{L_2} in Mode 1 derived in CHAPTER 2 as (2-80) and (2-81) and using them here directly as (3-89) and (3-90), we have;

$$\dot{i_{L_1}} = \beta_{14} i_{L_1} - \beta_{15} v_{C_1} + \beta_{16} i_{L_2} + \beta_{15} v_{C_o} + \beta_{17} v_i - \beta_{18} i_o \tag{3-89}$$

$$\dot{i_{L_2}} = \beta_{19} i_{L_1} + \beta_{20} v_{C_1} + \beta_{21} i_{L_2} - \beta_{20} v_{C_o} - \beta_{22} v_i + \beta_{23} i_o \tag{3-90}$$

where

$$\beta_{14} = \frac{\alpha_2\alpha_5 - \alpha_1\alpha_7}{\Delta_1} \qquad \beta_{15} = \frac{\alpha_1}{\Delta_1}$$

$$\beta_{16} = \frac{\alpha_2\alpha_6 - \alpha_1\alpha_8}{\Delta_1} \qquad \beta_{17} = \frac{\alpha_2}{\Delta_1}$$

$$\beta_{18} = \frac{\alpha_1\alpha_9}{\Delta_1} \qquad \beta_{19} = \frac{\alpha_3\alpha_7 - \alpha_4\alpha_5}{\Delta_1}$$

$$\beta_{20} = \frac{\alpha_3}{\Delta_1} \qquad \beta_{21} = \frac{\alpha_3\alpha_8 - \alpha_4\alpha_6}{\Delta_1}$$

$$\beta_{22} = \frac{\alpha_4}{\Delta_1} \qquad \beta_{23} = \frac{\alpha_3\alpha_9}{\Delta_1}$$

Note that i_{L_1} and i_{L_2} terms have been added to the equations different from the ideal case. Besides, the coefficients of other terms have changed.

Next step is to obtain derivatives of capacitor voltages. Before proceeding further, an important point should be considered: Equivalent series resistance, ESRs of the capacitors are included in the element model. In this situation, capacitor voltage v_{C_x} would normally be expected to include the voltage drop on ESR. However, state-space averaging method, SSAM is based on state-variables, which are selected as the variables representing the energy content of the energy storing elements. For capacitors, state-variables are the voltages on them. Including the ESR voltage drops on capacitor voltages would be wrong because it would not give the right information about its stored energy. Therefore, in the following equations, v_{C_x}represents the voltage of ideal capacitor and not the voltage drop on ESR. Actually, the same argument applies to other parasitic elements, as well.

For v_{C_1}*:*

$$\dot{v_{C_1}} = -\beta_{24} i_{L_2} \tag{3-91}$$

where

$$\beta_{24} = \frac{1}{C_1}$$

For v_{C_o}*:*

$$\dot{v_{C_o}} = \beta_{25} i_{L_2} - \beta_{25} i_o \tag{3-92}$$

where

$$\beta_{25} = \frac{1}{C_o}$$

Then the following equation matrix is obtained. Note that the dimensions of b matrix and u vector increase. This modification is needed in Mode 2 and does not affect this mode practically. Still, the modification is applied here for the consistency in dimensions of the matrices. The reason of this change will be explained in Mode 2 analysis.

$$\begin{bmatrix} \dot{i_{L_1}} \\ \dot{v_{C_1}} \\ \dot{i_{L_2}} \\ \dot{v_{C_o}} \end{bmatrix} = \begin{bmatrix} \beta_{14} & -\beta_{15} & \beta_{16} & \beta_{15} \\ 0 & 0 & -\beta_{24} & 0 \\ \beta_{19} & \beta_{20} & \beta_{21} & -\beta_{20} \\ 0 & 0 & \beta_{25} & 0 \end{bmatrix} \begin{bmatrix} i_{L_1} \\ v_{C_1} \\ i_{L_2} \\ v_{C_o} \end{bmatrix} + \begin{bmatrix} \beta_{17} & -\beta_{18} & 0 \\ 0 & 0 & 0 \\ -\beta_{22} & \beta_{23} & 0 \\ 0 & -\beta_{25} & 0 \end{bmatrix} \begin{bmatrix} v_i \\ i_o \\ v_D \end{bmatrix} \tag{3-93}$$

The following matrices are obtained by addition of duty-factor. Since these matrices are valid in Mode 1, their elements are multiplied by k.

$$ka_1 = \begin{bmatrix} k\beta_{14} & -k\beta_{15} & k\beta_{16} & k\beta_{15} \\ 0 & 0 & -k\beta_{24} & 0 \\ k\beta_{19} & k\beta_{20} & k\beta_{21} & -k\beta_{20} \\ 0 & 0 & k\beta_{25} & 0 \end{bmatrix} \tag{3-94}$$

$$kb_1 = \begin{bmatrix} k\beta_{17} & -k\beta_{18} & 0 \\ 0 & 0 & 0 \\ -k\beta_{22} & k\beta_{23} & 0 \\ 0 & -k\beta_{25} & 0 \end{bmatrix} \tag{3-95}$$

$y(t)$ is written in the following manner. Before that, v_o should be obtained because it seems to be different in this analysis compared to that in the previous analysis. i_i remains the same.

$$v_o = v_{C_o} + i_{C_o} R_{C_o} \tag{3-96}$$

$$v_o = R_{C_o} i_{L_2} + v_{C_o} - R_{C_o} i_o \tag{3-97}$$

$$y = \begin{bmatrix} v_o \\ i_i \end{bmatrix} = \begin{bmatrix} 0 & 0 & \beta_{26} & 1 \\ 1 & 0 & 0 & 0 \end{bmatrix} \begin{bmatrix} i_{L_1} \\ v_{C_1} \\ i_{L_2} \\ v_{C_o} \end{bmatrix} + \begin{bmatrix} 0 & -\beta_{26} & 0 \\ 0 & 0 & 0 \end{bmatrix} \begin{bmatrix} v_i \\ i_o \\ v_D \end{bmatrix} \tag{3-98}$$

where

$$\beta_{26} = R_{C_o}$$

As a result, the following matrices are obtained as;

$$kc_1 = \begin{bmatrix} 0 & 0 & k\beta_{26} & k \\ k & 0 & 0 & 0 \end{bmatrix} \tag{3-99}$$

$$kd_1 = \begin{bmatrix} 0 & -k\beta_{26} & 0 \\ 0 & 0 & 0 \end{bmatrix} \tag{3-100}$$

3.4.2 State-Space Equation Set in Mode 2

Equivalent circuit in Mode 2 is as shown in Figure 3-18.

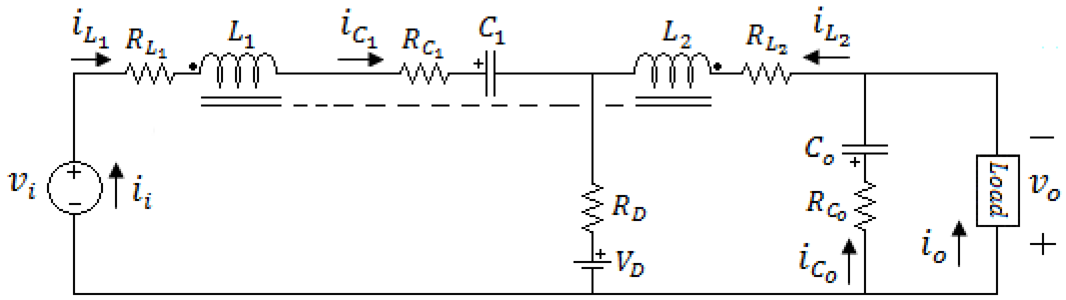

Figure 3-18: Equivalent circuit schematic of CIĆC with parasitic elements in Mode 2

Burrowing (2-82) and (2-83) from CHAPTER 2, we have;

$$\dot{i}_{L_1} = \beta_{27} i_{L_1} - \beta_{28} v_{C_1} + \beta_{29} i_{L_2} + \beta_{30} v_{C_o} + \beta_{28} v_i - \beta_{31} i_o + \beta_{32} V_D \qquad (3\text{-}101)$$

$$\dot{i}_{L_2} = \beta_{33} i_{L_1} + \beta_{34} v_{C_1} + \beta_{35} i_{L_2} - \beta_{36} v_{C_o} - \beta_{34} v_i + \beta_{37} i_o + \beta_{38} V_D \qquad (3\text{-}102)$$

where

$$\beta_{27} = \frac{\alpha_2\alpha_{10} - \alpha_1\alpha_{12}}{\Delta_1} \qquad \beta_{28} = \frac{\alpha_2}{\Delta_1}$$

$$\beta_{29} = \frac{\alpha_2\alpha_{11} - \alpha_1\alpha_{13}}{\Delta_1} \qquad \beta_{30} = \frac{\alpha_1}{\Delta_1}$$

$$\beta_{31} = \frac{\alpha_1\alpha_{14}}{\Delta_1} \qquad \beta_{32} = \frac{\alpha_1 - \alpha_2}{\Delta_1}$$

$$\beta_{33} = \frac{\alpha_3\alpha_{12} - \alpha_4\alpha_{10}}{\Delta_1} \qquad \beta_{34} = \frac{\alpha_4}{\Delta_1}$$

$$\beta_{35} = \frac{\alpha_3\alpha_{13} - \alpha_4\alpha_{11}}{\Delta_1} \qquad \beta_{36} = \frac{\alpha_3}{\Delta_1}$$

$$\beta_{37} = \frac{\alpha_3\alpha_{14}}{\Delta_1} \qquad \beta_{38} = \frac{\alpha_4 - \alpha_3}{\Delta_1}$$

In Mode 2 operation, diode is conducting and its constant voltage drop V_D appears in the equations. Where will it be placed in matrix representation? It is not a state-variable. Actually, it appears as kind of a voltage sink in the circuit in Mode 2. That is, it can be regarded as a constant input to the circuit. Consequently, it is going to be added to u vector. Now, other state-variables, namely capacitor voltages, can be written in the following manner.

For v_{C_1}*:*

$$\dot{v_{C_1}} = \beta_{24} i_{L_1} \tag{3-103}$$

For v_{C_o}*:*

$$\dot{v_{C_o}} = \beta_{25} i_{L_2} - \beta_{25} i_o \tag{3-104}$$

The following equation is obtained.

$$\begin{bmatrix} \dot{i_{L_1}} \\ \dot{v_{C_1}} \\ \dot{i_{L_2}} \\ \dot{v_{C_o}} \end{bmatrix} = \begin{bmatrix} \beta_{27} & -\beta_{28} & \beta_{29} & \beta_{30} \\ \beta_{24} & 0 & 0 & 0 \\ \beta_{33} & \beta_{34} & \beta_{35} & -\beta_{36} \\ 0 & 0 & \beta_{25} & 0 \end{bmatrix} \begin{bmatrix} i_{L_1} \\ v_{C_1} \\ i_{L_2} \\ v_{C_o} \end{bmatrix} + \begin{bmatrix} \beta_{28} & -\beta_{31} & \beta_{32} \\ 0 & 0 & 0 \\ -\beta_{34} & \beta_{37} & \beta_{38} \\ 0 & -\beta_{25} & 0 \end{bmatrix} \begin{bmatrix} v_i \\ i_o \\ v_D \end{bmatrix}$$

(3-105)

In Mode 2, the duration is $(1-k)$. Hence,

$$(1-k)a_2 = \begin{bmatrix} (1-k)\beta_{27} & -(1-k)\beta_{28} & (1-k)\beta_{29} & (1-k)\beta_{30} \\ (1-k)\beta_{24} & 0 & 0 & 0 \\ (1-k)\beta_{33} & (1-k)\beta_{34} & (1-k)\beta_{35} & -(1-k)\beta_{36} \\ 0 & 0 & (1-k)\beta_{25} & 0 \end{bmatrix}$$

(3-106)

$$(1-k)b_2 = \begin{bmatrix} (1-k)\beta_{28} & -(1-k)\beta_{31} & (1-k)\beta_{32} \\ 0 & 0 & 0 \\ -(1-k)\beta_{34} & (1-k)\beta_{37} & (1-k)\beta_{38} \\ 0 & -(1-k)\beta_{25} & 0 \end{bmatrix} \tag{3-107}$$

$y(t)$ is the same with that in Mode 1. Thus,

$$(1-k)c_2 = \begin{bmatrix} 0 & 0 & (1-k)\beta_{26} & (1-k) \\ (1-k) & 0 & 0 & 0 \end{bmatrix} \tag{3-108}$$

$$(1-k)d_2 = \begin{bmatrix} 0 & -(1-k)\beta_{26} & 0 \\ 0 & 0 & 0 \end{bmatrix} \tag{3-109}$$

3.4.3 Averaging of Matrices in Mode 1 and Mode 2

Averaged matrices a, b, c, d of $a_1, b_1, c_1, d_1, a_2, b_2, c_2, d_2$ and k are obtained as follows;

$$a = ka_1 + (1-k)a_2 = \begin{bmatrix} \beta_{27} + k(\beta_{14} - \beta_{27}) & -\beta_{28} + k(\beta_{28} - \beta_{15}) & \beta_{29} + k(\beta_{16} - \beta_{29}) & \beta_{30} + k(\beta_{15} - \beta_{30}) \\ \beta_{24} - k\beta_{24} & 0 & -k\beta_{24} & 0 \\ \beta_{33} + k(\beta_{19} - \beta_{33}) & \beta_{34} + k(\beta_{20} - \beta_{34}) & \beta_{35} + k(\beta_{21} - \beta_{35}) & -\beta_{36} + k(\beta_{36} - \beta_{20}) \\ 0 & 0 & \beta_{25} & 0 \end{bmatrix} \tag{3-110}$$

$$b = kb_1 + (1-k)b_2 = \begin{bmatrix} \beta_{28} + k(\beta_{17} - \beta_{28}) & -\beta_{31} + k(\beta_{31} - \beta_{18}) & \beta_{32} - k\beta_{32} \\ 0 & 0 & 0 \\ -\beta_{34} + k(\beta_{34} - \beta_{22}) & \beta_{37} + k(\beta_{23} - \beta_{37}) & \beta_{38} - k\beta_{38} \\ 0 & -\beta_{25} & 0 \end{bmatrix} \tag{3-111}$$

$$c = kc_1 + (1-k)c_2 = \begin{bmatrix} 0 & 0 & \beta_{26} & 1 \\ 1 & 0 & 0 & 0 \end{bmatrix} \tag{3-112}$$

$$d = kd_1 + (1-k)d_2 = \begin{bmatrix} 0 & -\beta_{26} & 0 \\ 0 & 0 & 0 \end{bmatrix} \tag{3-113}$$

As a result, state-space averaged model of the circuit can be represented in (3-114) and (3-115).

$$\begin{bmatrix} \dot{i_{L_1}} \\ \dot{v_{C_1}} \\ \dot{i_{L_2}} \\ \dot{v_{C_o}} \end{bmatrix} = \begin{bmatrix} \beta_{27} + k(\beta_{14} - \beta_{27}) & -\beta_{28} + k(\beta_{28} - \beta_{15}) & \beta_{29} + k(\beta_{16} - \beta_{29}) & \beta_{30} + k(\beta_{15} - \beta_{30}) \\ \beta_{24} - k\beta_{24} & 0 & -k\beta_{24} & 0 \\ \beta_{33} + k(\beta_{19} - \beta_{33}) & \beta_{34} + k(\beta_{20} - \beta_{34}) & \beta_{35} + k(\beta_{21} - \beta_{35}) & -\beta_{36} + k(\beta_{36} - \beta_{20}) \\ 0 & 0 & \beta_{25} & 0 \end{bmatrix} \begin{bmatrix} i_{L_1} \\ v_{C_1} \\ i_{L_2} \\ v_{C_o} \end{bmatrix} + \begin{bmatrix} \beta_{28} + k(\beta_{17} - \beta_{28}) & -\beta_{31} + k(\beta_{31} - \beta_{18}) & \beta_{32} - k\beta_{32} \\ 0 & 0 & 0 \\ -\beta_{34} + k(\beta_{34} - \beta_{22}) & \beta_{37} + k(\beta_{23} - \beta_{37}) & \beta_{38} - k\beta_{38} \\ 0 & -\beta_{25} & 0 \end{bmatrix} \begin{bmatrix} v_i \\ i_o \\ v_D \end{bmatrix} \tag{3-114}$$

$$y = \begin{bmatrix} v_o \\ i_i \end{bmatrix} = \begin{bmatrix} 0 & 0 & \beta_{26} & 1 \\ 1 & 0 & 0 & 0 \end{bmatrix} \begin{bmatrix} i_{L_1} \\ v_{C_1} \\ i_{L_2} \\ v_{C_o} \end{bmatrix} + \begin{bmatrix} 0 & -\beta_{26} & 0 \\ 0 & 0 & 0 \end{bmatrix} \begin{bmatrix} v_i \\ i_o \\ v_D \end{bmatrix} \qquad (3\text{-}115)$$

3.4.4 Decomposition of Averaged Model into Steady-State and Dynamic Models

Separation is done in the same way followed in Section 3.3.4.

$$\begin{bmatrix} \dot{I}_{L_1} + \dot{\tilde{i}}_{L_1} \\ \dot{V}_{C_1} + \dot{\tilde{v}}_{C_1} \\ \dot{I}_{L_2} + \dot{\tilde{i}}_{L_2} \\ \dot{V}_{C_o} + \dot{\tilde{v}}_{C_o} \end{bmatrix} =$$

$$\begin{bmatrix} \gamma_{16} + \tilde{k}\gamma_{17} & \gamma_{18} + \tilde{k}\gamma_{19} & \gamma_{20} + \tilde{k}\gamma_{21} & \gamma_{22} + \tilde{k}\gamma_{23} \\ \gamma_{24} - \tilde{k}\gamma_{25} & 0 & \gamma_{26} - \tilde{k}\gamma_{25} & 0 \\ \gamma_{27} + \tilde{k}\gamma_{28} & \gamma_{29} + \tilde{k}\gamma_{30} & \gamma_{31} + \tilde{k}\gamma_{32} & \gamma_{33} + \tilde{k}\gamma_{34} \\ 0 & 0 & \gamma_{35} & 0 \end{bmatrix} \begin{bmatrix} I_{L_1} + \tilde{i}_{L_1} \\ V_{C_1} + \tilde{v}_{C_1} \\ I_{L_2} + \tilde{i}_{L_2} \\ V_{C_o} + \tilde{v}_{C_o} \end{bmatrix} +$$

$$\begin{bmatrix} \gamma_{36} + \tilde{k}\gamma_{37} & \gamma_{38} + \tilde{k}\gamma_{39} & \gamma_{40} - \tilde{k}\gamma_{41} \\ 0 & 0 & 0 \\ \gamma_{42} + \tilde{k}\gamma_{43} & \gamma_{44} + \tilde{k}\gamma_{45} & \gamma_{46} - \tilde{k}\gamma_{47} \\ 0 & -\gamma_{35} & 0 \end{bmatrix} \begin{bmatrix} V_i + \tilde{v}_i \\ I_o + \tilde{i}_o \\ V_D + \tilde{v}_D \end{bmatrix} \qquad (3\text{-}116)$$

where

$\gamma_{16} = \beta_{27} + K(\beta_{14} - \beta_{27})$ $\qquad$ $\gamma_{17} = (\beta_{14} - \beta_{27})$

$\gamma_{18} = -\beta_{28} + K(\beta_{28} - \beta_{15})$ $\qquad$ $\gamma_{19} = (\beta_{28} - \beta_{15})$

$\gamma_{20} = \beta_{29} + K(\beta_{16} - \beta_{29})$ $\qquad$ $\gamma_{21} = (\beta_{16} - \beta_{29})$

$\gamma_{22} = \beta_{30} + K(\beta_{15} - \beta_{30})$ $\qquad$ $\gamma_{23} = (\beta_{15} - \beta_{30})$

$\gamma_{24} = \beta_{24} - K\beta_{24}$ $\qquad$ $\gamma_{25} = \beta_{24}$

$\gamma_{26} = -K\beta_{24}$ $\qquad$ $\gamma_{27} = \beta_{33} + K(\beta_{19} - \beta_{33})$

$\gamma_{28} = (\beta_{19} - \beta_{33})$ $\qquad$ $\gamma_{29} = \beta_{34} + K(\beta_{20} - \beta_{34})$

$\gamma_{30} = (\beta_{20} - \beta_{34})$ $\qquad$ $\gamma_{31} = \beta_{35} + K(\beta_{21} - \beta_{35})$

$\gamma_{32} = (\beta_{21} - \beta_{35})$ $\qquad$ $\gamma_{33} = -\beta_{36} + K(\beta_{36} - \beta_{20})$

$$\gamma_{34} = (\beta_{36} - \beta_{20}) \qquad \gamma_{35} = \beta_{25}$$

$$\gamma_{36} = \beta_{28} + K(\beta_{17} - \beta_{28}) \qquad \gamma_{37} = (\beta_{17} - \beta_{28})$$

$$\gamma_{38} = -\beta_{31} + K(\beta_{31} - \beta_{18}) \qquad \gamma_{39} = (\beta_{31} - \beta_{18})$$

$$\gamma_{40} = \beta_{32} - K\beta_{32} \qquad \gamma_{41} = \beta_{32}$$

$$\gamma_{42} = -\beta_{34} + K(\beta_{34} - \beta_{22}) \qquad \gamma_{43} = (\beta_{34} - \beta_{22})$$

$$\gamma_{44} = \beta_{37} + K(\beta_{23} - \beta_{37}) \qquad \gamma_{45} = (\beta_{23} - \beta_{37})$$

$$\gamma_{46} = \beta_{38} - K\beta_{38} \qquad \gamma_{47} = \beta_{38}$$

$$y = \begin{bmatrix} V_o + \tilde{v}_o \\ I_i + \tilde{i}_i \end{bmatrix} = \begin{bmatrix} 0 & 0 & \beta_{26} & 1 \\ 1 & 0 & 0 & 0 \end{bmatrix} \begin{bmatrix} I_{L_1} + \tilde{i}_{L_1} \\ V_{C_1} + \tilde{v}_{C_1} \\ I_{L_2} + \tilde{i}_{L_2} \\ V_{C_o} + \tilde{v}_{C_o} \end{bmatrix} + \begin{bmatrix} 0 & -\beta_{26} & 0 \\ 0 & 0 & 0 \end{bmatrix} \begin{bmatrix} V_i + \tilde{v}_i \\ I_o + \tilde{i}_o \\ V_D + \tilde{v}_D \end{bmatrix} \tag{3-117}$$

Individual matrices can be extracted from (3-116) and (3-117) in the following manner. The same matrices with the ones in Section 3.3.4 are excluded in order not to repeat.

$$A = \begin{bmatrix} \gamma_{16} & \gamma_{18} & \gamma_{20} & \gamma_{22} \\ \gamma_{24} & 0 & \gamma_{26} & 0 \\ \gamma_{27} & \gamma_{29} & \gamma_{31} & \gamma_{33} \\ 0 & 0 & \gamma_{35} & 0 \end{bmatrix} \tag{3-118}$$

$$\tilde{a} = \begin{bmatrix} \tilde{k}\gamma_{17} & \tilde{k}\gamma_{19} & \tilde{k}\gamma_{21} & \tilde{k}\gamma_{23} \\ -\tilde{k}\gamma_{25} & 0 & -\tilde{k}\gamma_{25} & 0 \\ \tilde{k}\gamma_{28} & \tilde{k}\gamma_{30} & \tilde{k}\gamma_{32} & \tilde{k}\gamma_{34} \\ 0 & 0 & 0 & 0 \end{bmatrix} \tag{3-119}$$

$$B = \begin{bmatrix} \gamma_{36} & \gamma_{38} & \gamma_{40} \\ 0 & 0 & 0 \\ \gamma_{42} & \gamma_{44} & \gamma_{46} \\ 0 & -\gamma_{35} & 0 \end{bmatrix} \qquad \tilde{b} = \begin{bmatrix} \tilde{k}\gamma_{37} & \tilde{k}\gamma_{39} & -\tilde{k}\gamma_{41} \\ 0 & 0 & 0 \\ \tilde{k}\gamma_{43} & \tilde{k}\gamma_{45} & -\tilde{k}\gamma_{47} \\ 0 & 0 & 0 \end{bmatrix} \tag{3-120}$$

$$U = \begin{bmatrix} V_i \\ I_o \\ V_D \end{bmatrix} \qquad \tilde{u} = \begin{bmatrix} \tilde{v}_i \\ \tilde{i}_o \\ 0 \end{bmatrix} \tag{3-121}$$

Note that $\tilde{v}_D$ is taken as zero because diode forward voltage drop is assumed to be constant.

$$C = \begin{bmatrix} 0 & 0 & \beta_{26} & 1 \\ 1 & 0 & 0 & 0 \end{bmatrix} \qquad \tilde{c} = \begin{bmatrix} 0 & 0 & 0 & 0 \\ 0 & 0 & 0 & 0 \end{bmatrix} \tag{3-122}$$

$$D = \begin{bmatrix} 0 & -\beta_{26} & 0 \\ 0 & 0 & 0 \end{bmatrix} \qquad \tilde{d} = \begin{bmatrix} 0 & 0 \\ 0 & 0 \end{bmatrix} \tag{3-123}$$

3.4.5 Steady-State Model

Utilizing the matrices above, the following matrix equations are obtained.

$$\begin{bmatrix} 0 \\ 0 \\ 0 \\ 0 \end{bmatrix} = \begin{bmatrix} \gamma_{16} & \gamma_{18} & \gamma_{20} & \gamma_{22} \\ \gamma_{24} & 0 & \gamma_{26} & 0 \\ \gamma_{27} & \gamma_{29} & \gamma_{31} & \gamma_{33} \\ 0 & 0 & \gamma_{35} & 0 \end{bmatrix} \begin{bmatrix} I_{L_1} \\ V_{C_1} \\ I_{L_2} \\ V_{C_o} \end{bmatrix} + \begin{bmatrix} \gamma_{36} & \gamma_{38} & \gamma_{40} \\ 0 & 0 & 0 \\ \gamma_{42} & \gamma_{44} & \gamma_{46} \\ 0 & -\gamma_{35} & 0 \end{bmatrix} \begin{bmatrix} V_i \\ I_o \\ V_D \end{bmatrix} \tag{3-124}$$

$$\begin{bmatrix} V_o \\ I_i \end{bmatrix} = \begin{bmatrix} 0 & 0 & \beta_{26} & 1 \\ 1 & 0 & 0 & 0 \end{bmatrix} \begin{bmatrix} I_{L_1} \\ V_{C_1} \\ I_{L_2} \\ V_{C_o} \end{bmatrix} + \begin{bmatrix} 0 & -\beta_{26} & 0 \\ 0 & 0 & 0 \end{bmatrix} \begin{bmatrix} V_i \\ I_o \\ V_D \end{bmatrix} \tag{3-125}$$

First row of (3-124):

$$0 = \gamma_{16} I_{L_1} + \gamma_{18} V_{C_1} + \gamma_{20} I_{L_2} + \gamma_{22} V_{C_o} + \gamma_{36} V_i + \gamma_{38} I_o + \gamma_{40} V_D \tag{3-126}$$

Using (3-135):

$$V_{C_1} = -\frac{\gamma_{16} I_{L_1} + \gamma_{20} I_{L_2} + \gamma_{22} V_o + \gamma_{36} V_i + \gamma_{38} I_o + \gamma_{40} V_D}{\gamma_{18}} \tag{3-127}$$

This result will be used later.

Second row of (3-124):

$$0 = \gamma_{24} I_{L_1} + \gamma_{26} I_{L_2} \tag{3-128}$$

$$\frac{I_{L_1}}{I_{L_2}} = -\frac{\gamma_{26}}{\gamma_{24}} = -\frac{-K\beta_{24}}{\beta_{24}(1-K)} = \frac{K}{1-K} \tag{3-129}$$

It is the same result with the case of ideal electrical elements. It is not affected by the parasitic elements.

Third row of (3-124):

$$0 = \gamma_{27} I_{L_1} + \gamma_{29} V_{C_1} + \gamma_{31} I_{L_2} + \gamma_{33} V_o + \gamma_{42} V_i + \gamma_{44} I_o + \gamma_{46} V_D \tag{3-130}$$

$$V_{C_1} = -\frac{\gamma_{27} I_{L_1} + \gamma_{31} I_{L_2} + \gamma_{33} V_o + \gamma_{42} V_i + \gamma_{44} I_o + \gamma_{46} V_D}{\gamma_{29}} \tag{3-131}$$

Fourth row of (3-124):

$$0 = \gamma_{35} I_{L_2} - \gamma_{35} I_o \tag{3-132}$$

$$I_{L_2} = I_o \tag{3-133}$$

This result remains the same too.

First row of (3-115):

$$V_o = \beta_{26} I_{L_2} + V_{C_o} - \beta_{26} I_o \tag{3-134}$$

Using (3-133):

$$V_o = V_{C_o} \tag{3-135}$$

Even though ESR of the output capacitance makes the instantaneous output voltage differs from the voltage of the output capacitance, their mean values turn out to be the same, which is an expected result.

Second row (3-115):

$$I_i = I_{L_1} \tag{3-136}$$

This is just a trivial result.

(3-127) and (3-131) may be simplified as in the case of ideal elements. However, those equations are too complex to be handled successfully. Hence, they are utilized only for efficiency calculation. By equating both equations, the relationship between V_o and V_i can be derived.

$$V_o = \frac{\delta_2}{\delta_1} I_{L_1} + \frac{\delta_3}{\delta_1} I_{L_2} + \frac{\delta_4}{\delta_1} V_i + \frac{\delta_5}{\delta_1} I_o + \frac{\delta_6}{\delta_1} V_D \qquad (3\text{-}137)$$

where

$$\delta_1 = \gamma_{22}\gamma_{29} - \gamma_{18}\gamma_{33} \qquad \delta_2 = \gamma_{18}\gamma_{27} - \gamma_{16}\gamma_{29}$$

$$\delta_3 = \gamma_{18}\gamma_{31} - \gamma_{20}\gamma_{29} \qquad \delta_4 = \gamma_{18}\gamma_{42} - \gamma_{29}\gamma_{36}$$

$$\delta_5 = \gamma_{18}\gamma_{44} - \gamma_{29}\gamma_{38} \qquad \delta_6 = \gamma_{18}\gamma_{46} - \gamma_{29}\gamma_{40}$$

Then, the efficiency can be calculated as follows;

$$\eta = \frac{P_o}{P_i} = \frac{I_o V_o}{I_i V_i} = \frac{I_{L_2}}{I_{L_1}} \frac{V_o}{V_i}$$

Using (3-129), (3-133) and (3-137):

$$\eta = \frac{K'}{K} \cdot \frac{\left[\frac{\delta_2}{\delta_1} I_{L_1} + \frac{\delta_3}{\delta_1} I_{L_2} + \frac{\delta_4}{\delta_1} V_i + \frac{\delta_5}{\delta_1} I_o + \frac{\delta_6}{\delta_1} V_D\right]}{V_i}$$

I_{L_1} and I_{L_2}can be written in terms of I_o.

$$\eta = \frac{\frac{K'}{K}\frac{\delta_4}{\delta_1} V_i + \left(\frac{K'}{K}\frac{\delta_5 + \delta_3}{\delta_1} + \frac{\delta_2}{\delta_1}\right) I_o + \frac{K'}{K}\frac{\delta_6}{\delta_1} V_D}{V_i}$$

Further simplification gives the final efficiency expression in (3-138). It will be used and investigated in the design chapter. However, a clarification may be needed at this step: δ_x terms need not to be positive. Moreover, they should have signs such that I_o and V_D terms decrease the efficiency.

$$\eta = \left(\frac{K'}{K}\frac{\delta_4}{\delta_1}\right) + \left(\frac{K'}{K}\frac{\delta_5 + \delta_3}{\delta_1} + \frac{\delta_2}{\delta_1}\right)\frac{I_o}{V_i} + \left(\frac{K'}{K}\frac{\delta_6}{\delta_1}\right)\frac{V_D}{V_i} \qquad (3\text{-}138)$$

3.4.6 Dynamic Model and Transfer Functions

In this section, we will make use of (3-18) again. Simplification due to the constant matrices can be applied before using it. The simplified version of (3-18) is given in (3-139), as;

$$\tilde{y}(s) = C[sI - A]^{-1}\left[\tilde{a}(s)X + B\tilde{u}(s) + \tilde{b}(s)U\right] + D\tilde{u}(s) \tag{3-139}$$

Putting the matrices into their places gives the following equation matrices step by step. Note that superscript ‘p’ (probable usage forms: x^p or x_y^p) is used to label some parasitic terms in order to differentiate them from the corresponding terms in ideal case.

$$sI - A = \begin{bmatrix} s-\gamma_{16} & -\gamma_{18} & -\gamma_{20} & -\gamma_{22} \\ -\gamma_{24} & s & -\gamma_{26} & 0 \\ -\gamma_{27} & -\gamma_{29} & s-\gamma_{31} & -\gamma_{33} \\ 0 & 0 & -\gamma_{35} & s \end{bmatrix} \tag{3-140}$$

$$[sI - A]^{-1} = \frac{1}{\mathrm{det^p}\,([sI-A]^{-1})} \cdot \begin{bmatrix} F_7(s) & F_{11}(s) & F_{15}(s) & F_{19}(s) \\ F_8(s) & F_{12}(s) & F_{16}(s) & F_{20}(s) \\ F_9(s) & F_{13}(s) & F_{17}(s) & F_{21}(s) \\ F_{10}(s) & F_{14}(s) & F_{18}(s) & F_{22}(s) \end{bmatrix} \tag{3-141}$$

where

$$\mathrm{det^p}([sI - A]^{-1}) = s^4 - s^3\delta_7 + s^2\delta_8 + s\delta_9 + \delta_{10} \tag{3-142}$$

and

$$F_7(s) = s^3 - s^2\delta_{11} - s\delta_{12} \qquad F_8(s) = s^2\delta_{13} + s\delta_{14} - \delta_{15}$$

$$F_9(s) = s^2\delta_{16} + s\delta_{17} \qquad F_{10}(s) = s\delta_{18} + \delta_{19}$$

$$F_{11}(s) = s^2\delta_{20} + s\delta_{21} + \delta_{22}$$

$$F_{12}(s) = s^3 - s^2\delta_7 + s\delta_{23} + \delta_{24} \qquad F_{13}(s) = s^2\delta_{25} + s\delta_{26}$$

$$F_{14}(s) = s\delta_{27} + \delta_{28} \qquad F_{15}(s) = s^2\delta_{29} + s\delta_{30}$$

$$F_{16}(s) = s^2\delta_{31} + s\delta_{32} + \delta_{33} \qquad F_{17}(s) = s^3 - s^2\delta_{34} - s\delta_{35}$$

$$F_{18}(s) = s^2\delta_{36} - s\delta_{37} - \delta_{38} \qquad F_{19}(s) = s^2\delta_{39} + s\delta_{40} + \delta_{41}$$

$F_{20}(s) = s\delta_{42} + \delta_{43}$ $\qquad F_{21}(s) = s^2\delta_{44} + s\delta_{45} + \delta_{46}$

$F_{22}(s) = s^3 - s^2\delta_7 + s\delta_{47} + \delta_{48}$

and

$\delta_7 = \gamma_{16} + \gamma_{31}$

$\delta_8 = \gamma_{16}\gamma_{31} - \gamma_{33}\gamma_{35} - \gamma_{26}\gamma_{29} - \gamma_{18}\gamma_{24} - \gamma_{20}\gamma_{27}$

$\delta_9 = \gamma_{16}\gamma_{33}\gamma_{35} + \gamma_{16}\gamma_{26}\gamma_{29} + \gamma_{18}\gamma_{24}\gamma_{31} - \gamma_{20}\gamma_{24}\gamma_{29} - \gamma_{18}\gamma_{26}\gamma_{27}$
$\qquad - \gamma_{22}\gamma_{27}\gamma_{35}$

$\delta_{10} = \gamma_{18}\gamma_{24}\gamma_{33}\gamma_{35} - \gamma_{22}\gamma_{24}\gamma_{29}\gamma_{35}$ $\qquad \delta_{11} = \gamma_{31}$

$\delta_{12} = \gamma_{33}\gamma_{35} - \gamma_{26}\gamma_{29}$ $\qquad \delta_{13} = \gamma_{24}$

$\delta_{14} = \gamma_{26}\gamma_{27} - \gamma_{24}\gamma_{31}$ $\qquad \delta_{15} = \gamma_{24}\gamma_{33}\gamma_{35}$

$\delta_{16} = \gamma_{27}$ $\qquad \delta_{17} = \gamma_{24}\gamma_{29}$

$\delta_{18} = \gamma_{27}\gamma_{35}$ $\qquad \delta_{19} = \gamma_{24}\gamma_{29}\gamma_{35}$

$\delta_{20} = \gamma_{18}$ $\qquad \delta_{21} = \gamma_{20}\gamma_{29} - \gamma_{18}\gamma_{31}$

$\delta_{22} = \gamma_{22}\gamma_{29}\gamma_{35} - \gamma_{18}\gamma_{33}\gamma_{35}$

$\delta_{23} = \gamma_{16}\gamma_{31} - \gamma_{33}\gamma_{35} - \gamma_{20}\gamma_{27}$ $\qquad \delta_{24} = \gamma_{16}\gamma_{33}\gamma_{35} - \gamma_{22}\gamma_{27}\gamma_{35}$

$\delta_{25} = \gamma_{29}$ $\qquad \delta_{26} = \gamma_{18}\gamma_{27} - \gamma_{16}\gamma_{29}$

$\delta_{27} = \gamma_{29}\gamma_{35}$ $\qquad \delta_{28} = \gamma_{18}\gamma_{27}\gamma_{35} - \gamma_{16}\gamma_{29}\gamma_{35}$

$\delta_{29} = \gamma_{20}$ $\qquad \delta_{30} = \gamma_{18}\gamma_{26} + \gamma_{22}\gamma_{35}$

$\delta_{31} = \gamma_{26}$ $\qquad \delta_{32} = \gamma_{20}\gamma_{24} - \gamma_{16}\gamma_{26}$

$\delta_{33} = \gamma_{22}\gamma_{24}\gamma_{35}$ $\qquad \delta_{34} = \gamma_{16}$

$\delta_{35} = \gamma_{18}\gamma_{24}$ $\qquad \delta_{36} = \gamma_{35}$

$\delta_{37} = \gamma_{16}\gamma_{35}$ $\qquad \delta_{38} = \gamma_{18}\gamma_{24}\gamma_{35}$

$\delta_{39} = \gamma_{22}$ $\qquad \delta_{40} = \gamma_{20}\gamma_{33} - \gamma_{22}\gamma_{31}$

$\delta_{41} = \gamma_{18}\gamma_{26}\gamma_{33} - \gamma_{22}\gamma_{26}\gamma_{29}$ $\qquad \delta_{42} = \gamma_{26}\gamma_{33} + \gamma_{22}\gamma_{24}$

$\delta_{43} = \gamma_{20}\gamma_{24}\gamma_{33} + \gamma_{22}\gamma_{26}\gamma_{27} - \gamma_{16}\gamma_{26}\gamma_{33} - \gamma_{22}\gamma_{24}\gamma_{31}$

$\delta_{44} = \gamma_{33}$ $\qquad \delta_{45} = \gamma_{22}\gamma_{27} - \gamma_{16}\gamma_{33}$

$\delta_{46} = \gamma_{22}\gamma_{24}\gamma_{29} - \gamma_{18}\gamma_{24}\gamma_{33}$

$\delta_{47} = \gamma_{16}\gamma_{31} - \gamma_{26}\gamma_{29} - \gamma_{18}\gamma_{24} - \gamma_{20}\gamma_{27}$

$\delta_{48} = \gamma_{18}\gamma_{24}\gamma_{31} + \gamma_{16}\gamma_{26}\gamma_{29} - \gamma_{20}\gamma_{24}\gamma_{29} - \gamma_{18}\gamma_{26}\gamma_{27}$

Using (3-122):

$$C[sI-A]^{-1}=\frac{1}{\det^{\mathrm{p}}([sI-A]^{-1})}\cdot$$

$$\begin{bmatrix}\frac{\beta_{26}F_9(s)+F_{10}(s)}{F_7(s)} & \frac{\beta_{26}F_{13}(s)+F_{14}(s)}{F_{11}(s)} & \frac{\beta_{26}F_{17}(s)+F_{18}(s)}{F_{15}(s)} & \frac{\beta_{26}F_{21}(s)+F_{22}(s)}{F_{19}(s)}\end{bmatrix} \tag{3-143}$$

Using (3-119)-(3-121):

$$\tilde{a}(s)X+B\tilde{u}(s)=\begin{bmatrix}\tilde{k}(s)\gamma_{17} & \tilde{k}(s)\gamma_{19} & \tilde{k}(s)\gamma_{21} & \tilde{k}(s)\gamma_{23}\\ -\tilde{k}(s)\gamma_{25} & 0 & -\tilde{k}(s)\gamma_{25} & 0\\ \tilde{k}(s)\gamma_{28} & \tilde{k}(s)\gamma_{30} & \tilde{k}(s)\gamma_{32} & \tilde{k}(s)\gamma_{34}\\ 0 & 0 & 0 & 0\end{bmatrix}\begin{bmatrix}I_{L_1}\\ V_{C_1}\\ I_{L_2}\\ V_{C_o}\end{bmatrix}+$$

$$\begin{bmatrix}\gamma_{36} & \gamma_{38} & \gamma_{40}\\ 0 & 0 & 0\\ \gamma_{42} & \gamma_{44} & \gamma_{46}\\ 0 & -\gamma_{35} & 0\end{bmatrix}\begin{bmatrix}\tilde{v}_i(s)\\ \tilde{i}_o(s)\\ 0\end{bmatrix} \tag{3-144}$$

$$\tilde{a}(s)X+B\tilde{u}(s)=\begin{bmatrix}\tilde{k}(s)I_{L_1}\gamma_{17}+\tilde{k}(s)V_{C_1}\gamma_{19}+\tilde{k}(s)I_{L_2}\gamma_{21}+\tilde{k}(s)V_{C_o}\gamma_{23}\\ -\tilde{k}(s)I_{L_1}\gamma_{25}-\tilde{k}(s)I_{L_2}\gamma_{25}\\ \tilde{k}(s)I_{L_1}\gamma_{28}+\tilde{k}(s)V_{C_1}\gamma_{30}+\tilde{k}(s)I_{L_2}\gamma_{32}+\tilde{k}(s)V_{C_o}\gamma_{34}\\ 0\end{bmatrix}+$$

$$\begin{bmatrix}\tilde{v}_i(s)\gamma_{36}+\tilde{i}_o(s)\gamma_{38}\\ 0\\ \tilde{v}_i(s)\gamma_{42}+\tilde{i}_o(s)\gamma_{44}\\ -\tilde{i}_o(s)\gamma_{35}\end{bmatrix}=\begin{bmatrix}\tilde{k}(s)\delta_{49}+\tilde{v}_i(s)\gamma_{36}+\tilde{i}_o(s)\gamma_{38}\\ -\tilde{k}(s)\delta_{50}\\ \tilde{k}(s)\delta_{51}+\tilde{v}_i(s)\gamma_{42}+\tilde{i}_o(s)\gamma_{44}\\ -\tilde{i}_o(s)\gamma_{35}\end{bmatrix} \tag{3-145}$$

where

$$\delta_{49}=I_{L_1}\gamma_{17}+V_{C_1}\gamma_{19}+I_{L_2}\gamma_{21}+V_{C_o}\gamma_{23}$$

$$\delta_{50}=I_{L_1}\gamma_{25}+I_{L_2}\gamma_{25}$$

$$\delta_{51}=I_{L_1}\gamma_{28}+V_{C_1}\gamma_{30}+I_{L_2}\gamma_{32}+V_{C_o}\gamma_{34}$$

Using (3-143) and (3-145):

$$C[sI-A]^{-1}[\tilde{a}(s)X+B\tilde{u}(s)]=\frac{1}{\det^{\mathrm{p}}([sI-A]^{-1})}\cdot$$

$$\begin{bmatrix}\beta_{26}F_9(s)+F_{10}(s) & \beta_{26}F_{13}(s)+F_{14}(s) & \beta_{26}F_{17}(s)+F_{18}(s) & \beta_{26}F_{21}(s)+F_{22}(s)\\ F_7(s) & F_{11}(s) & F_{15}(s) & F_{19}(s)\end{bmatrix}\cdot$$

$$\begin{bmatrix}\tilde{k}(s)\delta_{49}+\tilde{v}_i(s)\gamma_{36}+\tilde{i}_o(s)\gamma_{38}\\ -\tilde{k}(s)\delta_{50}\\ \tilde{k}(s)\delta_{51}+\tilde{v}_i(s)\gamma_{42}+\tilde{i}_o(s)\gamma_{44}\\ -\tilde{i}_o(s)\gamma_{35}\end{bmatrix}=\begin{bmatrix}\tilde{k}(s)F_{23}(s)+\tilde{v}_i(s)F_{24}(s)+F_{25}(s)\tilde{i}_o(s)\\ \tilde{k}(s)F_{26}(s)+\tilde{v}_i(s)F_{27}(s)+F_{28}(s)\tilde{i}_o(s)\end{bmatrix} \qquad (3\text{-}146)$$

where

$$\begin{aligned}F_{23}(s)&=\delta_{49}[\beta_{26}F_9(s)+F_{10}(s)]-\delta_{50}[\beta_{26}F_{13}(s)+F_{14}(s)]\\ &\quad+\delta_{51}[\beta_{26}F_{17}(s)+F_{18}(s)]\\ F_{24}(s)&=\gamma_{36}[\beta_{26}F_9(s)+F_{10}(s)]+\gamma_{42}[\beta_{26}F_{17}(s)+F_{18}(s)]\\ F_{25}(s)&=\gamma_{38}[\beta_{26}F_9(s)+F_{10}(s)]+\gamma_{44}[\beta_{26}F_{17}(s)+F_{18}(s)]\\ &\quad-\gamma_{35}[\beta_{26}F_{21}(s)+F_{22}(s)]\\ F_{26}(s)&=\delta_{49}F_7(s)-\delta_{50}F_{11}(s)+\delta_{51}F_{15}(s)\\ F_{27}(s)&=\gamma_{36}F_7(s)+\gamma_{42}F_{15}(s)\\ F_{28}(s)&=\gamma_{38}F_7(s)+\gamma_{44}F_{15}(s)-\gamma_{35}F_{19}(s)\end{aligned}$$

Using (3-121) and (3-123):

$$D\tilde{u}(s)=\begin{bmatrix}0 & -\beta_{26} & 0\\ 0 & 0 & 0\end{bmatrix}\begin{bmatrix}\tilde{v}_i(s)\\ \tilde{i}_o(s)\\ 0\end{bmatrix}=\begin{bmatrix}-\beta_{26}\tilde{i}_o(s)\\ 0\end{bmatrix} \qquad (3\text{-}147)$$

Consequently, $\tilde{y}(s)$ is obtained by an addition of (3-147) to (3-146).

$$\tilde{y}(s)=\begin{bmatrix}\tilde{v}_o(s)\\ \tilde{i}_i(s)\end{bmatrix}=\frac{1}{\det^{\mathrm{p}}([sI-A]^{-1})}\cdot$$

$$\begin{bmatrix}\tilde{k}(s)F_{23}(s)+\tilde{v}_i(s)F_{24}(s)+F_{29}(s)\tilde{i}_o(s)\\ \tilde{k}(s)F_{26}(s)+\tilde{v}_i(s)F_{27}(s)+F_{28}(s)\tilde{i}_o(s)\end{bmatrix} \qquad (3\text{-}148)$$

where

$$F_{29}(s) = F_{25}(s) - \beta_{26}$$

As in the case of ideal elements, again there are six transfer functions to be inferred from (3-148).

Duty Factor to Output Voltage Transfer Function:

$$G^{p}_{v_o/k}(s) \stackrel{\text{def}}{=} \frac{\tilde{v}_o(s)}{\tilde{k}(s)} = \frac{F_{23}(s)}{\det^{\mathrm{p}}([sI-A]^{-1})} \tag{3-149}$$

Input Voltage to Output Voltage Transfer Function:

$$G^{p}_{v_o/v_i}(s) \stackrel{\text{def}}{=} \frac{\tilde{v}_o(s)}{\tilde{v}_i(s)} = \frac{F_{24}(s)}{\det^{\mathrm{p}}([sI-A]^{-1})} \tag{3-150}$$

Output Current to Output Voltage Transfer Function:

$$G^{p}_{v_o/i_o}(s) \stackrel{\text{def}}{=} \frac{\tilde{v}_o(s)}{\tilde{i}_o(s)} = \frac{F_{29}(s)}{\det^{\mathrm{p}}([sI-A]^{-1})} \tag{3-151}$$

Duty Factor to Input Current Transfer Function:

$$G^{p}_{i_i/k}(s) \stackrel{\text{def}}{=} \frac{\tilde{i}_i(s)}{\tilde{k}(s)} = \frac{F_{26}(s)}{\det^{\mathrm{p}}([sI-A]^{-1})} \tag{3-152}$$

Input Voltage to Input Current Transfer Function:

$$G^{p}_{i_i/v_i}(s) \stackrel{\text{def}}{=} \frac{\tilde{i}_i(s)}{\tilde{v}_i(s)} = \frac{F_{27}(s)}{\det^{\mathrm{p}}([sI-A]^{-1})} \tag{3-153}$$

Output Current to Input Current Transfer Function:

$$G^{p}_{i_i/i_o}(s) \stackrel{\text{def}}{=} \frac{\tilde{i}_i(s)}{\tilde{i}_o(s)} = \frac{F_{28}(s)}{\det^{\mathrm{p}}([sI-A]^{-1})} \tag{3-154}$$

It is not possible to express the transfer functions in explicit form due to the crowd of the terms. However, it can be said that each transfer function is the division of two polynomials in s. While the order of the numerator is at most 3, that of the denominator is constant at 4.

3.4.7 Verification of the Transfer Functions

The same procedure followed for coupled-inductor Ćuk converter, CIĆC with ideal elements will be repeated for CIĆC with parasitic elements in this section. Parameters of parasitic elements are taken from the final parameters in the design section. That is to say, they belong to the implemented circuit. Besides, calculations and simulations are realized at the same operating point in the ideal case.

Verification of $G^{p}_{v_o/k}(s)$*:*

In Figure 3-19, step response of the duty-factor-to-output voltage transfer function $G^{p}_{v_o/k}(s)$ is given. Horizontal axis is in seconds and vertical axis is in volts. As a step disturbance, again, 0.0025 increase in duty-factor is utilized. Mathematically, Figure 3-19 is the plot of the following function in time domain.

$$G^{p}_{v_o/k}(s)\cdot\frac{0.0025}{s}$$

It is plotted in Matlab with the following input parameters as an addition to parameters used in the verification of the transfer functions in ideal case. R_{L_1}, R_{DS}, R_{C_1}, R_{L_2}, R_{C_o} and R_D are the parameters of the practically implemented circuit. V_{C_o} is the parameter taken from the simulation which is aimed to be performed at the fourth end operating point.

$R_{L_1} = 6.2\ m\Omega$ $\quad$ $R_{DS} = 4.2\ m\Omega$

$R_{C_1} = 17\ m\Omega$ $\quad$ $R_{L_2} = 17.6\ m\Omega$

$R_{C_o} = 165\ m\Omega$ $\quad$ $R_D = 3\ m\Omega$

$V_{C_o} = 23.94\ V$

Physically, Figure 3-19 is the plot of the output voltage of the circuit operating at steady-state and disturbed with 0.0025 increase in the duty-factor at t = 0. By looking at the figure, it can be argued that the output voltage oscillates at the frequency of about 72Hz, which is close to the frequency of ideal case. However, because of the parasitic elements, the oscillation damps in a short time as expected.

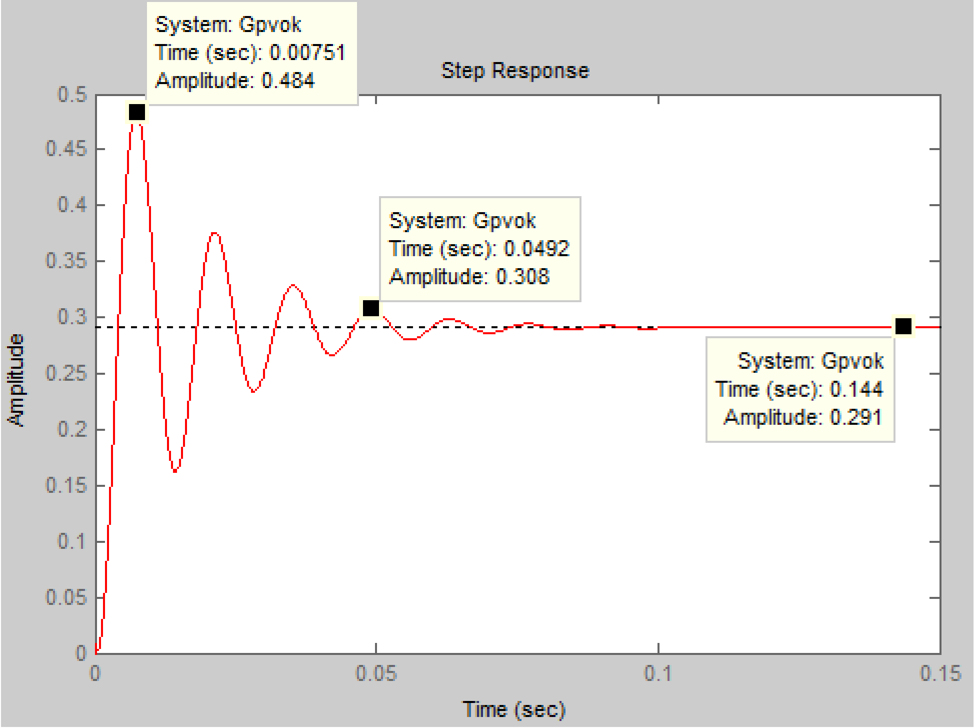

Figure 3-19: Step response of $G^{p}_{v_o/k}(s)$ in Matlab, $\Delta K = 0.0025$

In Figure 3-20, response of v_o to small step change in k at t = 250msec in Simplorer is shown. Similarly, horizontal axis is seconds and vertical axis is in volts. Since this is a small signal analysis, 23.94V-250msec point in Figure 3-20 corresponds to 0V-0sec in Figure 3-19. Grounding on this correspondence, it is seen that the figures are almost the same in terms of waveform behavior, phase, magnitude and frequency. As a result, $G^{p}_{v_o/k}(s)$ is verified.

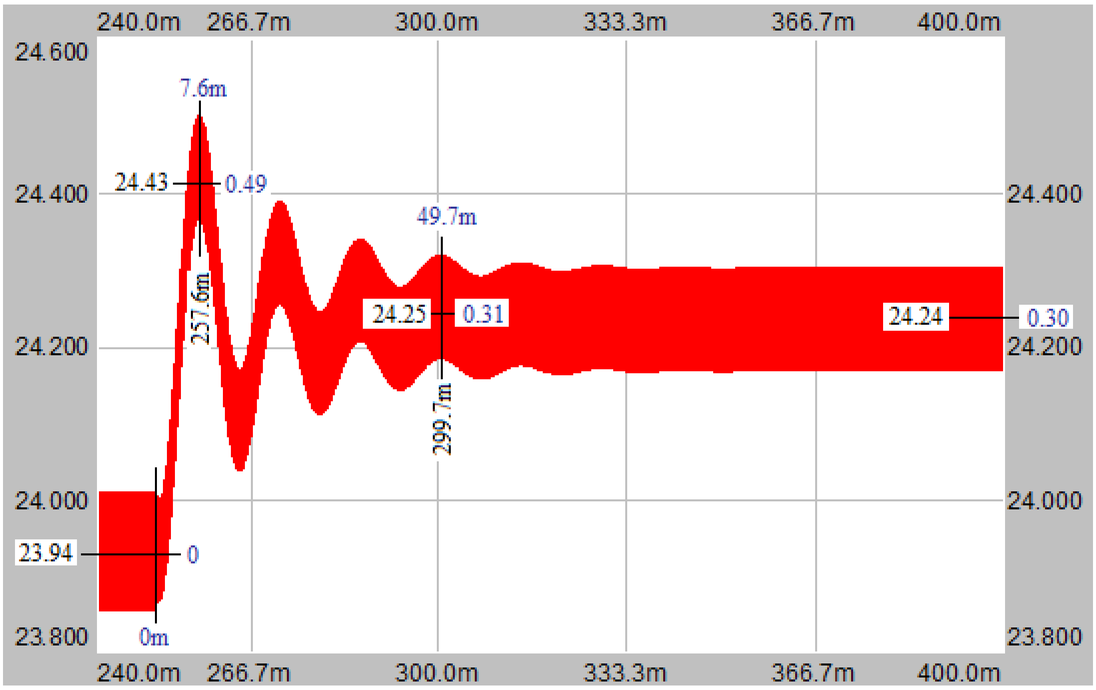

Figure 3-20: Response of v_o to small step change in k in Simplorer, parasitic elements, $\Delta K = 0.0025$

Verification of $G^{p}_{i_i/k}(s)$ *:*

The second output of the circuit is the input current. What the response of the input current is when the same step change in duty-factor occurs can be plotted by using the following function in time domain.

$$G^{p}_{i_i/k}(s) \cdot \frac{0.0025}{s}$$

Figure 3-21 says that when the duty-factor is increased 0.0025 much at t=0 at that operating point, the input current shows this variation in time. As expected, the horizontal axis is in seconds and the vertical axis is in Amperes. In order to see whether the derived transfer function is correct or not, the same situation is formed in Simplorer and the input current is observed in Figure 3-22. Note the similarity between the figures.

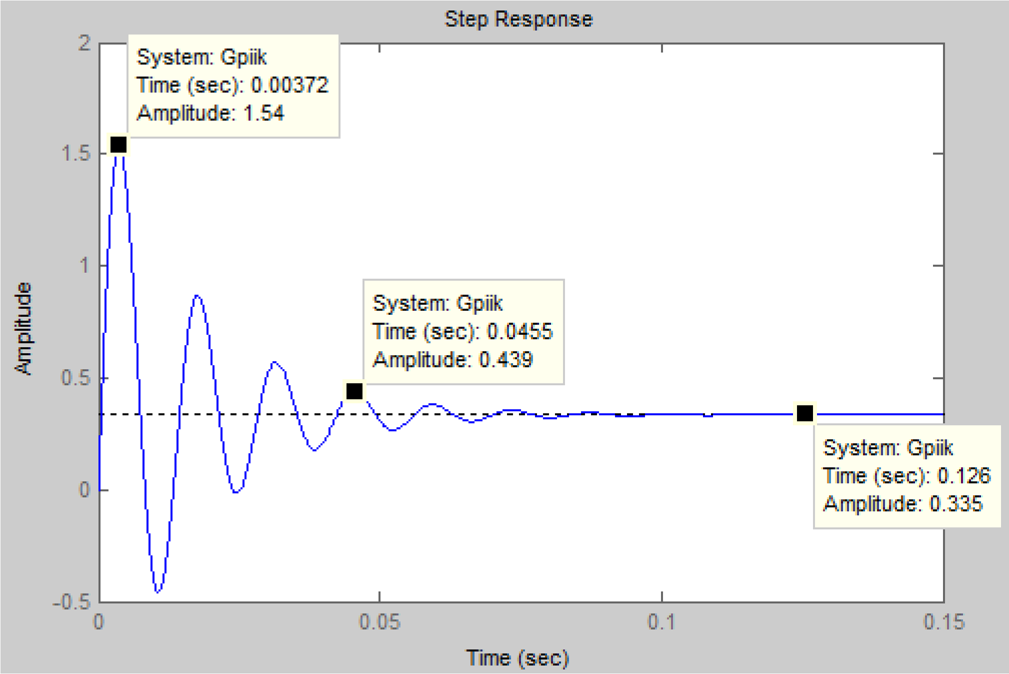

Figure 3-21: Step response of $G^{p}_{i_i/k}(s)$ in Matlab, $\Delta K = 0.0025$

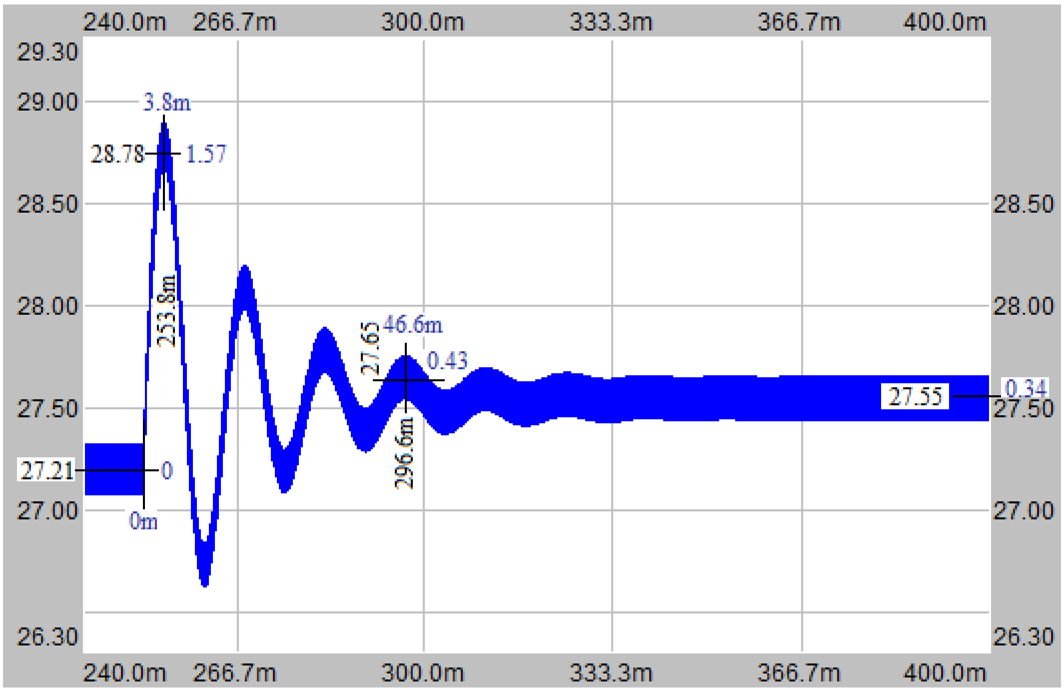

Figure 3-22: Response of i_i to small step change in k in Simplorer, parasitic elements, $\Delta K = 0.0025$

Verification of $G^{p}_{v_o/v_i}(s)$*:*

The response of the output voltage when 0.1V step change in input voltage occurs is plotted in Figure 3-23 by using the following function in time domain.

$$G^{p}_{v_o/v_i}(s) \cdot \frac{0.1}{s}$$

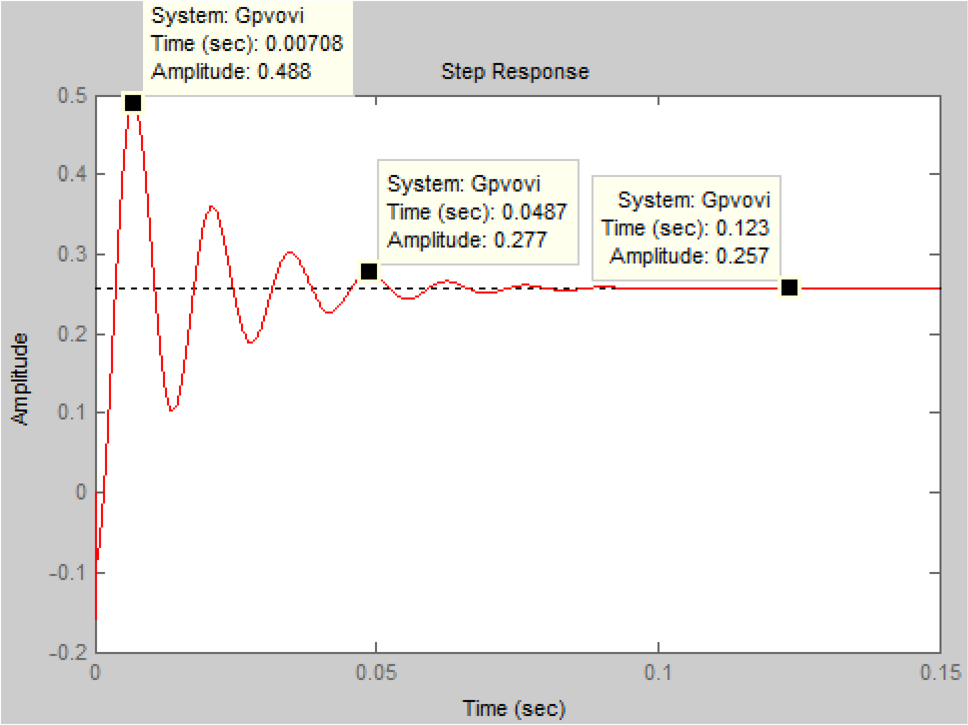

Figure 3-23: Step response of $G^{p}_{v_o/v_i}(s)$ in Matlab, $\Delta V_i = 0.1V$

The corresponding waveform in Simplorer is presented in Figure 3-24. $G^{p}_{v_o/v_i}(s)$ is validated in this way.

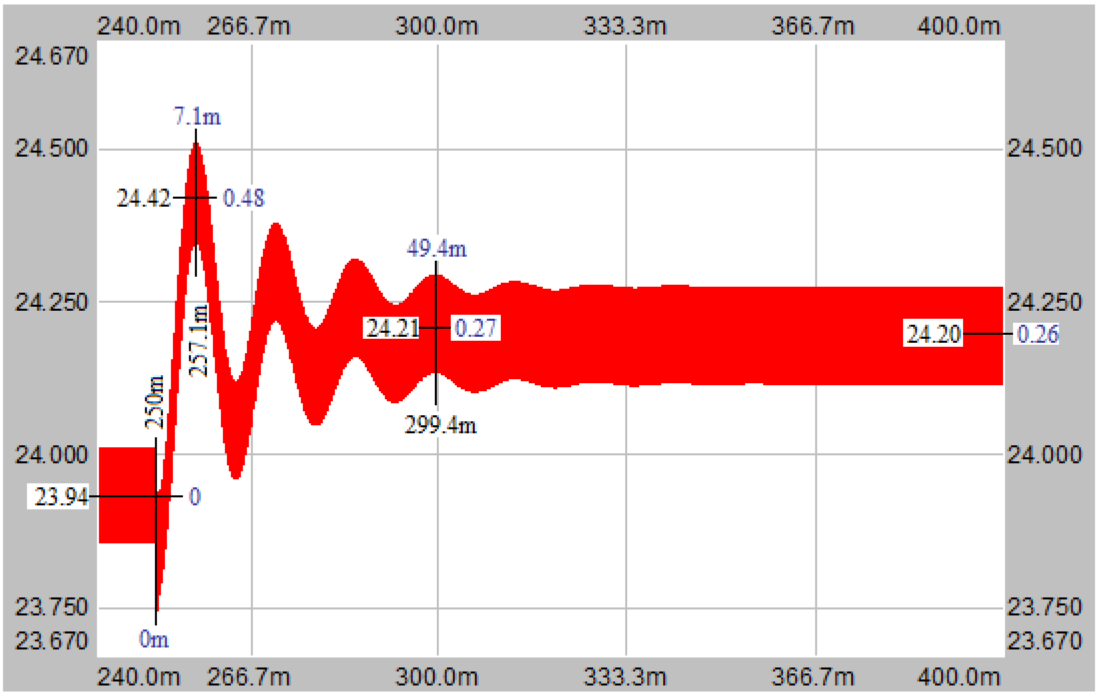

Figure 3-24: Response of v_o to small step change in v_i in Simplorer, parasitic elements, $\Delta V_i = 0.1V$

Verification of $G^{p}_{i_i/v_i}(s)$*:*

The response of the input current when 0.1V step change in input voltage occurs is plotted in Figure 3-25 by using the following function in time domain.

$$G^{P}_{i_i/v_i}(s)\ \cdot \frac{0.1}{s}$$

The corresponding waveform in Simplorer is introduced in Figure 3-26. In this manner, $G^{p}_{i_i/v_i}(s)$ is also verified.

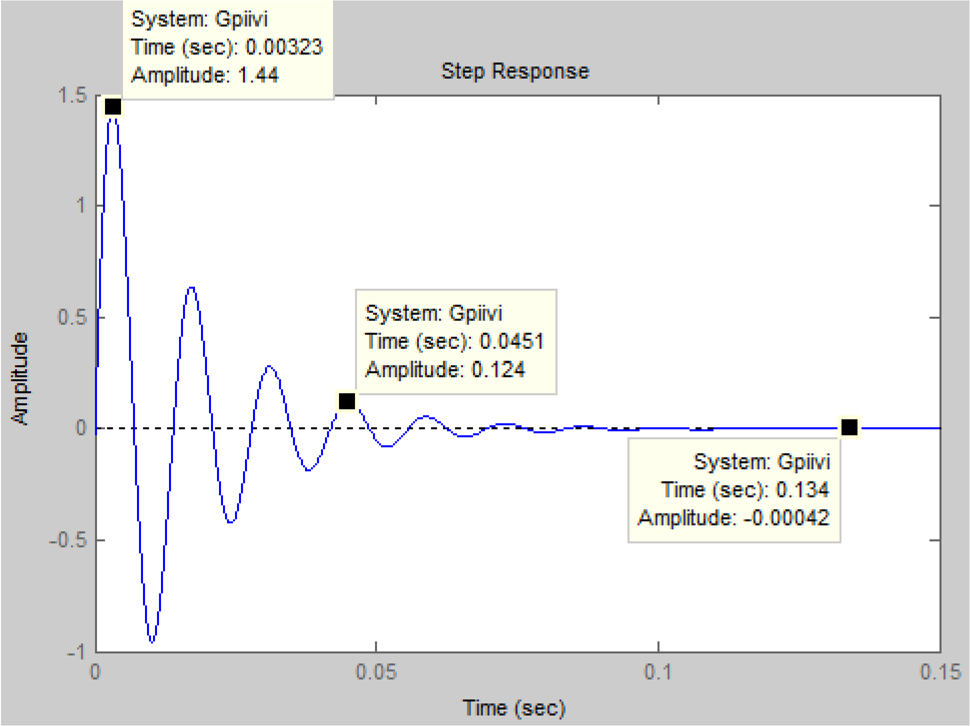

Figure 3-25: Step response of $G^{P}_{i_i/v_i}(s)$ in Matlab, $\Delta V_i = 0.1V$

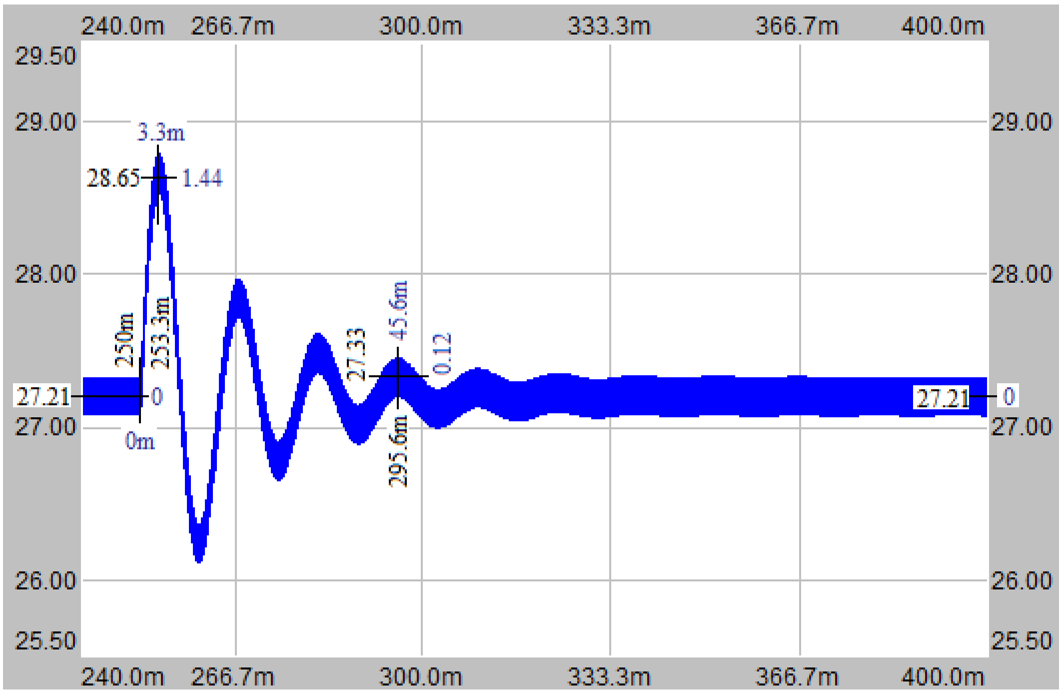

Figure 3-26: Response of i_i to small step change in v_i in Simplorer, parasitic elements, $\Delta V_i = 0.1V$

Verification of $G^p_{v_o/i_o}(s)$ *:*

The response of output voltage when 0.25A step change in output current happens is plotted in Figure 3-27 by using the following function in time domain.

$$G^p_{v_o/i_o}(s) \cdot \frac{0.25}{s}$$

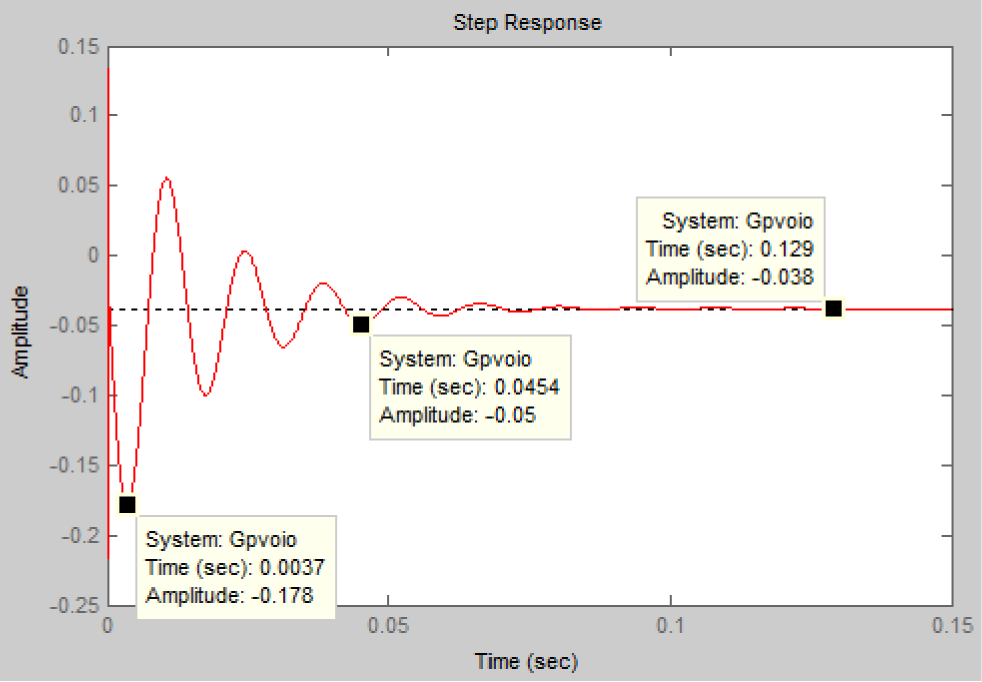

Figure 3-27: Step response of $G^p_{v_o/i_o}(s)$ in Matlab, $\Delta I_o = 0.25A$

The corresponding waveform in Simplorer is given in Figure 3-28. By grounding on the sufficient similarity between the figures, $G^p_{v_o/i_o}(s)$ is verified.

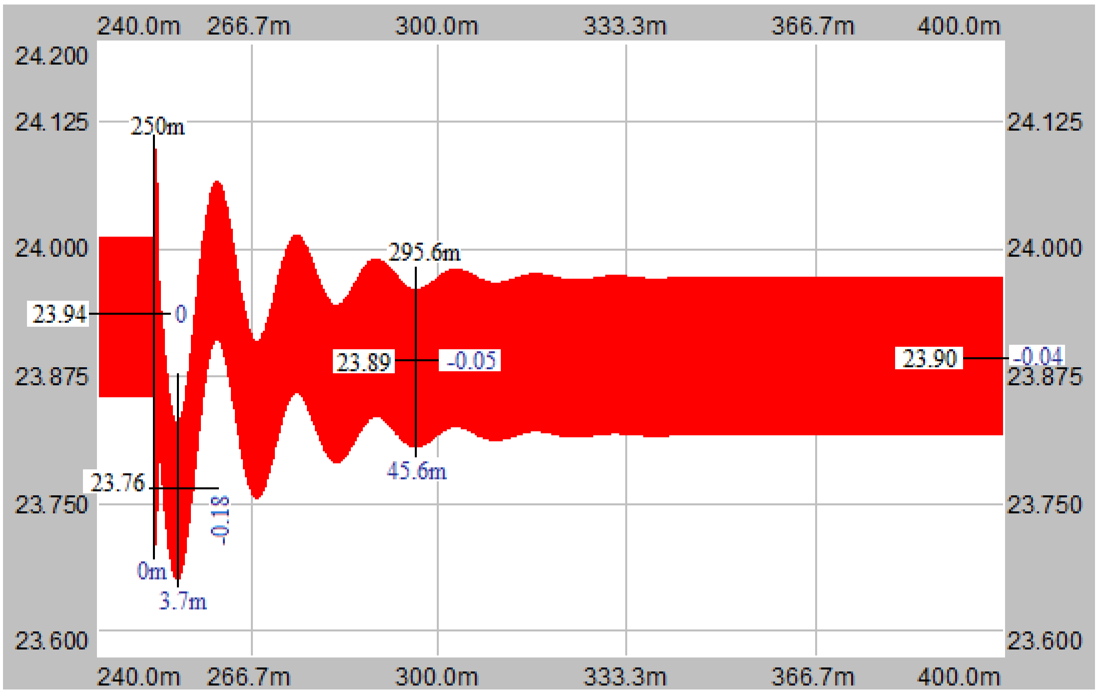

Figure 3-28: Response of v_o to small step change in i_o in Simplorer, parasitic elements, $\Delta I_o = 0.25A$

Verification of $G^{p}_{i_i/i_o}(s)$ *:*

The response of input current when 0.25A step change in output current happens is plotted in Figure 3-29 by using the following function in time domain.

$$G^{p}_{i_i/i_o}(s) \cdot \frac{0.25}{s}$$

The corresponding waveform in Simplorer is shown in Figure 3-30. Likewise, $G^{p}_{i_i/i_o}(s)$ is verified.

In conclusion, all of 6 transfer functions derived for CIĆC with parasitic elements have been validated.

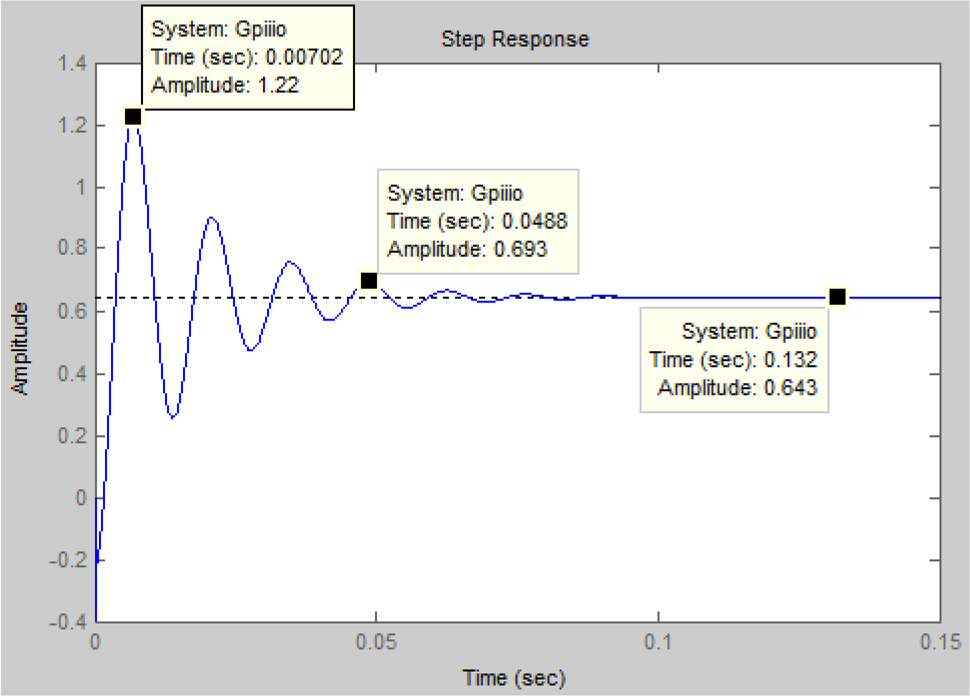

Figure 3-29: Step response of $G^{p}_{i_i/i_o}(s)$ in Matlab, $\Delta I_o = 0.25A$

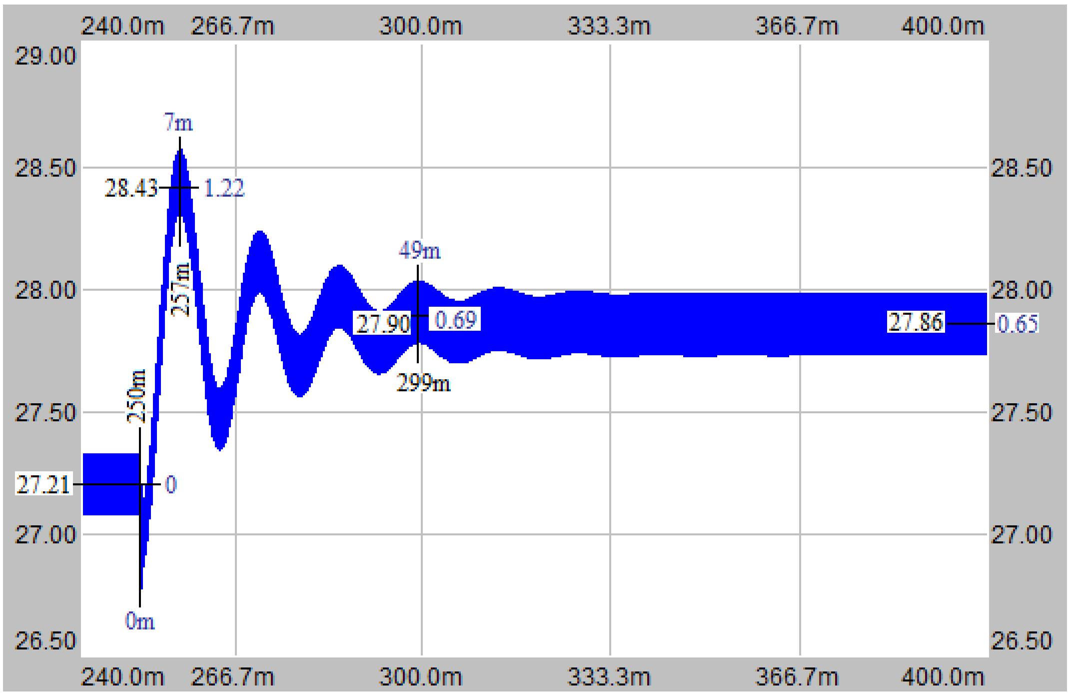

Figure 3-30: Response of i_i to small step change in i_o in Simplorer, parasitic elements, $\Delta I_o = 0.25A$

CHAPTER 4

DESIGN OF A COUPLED-INDUCTOR CUK CONVERTER

4.1 INTRODUCTION

This chapter comprises of two main topics. In the first topic, operational requirements of the converter are defined. Where it will be used, for what purpose it will be utilized and what are expected from the converter are given in details. Then, based on these data, technical requirements are determined. Second topic is the selection or design of the circuit components according to the technical requirements in the first topic. Then, the design will be verified by simulations or experimental tests wherever they are needed and possible.

4.2 OPERATIONAL REQUIREMENTS OF THE CONVERTER

Coupled-inductor Ćuk converter implemented in this work will be used mainly in one of the projects in ASELSAN. Therefore, the design criteria and parameters are determined by the project specifications. Before determining the design criteria, possible operating conditions must be considered at this point.

This converter will be used in the vehicle configuration of portable military equipment or military system. This equipment has two configurations: man-portable configuration and vehicle configuration. In man-portable configuration, the equipment is powered only by lithium-ion battery pack. According to the energy capacity of the battery pack, operating time of the equipment is determined. In vehicle configuration, again lithium-ion battery pack is utilized but it is not the unique energy source in this configuration. There exists another energy source, namely the battery group of the vehicle. It is desired to draw as much power as possible from this source to increase the operating time. Energizing the equipment only by the battery group of the vehicle, thereby eliminating the need for lithium-ion battery pack and providing a very long operating time compared to lithium-ion battery pack case is aimed. At this point, an interface problem arises: Input voltage level of the equipment does not match that of the vehicle battery. Actually, there are vehicles having different dc buses at different voltage levels in practice. The interface relating current levels is more sophisticated than that of voltage levels. Power is another problematic issue. Therefore, a dc-to-dc converter having voltage, current and/or power control modes is considered as a necessary element in the solution of this problem. The details are given in the following paragraphs.

In vehicle configuration, the converter will be fed by a vehicle battery and supply power to the equipment. Feeding of the converter can be realized in two ways:

- direct connection to vehicle battery,
- connection to vehicle battery through vehicle cigarette-lighter adapter (indirect connection).

This connection difference stems from the current carrying capability of the interconnecting elements. As it is assumed, in direct connection to the battery, current carrying capability depends on the input cable of the converter. That is, current limit is controllable. More current can be drawn by using a thick cable. However, cigarette lighter adapters have generally low current limits because they are not designed to supply much power.

If direct battery connection is feasible, the converter is desired to supply its rated power to the military equipment, or the load. The maximum power consumption of the military equipment is about 400W. In the beginning, the rated output power of the converter is thought of such that it can supply all the power needed by the equipment alone. However, after considering the operating conditions and restrictions, it is understood that this is not possible most of the time. The reason will be explained in the succeeding paragraphs. For the time being let’s go on with the second scenario. If direct battery connection is not possible, converter will be fed via vehicle cigarette-lighter adapter. In this scenario, the main power supply of the equipment is lithium ion (li-ion) batteries, which is normally the case for man-portable configuration of the equipment. Converter will be used as an auxiliary power supply. The objective, in doing this, is to extend the operating time with li-ion batteries by the support of the converter. It is clear that the more current the converter draws from the cigarette-lighter adapter, the longer the equipment operates. Converter can even eliminate the need for li-ion batteries if its output power meets 400W. However, vehicle cigarette lighter adapters have strict current limits. It differs from vehicle to vehicle. One can draw safely a current between 10A to 20A from a vehicle cigarette lighter adapter. Nevertheless, this current is not enough to feed the equipment alone, the reason of which will be explained later.

In most of the vehicles, nominal dc bus voltage is 12V, whose source is 12V lead-acid battery. In military vehicles, however, 2 series connected 12V lead-acid batteries (totally 24V) are common. Since the equipment is to be used in both military and civil vehicles, converter is required to be fed at both dc bus voltage levels. Besides, it is generally accepted that 12V-lead-acid battery voltage varies between 10V to 14V. When the vehicle is operating, its alternator charges the 12V-battery group at about 14V. When the vehicle is not operating but the battery is loaded, its voltage decreases below 12V. According to the load, it may decrease even below 10V. However, since deep discharging of the batteries decreases the life time of the battery, decreasing below a limit is generally not allowed. Hence, decreasing below 10V happens in extreme conditions. Converter is designed to operate under 10V, even down to 5V. Nevertheless, the lower limit for the input voltage at rated power is accepted as 10V. 10V-14V range for nominal 12V dc bus voltage corresponds to 20V-28V range in nominal 24V dc bus voltage. When both types of vehicles are considered, input voltage range is determined as 10V-28V.

$$10V \leq V_i \leq 28V \tag{4-1}$$

$$V_i^{min} = 10V \qquad V_i^{max} = 28V$$

Input voltage range has been determined. Now, the output voltage range must be identified. Voltage range of li-ion battery pack gives the necessary information. Li-ion cells have 3.6V nominal voltage. It is varying normally between 3.0V to 4.2V. In most of the military applications, nominal 28V is used as a dc voltage level. Hence, the li-ion battery pack used in the project, which is a standard battery pack in military applications, is formed by 8 li-ion cells connected in series. By this way, its nominal voltage is made to correspond to $3.6V/cell\ \times 8\ cells = 28.8V$. The maximum voltage level of the battery pack is $4.2V/cell\ \times 8\ cells = 33.6V$ and minimum is $3.0V/cell\ \times 8\ cells = 24.0V$. While the equipment (or the system) is being fed by li-ion battery pack, the voltage in the equipment’s input may vary between 24V and 33.6V. This corresponds to the output of the converter. The reason of this will be explained in the following paragraphs. As a result, the output voltage of the converter will vary between 24V to 33.6V.

$$24V \leq V_o \leq 33.6V \tag{4-2}$$

$$V_o^{min} = 24V \qquad V_o^{max} = 33.6V$$

At first sight, power demand of the system can be regarded as low. However, after some investigation it is seen that it is relatively high for a vehicle, which is generally not designed to supply such amount of extra power as an addition to its inherent loads such as electronic control, lighting, air conditioning and hydraulic systems. In a typical automobile, battery capacity is about 60AH (Ampere-Hour). This means that if the battery of the vehicle is loaded with 10A, it can give this amount of power for 6 hours roughly. While the engine of the vehicle is not operating, the only energy source is battery. Battery cannot withstand probably even an hour while supplying power only to air conditioning and lighting system.

Especially in 12V dc bus voltage, even 60A –for 1 hour supply duration- corresponds to a power of 720W. It means that the power consumption of a vehicle is about this amount. As seen, energy source is very limited in this mode. Actually, vehicles are designed to operate while its engine is active. While it is operating, an alternator mechanically powered by the engine supplies all the electrical power needed by the vehicle and charges the vehicle battery if power surplus exists at that instant. The capacity of alternators also changes from vehicle to vehicle but its order is about 70A for a typical automobile. This value is highly dependent on the rotational speed (rev/min) of the engine and generally given at the maximum horse power rotational speed, for example at 5000 rev/min. In other words, a moderate alternator can supply at most 980W electrical power to the vehicle. This power will decrease to its %80 roughly due to the variation in engine rotational speed. As mentioned above and also supported by the information gathered from the automobile producers, about 80% of the alternator power is already consumed by the vehicle itself. The long and the short of it, 400W-power demand of the equipment cannot be taken from the vehicle battery -and thereby the alternator- even via direct battery connection. As a result, whereas current carrying capability is a limiting factor in connection via cigarette lighter adapter, power handling capability of alternator is a limitation in direct connection to vehicle battery. At both connection modes, the converter will not meet the power demand of the equipment alone. Hence, both of the power sources -namely the li-ion battery pack and the converter- will be connected to the input of the equipment in parallel. This is why the input voltage of the equipment is the same as the output voltage of the converter. By the way, another important point should be highlighted. The system does not always consume 400W. Rather, it has gradual power consumption ranging from 25W to 400W. Therefore, it is highly possible that although both of the sources are connected, only the converter can feed the system in some situations. Note also that li-ion battery pack does not sink current in this mode owing to its internal hardware, probably a reverse current diode or its equivalent in terms of function. In order to make the converter the primary power source, control method should be determined accordingly. In the other mode, again priority should be given to the converter by the help of the control method. After all these evaluations, the following two operating modes are determined and design is implemented based on these restrictions in this work.

- *Direct Connection to Vehicle Battery*

In direct connection to the vehicle battery, the input power and the output voltage will be controlled. Input power control, which also brings instantaneous input current control, is chosen as 280W in order to supply nearly 250W to the load. Output voltage limit is determined as 34V. Being slightly greater than 33.6V, it is selected intentionally. When the input power does not exceed 280W, the converter can regulate its output voltage to 34V. At this voltage, even though the li-ion battery pack is in fully charged state (33.6V), it does not supply power to the system. By this way, it is guaranteed that the primary power source is converter in this mode. When the load exceeds 250W, the converter delivers its rated power to the system. At the same time, li-ion battery pack meets the rest of the power demand of the system, namely at most 150W. In this situation, since the converter is in input power limit, its output voltage is lower than 34V. Essentially, it is determined by the li-ion battery pack. As it is discharged, output voltage of the converter decreases. As mentioned

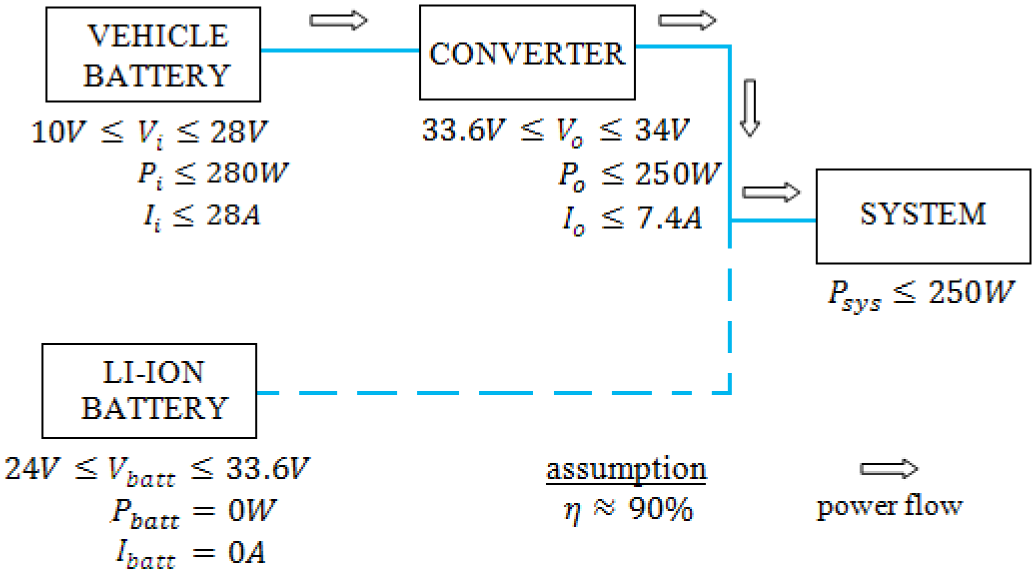

Figure 4-1 Direct connection to vehicle battery, $P_{sys} \leq 250W$

earlier, this voltage range is 24V-33.6V. These two operating possibilities in direct connection to the vehicle battery case are explained in Figure 4-1 and Figure 4-2. Investigating the figures from right to left makes them more understandable.

In Figure 4-1, the first possible case of direct connection to the vehicle battery is shown. In this case, power consumption of the system is lower than 250W. Hence, the converter meets the power requirement of the system alone. Dashed lines mean that there is a physical connection but no power flow. That is, li-ion battery pack is connected to the system but does not supply power to it because of the fact that its voltage is lower than the output voltage of the converter. Voltage and current level ranges are also specified in the figure. In determining the current levels, efficiency of the converter is assumed to be about 90%. Besides, arrows represent the direction of the power flow.

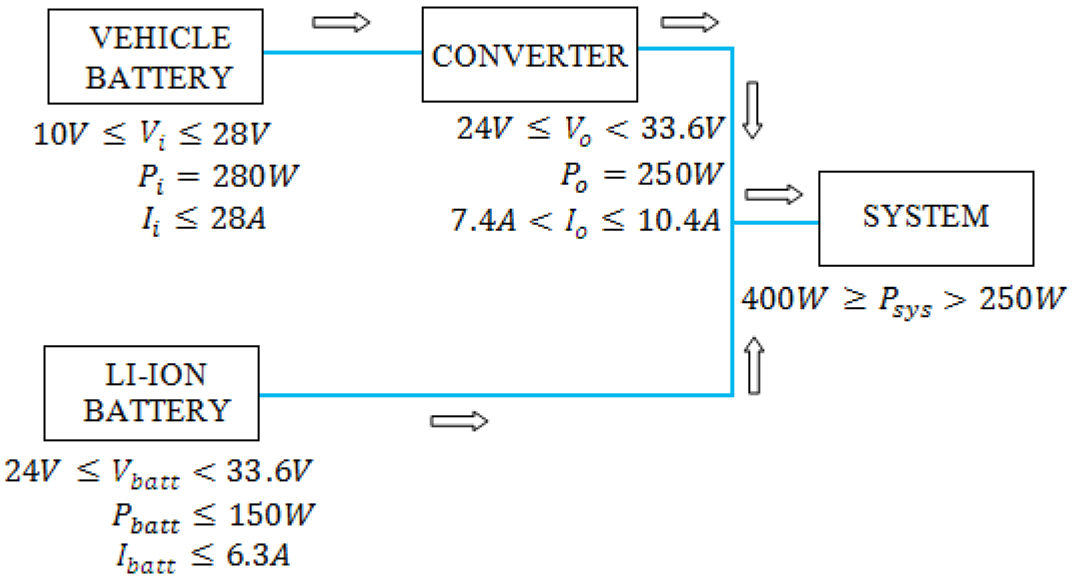

Figure 4-2 Direct connection to vehicle battery, $400W \geq P_{sys} > 250W$

In Figure 4-2, the second possible case of direct connection to the vehicle battery is shown. In this case, power demand of the system is between 250W and 400W. Both of the sources supply power to the system. The converter supplies 250W of the total power and the rest of the power demand, which is at most 150W, is supplied by li-ion battery pack. Again, the explanations in the previous figure are also valid here.

- *Connection to Vehicle Battery via Cigarette Lighter Adapter (Indirect Connection)*

In connection to the vehicle battery via cigarette lighter adapter, input current and output voltage will be limited. Input current limit is chosen as 10A and output voltage limit is determined as 34V. The reason behind 34V is the same with that in the direct connection case. It enables to make the converter the primary power source of the system. Input current limit (10A) is chosen according to the fuse and current carrying capabilities of cigarette lighter adapters in the vehicles that are possible to use for this purpose. As long as the load does not exceed the limit at which the input current is less than 10A, the converter can regulate its output voltage to 34V. At this voltage, the li-ion battery pack does not supply power to the system. In this case, one cannot specify a definite power limit because input voltage range is very wide. At 10A, the input power may be between 100W and 280W. Therefore, in indirect

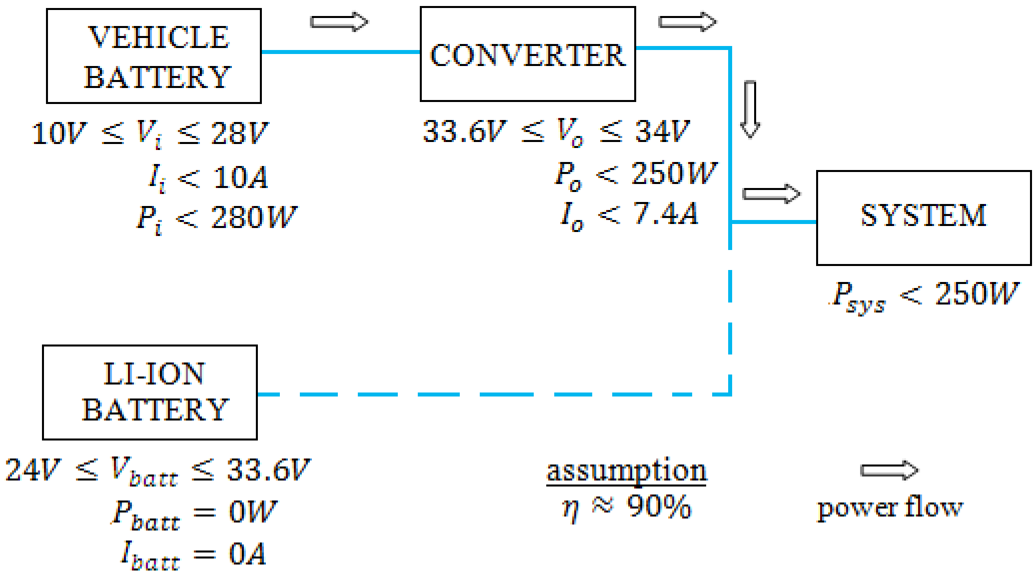

Figure 4-3 Connection to vehicle battery via cigarette lighter adapter, $I_i < 10A$ and $33.6V \leq V_o \leq 34V$

connection, the input current should be taken care. When the load forces the input current to exceed 10A in order to regulate its output voltage at 34V, the converter limits its input current to 10A and ceases to regulate its output voltage. As a result, the output voltage decreases and li-ion battery pack starts to supply power. Depending on the state of the battery pack charge and the operating conditions, the output voltage of the converter can be between 24V and 33.6V. In this case, $(V_i \cdot 10A \cdot \eta)$ of the system power demand is supplied by the converter, and the rest of the demand is supplied by the li-ion battery pack. These two operating possibilities are explained in Figure 4-3 and Figure 4-4. Again, investigating the figures from left to right eases to understand them.

In Figure 4-3, the first possible case of indirect connection to the vehicle battery is shown. In this case, the power consumption of the system is lower than at most 250W, which happens at the input voltage of 28V. This limit is 90W at the input voltage of 10V. Whatever the input voltage is, it is assumed that the converter meets the power requirement of the system in this case alone. Li-ion battery pack is connected to the system but does not supply power to it. Voltage and current level

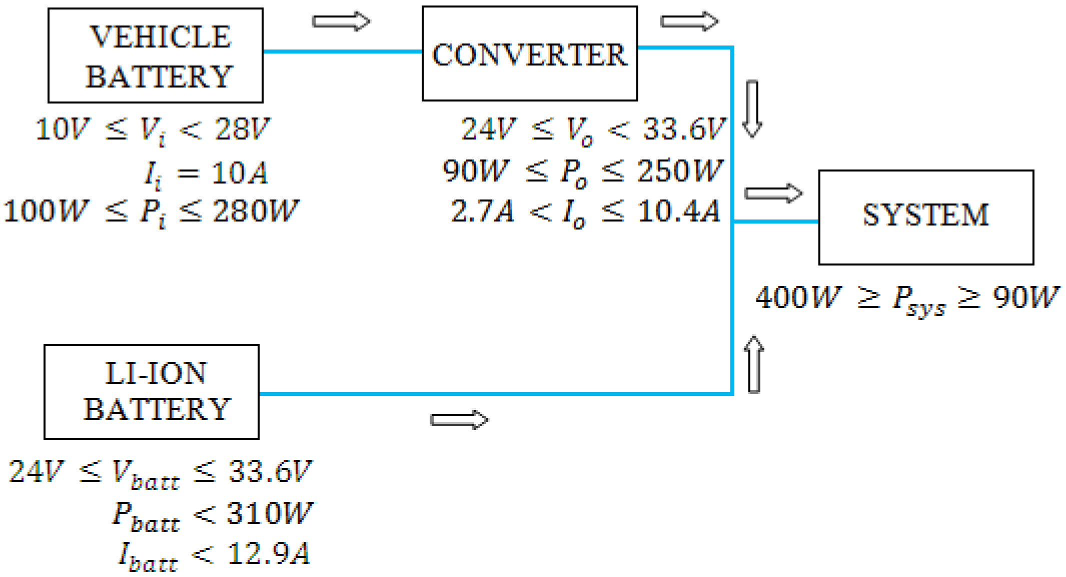

Figure 4-4 Connection to vehicle battery via cigarette lighter adapter, $I_i = 10A$ and $24V \leq V_o < 33.6V$

ranges are also specified in the figure by the efficiency assumption of about 90%.

In Figure 4-4, the second possible case of indirect connection to the vehicle battery is shown. In this case, power demand of the system is between 90W and 400W. Both of the sources supply power to the system. The converter supplies at least 90W (at $V_i = 10V$) and at most 250W (at $V_i = 28V$) of the total power, and the rest of the demand, which is at most 310W (at $V_i = 10V$) and 150W (at $V_i = 28V$), is supplied by li-ion battery pack.

Possible operational conditions are defined so far. Based on them, the following results are obtained in terms of the converter properties.

- Input voltage range of the converter is 10-28V, and output voltage range is 24V-34V. It means that the converter is required not only to step-up but also to step-down the input voltage. Ćuk dc-to-dc converter, which is one of the buck-boost converter types, is chosen for this purpose.

- The converter should be designed to supply 250W maximum within the input and output voltage ranges mentioned in (4-1) and (4-2).

- Especially in controlling the input current, instead of its instantaneous or peak value, its mean value will be controlled. However, in basic Ćuk converter, input current has such a waveform that it has a dc level and a triangular ac component (ripple) superimposed on it. An example to this kind of a waveform is shown in Figure 4-5. In this example, peak-to-peak ripple of

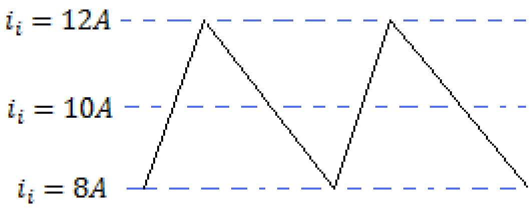

Figure 4-5 Input current waveform of a basic Ćuk converter with 40% peak-to-peak ripple

40% of the mean input current is selected typically just for illustration purpose. As understood from Figure 4-5 easily, the instantaneous value of the input current exceeds the current limit value in reality. In this situation, if the current protection mechanism of the cigarette lighter adapter is a fast acting one, it may be triggered by this type of current waveform. Even if the mechanism is a slow acting one, for example a fuse, this type of a waveform may have an adverse effect on it. Fuses normally have quite small internal resistances and they are heated up and become open by the heat caused by the RMS value of the current passing through them. As the ac component of the current waveform increases while its dc level is kept constant, its RMS value increases as well. For example, the waveform seen in Figure 4-5 has a mean value of 10A but RMS value greater than 10A. In this situation, fuse may be triggered as well due to the unwanted feature of the current waveform. In buck-boost converter topology, this situation is worse because it has pulsating input current waveform. Hence, Ćuk converter seems as a better solution. Moreover, coupled-inductor Ćuk converter with ripple-free input current version seems to be the best solution. As a result, CIĆC with ripple-free input current version is decided to design in this work.

- The converter is required to conduct different control strategies in direct and indirect connections to the vehicle battery. They are mentioned in the succeeding pages. Therefore, there must be a way for the converter to understand which control strategy to implement at that operation. When it is investigated, it is seen that this cannot be done automatically, for example by sampling the input and output voltages. Only an operator can determine the control strategy by looking at the connection type, direct or indirect. Hence, a manual switch will be added to the converter. It will have two positions. According to the position of it, the converter will run the corresponding control strategy.

- As mentioned earlier, in direct connection to the vehicle battery, output voltage and input power will be controlled. In order to do this, feedbacks will be taken from output voltage and input current. Most of the time, the system is expected to consume its rated power of 400W; therefore, the converter will be performing input power control. It will rarely control the output voltage. Hence, this control mode is called *'constant input power mode'* in this work.
- In indirect connection to the vehicle battery, output voltage and input current will be controlled. In this control mode, again, input current and output voltage will be taken as feedbacks. Similar to the direct connection case, the converter will control the input current most of the time. Therefore, this control mode is called *'constant input current mode'*.

At this point, selection and design of the circuit components can be performed.

4.3 SELECTION AND DESIGN OF THE CIRCUIT COMPONENTS

In this section; selection of the switch, diode, energy transferring capacitor (C_1) and output capacitor (C_o) will be detailed and based on the technical requirements. Then, the coupled-inductor providing ripple-free input current will be designed.

4.3.1 Selection of MOSFET

First of all, why MOSFET is selected may be required to explain. As mentioned earlier, the switching frequency is determined as 100 kHz. When it is searched, it is seen that 100kHz is reasonable at this power rating.[5] When the operating voltage levels, current levels and the switching frequency are taken into consideration, MOSFET is seen as the most suitable switch. Another possibility is IGBT, but it is more suitable at lower frequencies and higher voltage/higher current applications. When the switch market is searched, even for the most suitable IGBT for this application, total loss (conduction loss and switching loss) turns out to be higher than that of a moderate MOSFET. Hence, after a short market search, MOSFET is determined as the switch.

Now, to which voltage and current stresses the selected switch must withstand will be determined. Then, based on this information, a suitable switch will be selected according to its total loss. Necessary data needed in selection of the switch is given in Table 4-1. The maximum voltage, current and power dissipation stresses occur at ‘end operating points’, at which the voltage levels are at their maximum or minimum. Hence, these operating points are considered throughout the selection and design of the circuit components. There are four end operating points.

First End Operating Point:	$V_i =$10V and $V_o =$24V
Second End Operating Point:	$V_i =$10V and $V_o =$34V
Third End Operating Point:	$V_i =$28V and $V_o =$24V
Fourth End Operating Point:	$V_i =$28V and $V_o =$34V

The efficiency of the coupled-inductor Ćuk converter, CIĆM is assumed to be 90% in the preparation of Table 4-1. One may refer to the circuit schematic of CIĆM with parasitic elements in Figure 3-16 for the labels in the tables of this section. The instantaneous values, with small letters, are shown in that figure. In the tables, however, steady-state (or mean) values, with capital letters, are used; because it makes more sense. Similarly, mean value of the duty-factor, K is used in the tables. V_{tot}, I_{tot} and I_Q^{rms} labels are new. When the switch or the diode is on, it carries the sum of i_{L_1} and i_{L_2}, which corresponds to the sum of input and output currents. This value is labeled by I_{tot}. When the switch or the diode is off, it blocks V_{C_1}, which is the sum of input and output voltages. This value is labeled by V_{tot}. I_Q^{rms} is the RMS current of the switch. It will be used in power loss calculation.

Table 4-1 Voltage and current stresses on the switch

V_i /V	I_i /A	V_o /V	I_o /A	K	$1-K$	V_{tot} /V	I_{tot} /A	I_Q^{rms} /A
10	27,8	24	10,4	0,706	0,294	34	38,2	32,1
10	27,8	34	7,4	0,773	0,227	44	35,1	30,9
28	9,9	24	10,4	0,462	0,538	52	20,3	13,8
28	9,9	34	7,4	0,548	0,452	62	17,3	12,8

As inferred from Table 4-1, the selected switch has to withstand 62V during $(1-K)/f_s$ time interval, where f_s is the switching frequency. However, the voltage rating of the selected MOSET should be higher than this because of the voltage overshoots during transient period. Note also that C_1 voltage is not pure dc, however its voltage ripple is around 1-2% of its mean voltage and considered as negligible. This topic will be elaborated in C_1 selection section. In terms of current rating, it is seen that the switch carries at most 38.2A during K/f_s time interval. Again, there is a ripple current on L_2 inductor but it is at negligible level. 62V and 38.2A values can be regarded as the continuous operating conditions, because they are applied to the switch for relatively long time periods compared to the transient periods and they are periodic waveforms. As a result, the switch should be selected using this data.

I_Q^{rms} will be used in conduction loss calculation for the switch. This value is simply obtained by 'root mean square' definition.

$$F^{rms} = \sqrt{\frac{1}{T_s}\int_0^{T_s} f(t)^2 dt} \tag{4-3}$$

where T_s is the switching period. The switch carries current during KT_s time interval only. Hence, when this simplification is applied to (4-3), it yields;

$$I_Q^{rms} = I_{tot}\sqrt{K} \tag{4-4}$$

Hence, the maximum RMS current which can be carried by the switch is given as;

$$I_Q^{rms} = 38.2\ A\ \sqrt{0.706} = 32.1\ A$$

Then, the conduction loss in the switch can be calculated by;

$$P_Q^{on} = (I_Q^{rms})^2 R_{DS} \tag{4-5}$$

As it is seen, even 10mΩ R_{DS}, which can be considered as a low resistance for a typical MOSFET at these ratings, causes 10.3W conduction loss. Since RMS value of the current is relatively high, a MOSFET with lower R_{DS} will be more suitable for the application; otherwise at least two switches will be paralleled.

$$P_Q^{on} = (32.1A)^2 \cdot 10m\Omega = 10.3\ W$$

Another important point in determining the suitable switch is the switching loss. The switching loss on the switch can be expressed as [2];

$$P_Q^{sw} = \frac{1}{2} V_{tot} I_{tot} (t_{rise} + t_{fall}) f_s \tag{4-6}$$

Hence, in order to keep P_Q^{sw} low, rise and fall times should be low for the switch selected for use. Consequently, MOSFET with the lowest total power dissipation among the available MOSFETs is chosen as the following one;

Company: Infineon	Part Number: IPP045N10N3 G
Continuous $V_{DS} = 100V$	Continuous $I_{DS} = 100A$
$R_{DS} = 4.2m\Omega$	$t_{rise} = 59nsec$
$t_{fall} = 14nsec$	

Note that:

$V_{tot} = 62V < 100V = V_{DS}$ and $I_{tot} = 38.2A < 100A = I_{DS}$

Thus, the conduction and the switching power losses at end operating points for the switch are calculated and tabulated as Table 4-2.

Table 4-2 Power dissipation on the switch at end operating points

V_i /V	I_i /A	V_o /V	I_o /A	P_Q^{on} /W	P_Q^{sw} /W	P_Q^{tot} /W
10	27,8	24	10,4	4,3	4,7	9,1
10	27,8	34	7,4	4,0	5,6	9,6
28	9,9	24	10,4	0,8	3,9	4,7
28	9,9	34	7,4	0,7	3,9	4,6

Table 4-2 shows that the switching losses are large. This implies that increasing the switching frequency is not reasonable due to the increasing switching loss.

4.3.2 Selection of Diode

As a diode type, power Schottky is chosen. The reason for this is its low on-state voltage drop and low reverse recovery time. Hence, they are generally preferred in high frequency switched mode power supplies.

The current and voltage stresses on it are given in Table 4-3.

Table 4-3 Voltage and current stresses on the diode

V_i /V	I_i /A	V_o /V	I_o /A	K	$1-K$	V_{tot} /V	I_{tot} /A	I_D /A	I_D^{rms} /A
10	27,8	24	10,4	0,706	0,294	34	38,2	11,2	20,7
10	27,8	34	7,4	0,773	0,227	44	35,1	8,0	16,7
28	9,9	24	10,4	0,462	0,538	52	20,3	11,0	14,9
28	9,9	34	7,4	0,548	0,452	62	17,3	7,8	11,6

Diode also carries the current I_{tot} during $(1-K)T_s$ time interval as the switch does and blocks V_{tot} during KT_s time interval. I_D is, as expected, the mean value of the diode current and I_D^{rms} is the RMS value of the diode current, and it is given by;

$$I_D^{rms} = I_{tot}\sqrt{1-K} \tag{4-7}$$

I_D and I_D^{rms} values are given for diode power loss calculations and will be used in the succeeding paragraphs. Before loss calculation, diode should be chosen according to voltage and current stresses. As understood from Table 4-3, selected diode has to withstand 38.2A and 62V. As a consequence, the following diode is chosen.

Company: ST Microelectronics	Part Number: STPS80170C
$V_{RRM} = 170V$	$I_{F(AV)} = 80A$
$V_D = 0.62V$	$R_D = 3m\Omega$

Note that:

$$V_{tot} = 62V < 170V = V_{RRM} \qquad I_{tot} = 38.2A < 80A = I_{F(AV)}$$

Actually, using 38.2A as a mean value is not exactly true. However, in many of the diode datasheets, there is no detailed information about allowable peak repetitive forward current. Therefore, 38.2A is used as the mean value to be on the safe side.

In the datasheet of this diode, the following equation is given for use in the conduction loss calculation as;

$$P_D^{on} = 0.62 \cdot I_D + 0.003 \cdot (I_D^{rms})^2 \tag{4-8}$$

From which, the following relationship is established;

$$P_D^{on} = V_D I_D + R_D (I_D^{rms})^2 \tag{4-9}$$

It is clearly seen that V_D and R_D must be as small as possible in order to have low power dissipation on the diode. This was the driving force in diode selection. In diodes, reverse recovery phenomenon causes switching loss. However, there is not any data about this issue in most of the diode datasheets. Especially in fast switching ones, no information related to reverse recovery loss is found. This loss may be negligible with respect to conduction loss. As a result, reverse recovery loss is neglected in this work.

Conduction losses of the diode at end operating points are given in Table 4-4.

Table 4-4 Power dissipation on the diode at end operating points

V_i /V	I_i /A	V_o /V	I_o /A	P_D^{on} /W
10	27,8	24	10,4	8,3
10	27,8	34	7,4	5,8
28	9,9	24	10,4	7,5
28	9,9	34	7,4	5,2

To sum up, power dissipation on the diode seems to be reasonable.

4.3.3 Selection of C_1

C_1 holds V_{tot} mean voltage. There is a voltage ripple on it at the switching frequency. The amplitude of the ripple voltage will be determined by the selection of the capacitor. In terms of current stress, C_1 is charged by i_{L_1} during KT_s and discharged by i_{L_2} during $(1-K)T_s$. That is to say, current stress on C_1 is severe. In order to see the effect of current stress, simple capacitor model should be investigated.

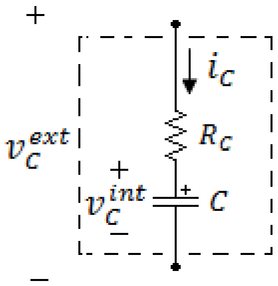

Figure 4-6 Simple capacitor model

As seen in Figure 4-6 and Figure 3-16, a capacitor has an equivalent series resistance, ESR. This resistance has two important effects. First, the RMS current passing through the capacitor causes power dissipation on the capacitor, which results in heating of itself. The amount of power dissipation can be calculated in the following and known manner. Note that although the mean value of the capacitor current is zero at steady-state, its RMS value can be very large.

$$P_C = (I_C^{rms})^2 R_C \tag{4-10}$$

The second important effect of ESR is related to voltage ripple on the capacitor. As mentioned earlier, capacitors have zero mean but nonzero RMS current values at steady-state operation. It means that i_C , in Figure 4-6, changes direction periodically. This change of direction leads to extra voltage ripple and this ripple is just because of ESR. Generally, only the following ripple source is considered: Increase or decrease of capacitor charge results in production of some ripple on the capacitor voltage. Referring to Figure 4-6;

$$C\frac{dv_C^{int}}{dt} = i_C \tag{4-11}$$

Note that v_C^{int} is used instead of v_C^{ext} in (4-11) because the voltage that cannot change instantaneously is v_C^{int}. Contrary to v_C^{int}, v_C^{ext} may change instantly when the magnitude or direction of i_C changes. v_C^{ext} can be expressed as;

$$v_C^{ext} = v_C^{int} + R_C i_C \tag{4-12}$$

In order to clarify the situation, let's consider that the circuit is transiting form Mode 2 to Mode 1. In Mode 2, i_{C_1} is the input current, which is constant at I_i. At this moment, (4-13) can be written, in which superscript t^- means that those quantities assume values equal to those resulting just before the switching instant.

$$(v_{C_1}^{ext})^{t^-} = (v_{C_1}^{int})^{t^-} + R_{C_1} I_i \tag{4-13}$$

In Mode 1, i_{C_1} is $-i_{L_2}$ with small ripple and it can be considered as constant. As mentioned earlier, mean value of i_{L_2} is equal to I_o. Therefore, (4-14) can be written in Mode 1. Similarly, superscript t^+ means that those quantities assume values equal to those resulting just after the switching instant.

$$(v_{C_1}^{ext})^{t^+} = (v_{C_1}^{int})^{t^+} - R_{C_1} I_o \tag{4-14}$$

Just before the switching, (4-13) is valid, but after the switching, (4-14) is valid. As a known fact, $v_{C_1}^{int}$ does not change instantly. Hence, $(v_{C_1}^{int})^{t^+}$ is equal to $(v_{C_1}^{int})^{t^-}$. However, $v_{C_1}^{ext}$ decreases instantly in this example. This fact is explained below step by step. The term $(\Delta V_{C_1}^{ext})^t$ represents the voltage change at the switching instant.

$$(\Delta V_{C_1}^{ext})^t \overset{\text{def}}{=} (v_{C_1}^{ext})^{t^+} - (v_{C_1}^{ext})^{t^-} \tag{4-15}$$

$$(\Delta V_{C_1}^{ext})^t = (v_{C_1}^{int})^{t^+} - R_{C_1} I_o - \left[(v_{C_1}^{int})^{t^-} + R_{C_1} I_i \right] \tag{4-16}$$

$$(\Delta V_{C_1}^{ext})^t = -R_{C_1}(I_i + I_o) = -R_{C_1} I_{tot} \tag{4-17}$$

This sharp voltage change occurs at each switching instant. Whereas v_{C_1} decreases $R_{C_1} I_{tot}$ much in Mode 2 to Mode 1 transition, it increases the same amount in Mode 1 to Mode 2 transition. As an addition to this sharp change, capacitor voltage changes because of the charge variation in it. Which kind of ripple will be more severe depends on the amount of current stress, size of the capacitance and ESR of the capacitor. These should be taken into account in the selection of the capacitors.

In capacitor selection, power dissipation is aimed to be at reasonable level and not to cause overheating of it. Another restriction comes from the assumptions made in CHAPTER 2. In those assumptions, voltage ripples on the capacitors are neglected. Therefore, capacitor voltage ripples should be limited in this section. When calculated, it has been observed that 2% peak-to-peak voltage ripple results in a reasonable capacitor bank for C_1. Furthermore, its voltage ripple is not as critical as that of the output capacitor. Its voltage ripple must be limited just in order to be as close as possible to constant capacitor voltage assumption. Consequently, 2% is a suitable choice for the voltage ripple percent of C_1.

When the available capacitors are searched, it is decided to use the following.

Company: Cubisic	Part Number: A710160
Type: Aluminium Electrolytic	$V_{max}^{op} = 100V$

$C = 1000uF$ $\qquad\qquad$ $ESR = 51m\Omega$

$I_{rms}^{per} = 10.8A$

Aluminium electrolytic type capacitor is selected because it has higher energy density among other capacitor types. In other words, it presents more capacitance for unit volume.

Note that the maximum capacitor voltage is greater than the maximum V_{tot}.

$$V_{tot}^{max} = 62V < 100V = V_{max}^{op}$$

I_{rms} is the permissible RMS current rating for the capacitor. In order to satisfy 2% voltage ripple and withstand the RMS current, it is necessary to parallel 3 of it. In this situation, R_{C_1} becomes 17mΩ and I_{rms} 32.4A. With these values, Table 4-5 is formed. It presents the ripple considerations at four end operating points for C_1.

Table 4-5 Voltage ripple consideration of C_1

V_i /V	I_i /A	V_o /V	I_o /A	$\Delta V_{C_1}^{esr}$ /V	$\Delta V_{C_1}^{c/d}$ /V	$\Delta V_{C_1}^{tot}$ /V	$Ripple\ Limit$ /V
10	27,8	24	10,4	0,649	0,025	0,674	0,680
10	27,8	34	7,4	0,597	0,019	0,616	0,880
28	9,9	24	10,4	0,346	0,016	0,362	1,040
28	9,9	34	7,4	0,294	0,013	0,307	1,240

The term $\varDelta V_{C_1}^{esr}$ represents the instantaneous voltage change on C_1, which is due to its ESR. In the analysis above, this voltage change is labeled by $(\varDelta V_{C_1}^{ext})^t$. From now on, it is labeled by $\varDelta V_{C_1}^{esr}$ in order to show the reason of the voltage change on the label. $\varDelta V_{C_1}^{c/d}$ is the voltage change due to the charging/discharging of the capacitor. Similarly, $\varDelta V_{C_1}^{int}$ is replaced by $\varDelta V_{C_1}^{c/d}$ for clarity. This voltage change is directly related to the energy transfer as follows;

$$P_o = \frac{1}{2} C_1 \left[(V_{tot} + \frac{\Delta V_{C_1}^{c/d}}{2})^2 - (V_{tot} - \frac{\Delta V_{C_1}^{c/d}}{2})^2 \right] f_s \tag{4-18}$$

$$P_o = \frac{1}{2} C_1 2 V_{tot} \Delta V_{C_1}^{c/d} f_s \tag{4-19}$$

$$\Delta V_{C_1}^{c/d} = \frac{P_o}{C_1 V_{tot} f_s} \tag{4-20}$$

As it can be understood from the derivation above, $\Delta V_{C_1}^{c/d}$ represents the peak-to-peak voltage ripple magnitude. Sum of $\Delta V_{C_1}^{esr}$ and $\Delta V_{C_1}^{c/d}$ gives the total voltage ripple on the capacitor, and it is named as $\Delta V_{C_1}^{tot}$ on the table. $Ripple\ Limit$ is 2% of the voltage on the capacitor, V_{tot}. As seen in Table 4-5, the maximum voltage ripple on the capacitor is less than the $Ripple\ Limit$ value at each end operating point. Also note that over 95% of the ripple is caused by the ESR of the capacitor. Instead of the selected capacitor, a capacitor bank with lower capacitance and ESR value might be chosen. That capacitor type may be ceramic or tantalum, which have lower energy density but lower ESR. In that situation, most of the ripple would be caused by charging/discharging instead of ESR. Besides, smaller capacitance would probably result in faster dynamic response at the expense of weaker stability. There is a trade-off between them. As a pure advantage, power loss would be lower in that situation. Since stability seems more important than the dynamic response in the project, the selected capacitor is preferred.

In order to verify the ripple considerations above, simulation is conducted with all parasitic components at one of the operating points: Full load, $V_i = 10V$, $V_o = 24V$. As seen in Figure 4-7, total ripple magnitude (671mV) is very close to the calculated one (674mV). There is a sharp change in the capacitor voltage, whose magnitude is as expected. Lines with lower slopes at the bottom and top are where the capacitor is being either charged or discharged. There is a small amplitude difference between them. It is due to the fact that i_{L_2} is not pure dc contrary to the prior assumption made. Due to the small current ripple on it, small amplitude difference is observed.

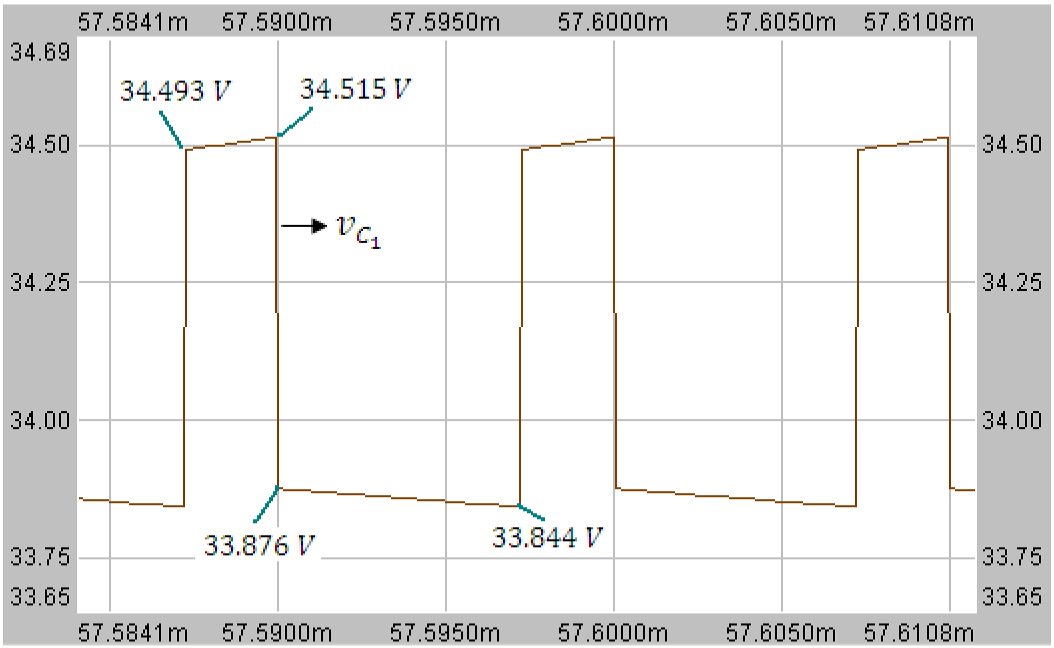

Figure 4-7 v_{C_1} waveform for voltage ripple consideration, full load, $V_i = 10V$, $V_o = 24V$

RMS current and power dissipation with the selected capacitor at each end operating points are given in Table 4-6.

Table 4-6 Power dissipation on C_1 at end operating points

V_i /V	I_i /A	V_o /V	I_o /A	K	$1-K$	$I_{C_1}^{rms}$ /A	$P_{C_1}^{tot}$ /W	$P_{C_1}^{each}$ /W
10	27,8	24	10,4	0,706	0,294	17,4	5,2	1,7
10	27,8	34	7,4	0,773	0,227	14,7	3,7	1,2
28	9,9	24	10,4	0,462	0,538	10,2	1,8	0,6
28	9,9	34	7,4	0,548	0,452	8,6	1,3	0,4

$I_{C_1}^{rms}$ is calculated by using the RMS definition in (4-3), as;

$$I_{C_1}^{rms} = \sqrt{{I_o}^2 K + {I_i}^2 (1-K)} \tag{4-21}$$

Note that the maximum RMS ripple current is less than the maximum allowable RMS current of the capacitor bank.

$$I_{C_1}^{rms} = 17.4A < 32.4A = I_{rms}^{per}$$

$P_{C_1}^{tot}$ term represents the total power dissipation on 3 capacitors and $P_{C_1}^{each}$ each of them. As it is seen in Table 4-6, C_1 capacitors have moderate power dissipations.

4.3.4 Selection of C_o

C_o holds the mean output voltage, V_o. Again, there is a voltage ripple on it at the switching frequency and its amplitude will be determined by C_o. That is, ripple voltage consideration of C_o resembles to that of C_1. However, their current waveforms are highly different. The current waveform of C_1 is dictated by the input and output inductors. Nevertheless, for C_o, the current waveform is determined by the output inductor current and the output current. (4-22) can be written by referring to Figure 3-16.

$$i_{C_o} = i_{L_2} - i_o \tag{4-22}$$

The difference current between i_{L_2} and i_o is supplied by C_o. Since the integral of it has to be zero at steady-state, C_o both sinks and supplies current within a period. This fact can be clarified by the help of Figure 4-8. Let's assume that the load sinks pure

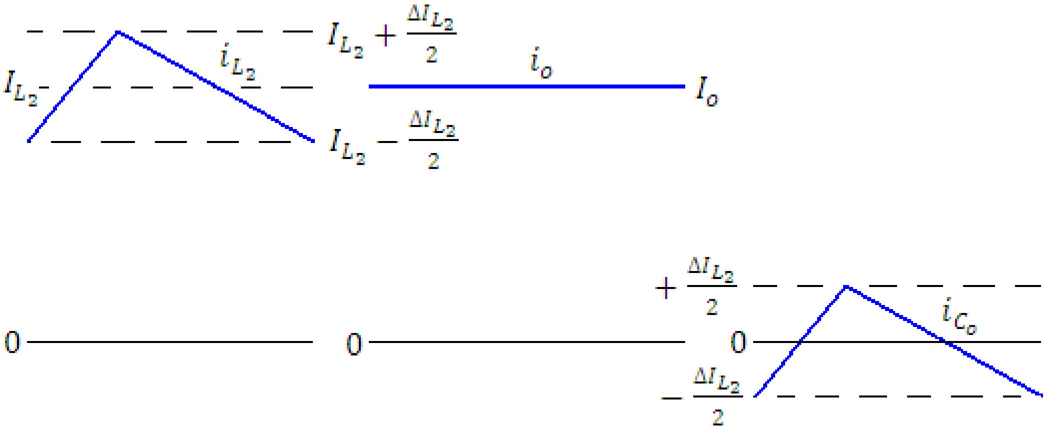

(a) (b) (c)

Figure 4-8 Current consideration of C_o, a) i_{L_2} waveform, b) i_o waveform, c) i_{C_o} waveform dc current. In this situation, the waveforms shown in Figure 4-8 are observed. As seen clearly, C_o has not severe current stress. It meets the current unbalance between the output current and the output inductor current. Hence, it may be called output filter capacitor. In order to determine the voltage ripple on C_o, some derivations are needed. Firstly, the ripple magnitude that is caused by ESR of the capacitor must be derived. As it is seen in Figure 4-8, peak-to-peak current change is ΔI_{L_2}. Hence, (4-23) can be written easily. Contrary to the ripple behavior in C_1 case, this voltage ripple does not change abruptly because current does not do so. Rather, it resembles to the ripple voltage due to charging or discharging of the capacitor.

$$\Delta V_{C_o}^{esr} = R_{C_o} \Delta I_{L_2} \tag{4-23}$$

The term $\Delta V_{C_o}^{esr}$ represents the peak-to-peak magnitude of the part of the voltage ripple caused only by ESR. Second part of the voltage ripple is labeled by $\Delta V_{C_o}^{c/d}$ and it is caused by charging and discharging of the capacitor. In order to find a relationship between $\Delta V_{C_o}^{c/d}$ and operating point parameters, Figure 4-9 can be helpful.

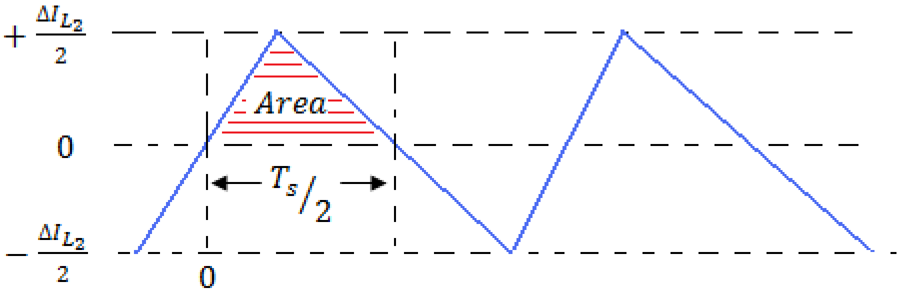

Figure 4-9 i_{C_o} waveform for voltage ripple consideration due to charging/discharging

C_o is charged during $T_s/2$ and discharged during successive $T_s/2$. Hence, its voltage increases shaded $Area$ much. Following equations can be written for the case;

$$i_{C_o} = C_o \frac{dv_{C_o}}{dt} \tag{4-24}$$

$$\int_0^{T_s/2} i_{C_o} dt = C_o \int_0^{\Delta V_{C_o}^{c/d}} dv_{C_o} \tag{4-25}$$

$$Area = C_o \Delta V_{C_o}^{c/d} \tag{4-26}$$

$$\frac{1}{2} \frac{\Delta I_{L2}}{2} \frac{T_s}{2} = C_o \Delta V_{C_o}^{c/d} \tag{4-27}$$

$$\Delta V_{C_o}^{c/d} = \frac{\Delta I_{L2}}{8 C_o f_s} \tag{4-28}$$

Similar derivation of (4-28) can also be found in [2]. This derivation is given intentionally in order to show the difference between C_1 and C_o in terms of voltage ripple consideration.

(4-23) and (4-28) are ready to use in determining the output capacitance. Before it, a simple modification may result in a better solution. 2% voltage ripple restriction for C_1 case seems a little bit looser for the output voltage. C_1 voltage is inside the circuit contrary to C_o voltage, which is the output of the circuit. Hence, a stricter condition may be desired at this point. As a result, the ripple requirement on the output capacitor voltage is selected as 1%.

After some investigation, it is seen that using two of the following capacitor meets the voltage ripple requirement and cause a reasonable power loss.

Company: AVX Corporation	Part Number: 12105C475K4Z2A
Type: Ceramic Capacitor	$V_{max}^{op} = 50V$
$C = 4.7uF$	$ESR = 15m\Omega$
$I_{rms}^{per} = 3A$	

It is a surface mount ceramic capacitor. Since the current stress is very light and the transferred energy is very small, the required capacitance turns out to be low. This justifies using ceramic capacitor. Its ESR and I_{rms}^{per} being not given in its datasheet, they are taken from the datasheets of equivalent products. By paralleling two of it, the following values are obtained.

$C_o = 9.4uF$ $\qquad R_{C_o} = 7.5m\Omega$ $\qquad I_{rms}^{per} = 6A$

Using these values, Table 4-7 is formed. Note that ΔI_{L_2} data are taken for granted for the time being and will be explained in coupled-inductor design section.

Table 4-7 Voltage ripple consideration of C_o

V_i /V	I_i /A	V_o /V	I_o /A	ΔI_{L_2} /V	$\Delta V_{C_o}^{esr}$ /V	$\Delta V_{C_o}^{c/d}$ /V	$\Delta V_{C_o}^{tot}$ /V	$Ripple\ Limit$ /V
10	27,8	24	10,4	0,68	0,005	0,090	0,095	0,240
10	27,8	34	7,4	0,74	0,006	0,098	0,104	0,340
28	9,9	24	10,4	1,24	0,009	0,165	0,174	0,240
28	9,9	34	7,4	1,47	0,011	0,196	0,207	0,340

As it is seen in Table 4-7, over 94% of the ripple is caused by charging/discharging process of the capacitor. The reverse is valid in C_1 case. As mentioned earlier, this difference stems from the property of the circuit topology and the selected capacitor types. Note that total voltage ripple is smaller than $Ripple\ Limit$ at each operating point. Hence, voltage ripple requirement is met in this way. Actually, when it is investigated closely, it is observed that the peak points of $\Delta V_{C_o}^{esr}$ and $\Delta V_{C_o}^{c/d}$ do not totally coincide in time. In other words, their maximum points occur at different times, although they are close to each other. Assuming the coincidence of the peak values in time gives the maximum ripple voltage and this case is called as the worst case. To be on the safe side and for simplicity, the worst case is assumed and the design is implemented according to this assumption.

Now, the ripple voltage calculations will be verified by simulation. It is done with all parasitic components at the same end operating point: Full load, $V_i = 10V$, $V_o = 24V$. As seen in Figure 4-10, the waveform has no sharp voltage change as expected. Its magnitude (62mV) turns out to be lower than the calculated one (95mV). When its reason is searched, it is seen that i_{L_2} ripple is 0.45A instead of 0.68A as calculated. 62mV is the expected value for 0.45A. Hence, (4-28) is verified. The reason why L_2 current ripple turns out to be less than

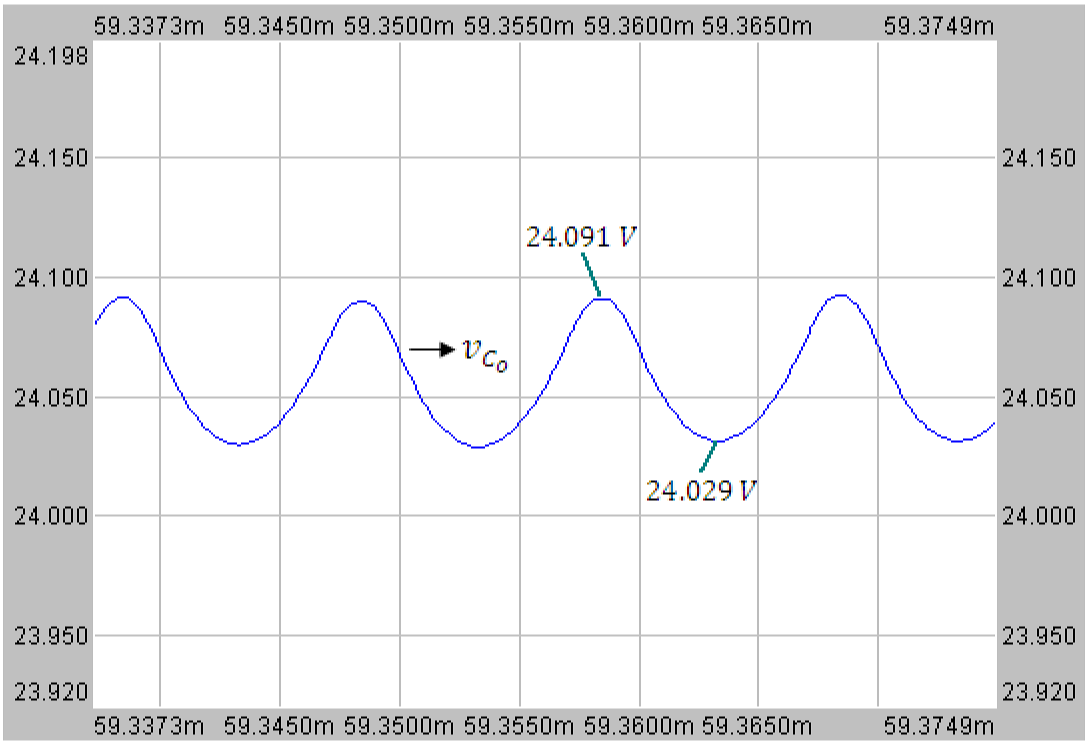

Figure 4-10 v_{C_o} waveform for voltage ripple consideration, full load, $V_i = 10V$, $V_o = 24V$

Calculated value is explained in Figure 2-22 and commented.

Now, let's look at the power loss on C_o. When the RMS current definition in (4-3) is applied to the waveform shown in Figure 4-9, the following equality can be derived.

$$I_{C_o}^{rms} = \frac{\Delta I_{L_2}}{2\sqrt{3}} \tag{4-29}$$

By utilizing this equality, power dissipation on the output capacitor is presented in Table 4-8. As seen in this table, total power loss on the output capacitor bank is in 1mW order. Hence, it is neglected.

Table 4-8 Power dissipation on C_o at end operating points

V_i /V	I_i /A	V_o /V	I_o /A	ΔI_{L_2} /V	$I_{C_o}^{rms}$ /A	$P_{C_o}^{tot}$ /W
10	27,8	24	10,4	0,68	0,20	0,0003
10	27,8	34	7,4	0,74	0,21	0,0003
28	9,9	24	10,4	1,24	0,36	0,0010
28	9,9	34	7,4	1,47	0,42	0,0014

4.3.5 Design of Coupled-Inductor

A coupled-inductor providing ripple-free input current is aimed to design in this section. First of all, its requirements such as the required inductances and the maximum current will be determined. Then, core material selection topic will be handled. Coupling requirement will be tried to meet. After theoretical work, practically implemented coupled-inductor will be investigated and tested. Its parameters will be measured and compared with the theoretical ones.

Let’s start with determining the inductances of the inductors. The coupled-inductor is aimed to provide ripple-free input current. As discussed in CHAPTER 2, L_1 has not a direct effect on the ripple current in this situation. L_2 will determine L_2 current ripple. Then, with respect to the parameters determining L_2, L_1 must have specific parameters in order to provide ripple-free input current waveform. In the same chapter, it is also mentioned that L_1 turns out to be slightly greater than L_2. Further details can be found there. In short, required L_2 must be determined first.

What kind of approach must be adopted in determining L_2? It is known that a larger inductance results in a large volume and weight. As an advantage, core loss and part of the copper loss caused by ac current diminish because the magnitudes of current and flux ripples decrease. In that situation, since the magnitudes of current ripple and flux ripple are smaller, complex calculations such as skin effect, proximity effect and hysteresis loss can be neglected. The inverse of all these comments can be argued for a smaller inductance. It is generally desired to have small components. Hence, a small inductance must be preferred. What must be the lower limit for the inductance? It is mentioned earlier that the minimum load of the system will be 25W, which corresponds to the 10% of the full load of converter. It means that the current at the output will be at least 10% of the full load. It is known that I_o is equal to I_{L_2}. In that situation, current waveforms similar to the ones shown in Figure 4-11 appear. Operating conditions are not given intentionally but note that the simulation is performed with the parasitic elements included. Assume that i_{L_2} hits the zero at its bottom, which is approximated in Figure 4-11. Further decrease in I_o or L_2 decreases

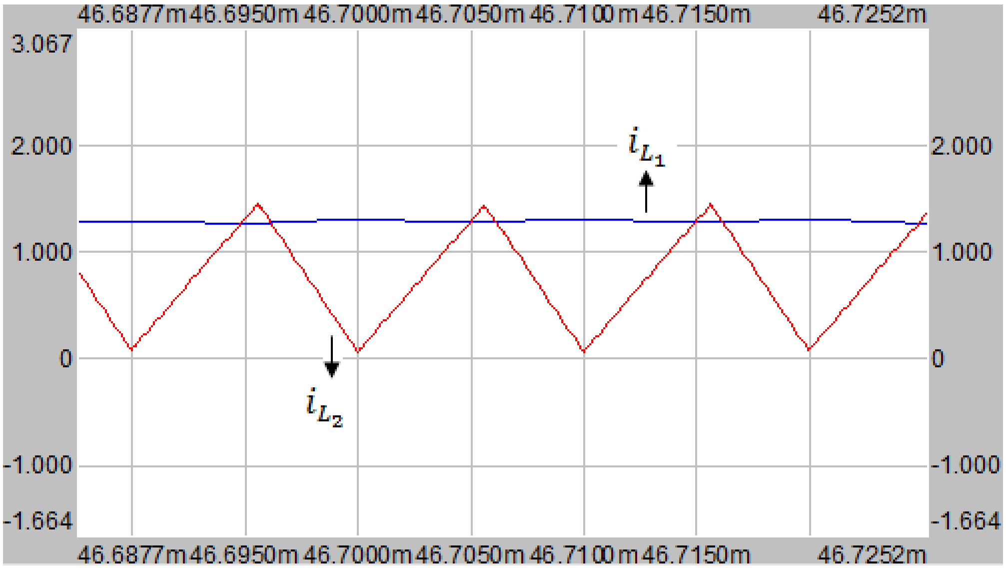

Figure 4-11 i_{L_1} and i_{L_2} waveforms at light load for the consideration of inductance lower limit

i_{L_2} below zero and change the direction. This point is chosen as the limit. In other words, L_2 will be determined such that even at the lightest load (i.e. 10% of the full load) at all possible operating points, i_{L_2} does not change the direction but just hits zero at the worst case. It is one of the many critical points. As long as its results are known, other critical points can be selected. Besides, it is worth pointing out that this point is not the boundary between CCM-DCM operations and brings a stricter limit than the boundary point.

The criterion has just been determined. As a next step, a relationship must be found between L_2 and other circuit parameters. Let's start with the known inductance relationship.

$$v_{L_2} = L_2 \frac{di_{L_2}}{dt} \tag{4-30}$$

Since the applied voltages are assumed to be constant, (4-30) can be simplified into (4-31).

$$L_2 = \frac{V_{L_2} \Delta t}{\Delta I_{L_2}} \tag{4-31}$$

V_{L_2} is either V_i , which occurs in Mode 1, or $-V_o$, which happens in Mode 2. Whichever is used, the result will be same. In Mode 1, V_{L_2} equals V_i and Δt equals KT_s. ΔI_{L_2} is 2 times 10% of the full load current. However, the full load current differs with respect to the output voltage (24V-34V) for that operating point. Meanwhile, duty-factor changes with the input voltage. Hence, the best way of determining L_2 is to calculate the required inductances at 10% load for the four end operating points and pick the maximum of them.

Table 4-9 Required L_2 values at 10% load at the end operating points

V_i /V	$I_i^{100\%}$ /A	V_o /V	$I_o^{100\%}$ /A	K	$I_o^{10\%}$ /A	L_2^{need} /uH
10	27,8	24	10,4	0,706	1,04	34
10	27,8	34	7,4	0,773	0,74	53
28	9,9	24	10,4	0,462	1,04	62
28	9,9	34	7,4	0,548	0,74	104

In Table 4-9, superscript 100% means the full load values and superscript 10% means 10% of the full load values. For example, for the first end operating point, mean value of the output current at %10 of the full load is 1.04A. It means that ΔI_{L_2} is 2.08A. Also, $V_{L_2}$is 10V and Δt is $0.706T_s$ at this operating point. Hence, the required L_2 is calculated by using these values and (4-31).

$$L_2 = \frac{10V \cdot 0.706 \cdot 10usec}{2.08A} \approx 34uH$$

The same calculation is done for each end operating points. As seen in Table 4-9, the worst case is the fourth end operating point. At this case, the required inductance turns out to be 104uH. Hence, L_2 must be designed according to this need. Decreasing below this value must be avoided.

$$L_2 \geq 104uH \tag{4-32}$$

The first specification of L_2 has just been determined. Now, the second specification, namely the maximum current of L_2, should be clarified. By taking the limit value of the inductance, the maximum current can be found for each end operating point. The maximum of them gives what is looked for. Note that if L_2 is determined to be greater than 104uH, the ripple magnitudes and the maximum current diminish further.

Table 4-10 The maximums and the minimums of i_{L_2} at full load and at end operating points

V_i /V	$I_i^{100\%}$ /A	V_o /V	$I_o^{100\%}$ /A	K	$I_{L_2}^{max}$ /A	$I_{L_2}^{min}$ /A	$Ripple\ Percent$ /%
10	27,8	24	10,42	0,706	10,75	10,08	6,49
10	27,8	34	7,35	0,773	7,72	6,98	10,06
28	9,9	24	10,42	0,462	11,04	9,80	11,88
28	9,9	34	7,35	0,548	8,09	6,62	20,00

As seen in Table 4-10, the maximum current that is carried by L_2 instantaneously is 11.04A. Also note that the peak-to-peak ripple percent of i_{L_2} turn out to be 20% at the fourth end operating point, which is not a surprise. Since the inductance limit value criterion is based on 10% and the maximum inductance is obtained at the fourth end operating point, superposing peak-to-peak 20% ac current waveform on 100% dc level at full load naturally gives 20% ripple at the same end operating point.

Required information in order to design L_2 has just been obtained. If it were an independent inductor, these data would be enough to start designing. Since it is coupled to L_1, a different way should be followed. It is known that i_{L_1} is constant and I_i. Its number of turns should be slightly greater than that of L_2. Besides, as explained in CHAPTER 2, fluxes created by L_1 and L_2 are additive. In order to ease the visualization, coupled-inductor core that is planned to use is given in Figure 4-12. Middle branch will carry the total flux. Right and left branches will share this flux equally.

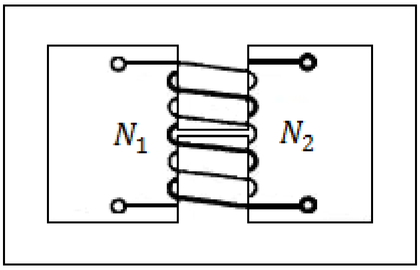

Figure 4-12 Coupled-inductor core planned to use

Coupled-inductor should be designed such that the maximum current density in copper and the maximum flux density in core must be at reasonable values. If the current density is adjusted to a relatively high value, copper loss turns out to be high. If the flux density is adjusted to a relatively high value, core loss turn out to be high and also the inductances decrease due to the nonlinear characteristics of B-H curves. Hence, these values should be under control in design procedure.

Inductor design highly depends on the selected core. Because, according to the core reluctance, required number of turns for a specified inductance is determined. After it is determined, flux density is checked whether it is beyond the previously determined limit or not. At the same time, whether that number of turns fits into the window area of the core or not is inspected. If the winding does not fit into the window area or flux density exceeds the limit, a larger core is selected. This procedure is applied as iteration until a suitable core with the minimum size is found. This approach is adopted here.

The design will be explained by the help of the following four tables; namely Table 4-11, Table 4-12, Table 4-13 and Table 4-14. These tables are correlated with each other. Because of this correlation and abundance of the parameters, iterations are implemented in a Microsoft Excel sheet. These tables are the snapshots of the result of the iteration. In other words, they belong to the ultimately selected core and windings.

Let's start with Table 4-11. As it is expected, the maximum current and flux densities occur at the maximum input and output current cases. When Table 4-10 is investigated, it is seen that the maximum of the sum of $I_i^{100\%}$ and $I_{L_2}^{max}$ occurs at the first end operating point. Hence, these values are written in Table 4-11. Required L_2 value (104.4uH) is another input. Diameter of the selected wire is 0.55mm. Instead of using single but thick wire, multiple of thin wire is preferred. Thin wire is generally used where ac current amplitude and switching frequency are high. In this way, skin effect is considered and thin wire is used in order to decrease the ac resistance of the wire. In this problem, i_{L_1} is always constant and i_{L_2} has at most 20% peak-to-peak ripple current at full load. Hence, even if the ac resistance of L_2 inductor were designed high, its loss would be low because ac current magnitude is very low. Still, skin depth may be checked. Its known formulation is given in (4-33).

$$\delta = \sqrt{\frac{2\rho}{\omega\mu}} = \sqrt{\frac{2\rho}{2\pi f_s \mu_r \mu_o}} = \sqrt{\frac{\rho}{\pi f_s \mu_r \mu_o}} \tag{4-33}$$

Skin depth is calculated as:

$$\delta = 0.206\, mm$$

Skin depth is defined as the distance from the surface to the inner of the conductor where current density is e^{-1} (≈ 0.37) of the surface current density. In a wire with 0.55mm diameter, depth of the innermost point is 0.275mm, which is close to the calculated skin depth. In short, this wire is selected such that ac losses on the windings can be neglected.

Let's continue with the other parameters in Table 4-11. Cross section area of a single wire is simply calculated as $\pi(0.55mm/2)^2 \approx 0.24\text{mm}^2$. Then, current density limit must be set in order calculate how many wire must be paralleled in order to carry that much of input and output currents. When many examples are investigated, it is seen that most of them are in the range of 2A/mm^2 to 6A/mm^2. Midpoint of them, 4A/mm^2, is selected and checked whether it is reasonable or not. In this situation, it is observed that windings have moderate series resistances and power dissipations, which will be presented in the following paragraphs. Of course, selecting a current density below 4A/mm^2 would be better, but in 4A/mm^2 case windings just about fit into the coil former, to which the windings are wound. Hence, 4A/mm^2 is evaluated as a satisfactory value. Using this information, required total cross section area for i_{L_1} is calculated as:

$$27.78\text{A}/4\text{Amm}^{-2} \approx 6.94\text{mm}^2$$

How many wires can provide this total cross section area is found as the ceiling value of $6.94\text{mm}^2/0.24\text{mm}^2$. By the way, due to the rounding of the numbers in the snapshots of the tables, some unimportant inconsistencies in the values of the parameters may be observed. They exist only in the snapshots and accumulative error is eliminated by use of Excel sheet, which keeps the numbers at large amount of decimal points. To sum up, it is obtained that 30 wires should be paralleled for L_1 and 12 wires for L_2. In that situation, current densities are set to just below 4A/mm^2 for both inductors.

At this step, whether the windings can fit into the selected coil former or not will be investigated. For L_1, net occupied area for 1 turn of 30 wires is calculated as:

$$30 \cdot 0.24\text{mm}^2 = 7.2\text{mm}^2$$

Number of turns is required now. This value comes from Table 4-14. As mentioned earlier, the design procedure is iterative and the tables are correlated. Determination of number of turns will be explained later. Let's take it for granted for the time being. Then, the net occupied area by 19.5 turns of 30 wires is calculated as:

$$19.5 \cdot 7.2\text{mm}^2 = 140.4\text{mm}^2$$

In Table 4-11, gross values are given. Net area is named as the area of circle, whereas gross area is considered as the area of the square which includes that circle. There is a correction factor of 4/π between the areas. As it is known, there exist areas between the circles which are not utilized. In order to asses more accurately, this correction is performed at this stage. As a result, gross occupied area of L_1 winding is calculated as:

$$140.4\mathrm{mm}^2 \cdot 4/\pi \approx 177\mathrm{mm}^2$$

Similarly, gross occupied area of L_2 winding is calculated as 66mm^2. Total of them is found as 243mm^2. Window area of the selected coil former is 462mm^2. At first sight it is seen that only 53% of the area is utilized. However, when practical winding issues are considered, this utilization factor seems to be reasonable. When the windings were wound, it has been observed that window utilization factor could be increased to at most 60%. However, it has been left as it is.

Table 4-11 Wire and window area considerations in coupled-inductor design

I_i *constant and maximum* /A	27,78
I_o *maximum* /A	10,75
L_2 /uH	104,4
Diameter of single wire /mm	0,55
Cross section area of a single wire /mm^2	0,24
Current density limit /Amm^{-2}	4
Required total cross section area for I_i /mm^2	6,94
Required number of parallel wires for I_i /#	30
Required total cross section area for I_o /mm^2	2,76
Required number of parallel wires for I_o /#	12
Gross occupied area by L_1 *winding* /mm^2	177
Gross occupied area by L_2 *winding* /mm^2	66
Gross occupied area by both windings /mm^2	243
Window area of coil former /mm^2	462

Let's go on with Table 4-12. In this table, some parameters of the selected core are given. Before it, the identification of the core is presented as;

Company: Epcos Part Number: PM 74/59

Material: Ferrite N27 Air gap: 3.8mm

First of all, why gapped ferrite core is chosen can be explained briefly. As it is known, there is a trade-off between high B_{sat} and low hysteresis loss in core material types. Ferrite materials have the lowest B_{sat} and hysteresis loss values; laminations have the highest B_{sat} and hysteresis loss values; and powdered cores are between them. At $f_s = 100kHz$, generally ferrite material is preferred for filter inductors.[5] By doing so, hysteresis loss is desired to keep at a low level; because filter inductors generally have relatively high flux swing. However, in this work, flux swing is relatively low: i_{L_1} is always constant and i_{L_2} has relatively low current ripple. By grounding on this fact, it would be argued that ferrite is not necessarily the optimum selection. For example, with its moderate hysteresis loss, powdered core would be selected. In that situation, it would provide smaller size and its hysteresis loss would be reasonable by the help of the low flux swing in the coupled-inductor. These arguments may be true; however, there is a special situation of the coupled-inductor. As mentioned in CHAPTER 2, there must be relationship between leakage and magnetizing inductances of L_1 and L_2 for complete ripple cancellation in L_1. As a known fact, inductance of an inductor decreases little or much as the current increases. In other words, reluctance of an inductor increases with increasing flux density. Characteristic of this change differs from material to material. This fact is observed in B-H curves. For example, air has a linear B-H curve, its slope is very low and magnetic saturation is not observed. B-H curves of ungapped ferrite materials are comprised of two ‘almost’ linear portions. First portion represents the magnetic permeability of ferrite material and its slope is very high. Once B_{sat} value is reached, the second linear portion is observed. Because of the saturation, its slope and hence magnetic permeability is low in this portion. This type of saturation is called ‘hard saturation’ or ‘sharp saturation’. B-H curves of gapped ferrite materials resemble to that of ungapped ferrite materials. The only difference is the slope of the first linear part. In gapped case, B_{sat} value is reached at a higher H value. In other words, magnetic permeability of the first portion is lower than the gapped case. This is achieved by adding a ‘discrete’ air gap to the core. In powdered cores, B-H curves are kind of a rising exponentials with decaying slope. Linear portion may be observed only after deep saturation. Magnetic saturation occurs gradually. This kind of saturation is called ‘soft saturation’. This characteristic stems from the internal structure of powdered cores. In their production process, powders of different compounds are brought together to form a core. ‘Distributed’ air gaps as ‘air bubbles’ are also added to the powder mix if higher H is desired at B_{sat}. Due to their non-homogeneous structure, they show different reluctance values at each operating point. It means that powdered cores exhibit different inductance values according to the current. Detailed explanation of this issue can be found in [29].

Based on the previous paragraph, it can be said that the leakage inductances of the coupled-inductor (namely L_{l1} and L_{l2}) are independent of i_{L_1} and i_{L_2}; because their reluctance paths are air. However, L_m depends on the current values. It would vary highly if powdered core was selected. Therefore, the balance between L_1 and L_2 would be satisfied probably at one operating point only. However, it is desired to have ripple-free input current at all possible operating points. Hence, using gapped ferrite material as a core and staying always at the first linear portion of it and avoiding magnetic saturation is regarded as the best solution.

Table 4-12 Necessary core data

Core Data	
A_L $/nHturn^{-2}$	315
$Assumed\ maximum(L_{12}/L_{22})\ ratio$	0,05
$Planned\ (N_1/N_2)\ ratio$	1,05
$Cross\ section\ area\ of\ core$ $/mm^2$	630
$Winding\ area\ of\ coil\ former$ $/mm^2$	462

Table 4-12 can be investigated now. In the datasheet of the selected core, instead of the equivalent reluctance of the core and the air gap, A_L value is given. In most of the core datasheets, this approach is adopted. A_L is defined as the inductance of the 1 turn wound on the core in nH. Hence, inductance for N turns can be calculated simply in the following manner.

$$L = N^2 A_L 10^{-9} \quad in\ H \tag{4-34}$$

Therefore, the reluctance value of the core, namely $\mathbb{R}_m$, can be deduced by equating (4-34) and (4-35).

$$L = \frac{N^2}{\mathbb{R}} \quad in\ H \tag{4-35}$$

$$\mathbb{R} = \frac{10^9}{A_L} \tag{4-36}$$

Using the equation above, $\mathbb{R}_m$ value is obtained in Table 4-13.

Required L_{22} has been determined previously. It is comprised of two values: $L_m{}'$ and L_{l2}. Since $\mathbb{R}_m$ is known, $L_m{}'$ can be set to any value by using N_2. However, L_{l2} value is indeterminate. When analyzed, it is seen that (N_1/N_2) ratio should be determined according to $(L_{l2}/L_m{}')$ ratio or simply (L_{l2}/L_{22}) ratio. More precisely, higher L_{l2} value necessitates higher (N_1/N_2) ratio for ripple-free input current waveform. Practical problems arise at this point. In order to have low leakage inductances, L_1 and L_2 windings are planned to wind simultaneously: The first group of wires of L_1, then the first group of wires of L_2, then the second group of wires of L_1, then the second group of wires of L_2 and goes on. In this situation, there is no chance to measure L_{l2} and then calculate and apply the necessary (N_1/N_2) ratio. Of course, measuring L_{l2} just after the first groups of wires of L_1 and L_2 windings are wound is possible but it does not give an accurate result. Because of the practical differences between the groups of windings of the same inductor, their individual inductances differ. It results in relatively high, for example 10%, difference between the measurements taken after the first groups of wires of L_1 and L_2 windings are wound and the measurements taken after all groups of wires of L_1 and L_2 windings are wound. This high difference may easily disturb the ‘balance’ established after the first groups of wires of L_1 and L_2 windings are wound. Actually, this approach was tried and resulted in failure. Hence, it was abandoned. As a solution, the following approach is found and adopted: Firstly, the maximum (L_{l2}/L_{22}) ratio is assumed. In this work, this value is assumed as 5%. According to this value, required (N_1/N_2) ratio according to (2-53) is obtained in the following manner.

$$\frac{L_{l2}}{L_{22}} = \frac{\frac{N_2^2}{\mathbb{R}_{l2}}}{\frac{N_2^2}{\mathbb{R}_{l2}}+\frac{N_2^2}{\mathbb{R}_m}} = \frac{\mathbb{R}_m//\mathbb{R}_{l2}}{\mathbb{R}_{l2}} = \frac{5}{100}$$

If $\mathbb{R}_{l2}$ is taken as 100, $\mathbb{R}_m$ is calculated as 5.26. Then, (N_1/N_2) ratio can be found as:

$$\frac{N_1}{N_2} = \frac{\mathbb{R}_m}{\mathbb{R}_{l2}//\mathbb{R}_m} = \frac{5.26}{5} \approx 1.05$$

If the measured (L_{l2}/L_{22}) ratio turns out to be lower than 5%, $\mathbb{R}_m/(\mathbb{R}_{l2}//\mathbb{R}_m)$ ratio is planned to make 1.05 by adding a series connected ‘adjustment’ inductor to L_2 inductor as a leakage inductor. In other words, if the leakage inductance of L_2 winding turns out to be smaller than expected, the above equation is satisfied by increasing L_{l2} via the addition of series connected adjustment inductor to L_2 winding. Hence, there is no need to modify the coupled-inductor, which is not really practical. However, if (L_{l2}/L_{22}) ratio turns out to be greater than 5%, then (N_1/N_2) ratio has to be increased, which means rewinding of the coupled-inductor. Because of this reason, the maximum (L_{l2}/L_{22}) ratio is assumed at the beginning. After some trial, 5% is considered as a reasonable value.

Other parameters on Table 4-12 can be explained briefly. Cross section area of the core is the minimum area from where total fluxes of the inductors pass through. Hence, this area will determine the flux density. Winding area of coil former is the allowable area where all windings can cross over.

Let’s continue with Table 4-13. In this table, what must be the output parameters according to the input parameters is calculated. However, since its outputs do not turn out to be practical, tiny modifications are applied to this table and Table 4-14 is obtained.

Explanation of $\mathbb{R}_m$, which is seen in Table 4-13, is given in the previous paragraphs. $L_m{}'$ is calculated by using $L_{22} = 104.4uH$ and $(L_{l2}/L_{22}) = 0.05$. Once $L_m{}'$ is obtained, required N_2 can be calculated easily by utilizing the following relationship.

$$L_m{}' = \frac{N_2^2}{\mathbb{R}_m} \tag{4-37}$$

As a next step, N_1 is calculated by using (N_1/N_2) ratio. Note that N_1 and N_2 values are 18.7 and 17.8, which are not very practical. Therefore, Table 4-13 is labelled as theoretical.

Table 4-13 Theoretical outputs with respect to core data

Theoretical Outputs with Respect to Core Data	
$\mathbb{R}_m\ /H^{-1}$	3174603
$L_m{}'\ /uH$	99,4
$N_2\ /Turn$	17,8
$N_1\ /Turn$	18,7
$F_{tot}\ /ATurn$	709
$\Phi_m\ /uWeb$	223
$B_{max}\ /T$	0,35

As it is known, magnetomotive force (MMF) can be expressed as:

$$F = NI$$

Since MMFs of the coupled-inductors are additive, the maximum total MMF can be defined in the following manner. I_i and $I_o$values are taken from Table 4-11.

$$F_{tot} = N_1 I_i + N_2 I_o = 18.7Turn \cdot 27.78A + 17.8Turn \cdot 10.75A \approx 709ATurn$$

In order to find the flux, the following equality can be utilized.

$$F_{tot} = \Phi_m \mathbb{R}_m \tag{4-38}$$

Hence, Φ_m can be calculated as:

$$709ATurn\ /\ 3174603H^{-1} = 223uWeb$$

This is the maximum flux present in the core. The maximum flux density can be calculated by using the following equality.

$$\Phi_m = B_{max} \cdot Cross\ Section\ Area\ of\ Core \tag{4-39}$$

$$B_{max} = \frac{223uWeb}{630mm^2} = 0.35T$$

When the datasheet of core material is investigated, it is seen that 0.35T remains on the first linear portion of the B-H curve. That is, magnetic saturation is avoided and almost constant magnetic permeability is expected. The snapshot of the B-H curve of the used core is given in Figure 4-13.

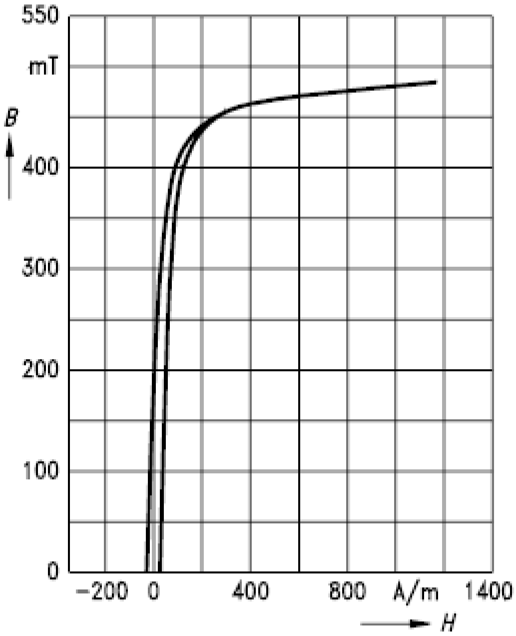

Figure 4-13 B-H curve of the selected core material [30]

At this point, all the parameters seem to be reasonable and iteration is finished. Actually, two conditions are checked. First one is whether the windings fit into the coil former or not. Second one is whether the maximum flux density is lower than saturation flux density of the core or not.

As mentioned earlier, N_1 and N_2 values are needed to be modified just for practical purposes. In this work, rounding to the closest higher value is preferred. Besides, owing to the geometry of the coil former, quarter turn is realizable. As a result, Table 4-14 is obtained.

Table 4-14 Practical outputs with respect to core data

Practical Outputs with Respect to Core Data	
N_2 /Turn	18,25
N_1 /Turn	19,5
N_1/N_2	1,068
L_m' /uH	104,9
F_{tot} /ATurn	738
Φ_m /uWeb	232
B_{max} /T	0,37

For illustration purpose, photographs of the designed and implemented coupled-inductor are presented in Figure 4-14 and Figure 4-15.

Figure 4-14 Designed and implemented coupled-inductor, photograph 1

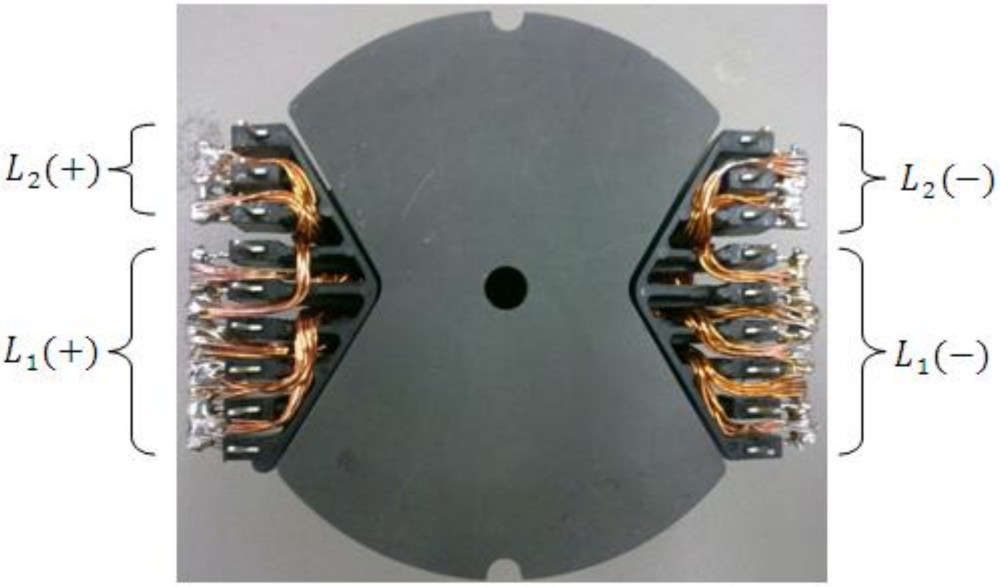

Figure 4-15 Designed and implemented coupled-inductor, photograph 2

After the coupled-inductor is implemented, some measurements are taken in order to determine magnetizing and leakage inductances. In order to ease the visualization, the equivalent coupled-inductor model is given in Figure 4-16.

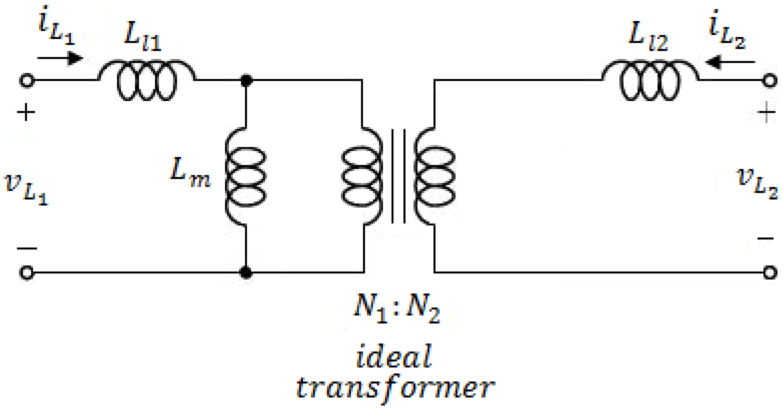

Figure 4-16 Equivalent coupled-inductor model

Similar to transformer, open circuit and short circuit test can be applied in order to find the model parameters of the coupled-inductor. They are given as;

$$L_1^{\mathrm{L_2\_open}} = L_{l1} + L_m = 126.3uH \tag{4-40}$$

$$L_1^{\mathrm{L_2\_short}} = L_{l1} + L_m // L_{l2}{}' \approx L_{l1} + L_{l2}{}' = 3uH \tag{4-41}$$

$$L_2^{\mathrm{L_1\_open}} = L_{l2} + L_m{}' = 111.5uH \tag{4-42}$$

$$L_2^{\mathrm{L_1\_short}} = L_{l2} + L_m{}' // L_{l1}{}' \approx L_{l2} + L_{l1}{}' = 2.8uH \tag{4-43}$$

(4-40)-(4-41) or (4-42)-(4-43) can used in order to determine the parameters: L_{l1}, L_{l2} and L_m. By the way, the following assumptions are utilized in order to find a solution set.

$$L_{l1}{}' \approx L_{l2} \qquad \text{and} \qquad L_{l2}{}' \approx L_{l1} \tag{4-44}$$

When the measurements belonging to the first winding side are used, the following parameters are found.

$$L_{l1} = 1.5uH \qquad L_{l2} = 1.3uH \qquad L_m = 124.8uH$$

As mentioned in CHAPTER 2, L_{12} must be equal to L_{22} in order to satisfy ripple-free input current waveform condition.

$$L_{12} = L_m \frac{N_2}{N_1} = 124.8uH \cdot \frac{18.25}{19.5} = 116.8uH$$

$$L_{22} = L_m' + L_{l2} = L_m \left(\frac{N_2}{N_1}\right)^2 + L_{l2} = 124.8 \left(\frac{18.25}{19.5}\right)^2 + 1.3 = 110.6uH$$

From the calculations above, it is seen that there is a difference between L_{12} and L_{22}. As mentioned at the beginning, this difference is expected. As a solution, an 'adjustment' inductor is used as an addition to the leakage inductance L_{l2}.

$$L_{l2}^{adj} = L_{12} - L_{22} = 116.8 - 110.6 = 6.2uH$$

Adding a discrete inductor with the value of 6.2uH in series with positive terminal of L_2 winding satisfies the condition, thereby providing ripple-free input current at all operating points. As a consequence, the following model and parameters are valid from now on.

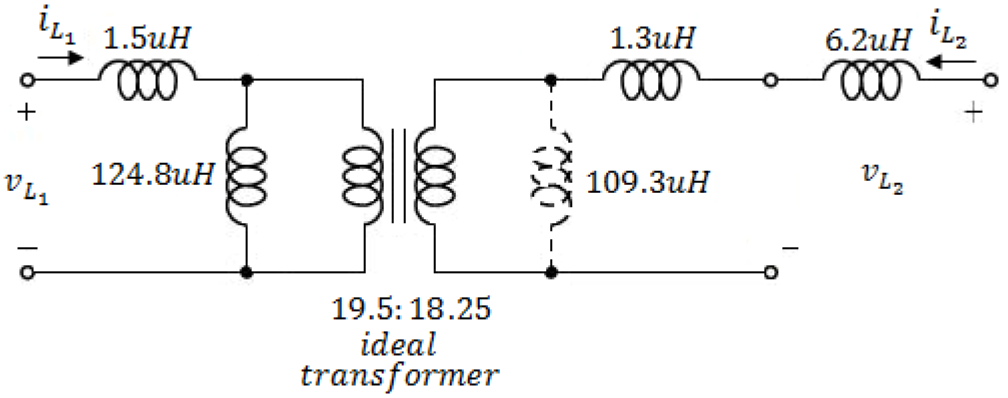

Figure 4-17 Adjusted coupled-inductor model and its parameters

Whether the adjustment inductor approach is correct or not will be checked by simulation. For this purpose $\mathbb{R}_m$, $\mathbb{R}_{l1}$ and $\mathbb{R}_{l2}$ values can be deduced in the following manner.

$$1.5uH = \frac{19.5^2}{\mathbb{R}_{l1}} \quad \rightarrow \quad \mathbb{R}_{l1} = 253.5 \cdot 10^6\ H^{-1}$$

$$1.3uH = \frac{18.25^2}{\mathbb{R}_{l1}} \quad \rightarrow \quad \mathbb{R}_{l2} = 256.2 \cdot 10^6\ H^{-1}$$

$$124.8uH = \frac{19.5^2}{\mathbb{R}_m} \quad \rightarrow \quad \mathbb{R}_m = 3046875\ H^{-1}$$

As an addition to the above values, the following values are used in the simulation.

$$N_1 = 19.5 \qquad N_2 = 18.25 \qquad L_{l2}^{adj} = 6.2uH$$

Simulation is performed with the ideal elements in order not to mix the reverse effect of parasitic elements with the possible failure of the approach. It is performed at $V_i = 10V$, $V_o = 24V$ and full load. Validity of the approach can be verified by the help of Figure 4-18 and Figure 4-19. As seen in Figure 4-18, the envelope of the input current is very narrow. When a closer look is taken at the input current in Figure 4-19, it is seen that the percent of the peak-to-peak current ripple is less than 0.2%. As a result, the approach is validated.

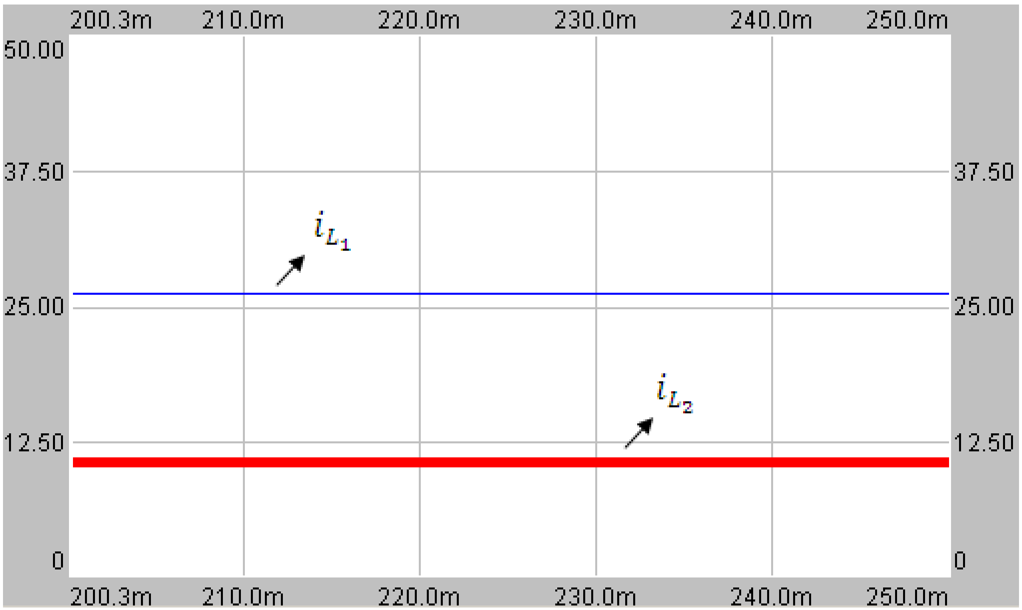

Figure 4-18 i_{L_1} and i_{L_2} waveforms when the adjustment inductor approach is applied

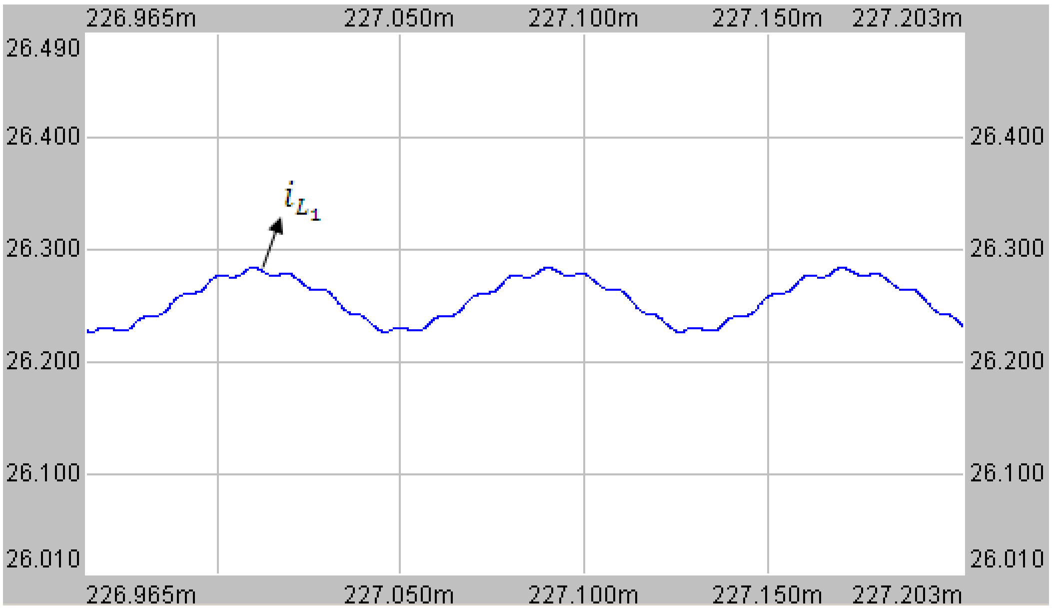

Figure 4-19 Detailed i_{L_1} waveform when the adjustment inductor approach is applied

At this step, inclusion of the parasitic resistances of the windings into the implemented coupled-inductor model is planned. They can be calculated by using the basic resistance formula.

$$R = \frac{\rho L}{A} \tag{4-45}$$

As used earlier, $\rho = 1.68 \cdot 10^{-8} \Omega m$ for copper. Cross section area of a single wire was calculated as 0.24mm^2 in the previous analyses. L is the mean length of a single wire. Mean length path is shown in Figure 4-20. It is assumed that all the wires pass through the mid-circle between the inner and output circles of the coil former.

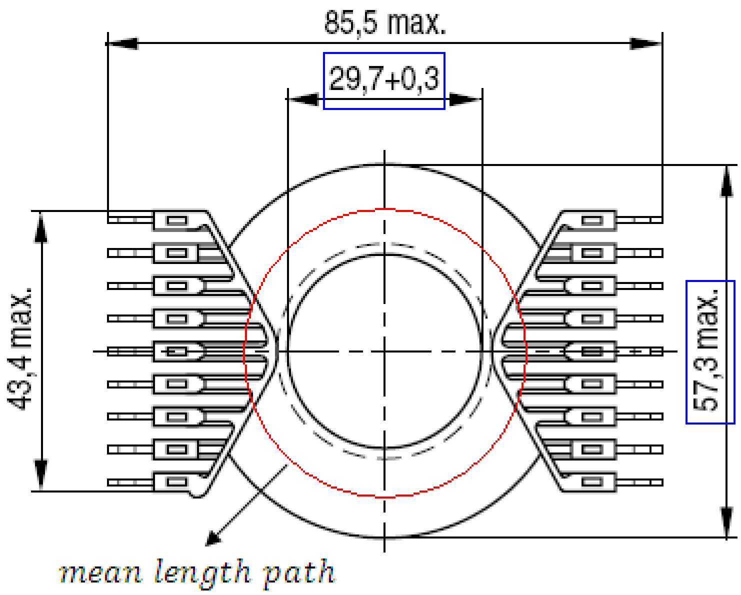

Figure 4-20 Mean length path of the coil former [31]

Diameter and perimeter of the circle are calculated as:

$$(57.3 + 29.7)/2 = 43.5mm$$

$$\pi \cdot 43.5 \approx 137mm = 0.137m$$

Firstly, let's calculate the parasitic resistance of L_1 winding. Resistance of a single wire is calculated easily.

$$R_{L_1}^{single} = \frac{(1.68 \cdot 10^{-8}) \cdot (0.137 \cdot 19.5)}{0.24 \cdot 10^{-6}} = 187\ m\Omega$$

As given in Table 4-11, there are 30 parallel wires.

$$R_{L_1} = \frac{187}{30} = 6.2\ m\Omega$$

Parasitic resistance of L_2 winding is calculated similarly.

$$R_{L_2}^{single} = \frac{(1.68 \cdot 10^{-8}) \cdot (0.137 \cdot 18.25)}{0.24 \cdot 10^{-6}} = 175\ m\Omega$$

As presented in Table 4-11, there exist 12 parallel wires in L_2 winding.

$$R_{L_2} = \frac{175}{12} = 14.6\ m\Omega$$

Parasitic resistance of the adjustment inductor should be considered as well. As mentioned earlier, 6.2uH is required. In order to obtain this inductance value, 3 of 2uH inductor is decided to use. Note that rather than 6.2uH, 6uH will be used due to the availability of the inductors. This much inconsistency may also stem from the measurement error of the coupled-inductor parameters or the parasitic elements easily. Therefore, trying to find exactly 6.2uH is regarded as a useless effort. Necessary data of the selected adjustment inductor is given as;

Company: Coilcraft	Part Number: SER2010-202MLB
Core Type: Ferrite	$L = 2uH\ (\mp 20\%)$
$I_{sat}(@10\%\ ind.drop) = 27A$	$I_{rms}(@20C^{o}\ temp.rise) = 27A$
$DC\ Resistance = 1m\Omega$	

Since 3 of it will be used in series, total resistance is 3mΩ.

$$R_{L_2}^{adj} = 3\ m\Omega$$

As a result, equivalent coupled-inductor model with parasitic resistances can be formed. It is seen in Figure 4-21.

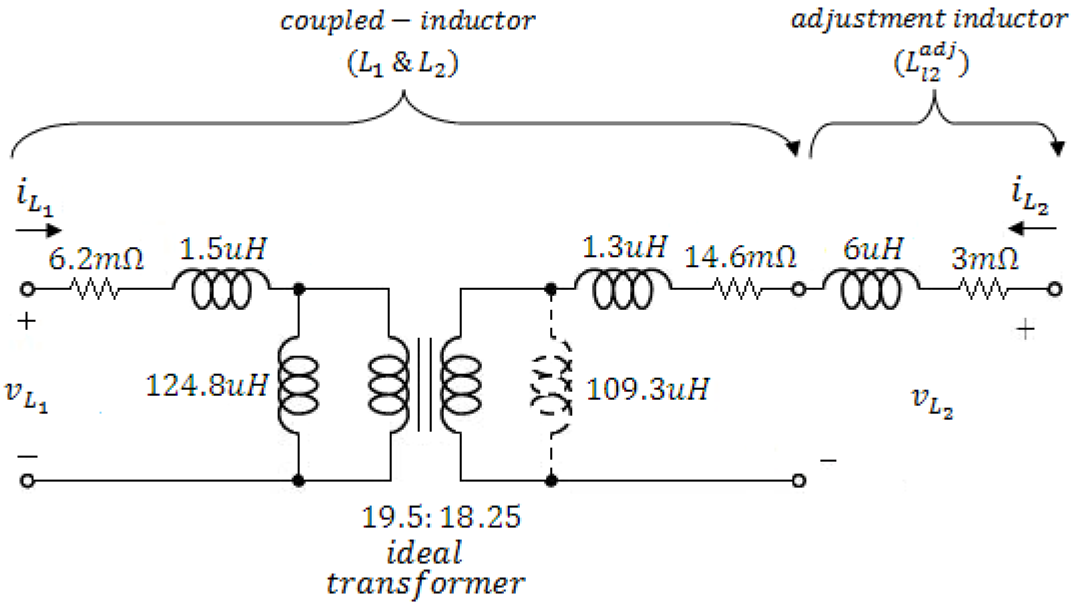

Figure 4-21 Adjusted coupled-inductor model and its parameters with parasitic resistances

Power dissipations of the inductors at each end operating point should be considered at this stage. In Table 4-15, required data is given.

Table 4-15 Power dissipation on the coupled-inductor and the adjustment inductor at end operating points

V_i /V	I_i /A	V_o /V	I_o /A	ΔI_{L_2} /V	$I_{L_2}^{rms}$ /A	P_{L_1} /W	P_{L_2} /W	$P_{L_2^{adj}}$ /W	P_L^{tot} /W
10	27,8	24	10,42	0,68	10,42	4,8	1,6	0,3	6,7
10	27,8	34	7,35	0,74	7,36	4,8	0,8	0,2	5,7
28	9,9	24	10,42	1,24	10,42	0,6	1,6	0,3	2,5
28	9,9	34	7,35	1,47	7,37	0,6	0,8	0,2	1,6

As it is known, power dissipation on a resistor depends on the RMS value of current passing through it. Hence, RMS values of i_{L_1} and i_{L_2} should be determined first. Since i_{L_1} is constant, its RMS value is the same with its mean value.

$$I_{L_1}^{rms} = I_i \tag{4-46}$$

As shown in Figure 4-8, i_{L_2} has a dc level and ac triangular waveform superimposed on dc level.

$$i_{L_2} = i_{L_2}(t) = I_o + \tilde{i}_{L_2}(t) \tag{4-47}$$

Its dc level is equal to I_o. Peak-to-peak magnitude of $\tilde{i}_{L_2}(t)$ is labeled as ΔI_{L_2}. ac triangular waveform is not necessarily equal i.e. duty-factor is generally different than 0.5. By using the RMS value definition in (4-3), $I_{L_2}^{rms}$ can be found in the following manner. Since its ripple percent is very low, $I_{L_2}^{rms}$ is expected to be very close to its mean value. Still, the analysis seems to be necessary as a check.

$$I_{L_2}^{rms} = \sqrt{\frac{1}{T_s}\int_0^{T_s}\left[i_{L_2}(t)\right]^2 dt} = \sqrt{\frac{1}{T_s}\int_0^{T_s}\left[I_o + \tilde{i}_{L_2}(t)\right]^2 dt} \tag{4-48}$$

$$I_{L_2}^{rms} = \sqrt{\frac{I_o^2}{T_s}\int_0^{T_s} dt + \frac{1}{T_s}\int_0^{T_s}\left[\tilde{i}_{L_2}(t)\right]^2 dt + \frac{2I_o}{T_s}\int_0^{T_s}\tilde{i}_{L_2}(t)dt} \tag{4-49}$$

Note that the integral of $\tilde{i}_{L_2}(t)$ is zero.

$$I_{L_2}^{rms} = \sqrt{I_o^2 + \frac{1}{T_s}\int_0^{T_s}\left[\tilde{i}_{L_2}(t)\right]^2 dt} \tag{4-50}$$

By using (4-29), the following data can be inferred.

$$\frac{1}{T_s}\int_0^{T_s}\left[\tilde{i}_{L_2}(t)\right]^2 dt = \left(\frac{\Delta I_{L_2}}{2\sqrt{3}}\right)^2 = \frac{\Delta I_{L_2}^2}{12} \tag{4-51}$$

As a consequence, $I_{L_2}^{rms}$ can be expressed in the simplest form as;

$$I_{L_2}^{rms} = \sqrt{I_o^2 + \frac{\Delta I_{L_2}^2}{12}} \tag{4-52}$$

As seen in Table 4-15, $I_{L_2}^{rms}$ turns out to be closer to I_o as expected.

Once the RMS values of currents are obtained, power dissipations on the inductors can be calculated. As observed in Table 4-15, most of the power is dissipated on L_1 inductor when the input current is high. Besides, the power dissipation on the adjustment inductor is very low.

At this point, simulation seems to be necessary at least at one end operating point, because

- Practical inductances turn out to be a little different than the targeted inductances as expected. The effect of this change is desired to know.
- Real values of parasitic resistances of the circuit elements are determined and included into the circuit schematic. Its effect is desired to know.
- Rather than the necessary 6.2uH, 6uH is used as an adjustment inductor. Its influence is another question mark.
- Flux density in the core is never verified by simulation. It is desired to be checked.

For this purpose, the end operating at which the current and hence flux densities are at their maximum is chosen. At this operating point; $V_i = 10V$, $V_o = 24V$ and $P_o \approx 250W$.

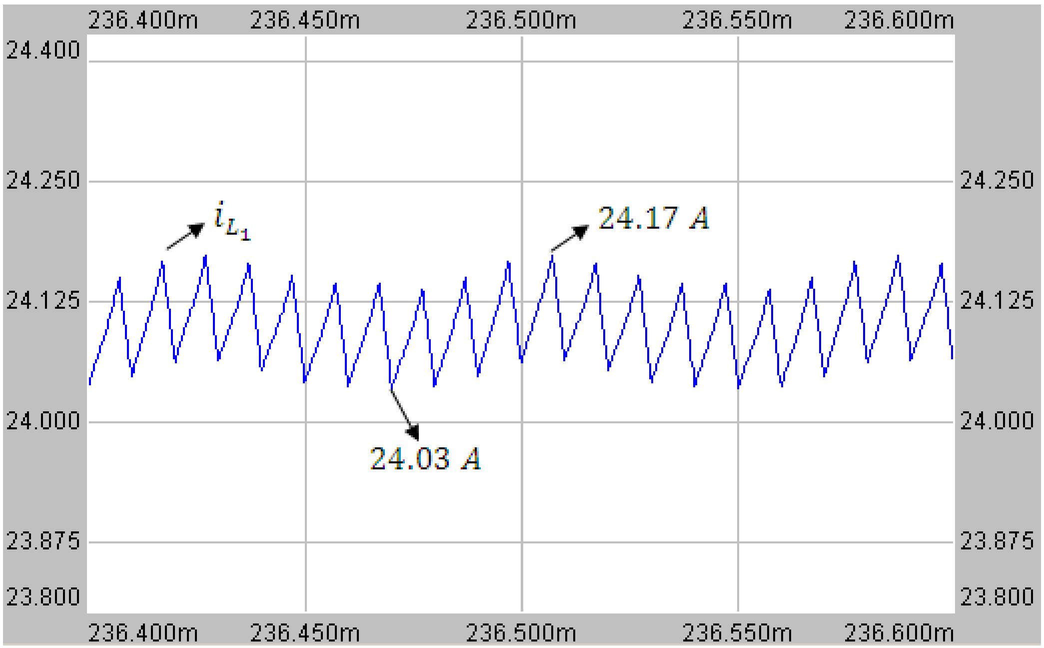

Figure 4-22 Detailed i_{L_1} waveform at final configuration

In Figure 4-22, the current ripple of i_{L_1} together with oscillation is observed. Its peak-to-peak ripple percent is 0.58%. This value is 0.49% in parasitic element case in Figure 2-21. This very small difference can be explained by the difference between 6.2uH and 6uH in adjustment inductance value.

In Figure 4-23, the current ripple of i_{L_2} together with very small oscillation is observed. Its peak-to-peak ripple percent is about 4.9%. This value is 4.1% in parasitic element case in Figure 2-22. This result is also consistent with the previous one.

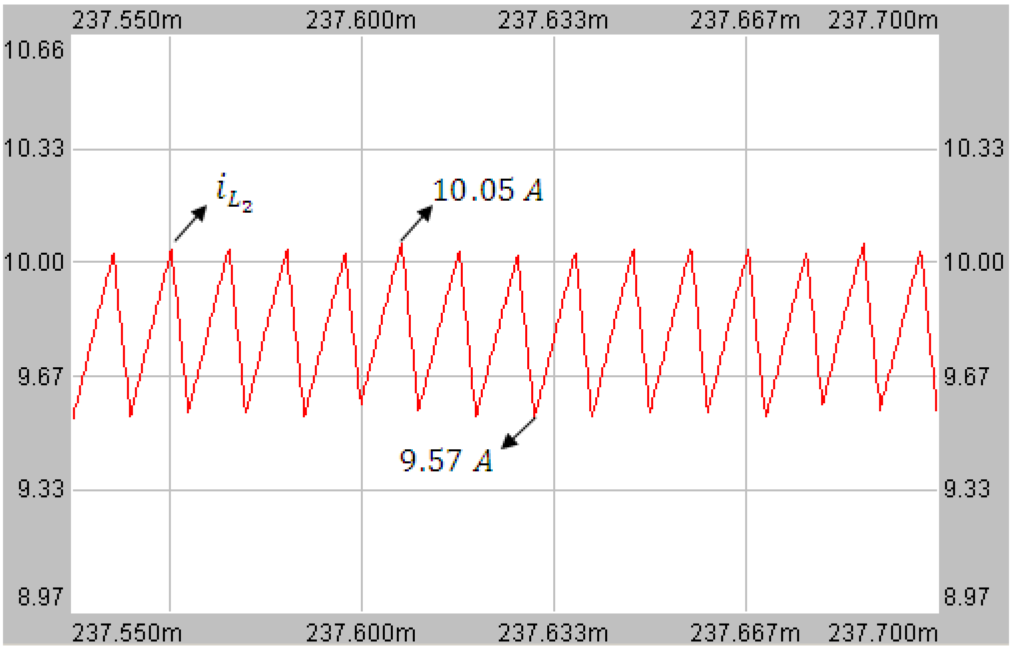

Figure 4-23 Detailed i_{L_2} waveform at final configuration

In Figure 4-24, mutual flux (Φ_m) is observed. Its maximum determines the maximum flux density in the core. Its peak is 214.6uWeb. This value is calculated as 232uWeb in Table 4-14, which is close enough to the simulation result. Besides, it is known from Table 4-12 that cross section area of core is 630mm^2. Hence, the maximum flux density in the core is calculated as:

$$214.6uWeb/630mm^2 = 0.34T$$

The maximum flux density is also close enough to the calculated value (0.37T) in Table 4-14. Another issue is the flux swing. Peak-to-peak flux swing percent is about 1.6%. Since it is very low, core losses are not calculated and neglected in this work.

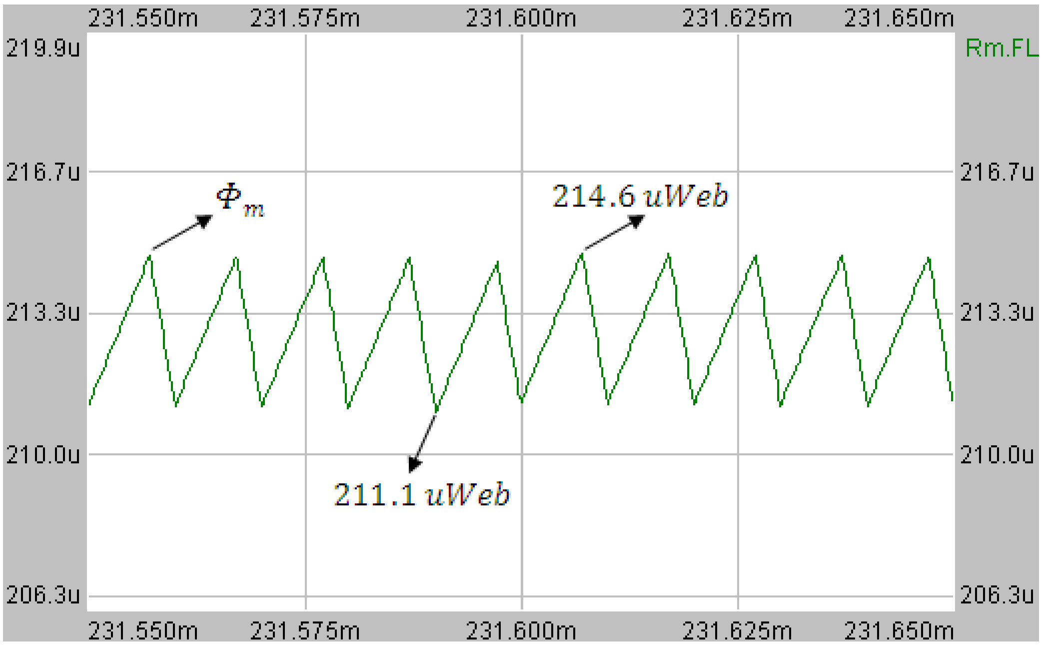

Figure 4-24 Mutual flux (Φ_m) waveform at final configuration and at the fourth end operating point

Finally, an experimental test is performed on the designed coupled-inductor. The test is implemented based on the physical interpretation given in CHAPTER 2. In this test, a sinusoidal voltage waveform at 100 kHz is applied to L_2 'side'. Voltage is applied not only to L_2. Rather, it is applied to the combination of L_2 and the adjustment inductor. For simplicity, this voltage will be labeled by $v_{L_2}^{comb}$ from now on. L_1 is left open. Voltage measurements are taken from L_1 as v_{L_1} and L_2 plus adjustment inductor combination as $v_{L_2}^{comb}$. Four different measurements are taken. In the first measurement, no adjustment inductor is used and voltage is directly applied to L_2. In the second measurement, 2uH adjustment inductor is used and voltage is applied to L_2 winding plus 2uH adjustment inductor combination. Similarly, 4uH and 6uH adjustment inductors are added to L_2 in third and fourth measurements respectively. Result of the test can be seen in Table 4-16. Moreover, screenshot of v_{L_1} and $v_{L_2}^{comb}$ voltage waveforms on the oscilloscope screen at the fourth measurement is given in Figure 4-25.

Table 4-16 Experimental test result of the implemented coupled-inductor

Adjustment Inductance /uH	*Applied Voltage on L_2 Side /V*	*Measured Voltage on L_1 Winding /V*	*Voltage Ratio*
0	9,36	10,20	1,09
2	9,28	9,84	1,06
4	9,44	9,68	1,03
6	9,36	9,36	1,00

As the adjustment inductance value comes close to 6.2uH, the induced voltage on L_1 approximates to $v_{L_2}^{comb}$. For example, when 6uH is added in series with L_2, the same voltage (9.36V) with $v_{L_2}^{comb}$ is seen on the magnetizing inductance L_m. If the same voltage is applied to L_1 in this situation, the voltage on L_{l1} will turns out

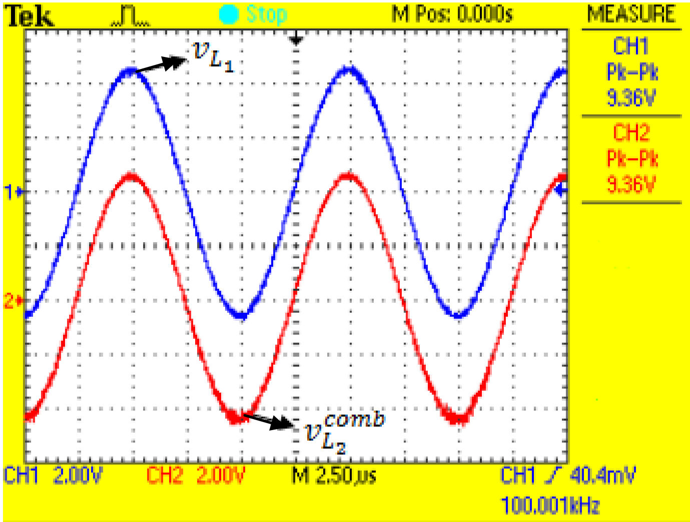

Figure 4-25 Experimental waveforms of v_{L_1} and $v_{L_2}^{comb}$ with 6uH adjustment inductor

to be zero. It means that i_{L_1} remains the same and ripple-free input current requirement is satisfied.

CHAPTER 5

CONTROLLER DESIGN

5.1 INTRODUCTION

The design of the controller for the implemented circuit will be given in this chapter. For this purpose, the transfer functions obtained in CHAPTER 3 using state-space averaging method will be utilized.

There are no well-defined criteria set at the beginning for the controller. As mentioned earlier, the converter will be used in parallel with li-ion battery pack, which has a voltage changing between 24V-33.6V. There is also a switching voltage regulator at the front end of the system, namely the military equipment. For this reason, there is not any strict voltage regulation requirement. The input voltage range of the system is 16V-55V. Probably, input current waveform requirement is more restrictive. Circuit breaker or fuse at the cigarette lighter adapter of a vehicle should not be activated, especially at the transient instants. Although the restrictions are relatively looser and not well-defined, the controller performance is tried to keep as high as possible.

At the very beginning, selection of the control technique in terms of analog or digital is considered. Speed of analog control is compared with modifiability of digital control. Element of analog control is the hardware composed of operational amplifier, capacitors and resistor. Since what type of a controller would be used was not known at the beginning, many analog controller hardware infrastructures would be reserved on printed circuit board. However, digital controller element is just software in a microcontroller, which is very easy to modify. In order to utilize this advantage of digital control, it must be verified that the speed of digital control is enough for this application. Then, the maximum speed of the microcontrollers in the market has been searched. Microchip's digital signal controller family specialized for switched-mode power supply applications is considered to be very reasonable for this purpose. At first sight, it seemed to be possible to close the control loop at each PWM cycle, 10 usec here. When the comparison of PWM carrier signal with the duty-factor reference signal in analog control is considered, the control loop frequency is equal to PWM frequency there. That is, the speed of a digital control may reach that of analog control. Hence, the speed disadvantage of digital control is considered to be overcome by using a Microchip's digital signal controller specialized for SMPS applications. As a result, digital control has been preferred. Among that controller family, dsPIC30F2020 was chosen because of its minimum number of peripherals. Three analog input channels (analog-to-digital conversion of output voltage, input current and input voltage), one PWM output and one general purpose input channel (mode selection between constant input current mode -CICM- and constant input power mode -CIPM-) is required in this application. Despite its minimum number of peripherals in that family, dsPIC30F2020 highly covers the need of this application.

Which control method, voltage mode control or current mode control, would be used was also be evaluated. Since the input current is required to control in both modes, namely CICM and CIPM, while limiting the output voltage to a set value of 34V, it is inevitable to use current mode control. In this method, input inductor current, i_{L_1}(or i_i) and output capacitor voltage, v_{C_o} (or v_o) are controlled in a cascaded manner. Since the input current can change faster than the output voltage, it is placed the inner loop. Output voltage loop is the outer control loop and gives a reference value for the input current according to the output voltage. Although current mode control is adopted in a reasonable manner, voltage mode control has also been examined. Before a more complicated current mode control, simpler voltage mode control has been desired to implement as an intermediate step. Voltage mode control simulations performed in Simplorer with many different controller parameters did not give a stable output voltage. There existed a small amplitude oscillation around the reference value. Oscillation frequency was the same with the frequency of the nearest pole of the duty-factor-to-output voltage transfer function, $G^{p}_{v_o/k}(s)$ to the origin in s-domain. Then, voltage mode control was applied on the implemented circuit experimentally and the same oscillation was observed. In that situation, a large oscillation in the input current was realized. With this high amplitude oscillation in input current, output voltage oscillation seemed to be inevitable. Since the ultimate aim is current mode control, further elaboration in voltage mode control was not performed and directly jumped to current mode control. Since current mode control has been performed easily and consistent with the calculations, voltage mode control of this circuit has then been evaluated as not easily applicable.

In the inner and outer control loops, PI controller is preferred. It is known that integral term lets the steady-state error be zero, which is a desired goal. Besides, in most of the industrial applications, PI controller is seen satisfactory. Therefore, PI controller is implemented as a first choice and gives a satisfactory result. Hence, other controller types are not tried.

Up to this point, the controller scheme is drawn roughly and it will be detailed in the following sections. According to the control block diagram and the related transfer functions found earlier, necessary controller functions will be obtained in s-domain. Then, using a bilinear transformation, controller functions will be converted into their z-domain correspondence. By inverse z-transformation, controller functions in discrete time domain will be obtained. Then, those functions will be embedded to dsPIC.

5.2 CONTROL BLOCK DIAGRAM

Based on the discussions above, the control block diagram of the circuit can be formed in the following manner.

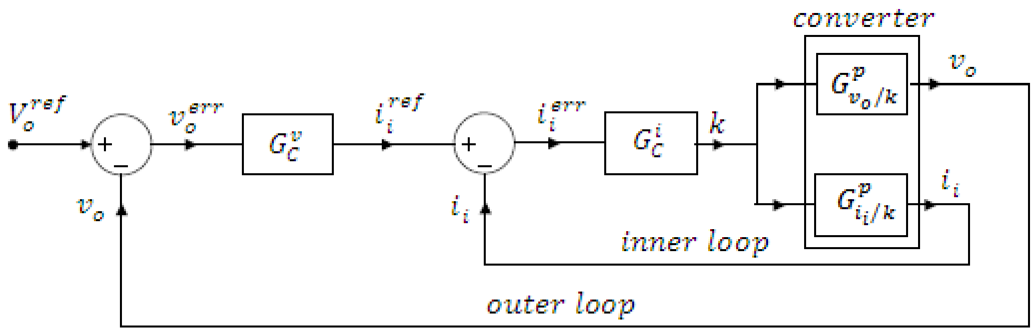

Figure 5-1 Control block diagram of the circuit

The difference between the reference output voltage, V_o^{ref} and the output voltage at that instant, v_o gives an output voltage error. This error is processed by voltage controller, G_C^v and produces an instantaneous input current reference, i_i^{ref}. Similarly, the difference between i_i^{ref} and the input current at that instant, i_i gives an input current error, i_i^{err}. Then, this error is processed by current controller, G_C^i and produces a duty-factor, k. This duty-factor is applied to the converter and the converter produces i_i and v_o according to input current-to-duty-factor transfer function, $G^p_{i_i/k}$ and output voltage-to-duty-factor transfer function, $G^p_{v_o/k}$. Afterwards, v_o and i_i are taken as feedbacks and this control cycle is repeated continuously. Note that the faster variable, i_i is placed into the inner loop. Although there are two cascaded loops, there is only one manipulated variable, namely duty-factor.

The control block diagram seen in Figure 5-1 may be regarded as more understandable than that in Figure 5-2. However, they are equal mathematically. Figure 5-2 is given because it is what is expected first when cascaded control is thought of. Hence, the succeeding discussions will continue on this figure rather than the previous one. In order to show the equivalency among the control block diagrams, (5-1) and (5-2) are given. Actually, only the relationship between duty-factor and output voltage is required to show.

$$G^p_{v_o/i_i}(s) = \frac{v_o(s)}{i_i(s)} = \frac{v_o(s)/k(s)}{i_i(s)/k(s)} = \frac{G^p_{v_o/k}(s)}{G^p_{i_i/k}(s)} \tag{5-1}$$

$$v_o(s) = i_i(s)G^p_{v_o/i_i}(s) = kG^p_{i_i/k}(s)\frac{G^p_{v_o/k}(s)}{G^p_{i_i/k}(s)} = kG^p_{v_o/k}(s) \tag{5-2}$$

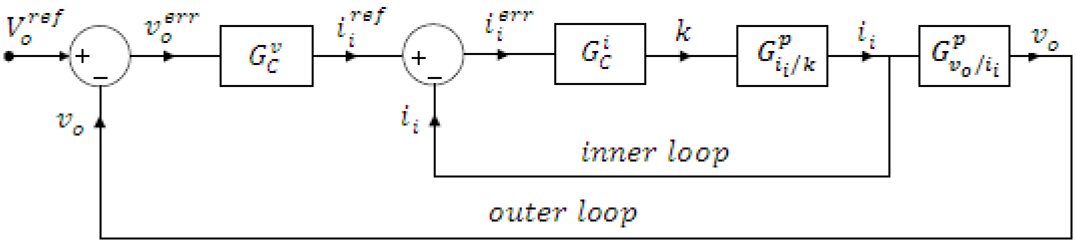

Figure 5-2 Mathematically equivalent control block diagram of the circuit

At this point, transfer functions of the control system, namely $G^p_{i_i/k}(s)$ and $G^p_{v_o/i_i}(s)$ are known. Hence, the controller transfer functions can be determined.

5.3 CONTROLLER DESIGN

There exist two control loops in the implemented circuit: current control loop and voltage control loop. From which loop must be started to design first? As it may be guessed, inner control loop is somehow independent of the outer control loop. The outer one only gives a reference value to the inner one. When the closed loop transfer function of the inner loop is written in the next section, it is seen that it does not include $G^p_{v_o/i_i}(s)$ or $G_C^v(s)$ terms. However, when the closed loop transfer function of the outer loop is written, it includes $G^p_{i_i/k}(s)$ or $G_C^i(s)$ terms. Therefore, $G_C^i(s)$ will be determined first and then $G_C^v(s)$ will be determined by considering $G_C^i(s)$ and the other transfer functions.

5.3.1 Controller Design of the Current Loop

Control block diagram of the inner loop, or current loop, is given solely in Figure 5-3.

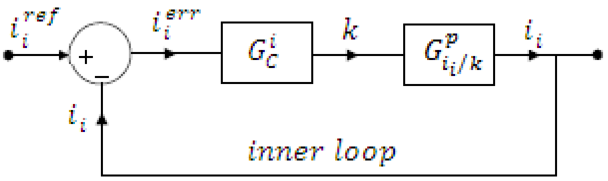

Figure 5-3 Control block diagram of the current loop

The closed loop transfer function of the current loop, $G_{CL}^i(s)$ can be written in the following manner.

$$i_i(s) = i_i^{err}(s)G_C^i(s)G_{i_i/k}^p(s) \tag{5-3}$$

$$i_i^{err}(s) = i_i^{ref}(s) - i_i(s) \tag{5-4}$$

$$G_{CL}^i(s) = \frac{i_i(s)}{i_i^{ref}(s)} = \frac{G_{i_i/k}^p(s)G_C^i(s)}{1+G_{i_i/k}^p(s)G_C^i(s)} \tag{5-5}$$

Denominator of a closed loop transfer function is defined as the characteristic equation. Characteristic equation of the closed loop transfer function of the current loop is labelled as $Q_i(s)$.

$$Q_i(s) = 1 + G_{i_i/k}^p(s)G_C^i(s) \tag{5-6}$$

By definition, characteristic equation is the summation of 1 (or more accurately $1\angle 0°$) and open loop transfer function. Therefore, open loop transfer function of the current loop, $G_{OL}^i(s)$ can be obtained in the following manner.

$$G_{OL}^i(s) = G_{i_i/k}^p(s)G_C^i(s) \tag{5-7}$$

At this point, $G_{i_i/k}^{p}(s)$ must be known in order design a current compensator, $G_C^i(s)$. $G_{i_i/k}^{p}(s)$, or the other transfer functions derived before, has the following terms parametrically: $N_1, N_2, \mathbb{R}_m, \mathbb{R}_{l1}, \mathbb{R}_{l2}, R_{L_1}, R_{L_2}, C_1, C_o, R_{C_1}, R_{C_o}, R_{DS}, R_D, K, V_{C_1}, V_{C_o}, I_{L_1}$ and I_{L_2}. Note that other than the circuit parameters, also operating point parameters take place in the transfer functions. In other words, the converter's transfer function changes as the operating point changes. As expected, transfer functions at different operating points are calculated and it is seen that there are only minor differences between the pole and zero locations of the transfer functions. Therefore, an operating point can be chosen and the transfer functions can be calculated at that point. Here, the first end operating point ($V_i = 10V, V_o = 24V$ and at full load) is chosen randomly. As a result; $G_{i_i/k}^{p}(s)$ is calculated in Matlab using the derived parametric transfer function in CHAPTER 3, the implemented circuit parameters and the numerical values of the operating point parameters.

$$G_{i_i/k}^{p}(s) = \frac{6.283 \cdot 10^4 \cdot s^3 + 4.381 \cdot 10^9 \cdot s^2 + 1.354 \cdot 10^{15} \cdot s + 1.375 \cdot 10^{17}}{s^4 + 1.236 \cdot 10^4 \cdot s^3 + 4.988 \cdot 10^9 \cdot s^2 + 5.861 \cdot 10^{11} \cdot s + 1.024 \cdot 10^{15}} \tag{5-8}$$

In order to get acquainted with $G_{i_i/k}^{p}(s)$, its pole-zero map in s-domain is given in Figure 5-4. Blue circles represent zeros and blue x's are used for poles. At the left figure, all poles and zeros of the related transfer function is shown but not seen

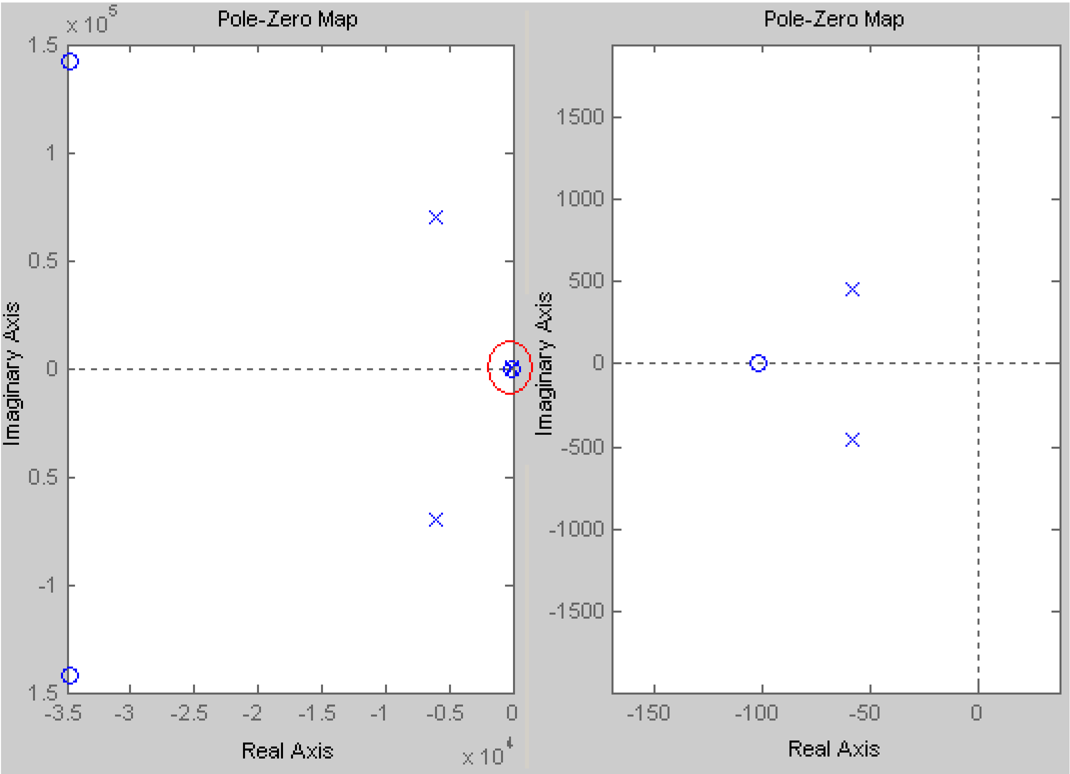

Figure 5-4 Pole-zero map of $G_{i_i/k}^{p}(s)$

easily. Hence, zoomed-in snapshot of the red circle is given at the right figure. As it is seen clearly, $G_{i_i/k}^{p}(s)$ has four poles and three zeros. Since all poles have negative real parts, $G_{i_i/k}^{p}(s)$ can be regarded as open loop stable. Moreover, all zeros have a negative real part, which makes $G_{i_i/k}^{p}(s)$ a minimum phase system. Minimum phase systems are known to be easy to control with respect to non-minimum phase systems, which have at least one zero at the right half plane. Besides, bode plot approach holds for minimum phase systems and is not necessarily valid for non-minimum phase systems. Since it is checked that $G_{i_i/k}^{p}(s)$ is a minimum phase system, bode plot approach can be applicable. In this approach, the aim is to get positive and proper phase and gain margins in the bode plot of $G_{OL}^{i}(s)$. Since $G_{i_i/k}^{p}(s)$ is constant, this will be provided by a proper $G_{C}^{i}(s)$.

As a starting point, the bode plot of $G_{i_i/k}^{p}(s)$ is given in Figure 5-5.

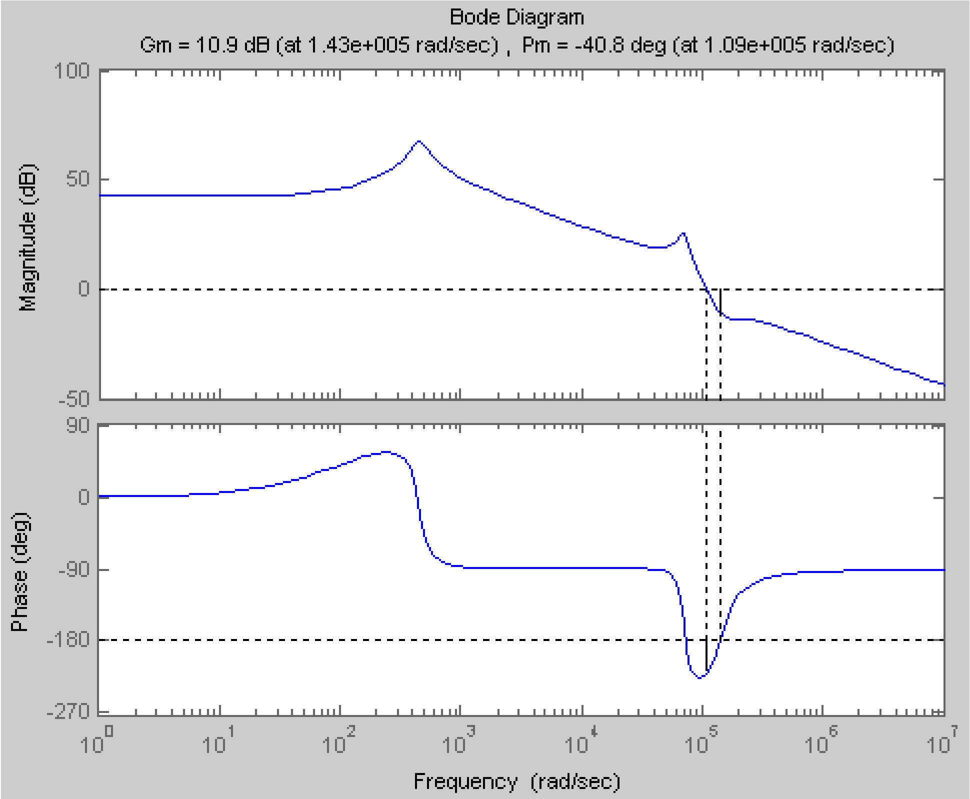

Figure 5-5 Bode plot of $G^{p}_{i_i/k}(s)$

This plot will be corrected to a desired shape by the help of $G_C^i(s)$. As mentioned earlier, PI controller is proposed as a controller. Its transfer function can be written in the following manner.

$$G_C^i(s) = K_p^i + \frac{K_i^i}{s} = K_p^i\left(\frac{s+K_i^i/K_p^i}{s}\right) \tag{5-9}$$

where K_p^i is the proportional gain of $G_C^i(s)$ and K_i^i integral gain. Superscript "i" stands for the current controller. As seen, $G_C^i(s)$ has a pole at the origin, a zero at $-K_i^i/K_p^i$ and a gain of K_p^i. Since the pole location is obvious, let it be added to $G_{OL}^i(s)$. In this way, determination of zero and gain will be easier. As it can be predicted from Figure 5-6, adding a zero about 1000rad/sec may make the phase plot move upward after 1000rad/sec. This is required because phase is very close to -180° between $10^3 - 10^5$rad/sec.

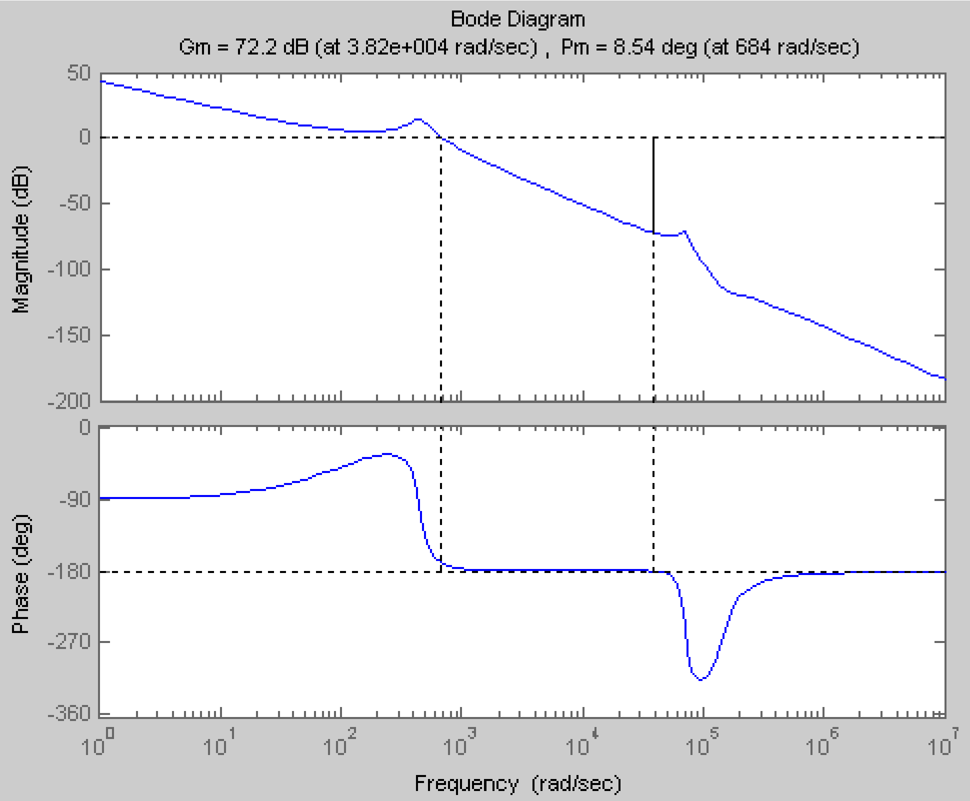

Figure 5-6 Bode plot of $G^{p}_{i_i/k}(s)/s$

By adding a real zero at -1000 in s-plane, the following bode plot is obtained. This zero placement brings the following restriction to $G_C^i(s)$;

$$-\frac{K_i^i}{K_p^i} = -1000 \tag{5-10}$$

Note that the phase is almost always greater than -180° expect a frequency band about 10^5 rad/sec in Figure 5-7. At this step, only the gain variable is left to adjust the phase and gain margins. Figure 5-7 is actually drawn such that $K_p^i = 1$. Should K_p^i be increased or decreased? If it is increased, magnitude plot moves upward. In that situation, the magnitude plot will cross 0dB at a higher frequency and phase margin will be positive. However, as the magnitude plot moves upward, gain margin decreases. In order to have a positive phase margin, gain margin decreases below zero. Hence, increasing the gain is not good idea. What if the gain is decreased?

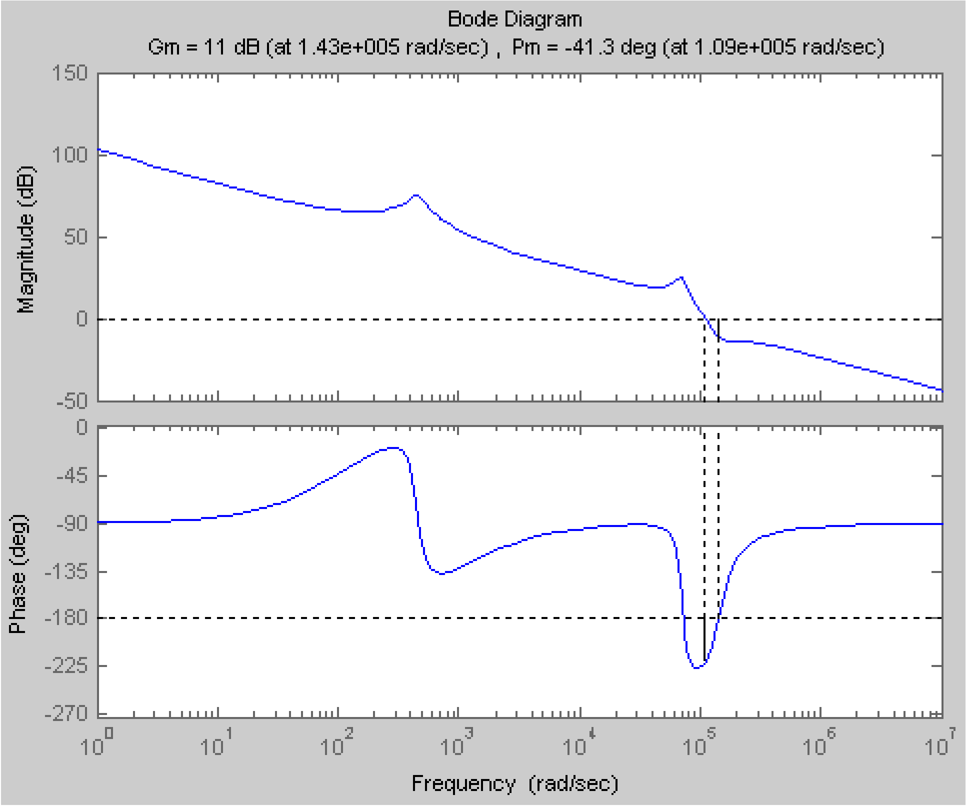

Figure 5-7 Bode plot of $G^{p}_{i_i/k}(s)\cdot(s+1000)/s$

When it is decreased, magnitude plot moves downward. The magnitude plot will cross 0dB at a lower frequency and phase margin will be positive. At the same time, gain margin increases as well. As a result, gain must be decreased.

Using the "sisotool" function of Matlab, this gain iteration can be performed in an online manner. At the gain of 0.0035, reasonable gain and phase margins are obtained. It is seen in Figure 5-8. Theoretically, positive phase and gain margins are sufficient in order to have a stable loop. In practical, it is generally accepted that the phase margin must be larger than 45° because of the practical reasons. It is recommended that it should be between 45°-60°. Actually, this phase margin defines a critically damped step response. While larger phase margin results in an overdamped response, smaller phase margin leads to an underdamped response. That is, increasing phase margin much makes the converter slower. Decreasing phase margin much risks the stability of the converter. Hence, as seen in Figure 5-8, phase

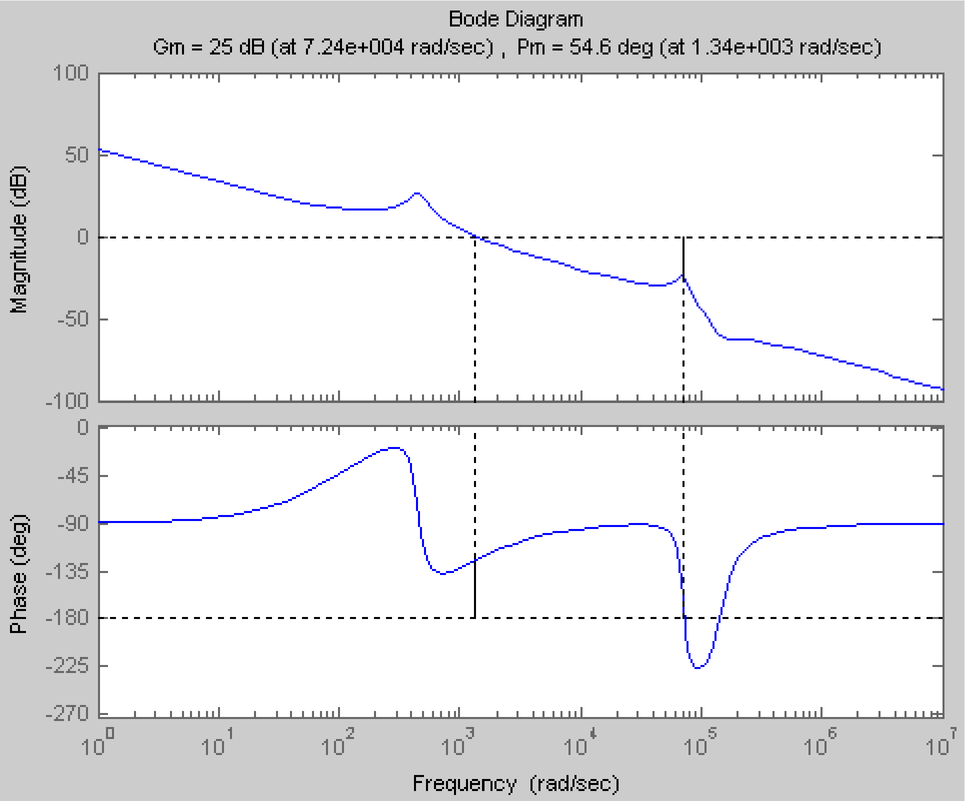

Figure 5-8 Bode plot of open loop transfer function, $G_{OL}^{i}(s)$

margin of 54.6° is obtained. There is no strict requirement on gain margin except its sign. 6-12 dB gain margin is recommended. Gain margin of 25dB is left as it is. Gain of 0.0035 brings another restriction to the controller transfer function.

$$K_p^i = 0.0035 \tag{5-11}$$

Using (5-10), integral gain can be calculated as:

$$K_i^i = 3.5 \tag{5-12}$$

As a result, transfer function of the current controller is determined in s-domain.

$$G_C^i(s) = K_p^i + \frac{K_i^i}{s} = 0.0035 + \frac{3.5}{s} \tag{5-13}$$

It will be converted to its z-domain and discrete time domain equivalents in the succeeding sections. Before it, transfer function of the voltage controller will be determined.

Finally, bode plot of the closed loop transfer function is given in Figure 5-9 as an information about frequency response of the current loop.

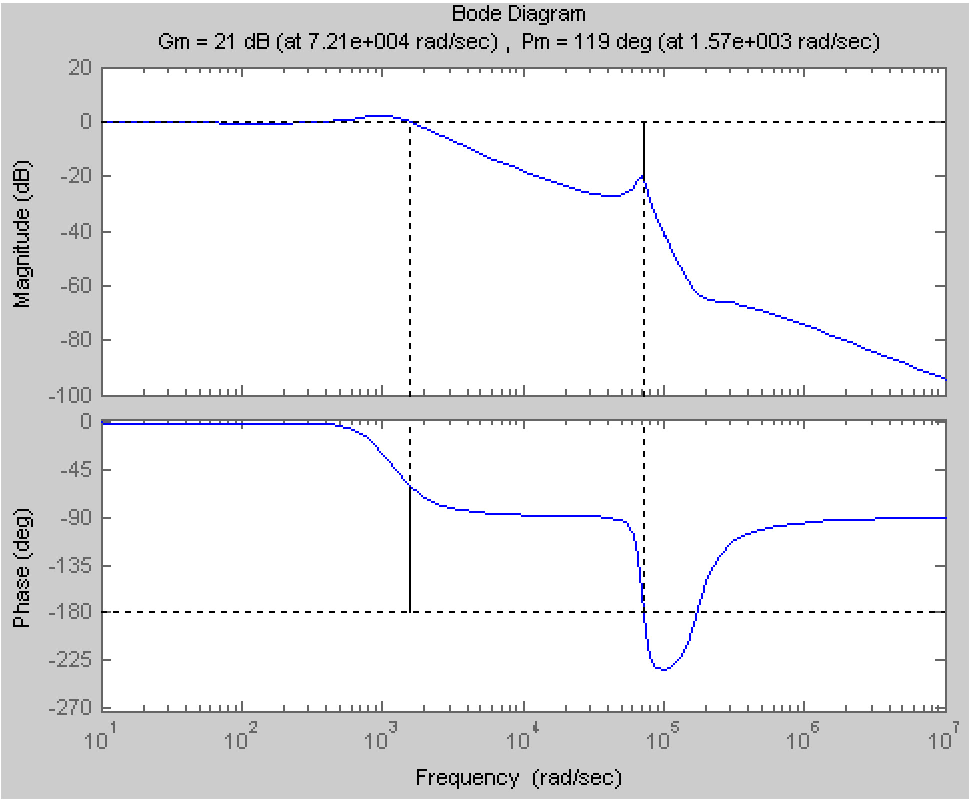

Figure 5-9 Bode plot of $G_{CL}^{i}(s)$

5.3.2 Controller Design of the Voltage Loop

Simplified version of control block diagram of the outer loop, or voltage loop, is shown in Figure 5-3. Note that the current loop seen in Figure 5-2 is replaced with its closed loop equivalent.

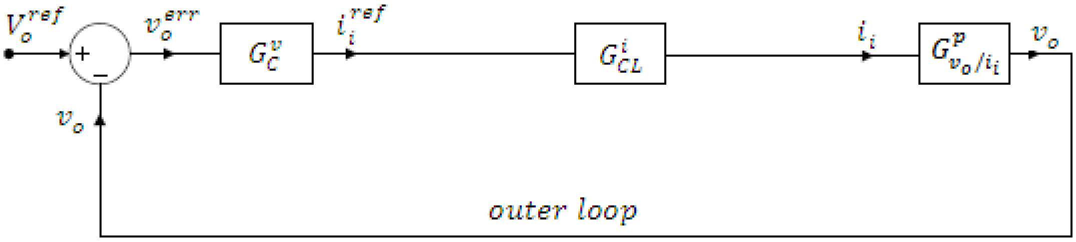

Figure 5-10 Control block diagram of the voltage loop

The closed loop transfer function of the voltage loop, $G_{CL}^v(s)$ can be written in the following manner.

$$v_o(s) = v_o^{err}(s)G_C^v(s)G_{CL}^i(s)G_{v_o/i_i}^p(s) \tag{5-14}$$

$$v_o^{err}(s) = V_o^{ref}(s) - v_o(s) \tag{5-15}$$

$$G_{CL}^v(s) = \frac{v_o(s)}{V_o^{ref}(s)} = \frac{G_C^v(s)G_{CL}^i(s)G_{v_o/i_i}^p(s)}{1+G_C^v(s)G_{CL}^i(s)G_{v_o/i_i}^p(s)} \tag{5-16}$$

By using $G_{CL}^i(s)$ definition in (5-5) and $G_{v_o/i_i}^p(s)$ definition in (5-1), more simplified version of $G_{CL}^v(s)$ can be obtained. It can be observed in (5-17). Note that $G_{CL}^v(s)$ includes all the transfer functions that exist in the cascaded loop.

$$G_{CL}^v(s) = \frac{G_C^v(s)G_C^i(s)G_{v_o/k}^p(s)}{1+G_C^i(s)G_{i_i/k}^p(s)+G_C^v(s)G_C^i(s)G_{v_o/k}^p(s)} \tag{5-17}$$

As performed in the current loop, characteristic equation of the closed loop transfer function of the voltage loop, $Q_v(s)$ can be written similarly.

$$Q_v(s) = 1 + G_C^i(s)G_{i_i/k}^p(s) + G_C^v(s)G_C^i(s)G_{v_o/k}^p(s) \tag{5-18}$$

Then, open loop transfer function of the voltage loop, $G_{OL}^v(s)$ can be obtained in the following manner.

$$G_{OL}^v(s) = G_C^i(s)G_{i_i/k}^p(s) + G_C^v(s)G_C^i(s)G_{v_o/k}^p(s) \tag{5-19}$$

As it is seen clearly, $G^{v}_{OL}(s)$ is not composed of the multiplication of some transfer function with the controller transfer function of that loop, $G^{v}_{C}(s)$ here. Therefore, it is not possible to follow the procedure applied for the design of the current controller. Instead of that approach, different zero and gain values will be tried until a proper phase and gain margins are obtained in Matlab. While doing it, minimum phase property of $G^{v}_{OL}(s)$ must be checked at each trial. There exists a risk here because $G^{p}_{v_o/k}(s)$ already has a right half-plane zero pair. Its pole-zero map is shown in Figure 5-11. At the left figure, all poles and zeros of the related transfer function is shown but not seen easily. Hence, zoomed-in snapshot of the red circle is given at the right figure. Note that $G^{p}_{v_o/k}(s)$ has a zero pair with positive real part. Hence, just satisfying positive phase and gain margins does not mean that the closed loop system is stable. For bode plot approach to be valid, it must be verified that open loop transfer function has minimum phase property. Meanwhile, the reason why voltage mode control could not be achieved easily is probably the non-minimum phase property of the sole converter transfer function, $G^{p}_{v_o/k}(s)$.

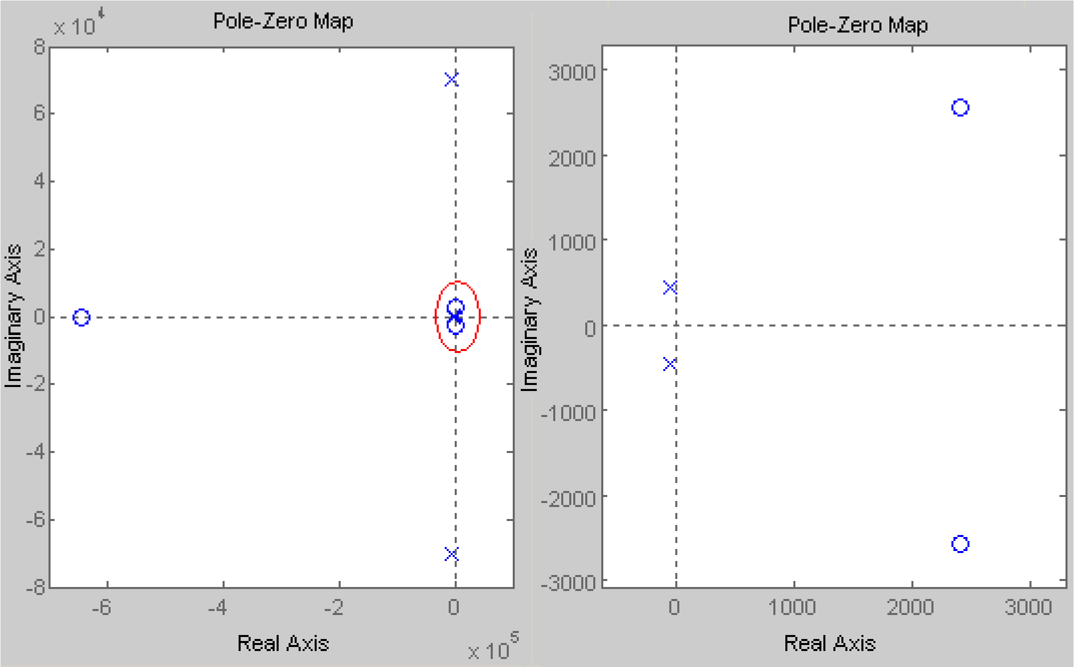

Figure 5-11 Pole-zero map of $G^{p}_{v_o/k}(s)$

As mentioned earlier, again PI controller is proposed as a controller. Its transfer function can be written in the following manner.

$$G_C^v(s) = K_p^v + \frac{K_i^v}{s} = K_p^v\left(\frac{s+K_i^v/K_p^v}{s}\right) \qquad (5\text{-}20)$$

where K_p^v is the proportional gain of $G_C^v(s)$ and K_i^v integral gain. Superscript "v" stands for the voltage controller. Now, the aim is to find a voltage controller transfer function that gives proper phase and gain margins. After several zero and gain trial in Matlab, the following values is determined.

$$-\frac{K_i^v}{K_p^v} = -1000 \qquad (5\text{-}21)$$

$$K_p^v = 1.6 \qquad (5\text{-}22)$$

Therefore, K_i^v is calculated as:

$$K_i^v = 1600 \qquad (5\text{-}23)$$

As a result, transfer function of the voltage controller turn out to be:

$$G_C^v(s) = K_p^v + \frac{K_i^v}{s} = 1.6 + \frac{1600}{s} \qquad (5\text{-}24)$$

Now, minimum phase property must be checked in order to rely on bode plot. Pole-zero map of $G_{OL}^v(s)$ is given in Figure 5-12. The same arguments about reading the pole-zero maps also hold here. Besides, as it can be guessed, some poles and zeros coincide. This is because of the fact that Matlab does not perform pole-zero cancellation. It is seen that all poles and zeros have negative real parts. In other words, it is a minimum phase system.

Bode plot of $G_{OL}^v(s)$ is shown in Figure 5-13. As it is seen, phase margin is 56° and gain margin is 26.9 dB, which are reasonable values as mentioned earlier.

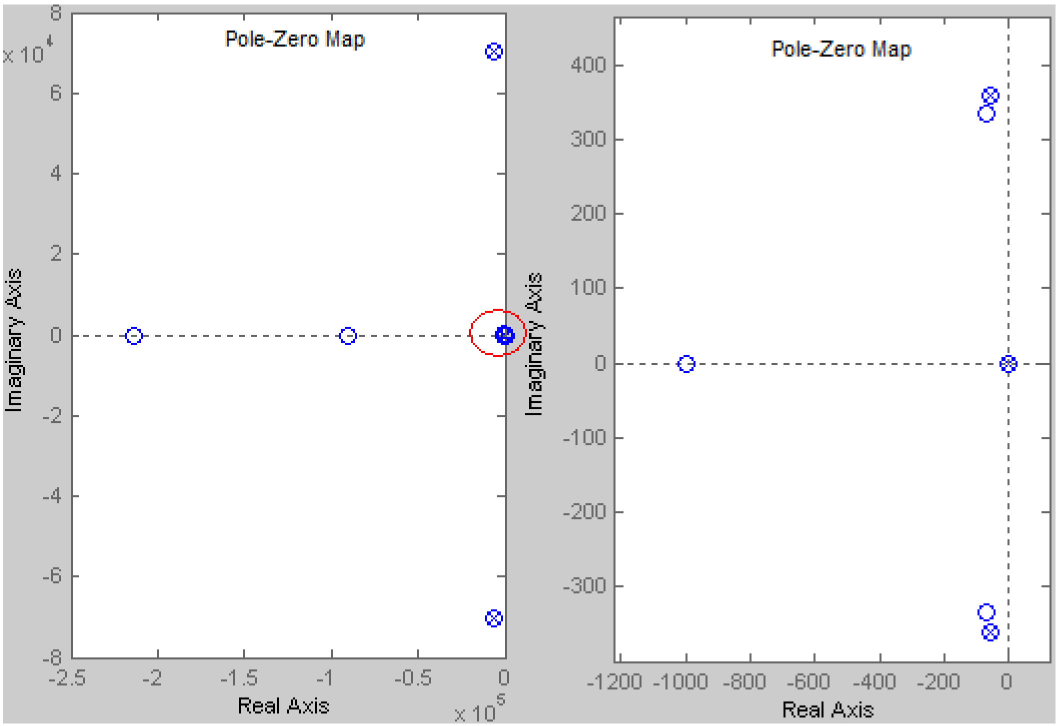

Figure 5-12 Pole-zero map of $G_{OL}^{v}(s)$

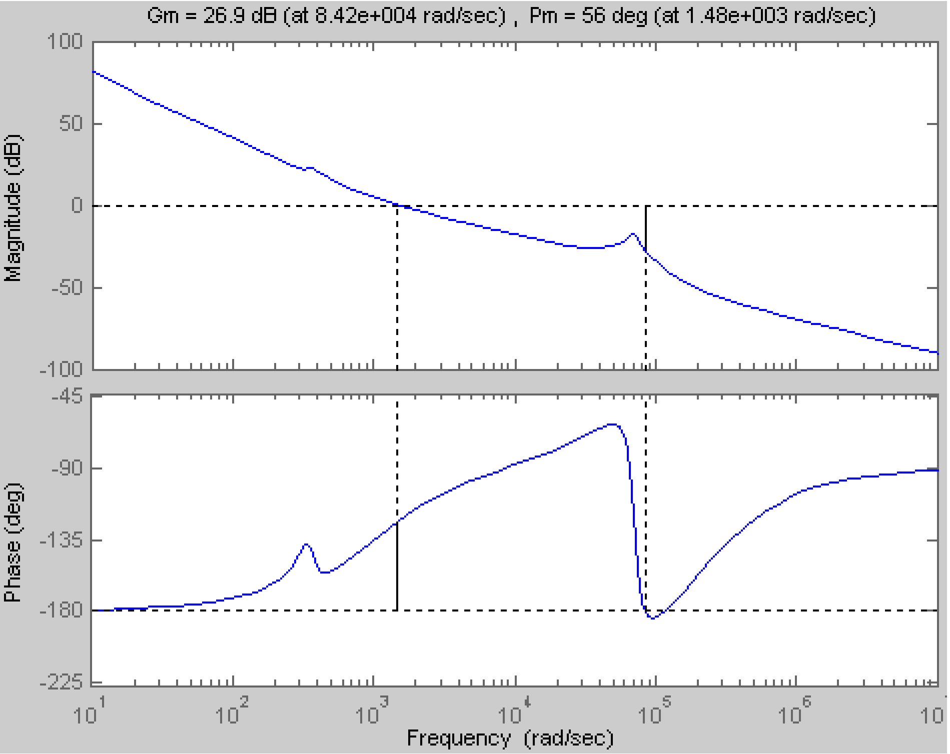

Figure 5-13 Bode plot of $G_{OL}^{v}(s)$

As a final graph, bode plot of the closed loop transfer function is shown in Figure 5-14 as an information about frequency response of the controlled converter.

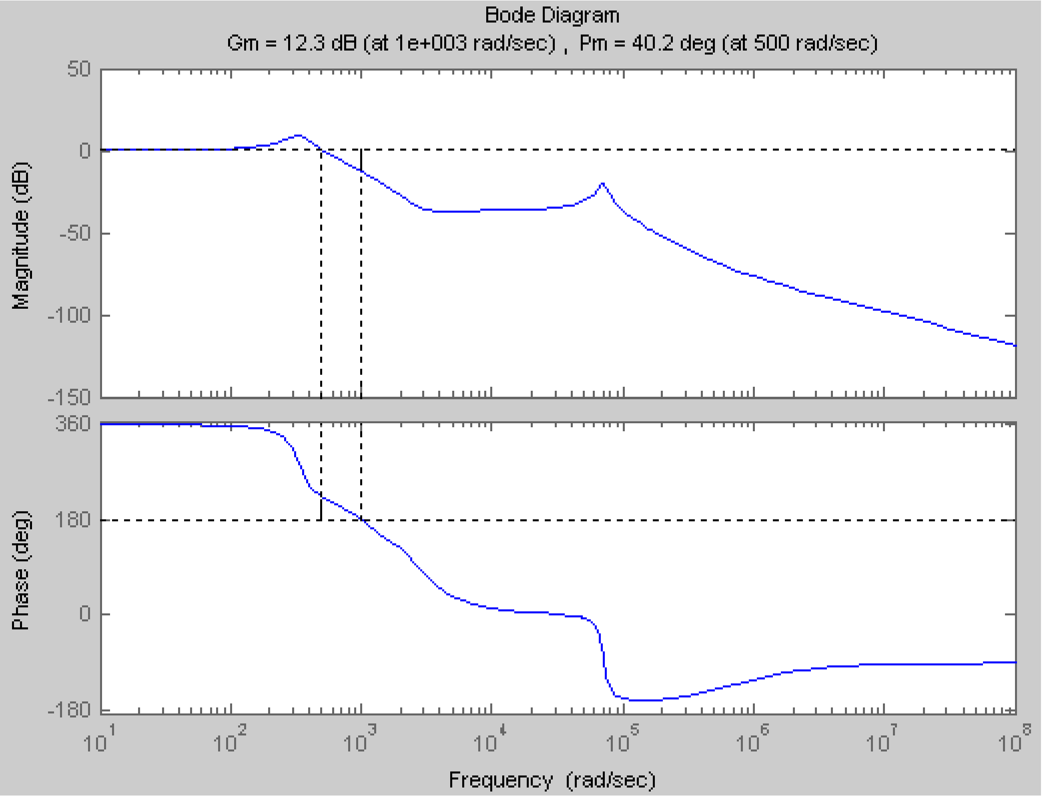

Figure 5-14 Bode plot of $G_{CL}^{v}(s)$

5.4 DOMAIN CONVERSIONS

Controller functions have been obtained in s-domain. In order to implement in a digital controller, these functions will be converted to their z-domain equivalent by using bilinear transformation. Then, by utilizing inverse z-transform, they will be converted to their discrete time domain equivalent.

Both of the controllers are in the following form;

$$G_c(s) = K_p + \frac{K_i}{s} \qquad (5\text{-}25)$$

There are few s-domain to z-domain transformation types. Bilinear transformation has been applied and given a satisfactory result. Hence, it will be given in this section. According to bilinear transformation, the following conversion is performed:

$$s \rightarrow \frac{2}{T_{samp}} \frac{1-z^{-1}}{1+z^{-1}} \tag{5-26}$$

where T_{samp} is the sampling frequency. Therefore, controller transfer function in z-domain, $G_c(z)$ can be obtained in the following manner.

$$G_c(z) = K_p + \frac{K_i}{\frac{2}{T_{samp}} \cdot \frac{1-z^{-1}}{1+z^{-1}}} \tag{5-27}$$

$$G_c(z) = \frac{K_p(1-z^{-1}) + \frac{K_i T_{samp}}{2}(1+z^{-1})}{1-z^{-1}} \tag{5-28}$$

At this stage, input-output relationship of the controller can be formed. Let the controller input be "e" and output be "u". While they will be named as $E(z)$ and $U(z)$ in z-domain, they are called $e[n]$ and $u[n]$ in discrete time domain. Hence, the following relationship exists.

$$U(z) = G_c(z)E(z) \tag{5-29}$$

$$U(z) = \frac{K_p(1-z^{-1}) + \frac{K_i T_{samp}}{2}(1+z^{-1})}{1-z^{-1}} \cdot E(z) \tag{5-30}$$

$$U(z) - z^{-1}U(z) = K_p\{E(z) - z^{-1}E(z)\} + \frac{K_i T_{samp}}{2}\{E(z) + z^{-1}E(z)\}$$

(5-31)

By using inverse z-transform, (5-31) is converted to its discrete time equivalent.

$$u[n] = u[n-1] + K_p\{e[n] - e[n-1]\} + \frac{K_i T_{samp}}{2}\{e[n] + e[n-1]\}$$

(5-32)

What does (5-32) mean? $u[n]$ is the current output of the controller and $u[n-1]$ is the previous output. $e[n]$ is the input to the controller at that sampling instant and

$e[n-1]$ is the previous sampled input. That is, the current output of the PI-controller is determined based on the previous output, the input at that sampling instant and the previous input. As a consequence, (5-32) is ready to implement in a digital signal controller.

5.5 APPLICATION SPECIFIC POINTS

Main ideas about controller design are given so far. This section includes some practical, complementary or application specific points, which are important as well.

As mentioned in the design chapter, the implemented circuit has two selectable modes: constant input current mode (CICM) and constant input power mode (CIPM). These modes have only one difference in terms control. When Figure 5-15 is investigated, it is seen that the controller outputs are limited. Limiter at the output of $G_C^i(s)$ is required in order to limit duty-factor. Otherwise it could result in shorting the switch for a relatively long time. This limit is chosen as 0.9 in this application. This part is the same for both CICM and CIPM. However, the limiter at the output of $G_C^v(s)$ is different. It will limit the input current reference to 10A in CICM and $(280W/V_i)A$ in CIPM. Input voltage will be sampled as an addition to output voltage and input current at each sampling instant in CIPM. In this way, the input current limit, which is the limit of i_i^{ref}, is determined in order to draw at most 280W from the input.

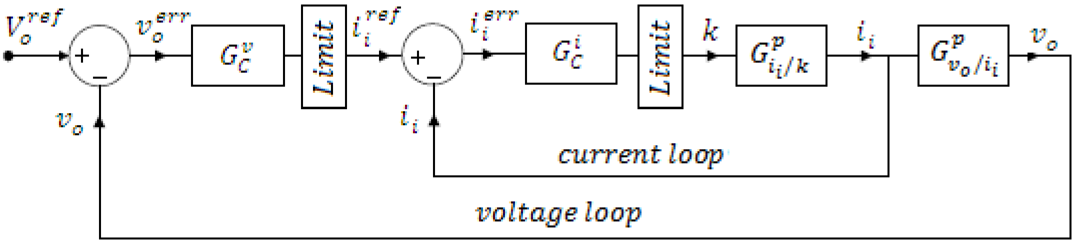

Figure 5-15 Control block diagram with the limiters

When a limit is applied at the output of the controller, a precaution must be taken. As long as the output of the controller is limited, its integral gain must be held at zero. Otherwise, a wrong interpretation is made by controller, which is observed in closed-loop simulations. As a result, the following "if statement" has been applied and therefore the last term (the integral term) of the equation is dropped so that;

$$If \quad u[n-1] = limit \quad \rightarrow \quad u[n] = u[n-1] + K_p\{e[n] - e[n-1]\}$$

Generally, it is not possible to use the transfer functions directly. Because of the voltage divisions in feedback paths, output range of the current sensors, analog-to-digital conversion output range and PWM value range; transfer function is normalized by a meaningful coefficients. For example, while duty-factor changes between 0-0.9 in s-domain, it corresponds to 7-9240 bit value in the used digital signal controller. Owing to these kinds of normalizations, $G_C^i(s)$ coefficients are multiplied by 613 in this application.

As it will be given in details, T_{samp} is determined as 1 switching period ($T_s = 10usec$) in CICM and 3 switching period in CIPM. When these values considered, the revised transfer functions are obtained. Transfer functions are now ready to use in digital signal controller.

In CICM:

Current Controller

$$u[n] = u[n-1] + 2.1455\{e[n] - e[n-1]\} + 0.0107\{e[n] + e[n-1]\} \tag{5-33}$$

Voltage Controller

$$u[n] = u[n-1] + 1.6\{e[n] - e[n-1]\} + 0.008\{e[n] + e[n-1]\} \tag{5-34}$$

In CIPM:

Current Controller

$$u[n] = u[n-1] + 2.1455\{e[n] - e[n-1]\} + 0.0321\{e[n] + e[n-1]\} \tag{5-35}$$

Voltage Controller

$$u[n] = u[n-1] + 1.6\{e[n] - e[n-1]\} + 0.024\{e[n] + e[n-1]\} \tag{5-36}$$

CHAPTER 6

EXPERIMENTAL RESULTS

6.1 INTRODUCTION

This chapter presents the experimental results of the designed and implemented circuit running in open-loop and closed-loop modes. For illustration purposes, its photographs are presented in Figure 6-1 and Figure 6-2, for a better understanding of which one may refer to Figure 3-16 for the circuit diagram and Figure 4-21 for the adjusted coupled-inductor model. At first, voltage and current waveforms of the circuit elements are given and compared with the theoretical analyses and the simulation results. Especially, the operation with the coupled-inductor providing ripple-free input current is investigated. Efficiency measurements at different operating points are also given. Secondly, closed-loop implementation will be handled. Starting with the transfer functions obtained in CHAPTER 3, necessary controller functions are determined and implemented via a microcontroller, or more accurately digital signal controller. Then, the possible dynamic responses of the circuit are given in order or evaluate the performance of the controller implementation.

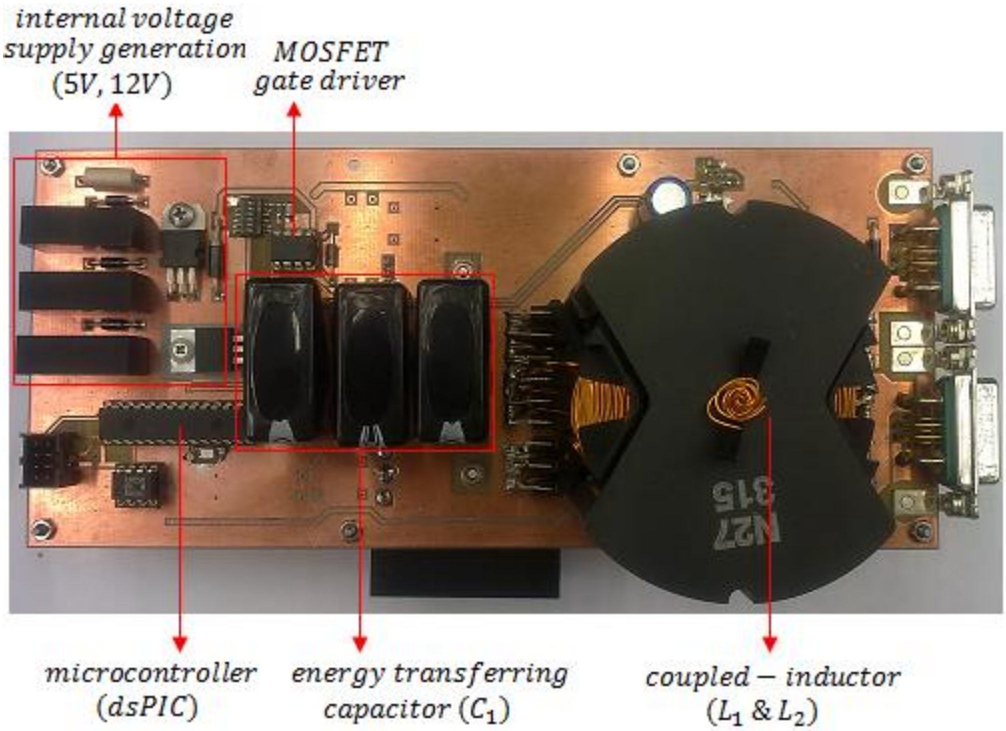

Figure 6-1 Top view of the implemented circuit

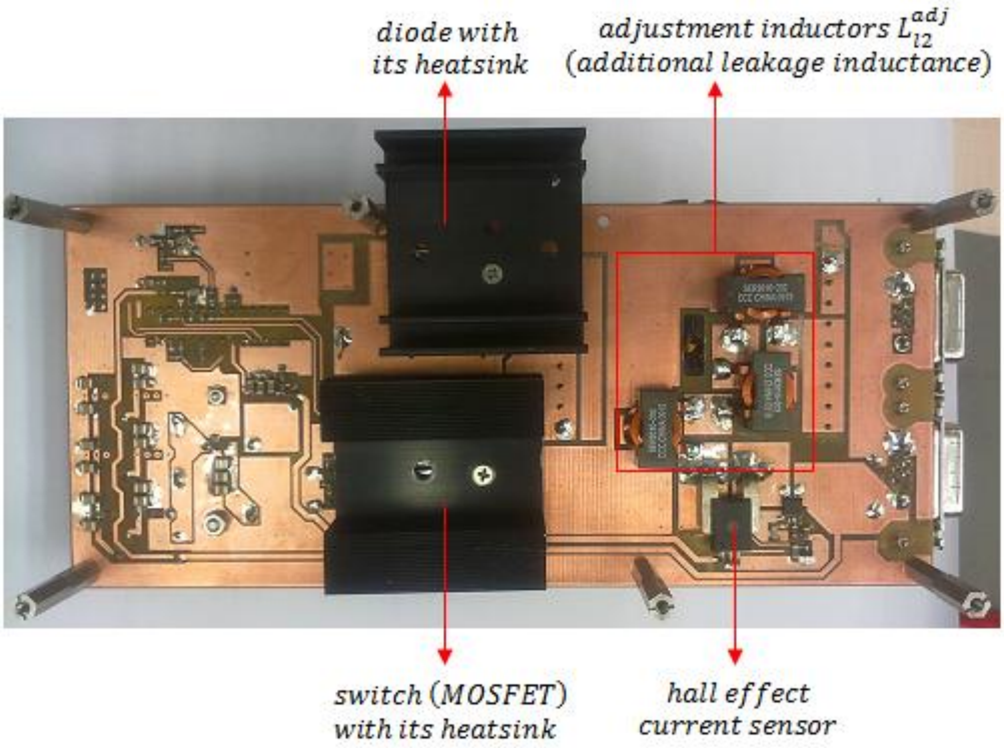

Figure 6-2 Bottom view of the implemented circuit

6.2 OPEN-LOOP RESULTS

In this section, important voltage and current waveforms of the implemented circuit running in open-loop mode are presented as verifications. Moreover, the efficiency of the converter in many operating points is given.

6.2.1 Voltage Waveforms

Important voltage waveforms of the switch, diode, output capacitor, input inductor and output inductor are presented in order to verify the design and implementation of the circuit.

6.2.1.1 Voltage Waveforms of the Switch and the Diode

Snapshots of the voltage waveforms are taken at two different operating points. One of them is the first end operating point, at which the current stress is at its maximum. Voltage overshoots due to the parasitic inductances of the paths carrying pulsating currents are planned to observe at this point. Voltage overshoots may lead to exceeding of the voltage ratings of the switch and diode. Another point is the fourth end operating point, where voltage stress is at its maximum. This point is regarded as another important operating point to investigate. All other operating points are considered to be between these two end operating points in terms of voltage stresses.

Voltage waveform of the switch at the first end operating point is seen in Figure 6-3. As expected, the switch blocks V_{tot} (≈34V), which is represented by ‘Cursor 2’ in the figure. Note that the zero voltage level is represented by ‘1’ at the left of the figure. The peak value of v_{DS} is 62.4V, which is represented by ‘Cursor 1’. Voltage rating of the MOSFET is 100V. That is, it is high enough for safe operation. There exists voltage overshoot of 28.8V, which is represented by ‘Delta’. It is considered as normal because almost 40A is switched in this situation. High di/dt may easily result in that much voltage overshoots.

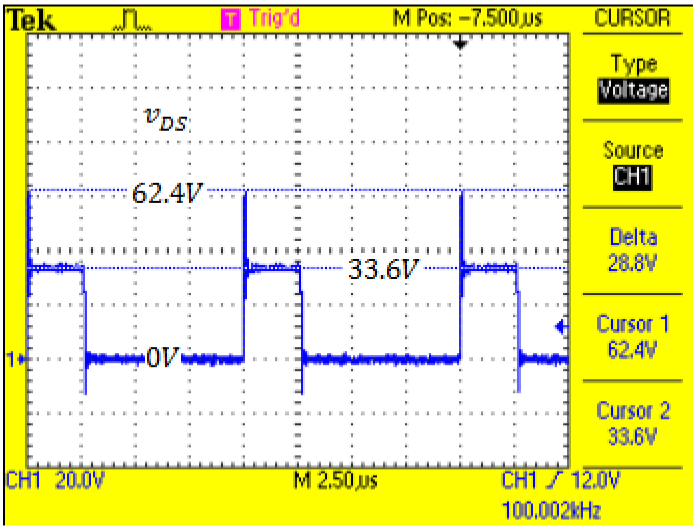

Figure 6-3 v_{DS} waveform at $V_i = 10V$, $V_o = 24V$ and full load

Anode-to-cathode voltage of the diode, v_{AC} is presented in Figure 6-4 at the same operating point. It blocks about V_{tot} similar to the switch. Its peak value is 53.6V. Voltage rating of the diode is 170V, which can be considered as over safe. Moreover, voltage overshoot on the diode is 21.6V.

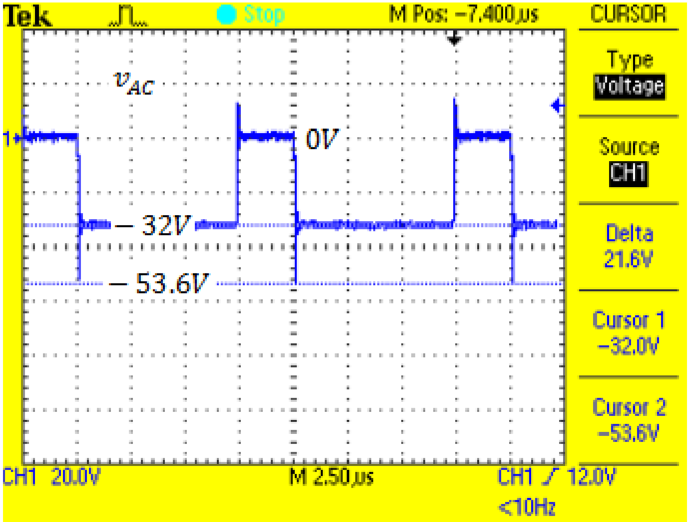

Figure 6-4 v_{AC} waveform at $V_i = 10V$, $V_o = 24V$ and full load

Voltage waveform of the switch at the fourth end operating point is seen in Figure 6-5. The switch blocks 59.2V, which is close to its expected value of 62V in this operating point. Its peak is 75.2V, which is small enough than the voltage rating of the switch. Besides, voltage overshoot is lower (16V) in this operating point because the switched current is lower here.

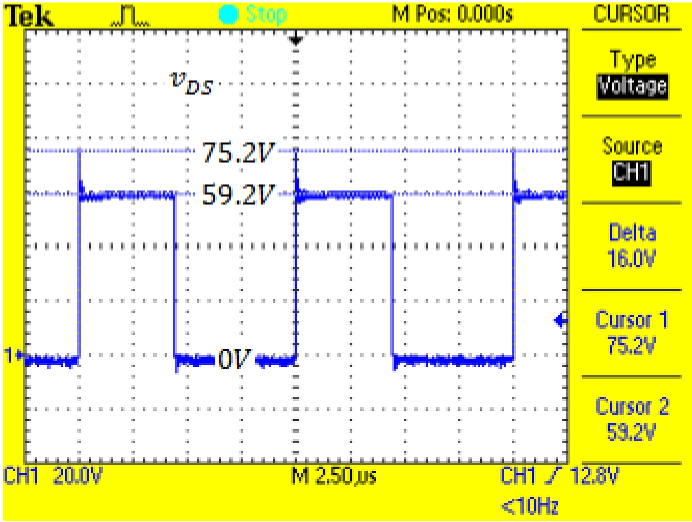

Figure 6-5 v_{DS} waveform at $V_i = 28V$, $V_o = 34V$ and full load

Voltage waveform of diode at the fourth end operating point is seen in Figure 6-6. It blocks 61.6V. Its peak is 72.8V and voltage overshoot is 11.2V. No extraordinary situation is observed.

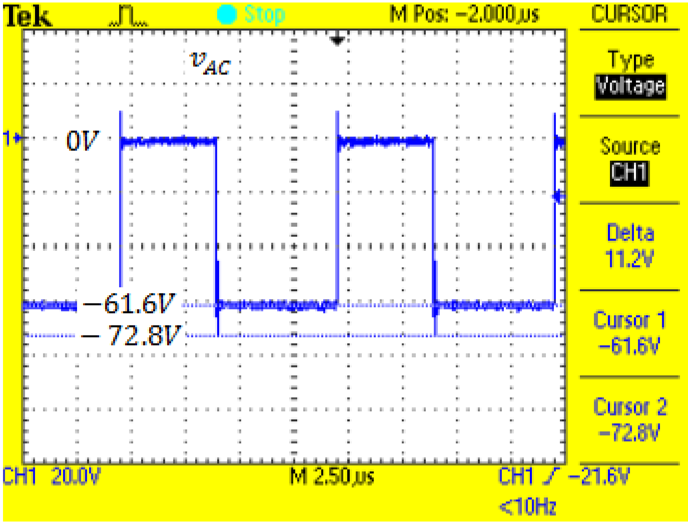

Figure 6-6 v_{AC} waveform at $V_i = 28V$, $V_o = 34V$ and full load

6.2.1.2 Voltage Waveforms of the Input and Output Inductors

Voltage waveforms of input and output inductors at the first and fourth operating points are given as verification. As it is seen in Figure 6-7, L_1 is exposed to the input voltage in Mode 1 and the inverse of the output voltage in Mode 2. This is an expected waveform. Also, the same waveform is observed on the combination of L_2 plus adjustment inductor, $v_{L_2}^{comb}$. Since it is same as v_{L_1}, $v_{L_2}^{comb}$ is not given intentionally. Instead, v_{L_2} (i.e. without the adjustment inductor) is presented in Figure 6-8. As it is aimed in the design process, high and low levels of v_{L_2} are a little bit lower than the cursors set at v_{L_1} measurement. Another point must be highlighted: Very high voltage overshoots are observed in the inductors. They stem from measurement errors. When the terminals of the oscilloscope probe are long and form a part of a sensitive loop, voltage spikes are observed at the switching instants. In this measurement, minimizing this loop could not been performed. Hence, the waveforms with voltage spikes have been presented obligatorily. Also, v_{C_1} waveform has not been given because of this reason. However, in measuring the voltage waveforms of the other circuit elements, the positive effect of minimizing the loop of the probe has been observed seriously. This problem and its solution are explained in Section 6.3.

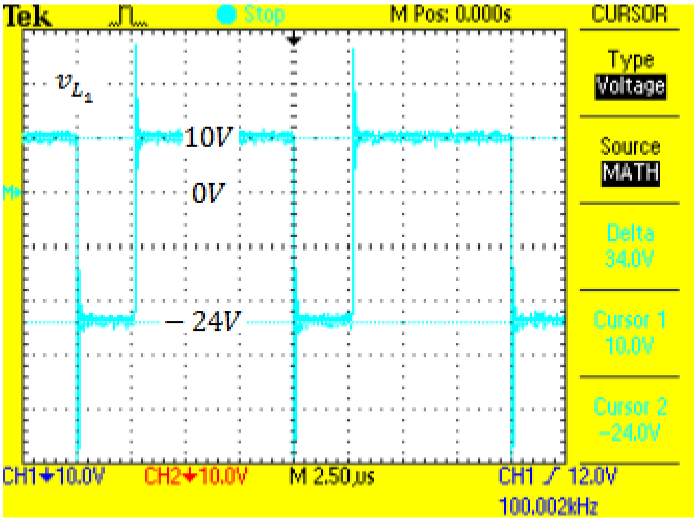

Figure 6-7 v_{L_1} waveform at $V_i = 10V$, $V_o = 24V$ and full load

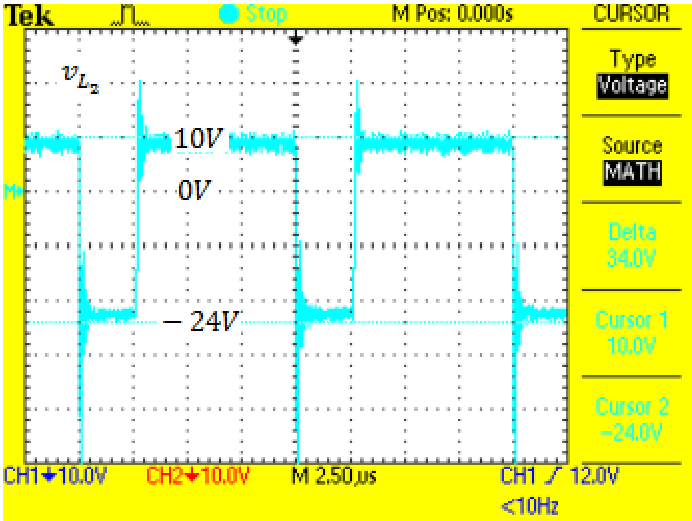

Figure 6-8 v_{L_2} waveform at $V_i = 10V$, $V_o = 24V$ and full load

The same arguments can also be applied in the fourth end operating point. As it is understood from Figure 6-9 and Figure 6-10, inductor windings see 28V in Mode 1 and -34V in Mode 2. Again, v_{L_2} is a little bit smaller than v_{L_2} in magnitude.

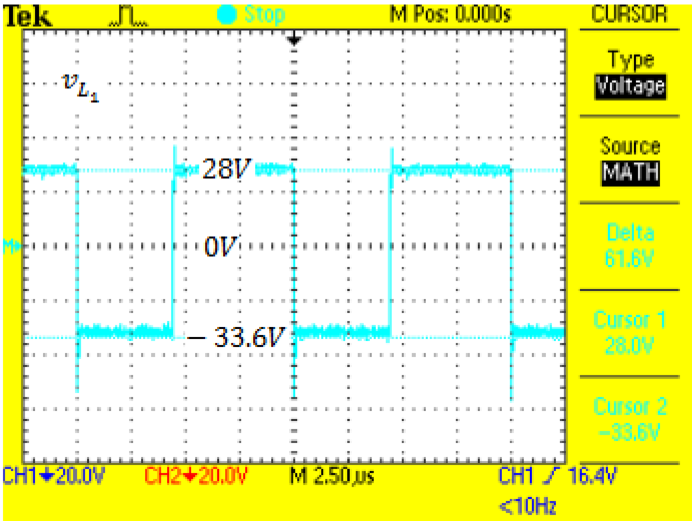

Figure 6-9 v_{L_1} waveform at $V_i = 28V$, $V_o = 234V$ and full load

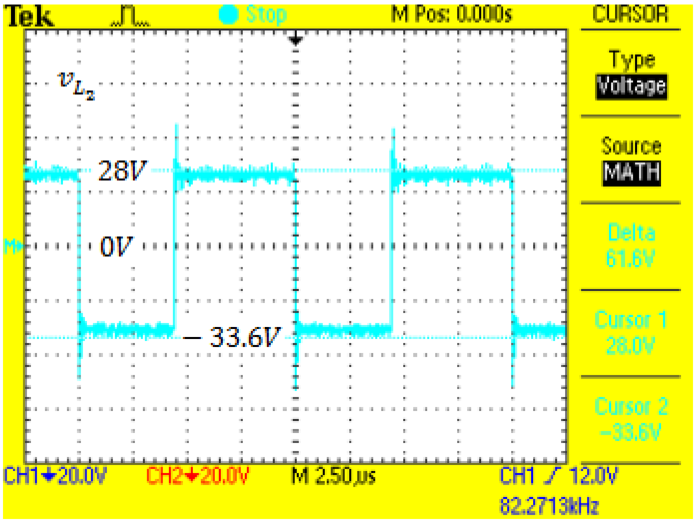

Figure 6-10 v_{L_2} waveform at $V_i = 28V$, $V_o = 234V$ and full load

6.2.1.3 Voltage Waveforms of the Output Capacitor

Voltage waveforms of the output capacitor at the first and fourth operating points are given as verification. In Figure 6-11, output voltage in the first operating point is given. When the theoretical value of the duty-factor in this operating point is calculated, it is found as 0.706. This figure is obtained at the duty-factor of 0.719,

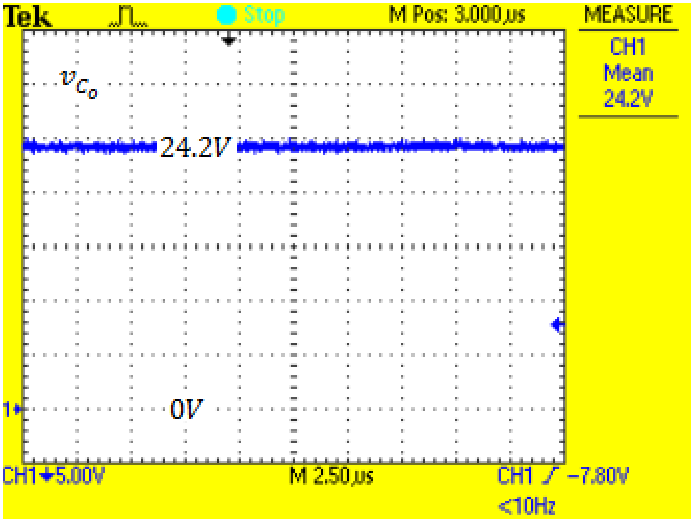

Figure 6-11 v_{C_o} waveform at $V_i = 10V$, $V_o = 24V$ and full load

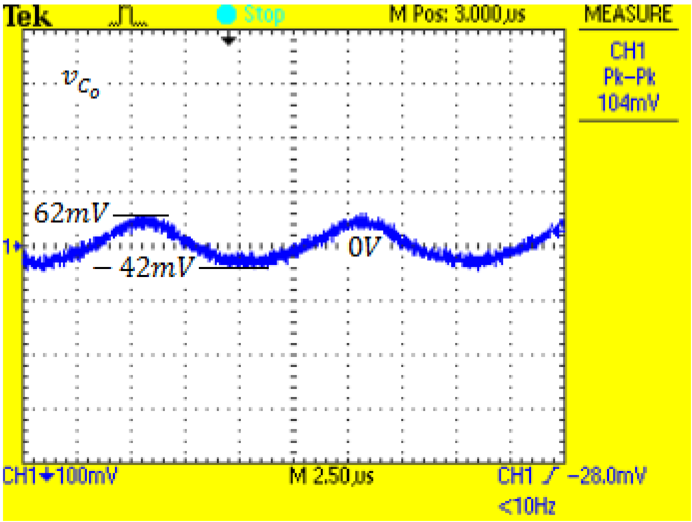

Figure 6-12 v_{C_o} waveform in ac coupling mode at $V_i = 10V$, $V_o = 24V$ and full load

which is very close to theoretical value. Moreover, voltage ripple of the output capacitor can be seen in Figure 6-12. Its peak-to-peak voltage ripple is measured as 104mV, which is very close to the calculated value for this operating value (95mV) and also within the 1% voltage ripple limit.

In Figure 6-13, output voltage at the fourth operating point is given. At this operating point, theoretical duty-factor is calculated as 0.548. This figure is obtained

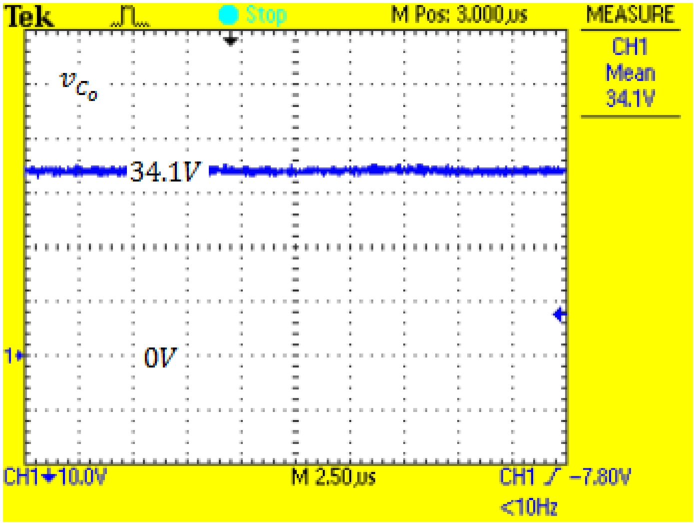

Figure 6-13 v_{C_o} waveform at $V_i = 28V$, $V_o = 34V$ and full load

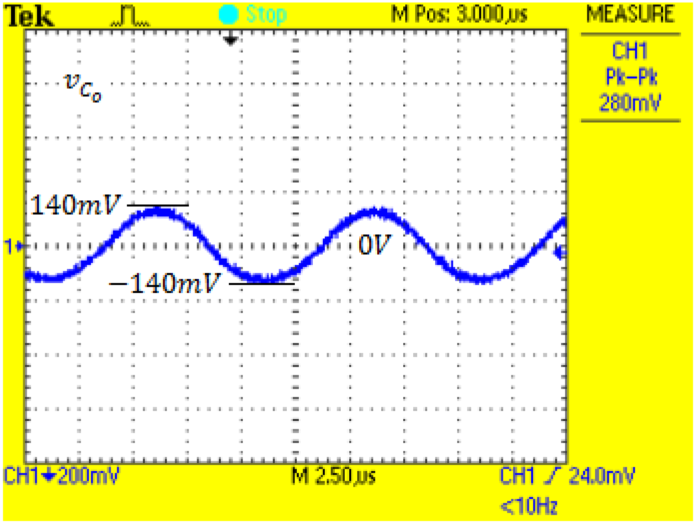

Figure 6-14 v_{C_o} waveform in ac coupling mode at $V_i = 28V$, $V_o = 34V$ and full load

at the duty-factor of 0.550, which is very close to theoretical value. Also, voltage ripple of the output capacitor can be seen in Figure 6-14. Its peak-to-peak voltage ripple is measured as 280mV, which is very close to the calculated value for this operating point, 207mV. By this way, the maximum of 1% voltage ripple condition is satisfied in this operating point, which is the worst case.

6.2.2 Current Waveforms

In this section, current waveforms of the input and output inductors will be given at two end operating points and three load levels. Two operating points are the first and the fourth operating points. Three load levels are full load, 50% load and 10% load. As it is known, input inductor current is the input current itself. However, output inductor current is not the output current exactly. It is flattened less or more by the output capacitor. Hence, output capacitor is extracted from the circuit while these current waveforms are being recorded in order to see the output inductor current only.

6.2.2.1 i_{L_1} and i_{L_2} Waveforms at the First End Operating Point

At this end operating point, the voltage levels are at their minimum and the current levels are at their maximum. i_{L_1} and i_{L_2} waveforms are observed while the output power is about 250W, 125W and 25W.

6.2.2.1.1 i_{L_1} and i_{L_2} Waveforms at Full Load for the First End Operating Point

Input current waveform at the first end operating point and full load is presented in Figure 6-15 and Figure 6-16. Note that the zero level is pointed as '4' at the left of the figure. Current waveforms have been measured by a current probe. While this measurement is taken, the scale of the current probe is at 50A/V. Hence, mean value of the input current is calculated as:

$$564mV \times 50A/V = 28.2A$$

Its peak-to-peak ripple current is also desired to show in Figure 6-15. However, since the scale is high in this snapshot (100mV/div or 5A/div), it gives an incorrect value. Hence, all ripple currents must be investigated in ac coupling mode and at low scale in order to get more accurate results. As a result, the ripple current on the input current in this operating condition is given in Figure 6-16. Its magnitude is very low such that it cannot even show a repetitive waveform. Probably, the ripple current magnitude is under the sensitivity of the measuring equipment. By accepting that the measurement is valid, its magnitude is calculated as:

$$4.8mV \cdot 50A/V = 0.24A$$

Therefore, peak-to-peak ripple percent of the input current is calculated as:

$$\left(\frac{0.24A}{28.2A}\right) \cdot 100 = 0.85\%$$

It is very low as expected. This value has been measured as 0.49% in the simulation. Hence, it is considered as a consistent result.

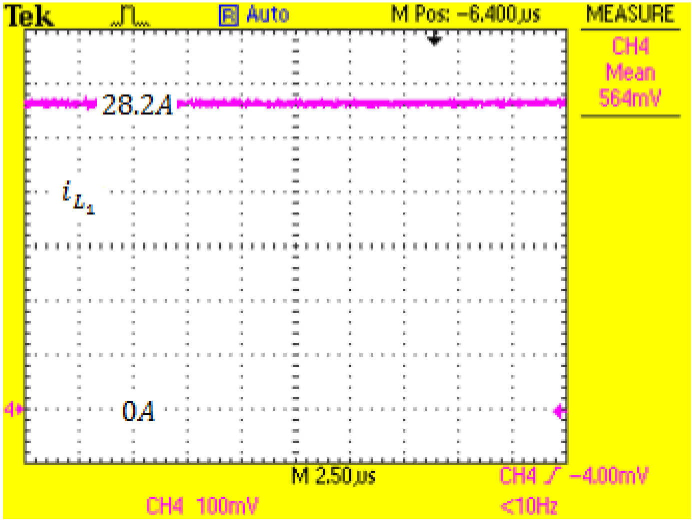

Figure 6-15 i_{L_1} waveform, 50A/V scale, $V_i = 10V$, $V_o = 24V$, full load

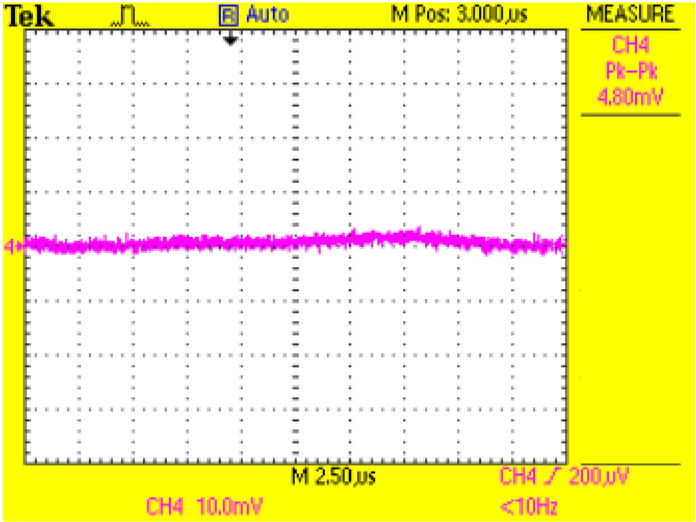

Figure 6-16 i_{L_1} waveform in ac coupling mode, 50A/V scale, $V_i = 10V$, $V_o = 24V$ and full load

Output inductor current waveform can be observed in Figure 6-17 and Figure 6-18. The scale of the current probe is 5A/V in this measurement. Hence, mean value of the output inductor is 10.2A, peak-to-peak ripple magnitude is 0.59A and ripple percent is 5.7%. Peak-to-peak ripple magnitude has been calculated as 0.68A at this operating point. The reason behind is the fact that the implemented/practical L_2 has turned out to be greater than the targeted/theoretical L_2. Moreover, ripple percent has been found as 4.1% in the simulation. This much deviation seems to be reasonable. Besides, its ac component is triangular as expected and simulated.

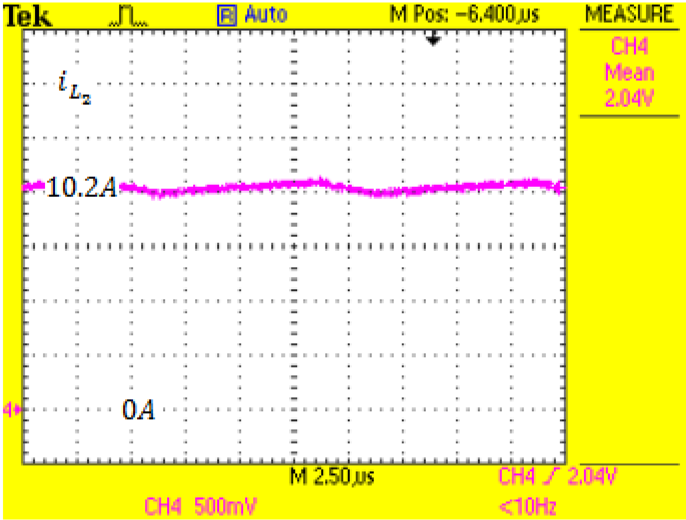

Figure 6-17 i_{L_2} waveform, 5A/V scale, $V_i = 10V$, $V_o = 24V$ and full load

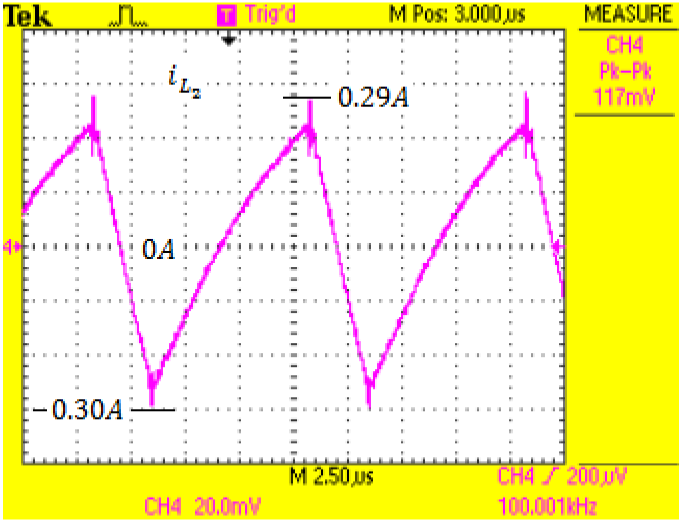

Figure 6-18 i_{L_2} waveform in ac coupling mode, 5A/V scale, $V_i = 10V$, $V_o = 24V$ and full load

6.2.2.1.2 i_{L_1} and i_{L_2} Waveforms at Half Load for the First End Operating Point

Input current waveform at the first end operating point and 50% load is presented in Figure 6-19 and Figure 6-20. As it can be calculated easily, mean value of the input inductor current is 13.3A, peak-to-peak ripple magnitude is 0.042A and ripple percent is 0.32%, which is very low as expected. Since the scale of the current probe is 5A/V rather than 50A/V, it gives more accurate result at low current level. This is probably why ripple current percent at 50% load turns out to be lower than that at full load. Besides, ac component of the current resembles to a sinusoidal as expected and simulated.

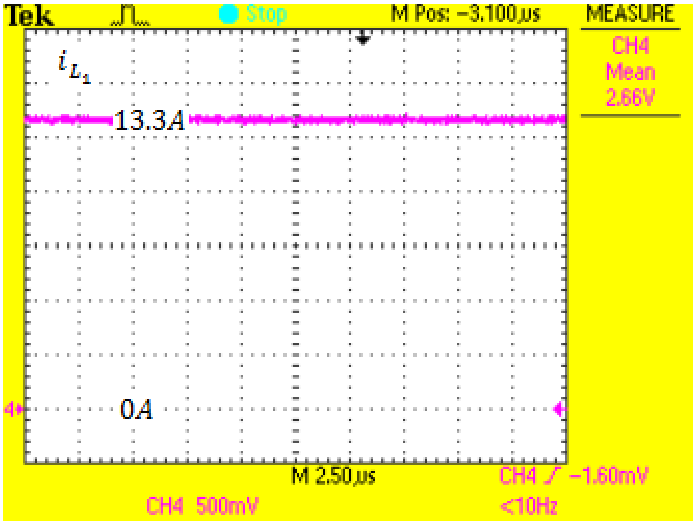

Figure 6-19 i_{L_1} waveform, 5A/V scale, $V_i = 10V$, $V_o = 24V$ and 50% load

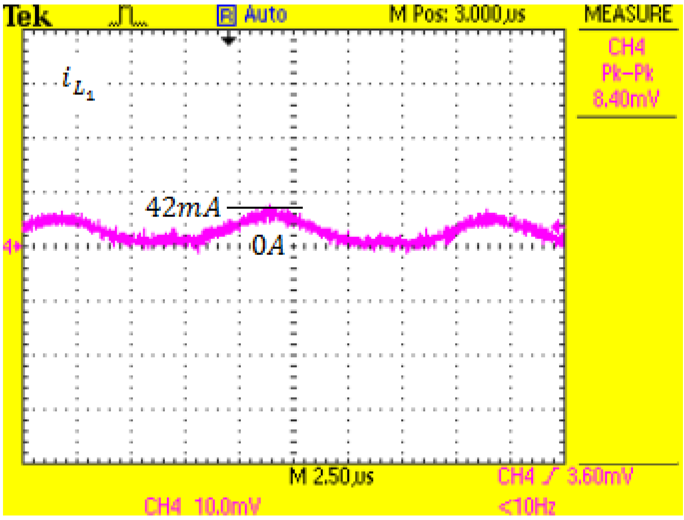

Figure 6-20 i_{L_1} waveform in ac coupling mode, 5A/V scale, $V_i = 10V$, $V_o = 24V$ and 50% load

Output current waveform at the first end operating point and 50% load is presented in Figure 6-21 and Figure 6-22. Mean value of the output inductor current is calculated as 5.05A, peak-to-peak ripple current magnitude as 0.545A and ripple percent as 10.8%. For the output current, peak-to-peak ripple current magnitude is expected to be the same for the same operating point regardless of the output power. This value turns out to be 0.59A at full load case and 0.545A at 50% load case,

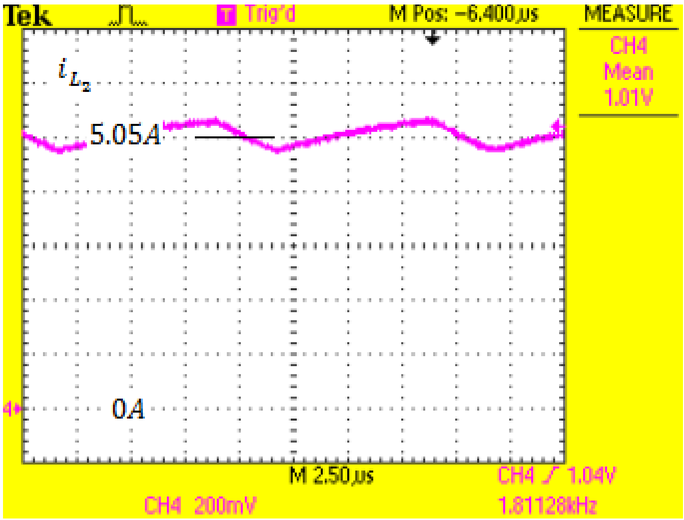

Figure 6-21 i_{L_2} waveform, 5A/V scale, $V_i = 10V$, $V_o = 24V$ and 50% load

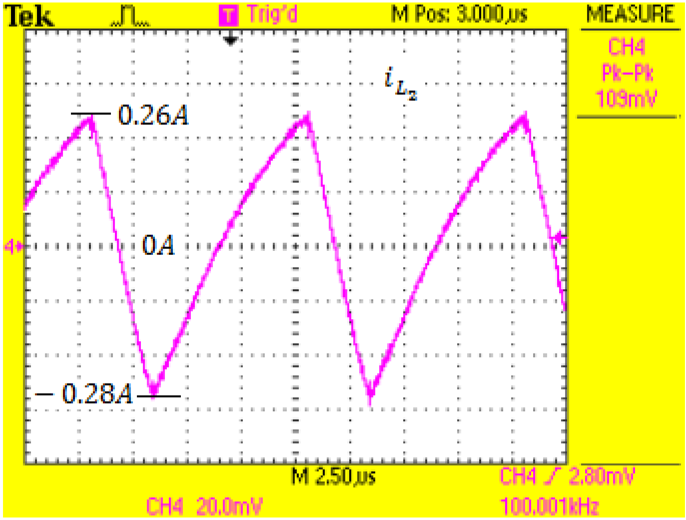

Figure 6-22 i_{L_2} waveform in ac coupling mode, 5A/V scale, $V_i = 10V$, $V_o = 24V$ and 50% load

which are very close. Besides, since the mean value decreases while the ripple magnitude remains the same, ripple current percent increases naturally. These results are also regarded as consistent.

6.2.2.1.3 i_{L_1} and i_{L_2} Waveforms at 10% Load for the First End Operating Point

Input current waveform at the first end operating point and 10% load is presented in Figure 6-23 and Figure 6-24. Mean value of the input inductor current is calculated as 2.59A, peak-to-peak ripple magnitude is 0.044A and ripple percent is 1.7%. Ripple current magnitude is still very low but the mean value is lower at this load level. Since the ripple current magnitude is not zero but very close to it due to the practical issues, increase in ripple percent with decreasing load is inevitable. This is also an expected result.

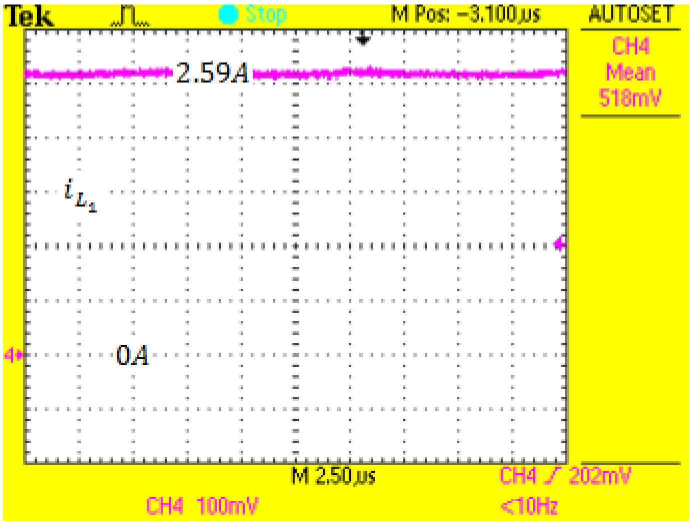

Figure 6-23 i_{L_1} waveform, 5A/V scale, $V_i = 10V$, $V_o = 24V$ and 10% load

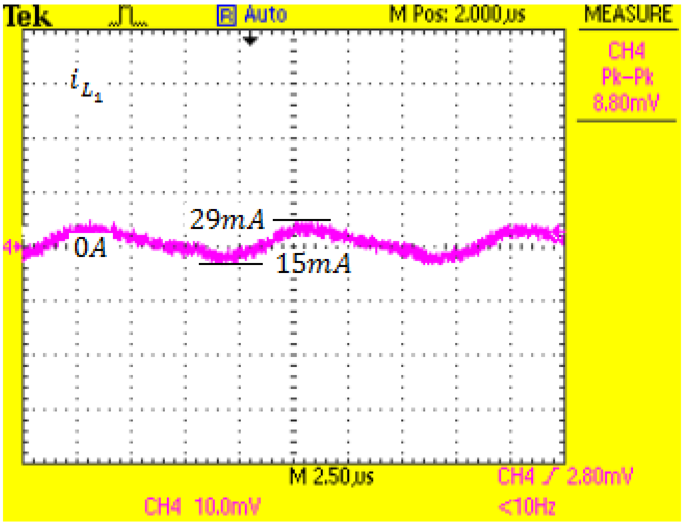

Figure 6-24 i_{L_1} waveform in ac coupling mode, 5A/V scale, $V_i = 10V$, $V_o = 24V$ and 10% load

Output current waveform at the first end operating point and 10% load is presented in Figure 6-25. Mean value of the output inductor current is calculated as 0.96A, peak-to-peak ripple current magnitude as 0.56A and ripple percent as 58.3%. Note that the ripple magnitude is the same with the previous load conditions at this end operating point. The same arguments at %50 load case are also valid here. No extraordinary situation is observed.

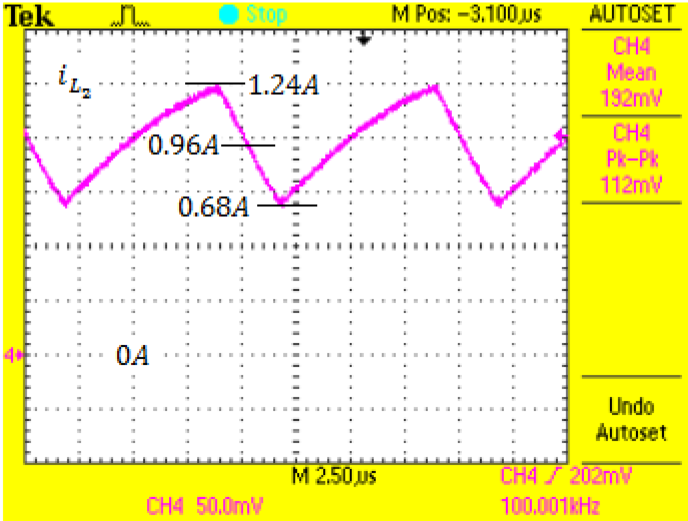

Figure 6-25 i_{L_2} waveform, 5A/V scale, $V_i = 10V$, $V_o = 24V$ and 10% load

6.2.2.2 i_{L_1} and i_{L_2} Waveforms at the Fourth End Operating Point

At this end operating point, the voltage levels are at their maximum and current levels are at their minimum. i_{L_1} and i_{L_2} waveforms are observed while the output power is about 250W, 125W and 25W.

6.2.2.2.1 i_{L_1} and i_{L_2} Waveforms at Full Load for the Fourth End Operating Point

Input current waveform at the fourth end operating point and full load is presented in Figure 6-26 and Figure 6-27. Mean value of the input inductor current is calculated as 9.3A, peak-to-peak ripple as 0.192A and ripple percent as 2%. Although it can be considered as very low, the ripple percent turns out to be higher in this operating point than in the first end operating point. Probably, the balance between the inductors is a little bit disturbed in this operating point due to the parasitic and nonlinear characteristics of the inductors and the other circuit components. Detailed investigation seems to be a useless effort. Besides, sinusoidal-like ac waveform is observed in this operating point more clearly.

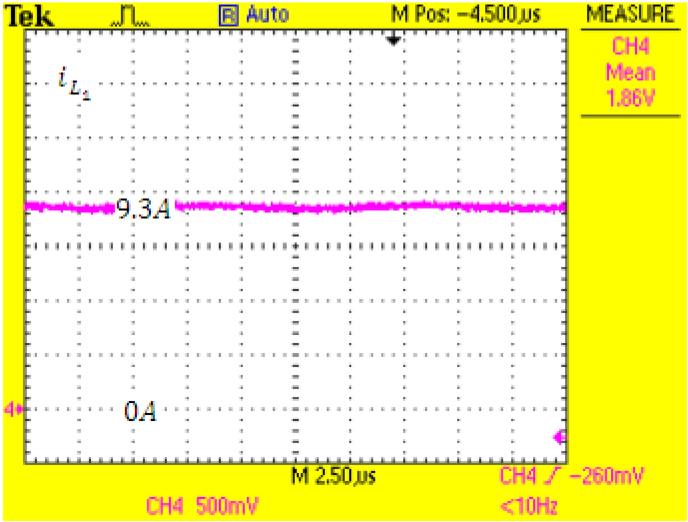

Figure 6-26 i_{L_1} waveform, 5A/V scale, $V_i = 28V$, $V_o = 34V$ and full load

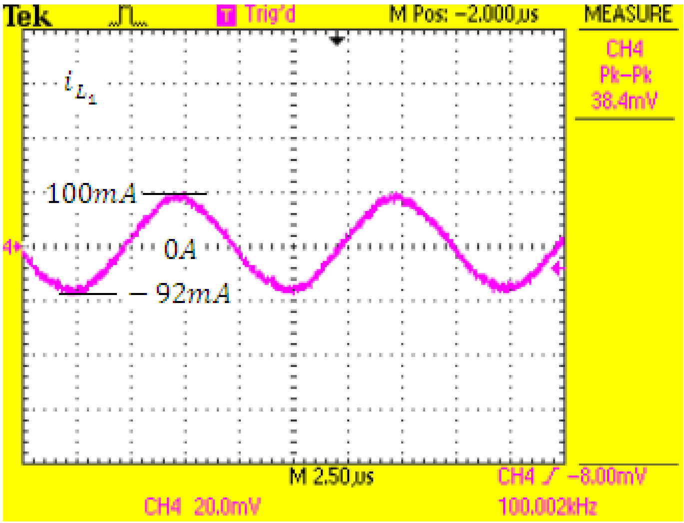

Figure 6-27 i_{L_1} waveform in ac coupling mode, 5A/V scale, $V_i = 28V$, $V_o = 34V$ and full load

Output current waveform at the fourth end operating point and full load is presented in Figure 6-28 and Figure 6-29. Mean value of the output inductor current is calculated as 7.2A, peak-to-peak ripple current magnitude as 1.22A and ripple percent as 16.9%. Current ripple magnitude has been calculated as 1.47A in the design section. The difference between 1.47A and 1.22A stems from the difference between the implemented L_2 and the simulated L_2, as explained earlier. Because of the same result the expected 20% ripple percent has turned out to be 16.9% in this operating condition.

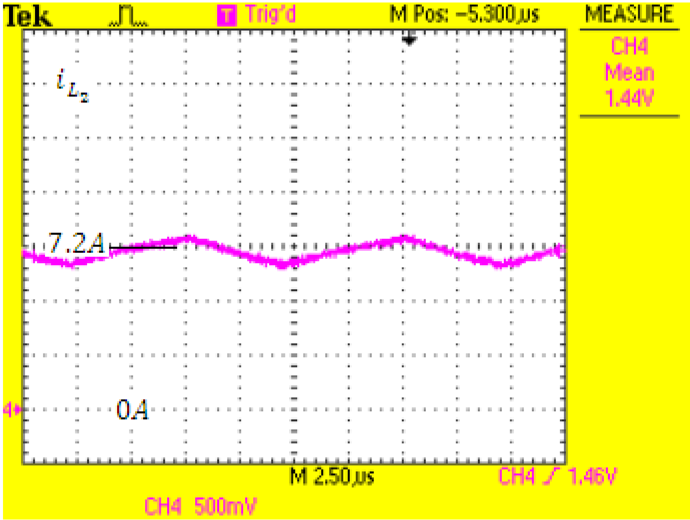

Figure 6-28 i_{L_2} waveform, 5A/V scale, $V_i = 28V$, $V_o = 34V$ and full load

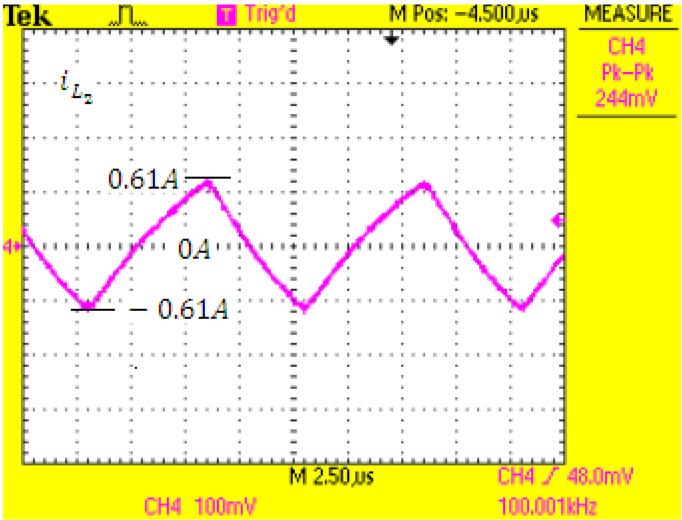

Figure 6-29 i_{L_2} waveform in ac coupling mode, 5A/V scale, $V_i = 28V$, $V_o = 34V$ and full load

6.2.2.2.2 i_{L_1} and i_{L_2} Waveforms at Half Load for the Fourth End Operating Point

Input current waveform at the fourth end operating point and 50% load is presented in Figure 6-30 and Figure 6-31. Mean value of the input inductor current is calculated as 4.61A, peak-to-peak ripple as 0.184A and ripple percent as 4%. Note that the ripple magnitude remains the same. Increase in the ripple percent is simply caused by the decrease in the input current. The same arguments at full load case are also valid here.

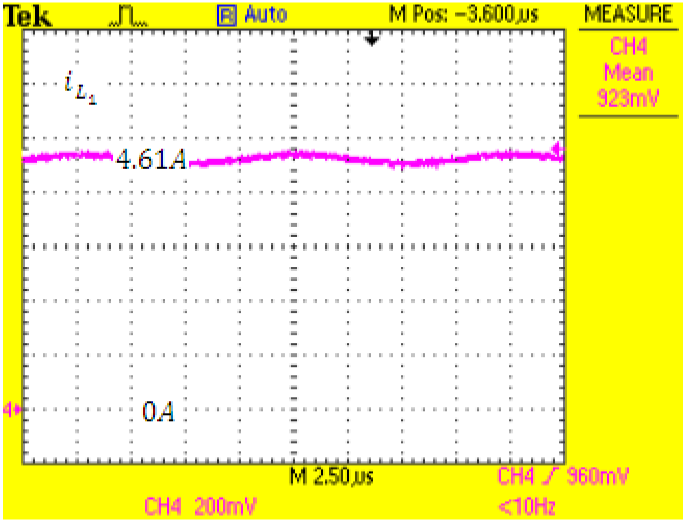

Figure 6-30 i_{L_1} waveform, 5A/V scale, $V_i = 28V$, $V_o = 34V$ and 50% load

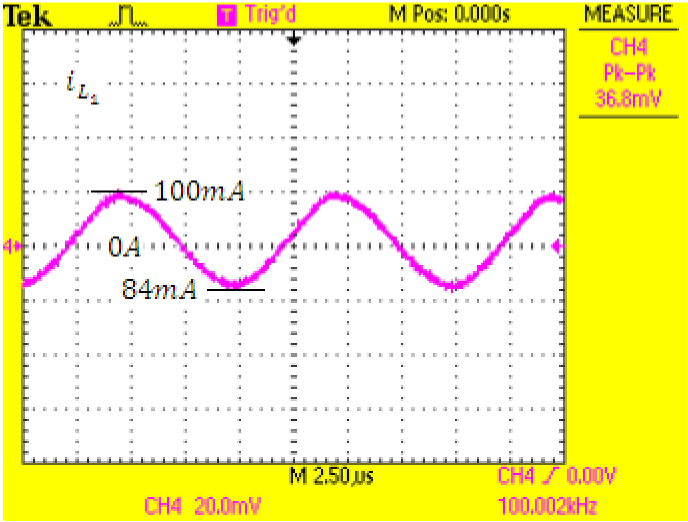

Figure 6-31 i_{L_1} waveform in ac coupling mode, 5A/V scale, $V_i = 28V$, $V_o = 34V$ and 50% load

Output current waveform at the fourth end operating point and 50% load is presented in Figure 6-32 and Figure 6-33. Mean value of the output inductor current is calculated as 3.58A, peak-to-peak ripple current magnitude as 1.19A and ripple percent as 33.2%. Note that the ripple amplitude remains the same as expected. There is no inconsistency observed in this operating point.

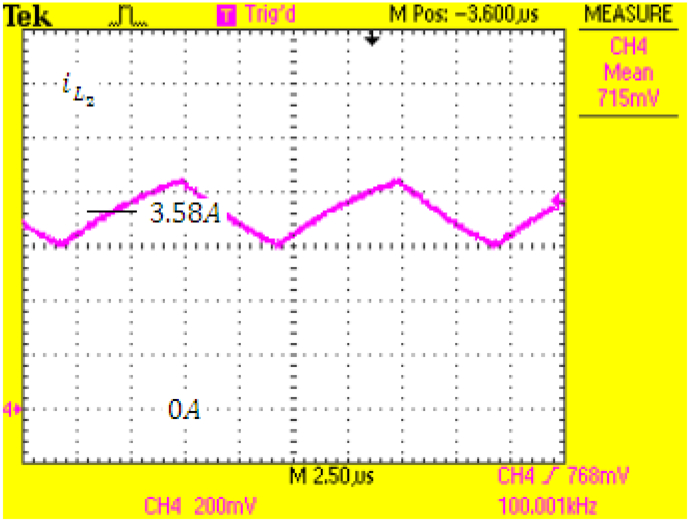

Figure 6-32 i_{L_2} waveform, 5A/V scale, $V_i = 28V$, $V_o = 34V$ and 50% load

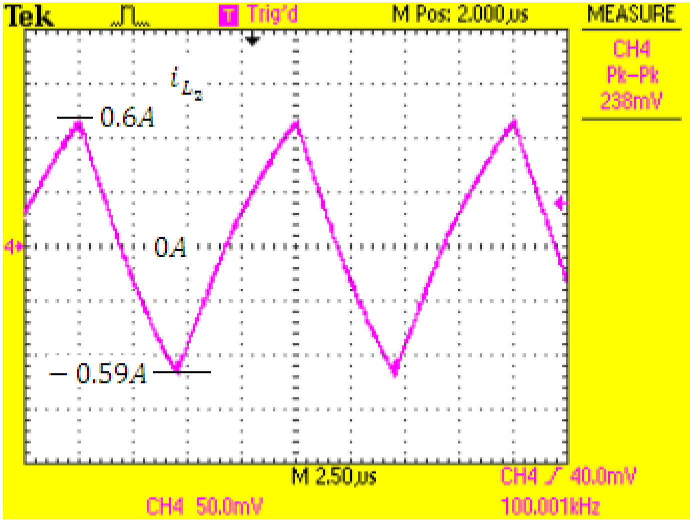

Figure 6-33 i_{L_2} waveform in ac coupling mode, 5A/V scale, $V_i = 28V$, $V_o = 34V$ and 50% load

6.2.2.2.3 i_{L_1} and i_{L_2} Waveforms at 10% Load for the Fourth End Operating Point

Input current waveform at the fourth end operating point and 10% load is presented in Figure 6-34 and Figure 6-35. Mean value of the input inductor current is calculated as 0.98A, peak-to-peak ripple as 0.19A and ripple percent as 19.4%. Note that the ripple magnitude remains the same. Increase in the ripple percent is simply caused by the decrease in the mean value of the input current. The same arguments at full load case are also valid here. From the input current waveforms at different load levels in this end operating point, the following comment can be inferred: Ripple current magnitudes at different load levels have turned out to be the same at this operating point. Hence, there exists probably an unbalance between the inductors. One can readjust the balance and get lower ripple percents. However, this time, the balance between the inductors at other operating points is disturbed.

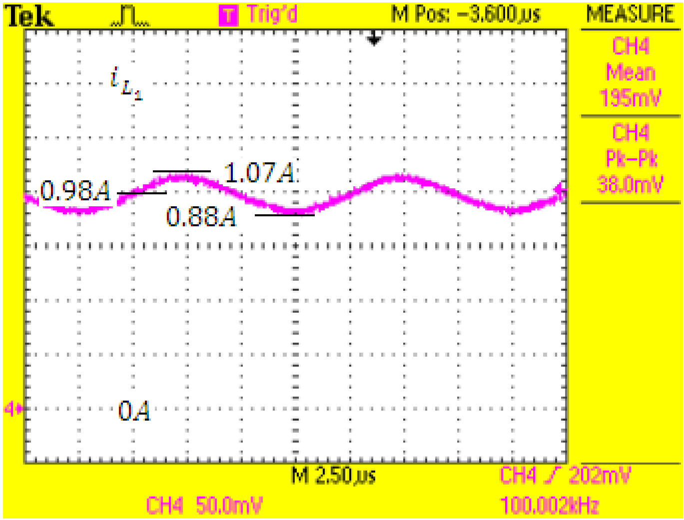

Figure 6-34 i_{L_1} waveform, 5A/V scale, $V_i = 28V$, $V_o = 34V$ and 10% load

Output current waveform at the fourth end operating point and 10% load is presented in Figure 6-35 and Figure 6-36. Mean value of the output inductor current is calculated as 0.68A, peak-to-peak ripple current magnitude as 1.17A and ripple percent as 172%. Note that the ripple amplitude remains the same as expected. Remind that the necessary L_2 is determined at this operating point and this load level. Hence, current waveform is expected to just hit the zero level. In this situation, ripple percent is expected to be 200%. When Figure 6-35 is investigated, it is seen that the

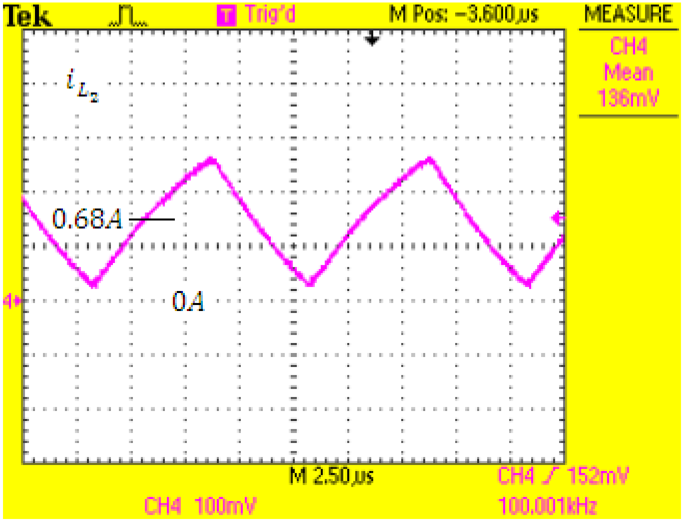

Figure 6-35 i_{L_2} waveform, 5A/V scale, $V_i = 28V$, $V_o = 34V$ and 10% load

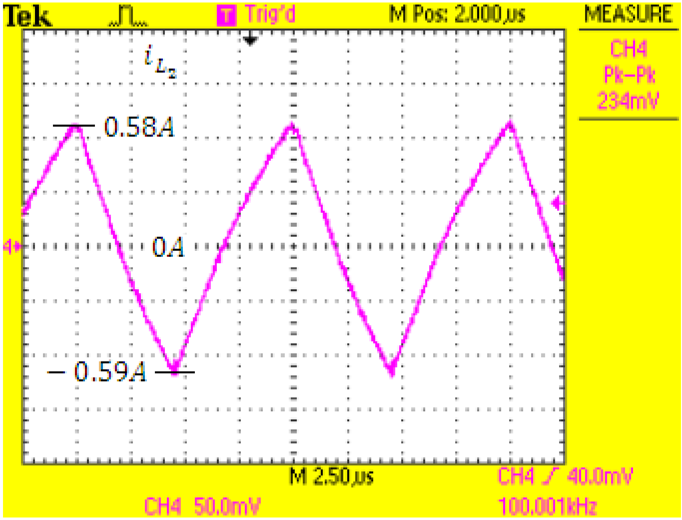

Figure 6-36 i_{L_2} waveform in ac coupling mode, 5A/V scale, $V_i = 28V$, $V_o = 34V$ and 10% load

bottom of the waveform is a little bit higher than zero. This is due to the higher value of implemented L_2. To sum up, the results are consistent with the previous simulations and calculations.

6.2.3 Efficiency of the Converter at Different Operating Conditions

In this section, measured efficiencies at the four end operating points and three different load levels are presented. All information can be found in Table 6-1. Input/output voltages are measured just at the input/output of the circuit. Input current is read from the panel of the source and the output current from the panel of the load, which are calibrated regularly. As it is seen in the table, the efficiency of the converter decreases at low input voltage (i.e. high input current) and full load cases. As explained in the design section, most of the power loss mechanisms are parasitic resistances of the circuit elements. This kind of power losses increase with the square of current magnitudes. Hence, at high current levels, decrease in efficiency is expected. At low load, base power losses such as diode forward voltage drop may dominate and decrease the efficiency. Generally, higher efficiencies are observed at moderate power levels. These facts can be seen in Table 6-1.

Table 6-1 Measured efficiencies at different operating points

Loading	Operating End Points	$V_i\ /V$	$I_i\ /A$	$P_i\ /W$	$V_o\ /V$	$I_o\ /A$	$P_o\ /W$	$\eta\ /\%$
Full	*First*	10,00	29,20	292,0	23,95	10,39	248,8	85,2
	Second	10,01	29,10	291,3	34,04	7,38	251,2	86,2
	Third	27,97	9,54	266,8	23,99	10,39	249,3	93,4
	Fourth	28,03	9,45	264,9	34,03	7,38	251,1	94,8
Half	*First*	9,99	13,68	136,7	24,07	5,18	124,7	91,2
	Second	9,99	13,61	136,0	34,03	3,68	125,2	92,1
	Third	27,99	4,71	131,8	24,07	5,18	124,7	94,6
	Fourth	27,99	4,70	131,6	34,05	3,68	125,3	95,2
10%	*First*	10,01	2,68	26,8	24,02	1,03	24,7	92,2
	Second	10,01	2,70	27,0	34,11	0,73	24,9	92,1
	Third	28,03	0,96	26,9	24,04	1,02	24,5	91,1
	Fourth	27,98	0,98	27,4	34,02	0,73	24,8	90,6

6.3 CLOSED-LOOP RESULTS

In this section, closed loop performance of the implemented circuit and the designed digital controller in (5-33)-(5-36) will be tested. As a disturbance, load current change is considered. In order to organize the test results in mind, the following reminders are given:

- The converter has two selectable modes: constant input current mode (CICM) and constant input power mode (CIPM). Each mode has two regulation modes.
- CICM explanation: In this mode, if no-load current is drawn by the equipment, the converter regulates its output voltage to 34V. As the load current increases, the input current increases as well. As long as the input current is lower than 10A, converter output voltage will be regulated to 34V. At this point, input power of the converter varies between 100W-280W according to the input voltage. Once the input current is started to regulate at 10A, output voltage starts to decrease. Its level is determined by the load current, but it is guaranteed by li-ion battery pack that it will not decrease below 24V.

- Each modes of regulation in CICM, namely output voltage regulation and input current regulation, has its own dynamic response characteristics. Moreover, transition between regulation types during dynamic response is possible, which also has different dynamic response characteristics. Therefore, the test results are grouped into:
    - ➢ Output voltage regulation mode
    - ➢ Input current regulation mode
    - ➢ Transition between regulation modes

  Test results are given at the transitions between the farthest possible points in each mode. Besides, since the input voltage is an important variable here, the results are repeated at the two end input voltages, namely 10V and 28V.
- CIPM explanation: The same arguments in CICM are also valid here. The only difference is the input current limit. While the input current limit is constant at 10A in CICM, it is determined as (280W/V_i)A in CIPM. That is, it is determined by the constant input power limit (280W) and the input voltage at that instant. Similarly, the same experimental results will be given for this mode.

Meanwhile, some practical issues are considered to be important in the

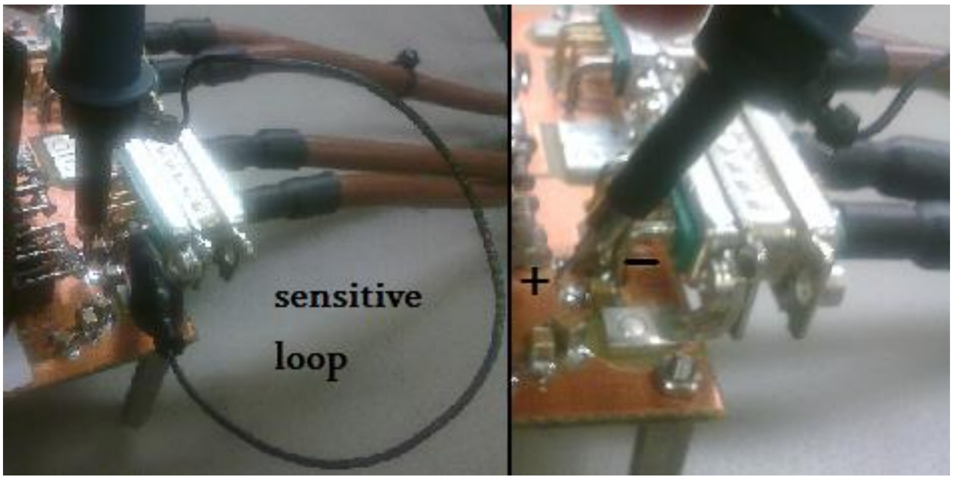

Figure 6-37 Noise-sensitive (left) and noise-immune (right) measurement techniques

evaluation of the experimental results. Hence, they will be highlighted first. While monitoring the output voltage in oscilloscope, it has been realized that the switching noise is coupled to the oscilloscope probe unless a precaution is not taken. Figure 6-37 and Figure 6-38 are given in order to clarify this situation.

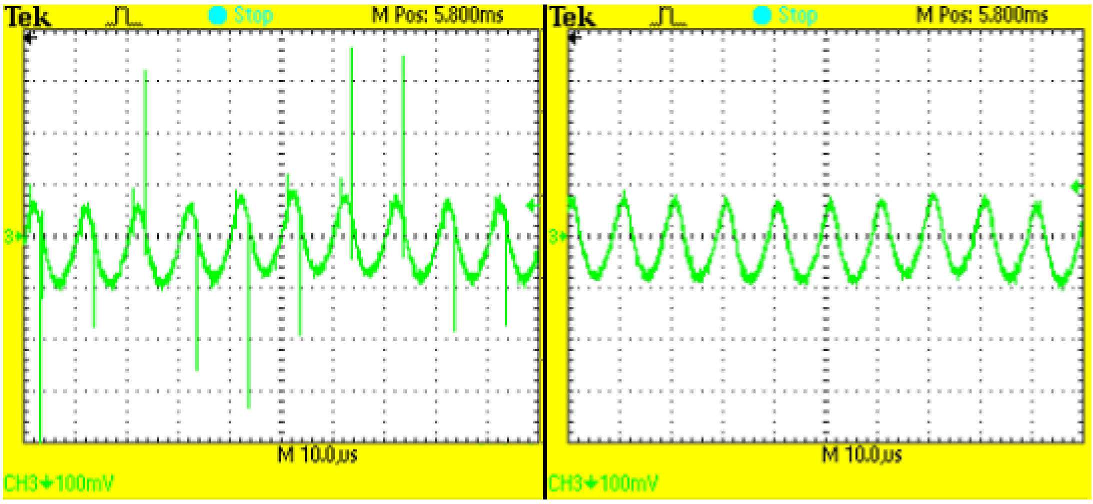

Figure 6-38 Results of noise-sensitive (left) and noise-immune (right) measurements

In open loop experimental results, noise-immune technique is used. In order to show low-amplitude voltage ripples, ac coupling mode suffices there. In closed-loop results, however, in order to show the small changes during transient responses, ac coupling mode is not proper. 34V must be looked at, for example, 500mV/div scale. Since this is not possible with the present equipments, a different solution is looked for. Another 34V is generated by another power supply. Ground of the oscilloscope probe is connected to this constant 34V and positive terminal of the probe is touched to 34V of the converter. In this way, 0V is observed in the oscilloscope probe at steady-state. Actually, 0V represents the reference of 34V for the converter. Because of this tricky but obligatory solution, physical distance between the positive and ground terminals of the probe increases. Hence, noise-sensitive measurement technique is used inevitably. In short, notches on the presented waveforms in closed-loop test results do not exist in reality and should be ignored.

Another measurement error stems from the oscilloscope itself. The waveform seen at the left of Figure 6-38 is obtained at 10usec/div time scale. The same waveform with 1msec/div time scale is shown at the left of Figure 6-39. Two waveforms are consistent. However, when this waveform is squeezed in time further, its waveform changes ambiguously. While a dense waveform similar to the left of Figure 6-39 is expected, a sinusoidal waveform is observed at 2.5msec/div time scale at the right of Figure 6-39. It is nonsense. Although its magnitude is somehow meaningful, its waveform is irrelevant. As a conclusion, this sinusoidal waveform at low frequency should be perceived as a band with the same magnitude.

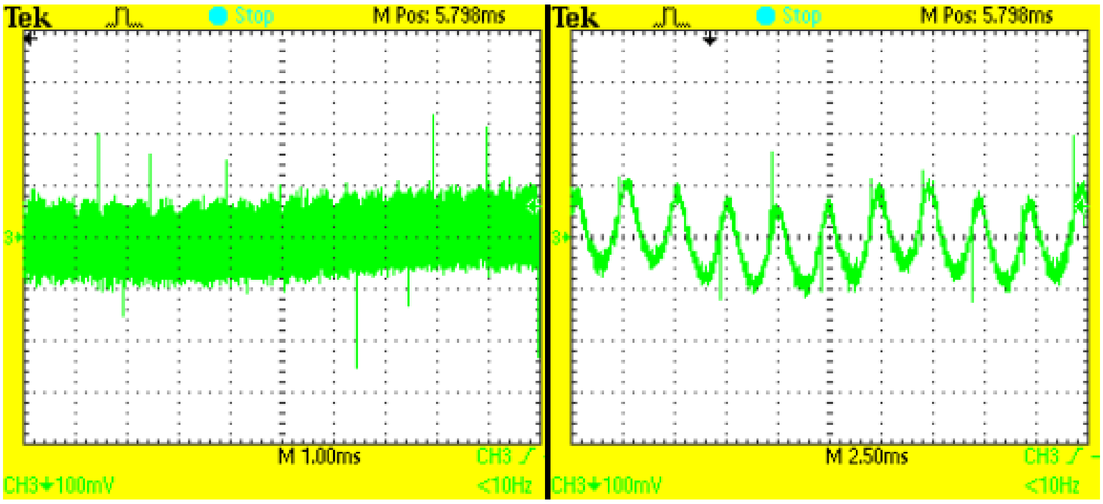

Figure 6-39 Output voltage waveforms in ac coupling mode at 1msec/div (left) and 2.5msec/div time scale

Now, closed-loop test results will be given in an organized manner as mentioned previously.

6.3.1 Constant Input Current Mode

Test results are grouped at the following subsections. Before it, the timing diagram of the control loop is desired to give. Owing to its powerful peripherals, the selected dsPIC makes it possible to refresh the duty-factor at a rate of switching frequency, 10usec. PWM signal (red) and timing signal (blue) are presented in

Figure 6-40. At $t = 0usec$, PWM signal goes high. After 1usec, ADC conversion starts in synchronous with PWM signal. 1usec delay is selected in order to get rid of the high noise levels formed at the switching instants. Then, at $t = 3.2usec$ ADC conversion is completed. ADC conversion of two channels, namely V_o and I_i, lasts 2.2usec. Just after ADC conversion, digital PI controller calculations are performed. It takes about 7.8usec. At $t = 11usec$, new duty-factor is determined. Although new PWM cycle starts 1usec earlier, new duty-factor immediately updated at that instant and is applied at that cycle. In this way, cycle by cycle control is achieved.

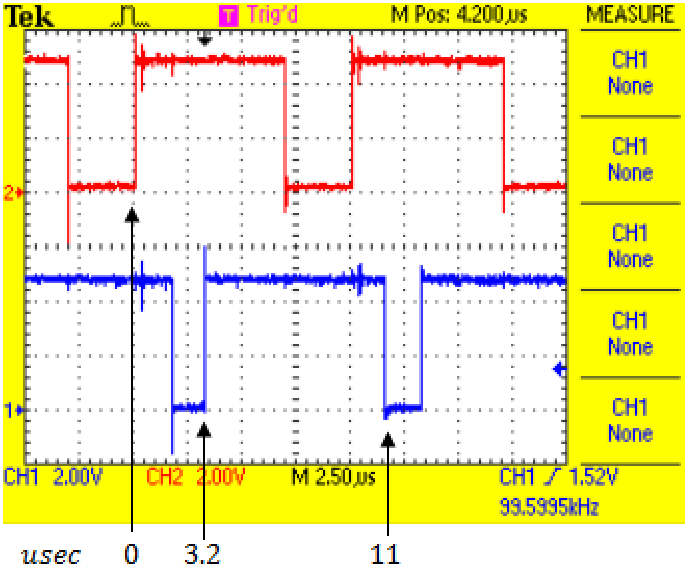

Figure 6-40 Timing diagram of the control loop in CICM

6.3.1.1 Output Voltage Regulation Mode

In this section, transient response of the two output variables, v_o and i_i, against step change in I_o will be given. I_o values are chosen such that they are either the minimum or the maximum output currents at which the output voltage regulation at 34V can be maintained. The minimum ones represent the no-load current of the converter at that input voltage. No load currents at different input voltages are given as;

$$I_o^{no-load} = 0.1A \quad @ \quad V_i = 10V$$

$$I_o^{no-load} = 0.2A \quad @ \quad V_i = 19V$$

$$I_o^{no-load} = 0.25A \quad @ \quad V_i = 28V$$

The maximum output currents represent the load currents at which the input current rises to just below 10A.

From now on, red waveforms represent i_i and green waveforms represent v_o. Besides, unless otherwise noted, current probe scale is at 5A/V. It will be at 50A/V only at two groups of graphs, where the input current is high.

The parameters defining the performance of the transient response such as rise time, settling time, maximum percent overshoot are not used regularly in these test results. Because the regulated variable does not deviate much from its reference value expect the exaggerated load current changes. In order to define these parameters, a reference band of 2% or %5 is determined beforehand. Even if this band is determined, these parameters may not carry sufficient information in some graphs. Hence, instead of using these parameters, presenting raw data is considered to be more meaningful in most case.

In Figure 6-41, the first snapshot is given. In order to get acquainted with these graphs, some explanations will be presented here. The step load current change from 0.1A to 2.6A occurs at the second time division from the left of the figures. It is realized at the input voltage of 10V. At $I_o = 0.1A$, i_i is calculated as:

$$200mV \cdot \frac{5A}{V} = 1A$$

Similarly, at $I_o = 2.6A$, i_i is about 10A. At the left figure, the reference of v_o is at the bottom of the voltage divisions. The reference of i_i is clearly seen by the pointer 2 (red) at the left of the figure. At the right figure, the reference of v_o is brought to zero, which is actually 34V as explained earlier with the name of tricky solution. When I_o changes, v_o deviates at most 640mV from the reference. Note that this deviation is within even 2% reference band, namely ∓680mV. In this situation, settling time is regarded as zero. As an additional information, it takes about 15msec for v_o to settle at the very near of the reference voltage. Besides, it is useful to consider that the output power changes 26 folds, between 3.4W and 88.4W.

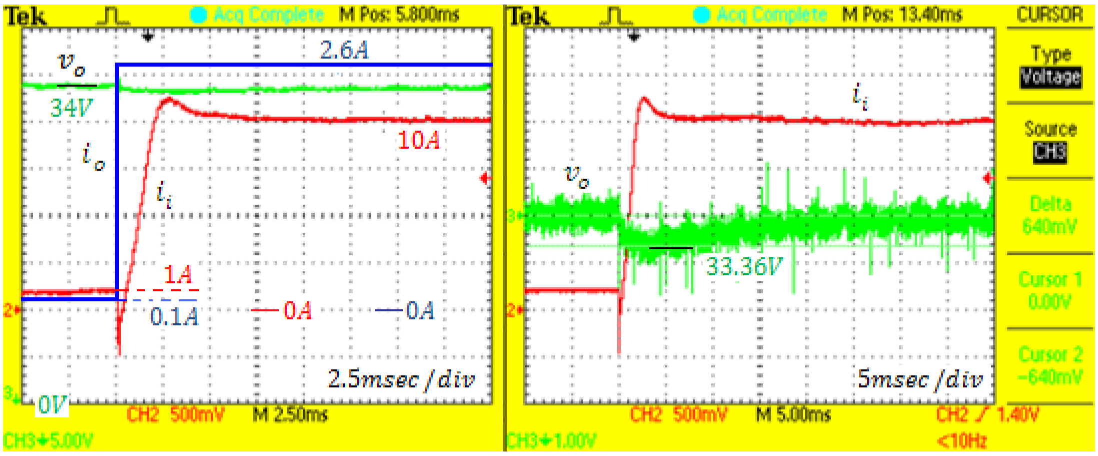

Figure 6-41 $V_i = 10V$, v_o (green) and i_i (red) waveforms at the transition of $I_o: 0.1A \rightarrow 2.6A$

Decrease in v_o when I_o increases is a familiar response. However, i_i decreases at that instant unexpectedly. When the pole zero map of the output current-to-input current transfer function, $G^p_{i_i i_o}(s)$ is investigated, it is seen that it has a right half-plane zero. It is given in Figure 6-42. Therefore, it is a non-minimum phase system. Such kind of systems may show this kind of responses: While it is expected to increase, it decrease first and then increase. Besides, it is not related to control action, because it drops instantaneously. Control action takes place after the error forms. This truth can also be verified by Figure 3-30 in CHAPTER 3.

When the dynamic response of i_i is considered, it is seen that it decreases from 1A to -2.5A instantly, then rises to 10A at 2msec, makes 12% overshoot and settles at 5msec.

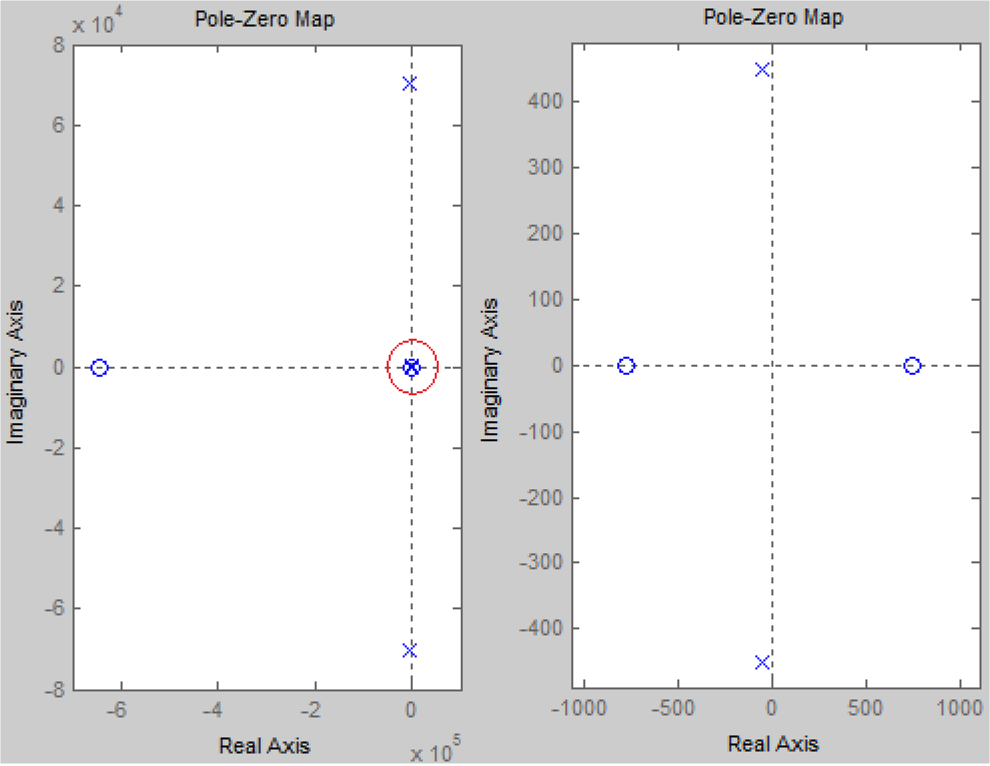

Figure 6-42 Pole-zero map of $G^{p}_{i_i i_o}(s)$

The inverse of this output current step change at the same operating point is given in Figure 6-43. This time i_i increases instantaneously from 10A to 11.5A and then settles to 1A at 2msec without overshoot. v_o shows the same deviation, 640mV

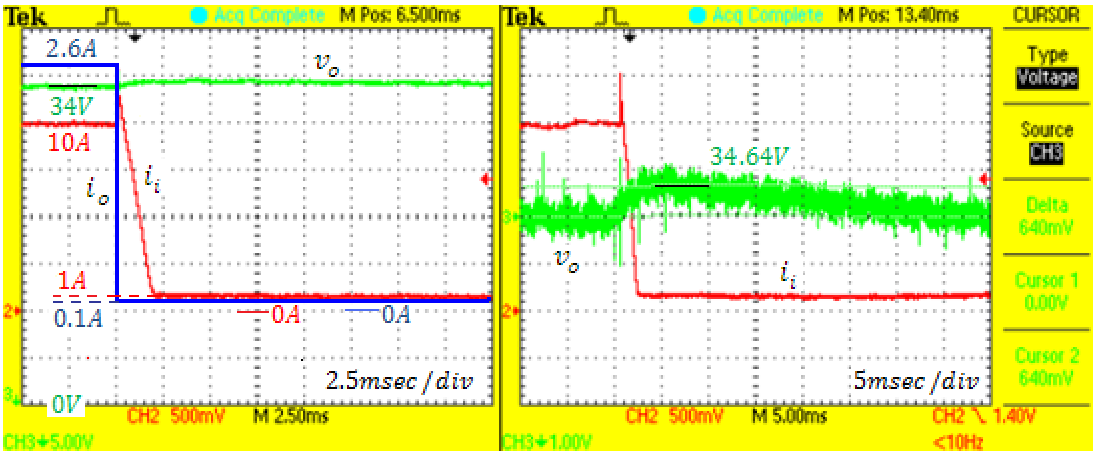

Figure 6-43 $V_i = 10V$, v_o and i_i waveforms at the transition of I_o: $2.6A \rightarrow 0.1A$

and zero settling time. Additionally, it takes about 30msec for v_o to settle at the very near of the reference voltage.

The previous two step changes will be repeated at $V_i = 28V$. The output power changes 29.2 folds, between 8.5W (3.4%) and 248.2W (99.28%). Note that this much change will not occur in the application. At most 25W to 250W output power change will be encountered. These widest possible changes are observed just in order to see the performance of the controller.

In Figure 6-44, it is seen that i_i decreases from 0.75A to -9A instantaneously and then rises to 10A at 1msec, makes 10% overshoot and settles to near 10A at 3msec. When the current reversal is ignored, it can be regarded as a good transient response. Response of v_o is even better. Its deviation is again 640mV, within 2% reference band. Note that while the output power changes from 3.4% to 99.28% of the converter's output power rating, the output voltage deviation stays within the reference band. Additionally, it takes about 15msec for v_o to settle at the very near of the reference voltage.

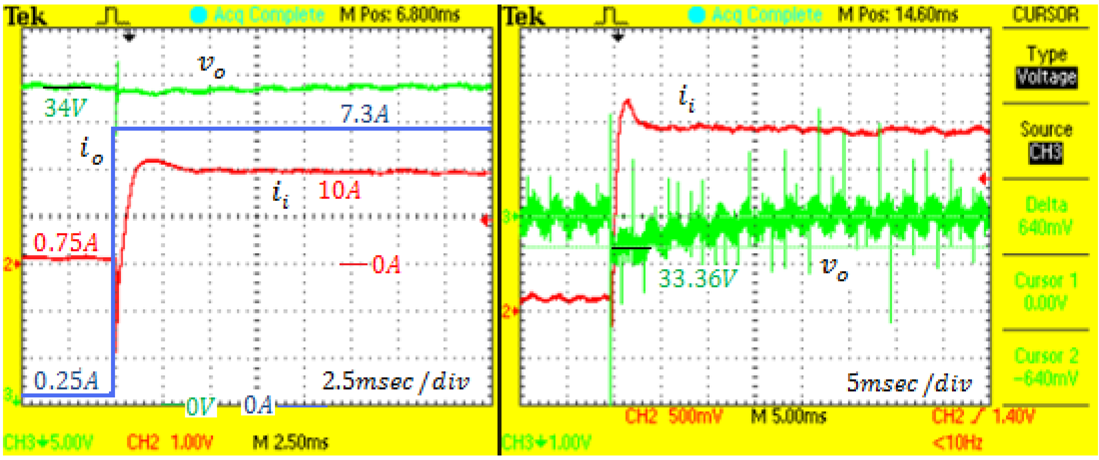

Figure 6-44 $V_i = 28V$, v_o and i_i waveforms at the transition of $I_o: 0.25A \rightarrow 7.3A$

Inverse operation of Figure 6-44 is presented in Figure 6-45. i_i follows the symmetric attitude of the previous result except the overshoot. No overshoot is observed at all in i_i. v_o deviates 760mV, which corresponds to 2.2% of the reference.

It enters within 2% reference band about 15msec and settles exactly to the reference at about 40msec.

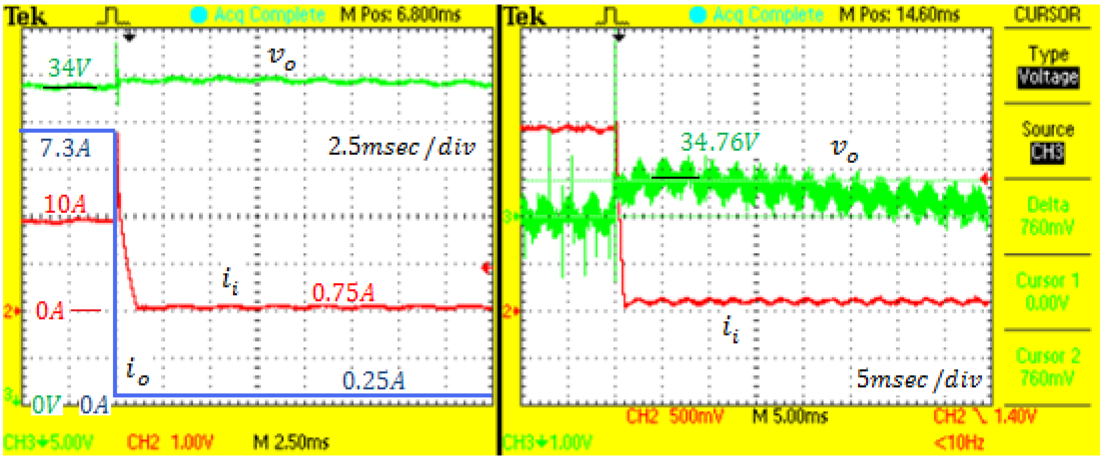

Figure 6-45 $V_i = 28V$, v_o and i_i waveforms at the transition of $I_o: 7.3A \rightarrow 0.25A$

6.3.1.2 Input Current Regulation Mode

In this section, again, transient response of v_o and i_i against step change in I_o will be given. In input current regulation mode, i_i is already limited to the current limit, 10A. I_o values in the following figures are determined accordingly: At the lower I_o, i_i just rise to 10A and v_o just decreases below 34V. At the higher I_o, i_i is still 10A and v_o decreases down to 24V. Besides, since V_i and i_i are constant, output power almost does not change at all. According to I_o, v_o takes a value between 24V and 34V. Actually, v_o is not controlled in this mode. It is doing free fall. What is controlled is i_i.

In Figure 6-46, it is seen that when I_o increases, v_o starts to decrease from just below 34V to just above 24V. Without control action, i_i is expected to decrease instantaneously (if non-minimum phase property is considered) and then increase above 10A. However, it is decremented to 10A by control action. As shown in Figure 6-46, i_i decreases from 10A to 9.2A instantly, then rises to 10.4A (4% overshoot) and stays there until v_o settles down to 24V. After v_o reaches 24V, i_i settles to 10A. The same waveform is also observed in closed-loop simulations. Although the current reference is formed correctly at 10A, i_i can not reach its reference as long as v_o does not reach 24V. The reason may stem from the coupling between the inductors or the control action itself.

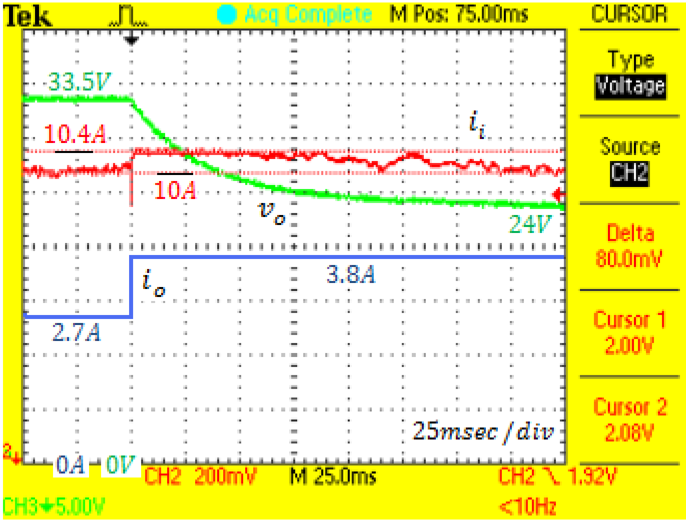

Figure 6-46 $V_i = 10V$, $V_o: 34V \rightarrow 24V$, v_o and i_i waveforms at the transition of $I_o: 2.7A \rightarrow 3.8A$

The inverse action is introduced in Figure 6-47. The same arguments given in the

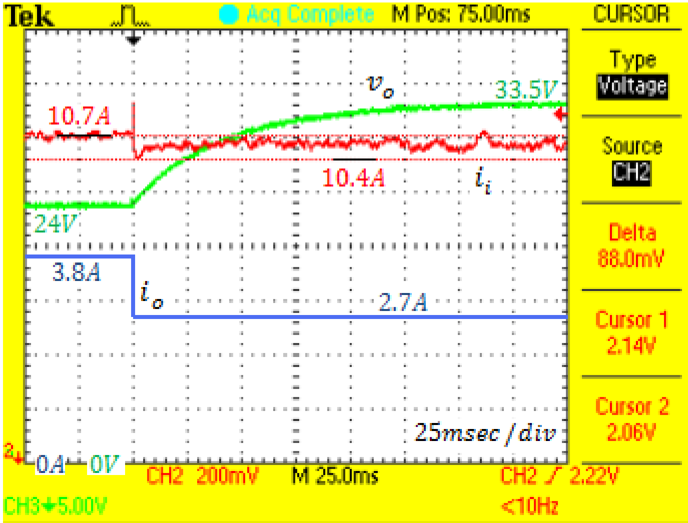

Figure 6-47 $V_i = 10V$, $V_o: 24V \rightarrow 34V$, v_o and i_i waveforms at the transition of $I_o: 3.8A \rightarrow 2.7A$

previous figure also apply here. Note that the output power is about 91W in these two figures.

Previous two measurements are repeated at $V_i = 28V$. This time, power level is at 253W. The above arguments hold for the following two measurements too. When I_o changes, i_i decreases from 10.25A to 6.75A immediately. Then it rises up to 10.9A. Although it does not stay at that level, it cannot return to its reference before V_o reaches 24V. It takes 100msec for i_i to reach exactly its reference.

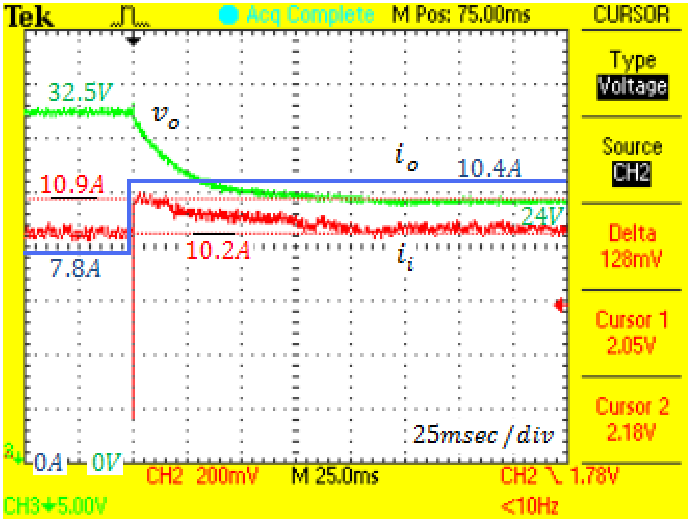

Figure 6-48 $V_i = 28V$, $V_o: 34V \rightarrow 24V$, v_o and i_i waveforms at the transition of $I_o: 7.8A \rightarrow 10.4A$

As it is clearly seen in Figure 6-49, i_i can returns to its reference more quickly during $V_o: 24V \rightarrow 34V$ transition, about 15msec.

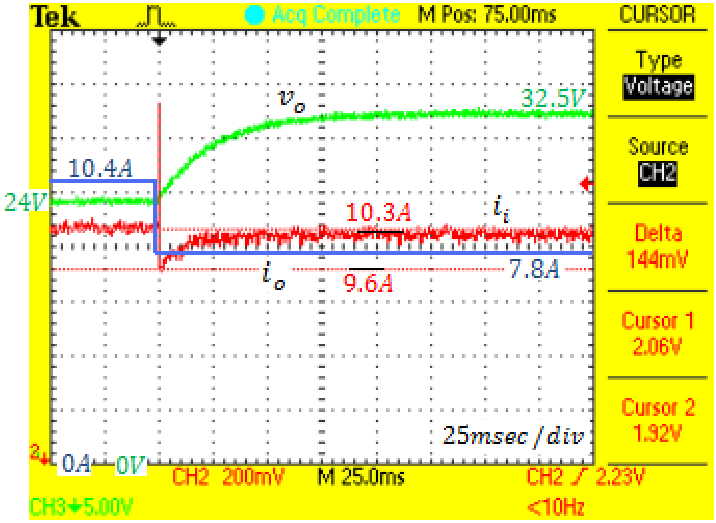

Figure 6-49 $V_i = 28V$, $V_o: 24V \rightarrow 34V$, v_o and i_i waveforms at the transition of $I_o: 10.4A \rightarrow 7.8A$

6.3.1.3 Transition between the Regulation Modes

In this section, the output current will be changed between no-load current and the current at which the output voltage decreases down to its lower limit, 24V. That is, I_o will be changed between the farthest points among two regulation modes. Therefore, regulation mode will change during these transitions. Different dynamic responses are expected.

In Figure 6-50 and Figure 6-51, output power is changed stepwise between 3.4W (1.36%) and 129.2W (51.68%) at $V_i = 10V$. When the load is increased, i_i increases to 10A at about 2 msec with a negligible overshoot. As expected, v_o falls down to 24V freely. When the load is decreased, i_i wants to decrease after its instant increase without control action. However, since v_o is under its reference, i_i is forced to be 10A until v_o reaches 34V. It can be observed in Figure 6-51. Most of 10A drawn from the input is used to charge the energy transferring (C_1) and output (C_o) capacitor during 30msec. Then, i_i decreases to 1A in 2.5msec. Also v_o increases from 24V to 34V in 30msec with 500mV overshoot, which is within 2% reference band.

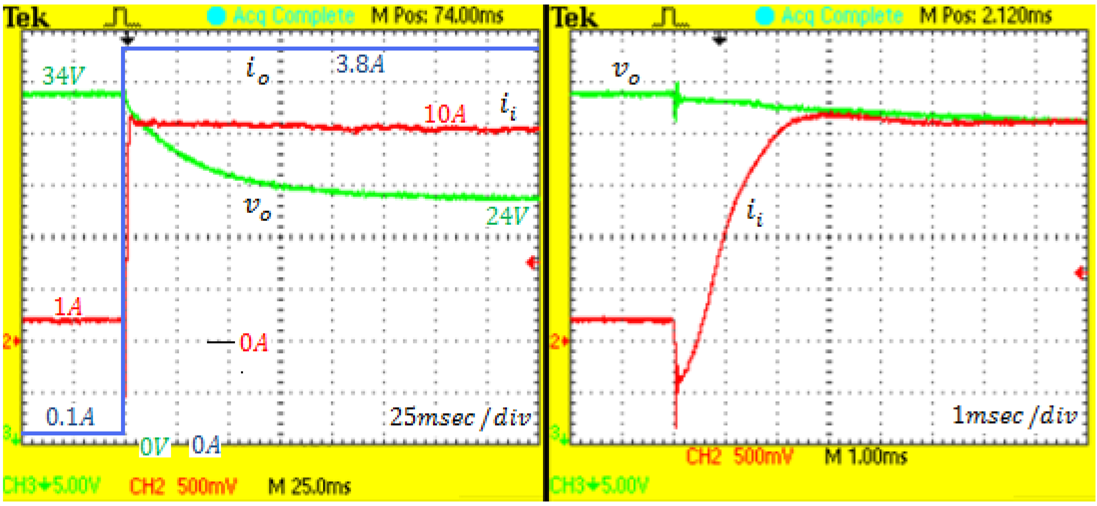

Figure 6-50 $V_i = 10V$, $V_o: 34V \rightarrow 24V$, v_o and i_i waveforms at the transition of $I_o: 0.1A \rightarrow 3.8A$

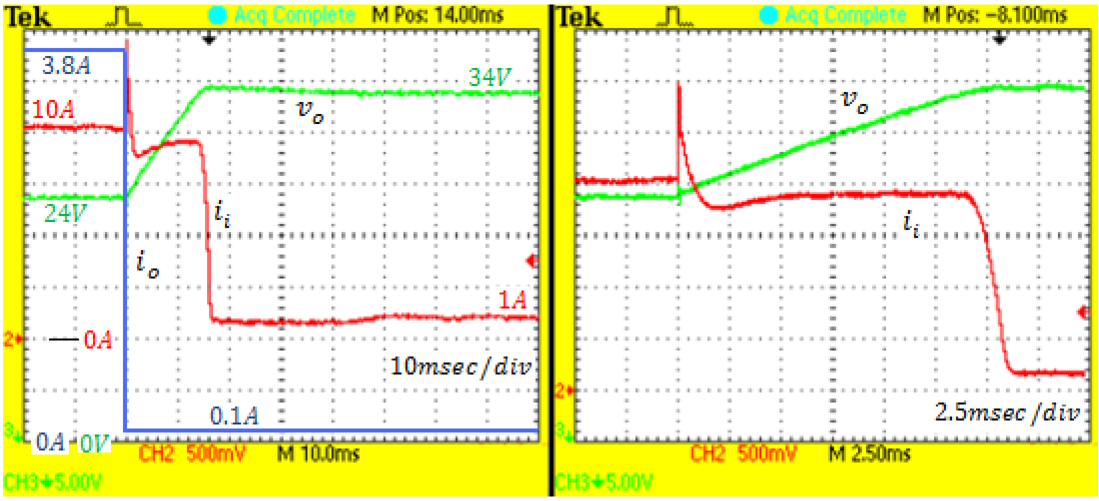

Figure 6-51 $V_i = 10V$, $V_o: 24V \rightarrow 34V$, v_o and i_i waveforms at the transition of $I_o: 3.8A \rightarrow 0.1A$

Previous two measurements are repeated at $V_i = 28V$ in Figure 6-52 and Figure 6-53. Output power changes between 8.5W (3.4%) and 250W (100%). When the load is increased, i_i increases from 1A to 10A in 0.8msec. It makes 20% overshoot and settles in 3.5msec. The similar arguments in $V_i = 10V$ case are valid when the load is decreased. However, this time, settling time of v_o is 7.5msec. Since the input voltage is high, C_1 and C_o is charged faster.

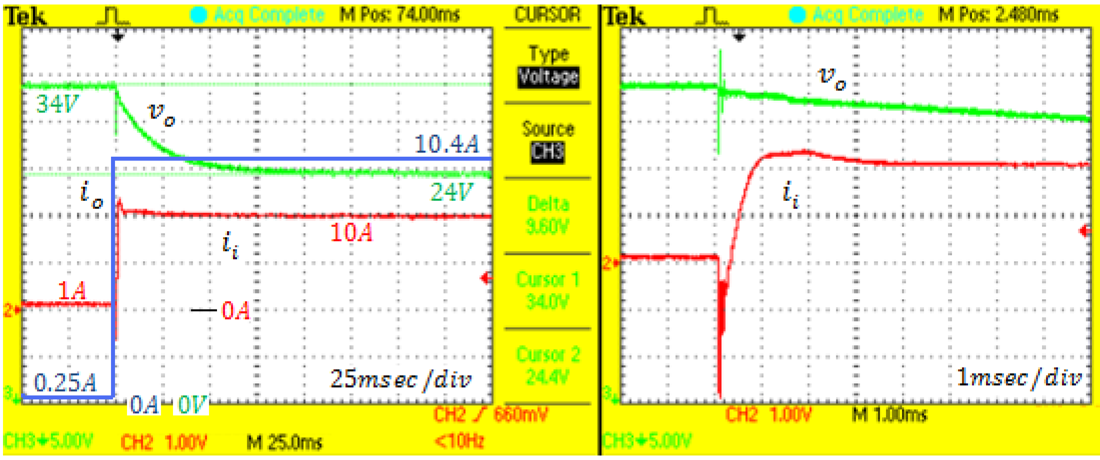

Figure 6-52 $V_i = 28V$, $V_o: 34V \rightarrow 24V$, v_o and i_i waveforms at the transition of $I_o: 0.25A \rightarrow 10.4A$

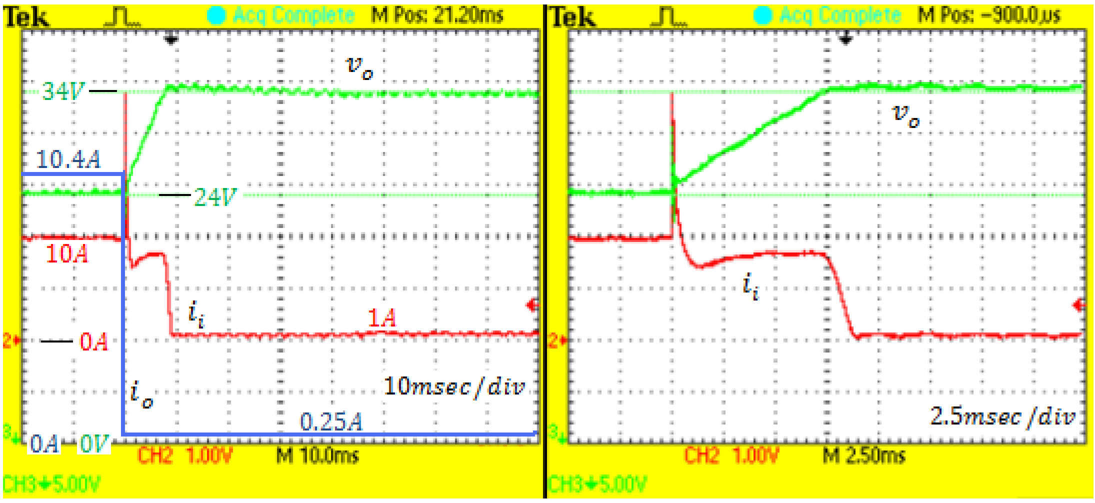

Figure 6-53 $V_i = 28V$, $V_o: 24V \rightarrow 34V$, v_o and i_i waveforms at the transition of $I_o: 10.4A \rightarrow 0.25A$

6.3.2 Constant Input Power Mode

Test results are classified at the following subsections. At first, the timing diagram of the control loop will be given. This time, the selected dsPIC makes it possible to refresh the duty-factor at a rate of 3 times the switching frequency, namely 30usec. PWM signal (red) and timing signal (blue) are shown in Figure 6-64. Similarly, at $t = 0usec$, PWM signal goes high. After 1usec, ADC conversion starts in synchronous with PWM signal. Then, at $t = 4.5usec$ ADC conversion is completed. ADC conversion of 3 channels, by the addition of V_i to the other 2 channels, lasts 3.5usec. Digital PI controller calculations take about 24.8usec. Because of the division of (280W/V_i), the required time for the calculations increases much. At $t = 29.3usec$, new duty-factor is determined. In this way, it is prepared for the new PWM cycle.

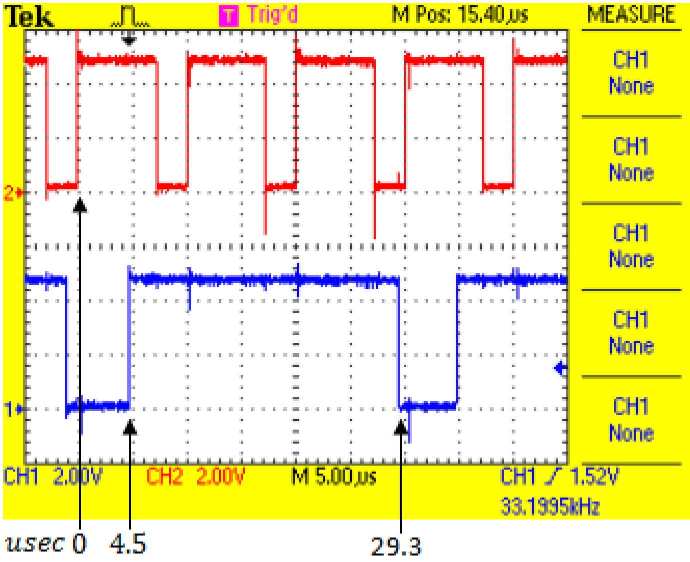

Figure 6-54 Timing diagram of the control loop for CIPM

In this control mode, the only difference is the current limit. While it is constant at 10A in CICM, it is calculated as (280W/V_i)A at each control cycle.

6.3.2.1 Output Voltage Regulation Mode

In this section, the load current is changed stepwise between no-load current and the current at which the input power is just below 280W. That is, the output voltage is regulated.

In Figure 6-55 and Figure 6-56, output power changes between 3.4W (1.36%) and 241.4W (96.56%). Current probe scale is at 50A/V in these two figures. Hence, i_i changes between 1A and 27.3A. Of course, energizing or de-energizing two 120uH-inductors with these current levels takes time. When the load current is increased as seen in Figure 6-55, v_o decreases until i_i increases to the load current level. i_i increases to 27.3A in 7.5msec. While this is happening, v_o decreases 3.6V (10.5%). It returns to its reference band in 40msec and settles exactly in 50msec. Note that the current response is nearly three times faster in CICM than in CIPM. Voltage response is directly related to the current response as seen in Figure 6-55. Since the way that will be taken by i_i is about 3 times 10A, the required time for i_i to settle increases about that much. C_1 and C_o stays alone in supplying the output power in this increased time interval. Hence, their voltage decreases much.

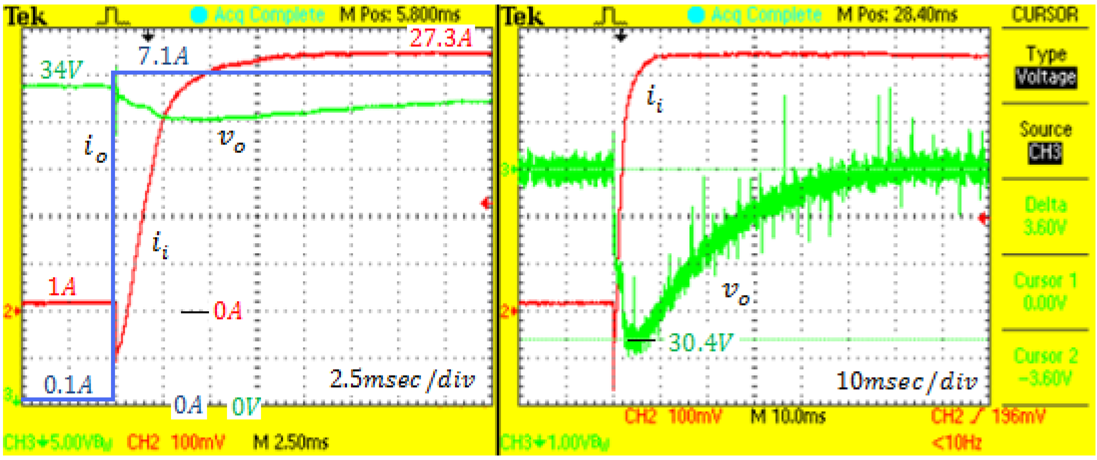

Figure 6-55 $V_i = 10V$, v_o and i_i waveforms at the transition of $I_o: 0.1A \rightarrow 7.1A$

When the load current is decreased, i_i decreases in 2.5msec without overshoot. This excessive current-time integral during this period is seen on C_1 and C_o as a voltage deviation. v_o deviates 2.76V (8.1%) and returns to its reference in 150msec.

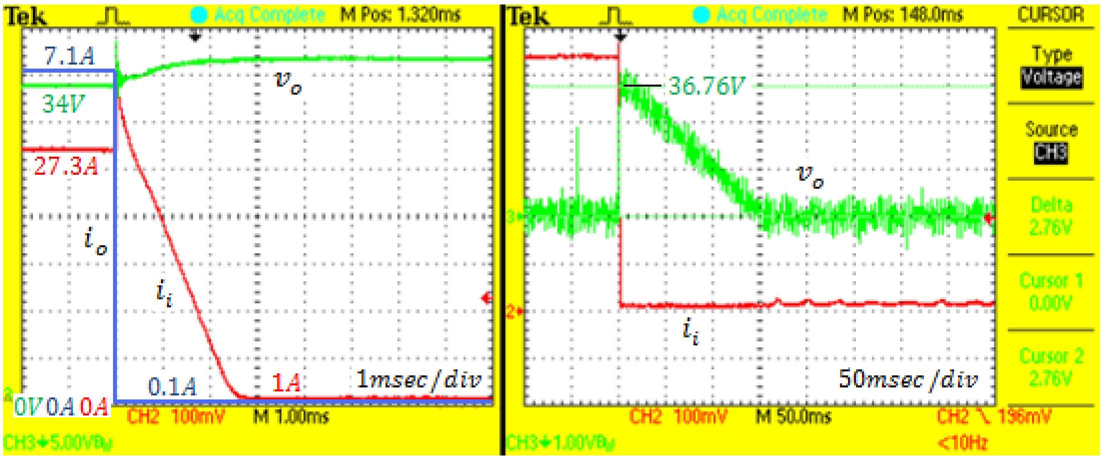

Figure 6-56 $V_i = 10V$, v_o and i_i waveforms at the transition of $I_o: 7.1A \rightarrow 0.1A$

Similar waveforms are observed at $V_i = 28V$ in Figure 6-57 and Figure 6-58. This time the output power changes between 8.5W (3.4%) and 255W (102%). When I_o is increased, i_i increases from 1A to 10A in 2msec. v_o deviates 1.24V (3.6%), reaches the reference band in 30msec and settles exactly there in 40msec. When I_o is decreased, i_i decreases from 10A to 1A in 1.8msec. v_o deviates again the same amount, reaches the reference band in 60msec and settles exactly there in 100msec.

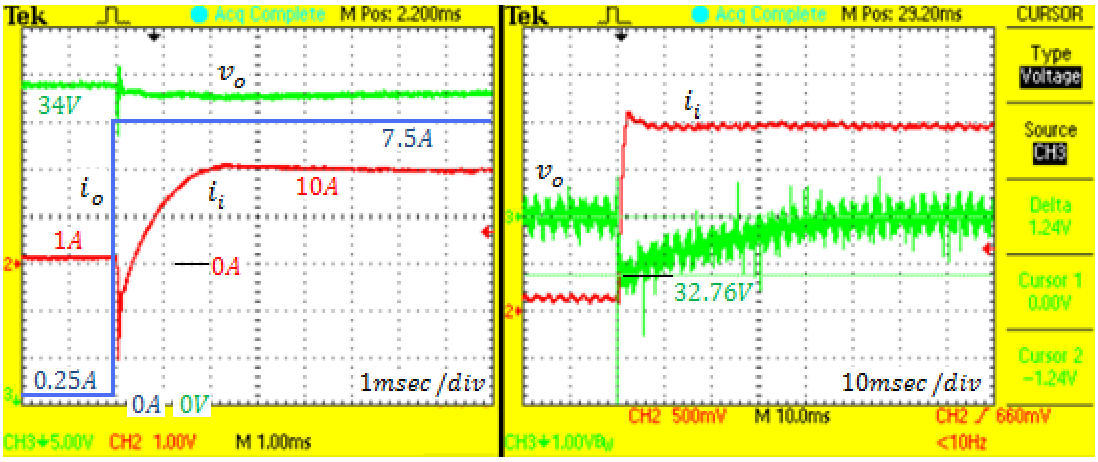

Figure 6-57 $V_i = 28V$, v_o and i_i waveforms at the transition of $I_o: 0.25A \rightarrow 7.5A$

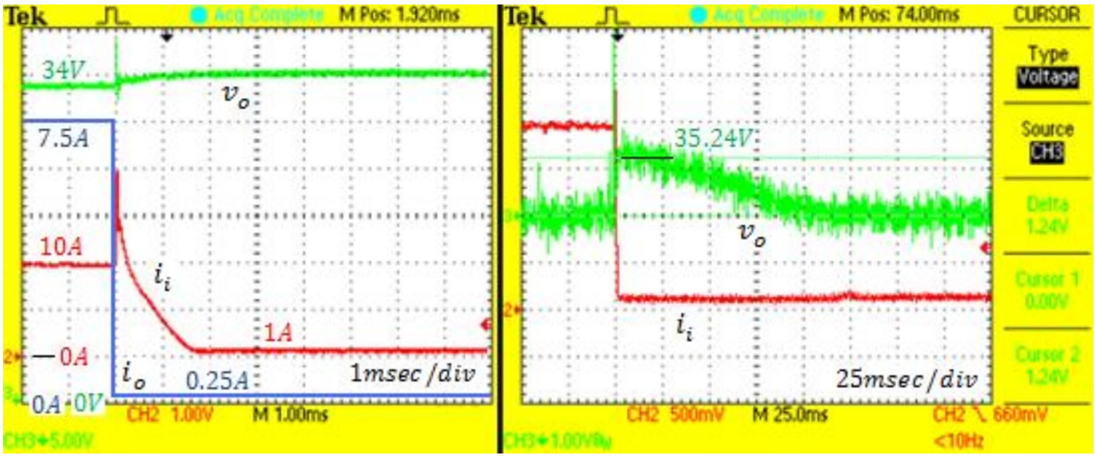

Figure 6-58 $V_i = 28V$, v_o and i_i waveforms at the transition of I_o: $7.5A \rightarrow 0.25A$

6.3.2.2 Input Power Regulation Mode

In this mode, rather than the output voltage, input power will be regulated to 280W. Since the input voltage is constant, what is regulated actually is the input current. Lower I_o values are the output currents at which the output voltage is just below 34V. Similarly, upper I_o values are the current at which the output voltage is just above 24V. However, at both ends, the input power is constant at about 280W.

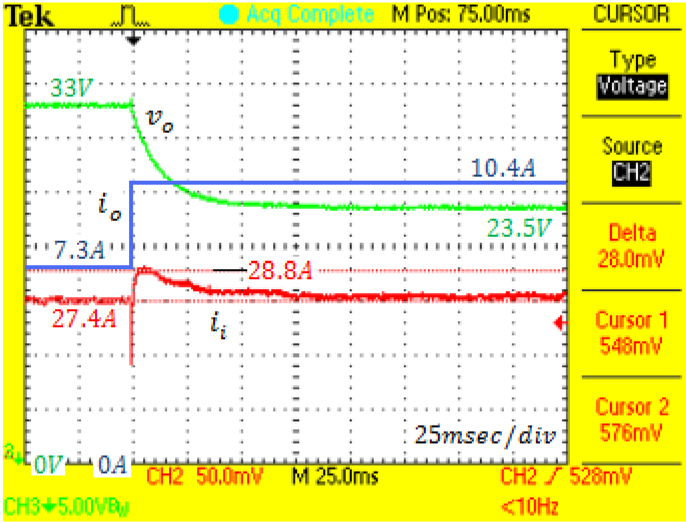

Figure 6-59 $V_i = 10V$, V_o: $34V \rightarrow 24V$, v_o and i_i waveforms at the transition of I_o: $7.3A \rightarrow 10.1A$

In Figure 6-59 and Figure 6-60, current probe scale is 50A/V. Input power is regulated to 274W. When I_o is increased, i_i deviates 1.4A (5.1%). It returns to its reference band in 32msec and settles exactly in 75msec. When I_o is decreased, i_i deviates 1.6A (6.1%). It has the same timing values. Note that Figure 6-59 and Figure 6-60 are highly symmetrical.

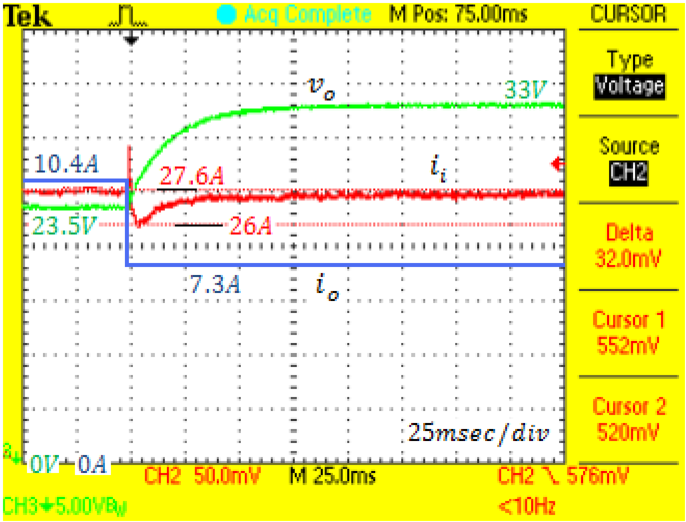

Figure 6-60 $V_i = 10V$, $V_o: 24V \rightarrow 34V$, v_o and i_i waveforms at the transition of $I_o: 10.1A \rightarrow 7.3A$

In Figure 6-61 and Figure 6-62, the previous measurements are repeated at $V_i = 28V$. Input power is again regulated to 274W. When I_o is increased, i_i deviates 0.8A (8%). It returns to its reference band in 40msec and settles exactly in 50msec. When I_o is decreased, i_i deviates 1A (10%). It has the same timing values. Again, Figure 6-61 and Figure 6-62 are highly symmetrical. In these four figures, it is observed that i_i cannot settle until v_o reaches its stable point.

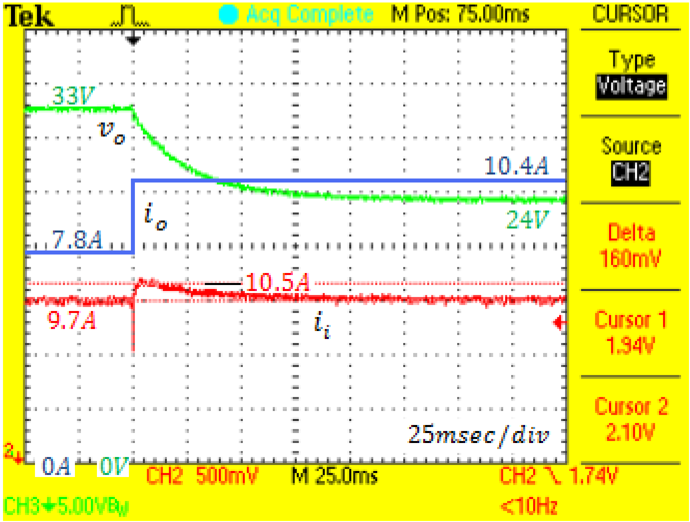

Figure 6-61 $V_i = 28V$, $V_o: 34V \rightarrow 24V$, v_o and i_i waveforms at the transition of $I_o: 7.8A \rightarrow 10.4A$

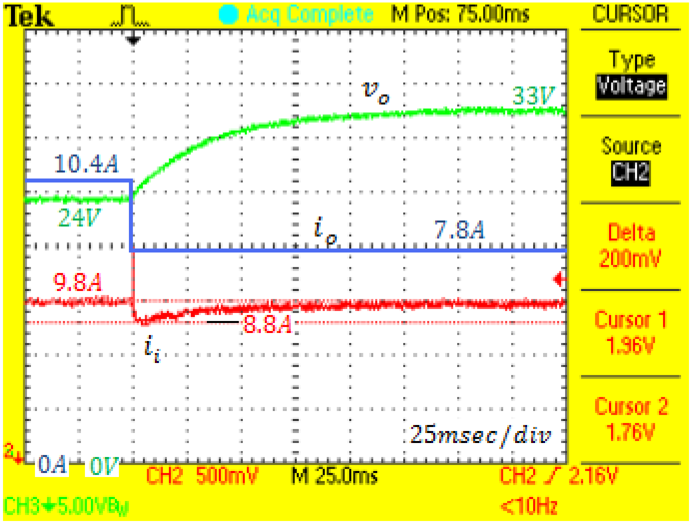

Figure 6-62 $V_i = 28V$, $V_o: 24V \rightarrow 34V$, v_o and i_i waveforms at the transition of $I_o: 10.4A \rightarrow 7.8A$

6.3.2.3 Transition between the Regulation Modes

In this section, the minimum I_o are selected as the no-load current and the maximum I_o are the output currents at which v_o drops to just above 24V. That is, the farthest points among output voltage regulation mode and input power regulation mode are used. Hence, the output power change is very high in these measurements.

In Figure 6-63 and Figure 6-64, current probe scale is at 50A/V. Output power changes between 3.4W (1.36%) and 242.4W (96.96%). When the figures are investigated, it is realized that the arguments in the corresponding section of CICM

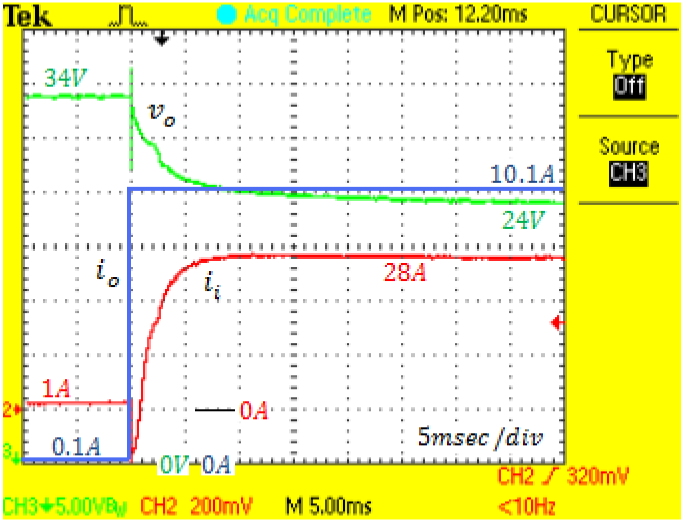

Figure 6-63 $V_i = 10V$, $V_o: 34V \rightarrow 24V$, v_o and i_i waveforms at the transition of $I_o: 0.1A \rightarrow 10.1A$

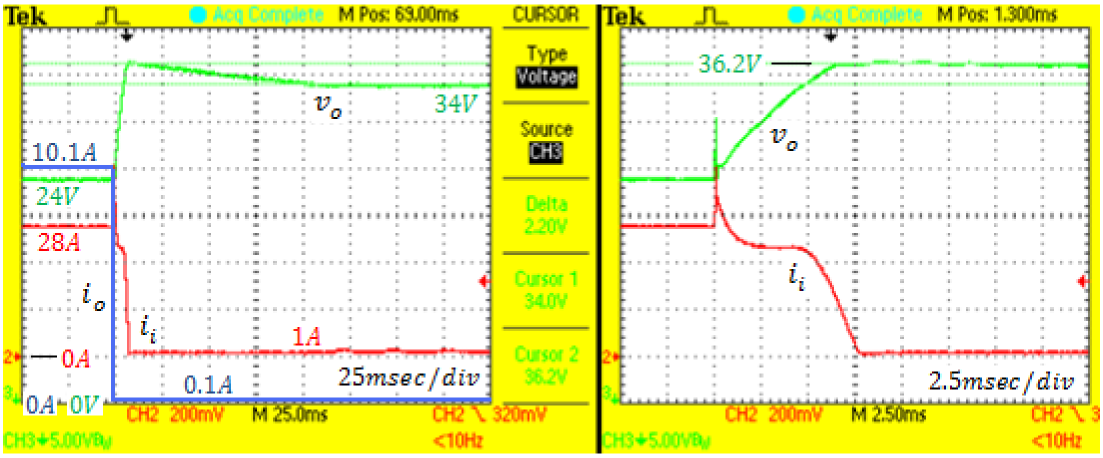

Figure 6-64 $V_i = 10V$, $V_o: 24V \rightarrow 34V$, v_o and i_i waveforms at the transition of $I_o: 10.1A \rightarrow 0.1A$

also holds here. When I_o is increased, i_i increases to about 28A in 7.5msec and v_o settles to 24V band at the same time. Just after I_o is decreased; v_o rises to 34V in 6msec, makes 2.2V (6.4%) overshoot, enters its reference band in 75msec and settles exactly in 100msec. i_i reaches its stable point in 7.5msec.

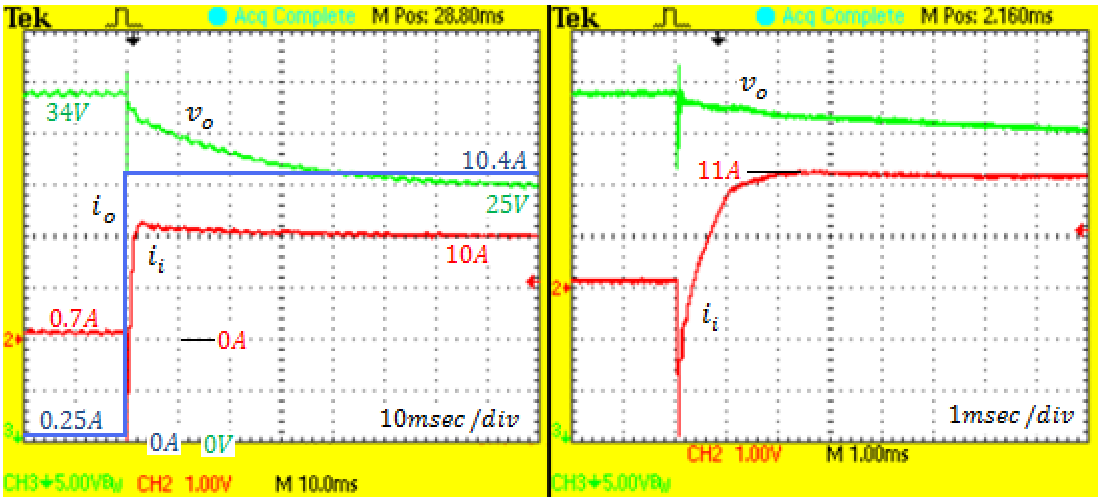

Figure 6-65 $V_i = 28V$, $V_o: 34V \rightarrow 24V$, v_o and i_i waveforms at the transition of $I_o: 0.25A \rightarrow 10.4A$

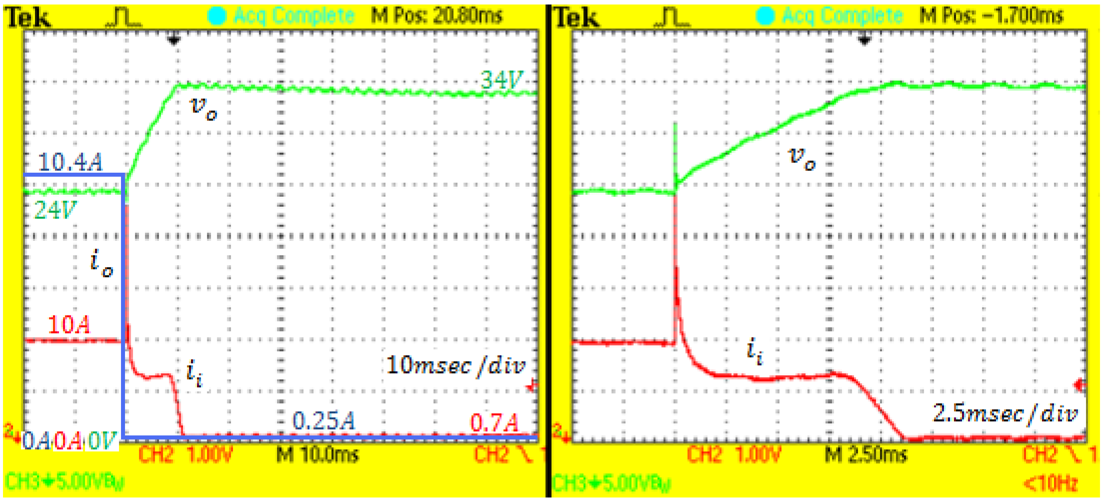

Figure 6-66 $V_i = 28V$, $V_o: 24V \rightarrow 34V$, v_o and i_i waveforms at the transition of $I_o: 10.4A \rightarrow 0.25A$

When the same transitions are repeated at $V_i = 28V$, Figure 6-65 and Figure 6-66 are obtained. Output power changes between 8.5W (3.4%) and 249.6W (99.84%). When I_o is increased; i_i increases to about 10A in 1.3msec, makes 15% overshoot. It settles exactly when v_o settles to 24V. When I_o is decreased; v_o rises to 34V in 8.5msec, makes 0.8V (2.3%) overshoot, enters its reference band in 25msec and settles exactly in 50msec. i_i reaches its stable point in 11.2msec.

CHAPTER 7

SUMMARY AND CONCLUSIONS

It has been observed that despite the presence of the parasitic elements and many practical problems in the implementation of the coupled-inductor Ćuk converter, satisfactory results are obtained in terms of voltage and current waveforms. Besides, in design process, in order to provide coupling condition, an adjustment inductor is added to one of the inductors. Ćuk has preferred to adjust the air gap in order to provide coupling. Since it necessitates very sensitive positioning and seems to be not practical, a more practical approach, namely adjustment inductor method, is suggested and verified by the simulations and implementation. Utilization of this method eases the implementation very much.

Implementation of integrated magnetic Ćuk converter is considered to be troublesome because there are two airgaps to be positioned sensitively in that case. Moreover, they are not independent. Hence, an iterative positioning must be performed during the circuit is operating. As Ćuk has suggested, iteration goes on until the ripple-free input and output currents are obtained. Following the application of adjustment inductor method to coupled-inductor, it is realized that the same method can also be applied to integrated magnetic structure. The balance between L_1 and L_a is provided by adding an adjustment inductor to L_a and ripple-free input current waveform can be obtained. Similarly, the balance between L_2 and L_b is provided by adding an adjustment inductor to L_b and ripple-free output current waveform can be reached. In this way, it is not struggled with dependency and sensitive positioning of the cores. Note that this approach is not validated for integrated magnetic structure and it is given just as a proposal for future works.

In theory, it is expected to get ripple-free input current waveforms at each operating point for the implemented circuit. In practice, however, due to the parasitic and nonlinear characteristics of the circuit elements, getting ripple-free input current waveform is expected to deteriorate to some extent. In the implemented circuit, this fact is observed. While a ripple percent well below 1% is obtained in one operating point, 2% ripple percent is reached at another operating point at the same load level. This low degradation may be regarded as the success in selection of the core material and type. Recall that the B-H curve of the selected core plays an important role in the deterioration of the ripple-free current waveform property with respect to the operating conditions.

In the implemented circuit, voltage overshoots turn out to be much lower than as expected. Since the switched current can be at most 40A, serious voltage overshoots are expected in the beginning. Therefore, use of RC snubber circuits are planned in order to limit the voltage overshoots on the switch and the diode. During layout process, much attention is paid to minimize the parasitic inductances of the paths where pulsating current pass. As a result, voltage overshoots turns out to be low and snubber circuits are not used.

The efficiency of the implemented converter can be regarded as high when the voltage, current and power levels are considered. Note that hard switching is utilized in the implemented circuit. Using this switching method, further increases in efficiencies are not possible. Ćuk has brought a solution to this problem and suggested Ćuk converter versions which are utilizing soft switching technique. In this way, switching losses are eliminated and only conduction losses remains. Moreover, since the switching frequency can be increased, dimensions of the filter elements (i.e. capacitors and inductors) decrease dramatically. As a result, more efficient and compact converter is obtained. For future work, soft switching versions of the Ćuk converter are strictly recommended. Detailed information about them can be found in [28, 32, 33].

In obtaining the transfer functions of the circuit, state-space averaging method has been used and it has given accurate results. Most of the time, a simpler method is used in the derivation of transfer functions of switching circuit. In that method, the circuit is generally divided into a switching structure, an isolation transformer (if it exists) and L-C output filter. Since a coupled-inductor has been utilized in the circuit, this division could not be accomplished and therefore that technique has not been realized. It is observed that state-space averaging method gives very accurate results in this type of extraordinary situations. It also lets the parasitic elements of the switching structure and the isolation transformer be included in the transfer functions. In the simple method, however, only the parasitic elements of the output L-C filter can be included.

In the control of the implemented circuit, some theoretical problems are encountered. Since the circuit has four energy storing elements with two inductors and two capacitors, the order of the denominator of the transfer functions turns out to be four. This order is two in most of the circuit topologies, which comes from the output L-C filter. Therefore, many of the widely known control approaches for the switching converters are not applicable. This may not be regarded as a problem. The real problem is that some transfer functions have zeros with positive real parts. These kinds of systems are called non-minimum phase systems and exhibits unfamiliar responses. Moreover, these systems are known to be hard to control and have slower dynamic responses with respect to minimum phase systems. These facts have been faced with during simulating and implementing the control of the circuit. For example, when voltage mode control was applied, the output voltage oscillated continuously. The use of current mode control has solved this problem. Besides, when the response times of the circuit are investigated, it may be argued that the system responds slowly. Trying to decrease the response times is possible by modifying the controller functions. However, doing so makes the output variables oscillates. As a consequence, the converter has to responds slowly in order to be stable and not to be oscillatory.

At the beginning, there are not any dynamic response specifications for the implemented circuit. Therefore, the circuit is designed according to steady-state specifications such as current and voltage ripples on the elements. When the dynamic response of the circuit is to be improved, it is realized that the poles and zeros of the derived transfer functions do not permit such an improvement. The locations of the poles and zeros depend on the parameters of the circuit elements. Hence, improving the dynamic response necessitates redesign of the circuit. As a result, the following conclusion is reached for future works: If the dynamic response of the converter is important for a particular application, the dynamic response specifications must be considered in the design phase of the circuit and in the selection phase of the circuit components. For example, for a little improvement in steady-state response, one may select a larger energy storing element. However, this may result in a much more degradation in dynamic response.

REFERENCES

[1]: Slobodan Ćuk, “Modelling, Analysis, and Design of Switching Converters”, Ph.D. thesis, *California Institute of Technology,* November 1976

[2]: Zekiye Günaydın, “Analysis and Design of a Ćuk Switching Regulator”, M.Sc. thesis, *Middle East Technical University*, May 2009

[3]: R.D.Middlebrook and S.Ćuk, “A General Unified Approach to Modelling Switching-Converter Power Stages”, *Proceedings of the IEEE Power Electronics Specialists Conference*, Cleveland, OH, June 1976

[4]: W.M.Polivka, P.R.K.Chetty and R.D.Middlebrook, “State-Space Average Modelling of Converters with Parasitic and Storage-Time Modulation”, In *Proceedings of the IEEE Power Electronics Specialists Conference*, Atlanta, GA, June 1980

[5]: Slobodan Ćuk, “Basics of Switched-Mode Power Conversion: Topologies, Magnetics, and Control”, *Advances in Switched-Mode Power Conversion Volumes I and II*, pp. 279-310, TESLAco, Pasadena, CA, July 1983

[6]: Slobodan Ćuk and R.D.Middlebrook, “A New Optimum Topology Switching DC-to-DC Converter”, *Proceedings of the IEEE Power Electronics Specialists Conference*, Palo Alto, CA, June 1977

[7]: Slobodan Ćuk and R.D.Middlebrook, “Coupled-Inductor Extension of a New Optimum Topology Switching DC-to-DC Converter”, *Proceedings of the IEEE Industry Applications Society Annual Meeting,* Los Angeles, CA, October 1977

[8]: Slobodan Ćuk, “Switching DC-to-DC Converter with Zero Input or Output Current Ripple”, *Proceedings of the IEEE Industry Applications Society Annual Meeting,* Toronto, ONT, October 1978

[9]: L.Rensink, A.Brown, S.P.Hsu and S.Ćuk, “Design of a Kilowatt Off-Line Switcher Using a Ćuk Converter”, *Proceedings of the Sixth National Solid-State Power Conversion Conference,* Miami Beach, FL, May 1979

[10]: Slobodan Ćuk, “A New Zero-Ripple Switching DC-to-DC Converter and Integrated Magnetics”, *Proceedings of the IEEE Power Electronics Specialists Conference,* Atlanta, GA, June 1980

[11]: Slobodan Ćuk and R.D.Middlebrook, “Advances in Switched-Mode Power Conversion Part I”, *Robotics Age,* Vol. 1, No. 2, pp. 6-19, Winter 1979

[12]: Slobodan Ćuk and R.D.Middlebrook, “Advances in Switched-Mode Power Conversion Part II”, *Robotics Age,* Vol. 2, No. 2, pp. 28-41, Summer 1980

[13]: Slobodan Ćuk, “New Magnetic Structures for Switching Converters”, *IEEE Transactions on Magnetics,* Vol. MAG-19, No. 2, pp. 75-83, March 1983

[14]: R.D.Middlebrook, “Generalized Theory of Switching DC-to-DC Converters”, *Proceedings of Region 6 Conference,* Anaheim, CA, February 1982

[15]: Alan Cocconi and Slobodan Ćuk, “Design of a 2kW, 100kHz Switching Regulator for Space Shuttle”, *Proceedings of the Fifth International PCI’82*, Geneva, Switzerland, September 1982

[16]: S.Ćuk and William M.Polivka, “Analysis of Integrated Magnetics to Eliminate Current Ripple in Switching Converters”, *Proceedings of the Sixth International PCI’83,* Orlando, FL, April 1983

[17]: S.Ćuk and John F. Brewer, “Low Noise, Low Cost 150W Off-Line Switcher”, *Powerconversion International Magazine,* Vol. 9, No. 4, April 1983

[18]: R.D.Middlebrook, “Design Considerations and Noise Reduction in Switching Converters”, *Powerconversion International Magazine,* 1983

[19]: Keyue M.Smedley and S.Ćuk, “Dynamics of One-Cycle Controlled Ćuk Converters”, *IEEE Transactions on Power Electronics,* Vol. 10, No. 6, November 1995

[20]: J.Mahdavi, A.Emadi and H.A.Toliyat, “Application of State Space Averaging Method to Sliding Mode Control of PWM DC/DC Converters”, *IEEE Industry Applications Society Annual Meeting,* New Orleans, Louisiana, October 1997

[21]: C.K.Tse and William C.Y.Chan, “Instability and Chaos in a Current-Mode Controlled Ćuk Converter”, *Hong Kong Polytechnic University,* 1995

[22]: Enrico Santi and S.Ćuk, “Modelling of One-Cycle Controlled Switching Converters”, *California Institute of Technology,* 1992

[23]: Vatché Vorpérian, “The Effect of the Magnetizing Inductance on the Small-Signal Dynamics of the Isolated Ćuk Converter”, *IEEE Transactions on Aerospace and Electronic Systems,* Vol. 2, No. 3, July 1996

[24]: Robert W.Erickson and D.Maksimović, “Fundamentals of Power Electronics”, Second Edition, Kluwer Academic Publishers, Massachusetts, January 2004

[25]: Philip T.Krein, “Elements of Power Electronics”, Oxford University Press, Oxford, New York, 1998

[26]: Slobodan Ćuk and R.D.Middlebrook, “DC-to-DC Switching Converter”, United States Patent, No. 4,184,197, January 1980

[27]: Enrico Santi, Aliso Viejo and S.Ćuk, “Low Profile Coupled Inductors and Integrated Magnetics”, United States Patent, No. 5,790,005, August 1998

[28]: Slobodan Ćuk, “Lossless Switching DC to DC Converter with DC Transformer”, United States Patent, No. 6,400,579 B2, June 2002

[29]: “Magnetic Core Characteristics”, Texas Instruments, 2001

[30]: “SIFERRIT Material N27”, Epcos, September 2006

[31]: “PM 74/59 Core and Accessories”, Epcos, September 2006

[32]: Slobodan Ćuk, “Lossless Switching Converter with DC Transformer”, United States Patent, No. 6,388,896, May 2002

[33]: Slobodan Ćuk, “Lossless Switching DC-to-DC Converter”, United States Patent, No. 6,462,962, October 2002